



**UNIVERSITY OF
BIRMINGHAM**

**Ultrasound-Responsive Silica Nanoparticles for
the Delivery of Antimicrobial Agents in
Dentistry**

By

Menisha Manhota

A thesis submitted to the University of Birmingham for the degree of

DOCTOR OF PHILOSOPHY

School of Chemistry

College of Engineering and Physical Sciences

University of Birmingham

March 2022

UNIVERSITY OF
BIRMINGHAM

University of Birmingham Research Archive

e-theses repository

This unpublished thesis/dissertation is copyright of the author and/or third parties. The intellectual property rights of the author or third parties in respect of this work are as defined by The Copyright Designs and Patents Act 1988 or as modified by any successor legislation.

Any use made of information contained in this thesis/dissertation must be in accordance with that legislation and must be properly acknowledged. Further distribution or reproduction in any format is prohibited without the permission of the copyright holder.

Abstract

Dental infections and diseases are a global health problem. They are caused by the failure to treat and remove biofilms from surfaces in the oral cavity. Current antimicrobial treatments are extensive and ineffective for localised antibiotic delivery to biofilms.

This work describes the first ultrasound-responsive silica nanoparticle (SNP) drug delivery system for antimicrobial agents. The optimised preparation of antimicrobial agent, cetylpyridinium chloride (CPC) has been successfully encapsulated into silica nanoparticles. The drug delivery system has shown promising stability with minimal leakage and enhanced release kinetics when exposed to ultrasonic cavitation, produced from an ultrasonic scaler device used in dentistry.

The **CPC@SNP** nanosystem was further investigated for its antimicrobial activity against *Streptococcus sanguinis* biofilms. A significant synergistic effect was shown by the combination of **CPC@SNP** and ultrasound compared to CPC alone. Therefore, showing a promising strategy for the localised and controlled delivery of antibiotics.

This proof-of-concept model, lead to the successful encapsulation of the antibiotic, ciprofloxacin (CPX) into SNPs with smaller NP sizes. The **CPX@SNP** nanosystem showed promising US-responsive release and enhanced antimicrobial activity against *Streptococcus mutans* biofilms compared to larger drug loaded SNPs.

Acknowledgments

Firstly, I would like to express my sincerest gratitude to my PhD supervisory team. Thank you to Prof. Zoe Pikramenou, for her continued guidance and support throughout my project. I would also like to thank my dental supervisors, Dr Sarah Kuehne, Dr Rachel Sammons, Prof. Damien Walmsley for training me in microbiology, always providing advice and being so positive.

I am fortunate to have had the opportunity to collaborate with other academics from various departments. Thank you to Dr Andrew Chetwynd and Christopher Stark for the training on the TGA instrument and the endless samples that I ran. Also, thank you to Paul Stanley who trained me on the SEM instrument to acquire wonderful images of my silica nanoparticles. Many thanks to Dr Feng Wang and Dr Yu-Lung Chiu for the long hours spent on the HR-TEM. The amazing technical staff in the School of Dentistry, as the microbiology work would not have been possible without them. Especially, Jianguo Liu for guiding me on the confocal microscope and SEM.

I have had the pleasure of being part of the ZP research group and I am grateful to past and current members; Sajni, Irene, Tasha, Jamie, Asier, Patrícia, Elena, Sarah, Luke, Andrew, and Maria. I have been lucky to have been surrounded by hard working, supportive and social people. Also thank you to other fellow PhD students in the Hannon group, at the School of Dentistry and Sci-Phy CDT programme for making my PhD experience enjoyable. I have made many life-long friendships, Sajni will always be my silica buddy, thank you to Lizzie for always being there to have coffee with me and the many others at the University.

Finally, I am extremely appreciative of having such amazing and loving family and friends. A special thanks to Nick for proof-reading my work and continuously challenging and encouraging me during my PhD. I could not have powered through my PhD without my mom, dad and sister, Ruby. They have been there every step of the way, through all the highs and lows and have inspired me to be the woman I am today.

Contents

Chapter 1: Introduction	1
1.1. An overview of the human oral microbiome	1
1.1.1. Biofilm formation in the oral cavity	2
1.1.2. Tooth structure & dental infections	4
1.2. Removal of biofilms in dentistry	7
1.2.1. The effects of ultrasound	10
1.3. Drug delivery systems	13
1.4. Nanoparticle drug delivery systems for antibacterial agents	16
1.4.1. Lipid-based nanoparticles	16
1.4.2. Polymeric particles	17
1.4.3. Metal-based NPs	18
1.5. Silica NPs	19
1.5.1. Non-porous silica nanoparticles (SNPs)	20
1.5.2. Mesoporous silica nanoparticles (MSNs)	22
1.5.3. Stimuli-responsive MSNs for bacterial infections	23
1.5.4. Ultrasonic-stimulated silica NPs for drug release	32
1.6. Research aims	47
1.7. References	49

Chapter 2: General Methods & Procedures	60
2.1. Synthesis of SNPs with Cetylpyridinium Chloride	60
2.1.1. Synthesis of plain non-porous SNP (Plain SNP).....	60
2.1.2. Synthesis of encapsulated CPC inside SNP (CPC \subset SNP)	60
2.1.3. Preparation of MCM-41 type MSN's	61
2.1.4. Synthesis of adsorbed drug loaded particles (CPC@MSN).....	62
2.1.5. Synthesis of templated drug loaded particles (CPC \subset MSN)	62
2.2. Synthesis of SNPs with Ciprofloxacin Hydrochloride	62
2.2.1 Synthesis of drug encapsulated CPX \subset SNPs via method A.....	63
2.2.2. Synthesis of drug encapsulated CPX \subset SNPs via method B.....	63
2.2.3. Synthesis of adsorbed drug loaded CPX@SNPs via method A or B	63
2.3. General procedures for nanoparticle characterisation.....	64
2.3.1. Sample preparation for imaging of CPC \subset SNP	65
2.4. Drug loading entrapment measurement.....	66
2.5. <i>In Vitro</i> drug-release studies	67
2.5.1. General drug release measurements	67
2.5.2. Ultrasound-responsive triggered drug release in short intervals.....	67
2.5.3. Investigation of drug leakage in static conditions	68
2.5.4. Continuous ultrasound with ultrasonic bath	68
2.6. Biological studies	68
2.6.1. General procedure & chemicals	68

2.6.2. Minimum inhibitory concentration (MIC) assay	69
2.6.3. Antimicrobial activity against planktonic <i>S. sanguinis</i>	71
2.6.4. Agar Diffusion Assay.....	71
2.6.5. Development of single-species biofilm model	74
2.6.6. Determination of CPC release from CPC \subset SNP for biofilm studies	76
2.6.7. Determination of CPX release from CPX \subset SNP for biofilm studies	77
2.6.8. Biofilm viability studies & ultrasonic scaler experimental set-up	77
2.6.9. Live/dead staining assay.....	78
2.6.10. Confocal laser scanning microscopy (CLSM) imaging.....	78
2.6.11. Image analysis of single-species biofilms	79
2.6.12. Colony counting method – colony forming units (CFUs)	82
2.6.13. Scanning electron microscopy (SEM) imaging of biofilms	82
2.7. Bacteria viability statistical analysis.....	83
2.7.1. Biofilms treated with CPC in Chapter 4.....	83
2.7.2. Biofilms treated with CPX in Chapter 5	84
2.8. References.....	85
Chapter 3: The Synthesis, Optimisation & Characterisation of Cetylpyridinium Chloride Loaded Silica Nanoparticles	86
3.1 Introduction.....	86
3.2 Chapter Outline	93
3.3 Results & Discussion.....	94

3.3.1.	Synthesis & optimisation of CPC loaded SNPs	94
3.3.2.	Characterisation of CPC \subset SNP drug delivery system	97
3.3.3.	<i>In Vitro</i> drug release studies of CPC \subset SNP	107
3.4	Conclusions.....	116
3.5.	Appendix	118
3.6.	References	160
Chapter 4: Biofilm Disruption through Controlled Antimicrobial Release from Ultrasound-Responsive Silica Nanoparticles		165
4.1.	Introduction.....	165
4.2.	Chapter Outline	167
4.3.	Results & Discussion.....	169
4.3.1.	Antimicrobial susceptibility testing of CPC and CPC loaded SNPs	169
4.3.2.	US-responsive CPC \subset SNP tested on single-species biofilm model	175
4.3.3.	Mechanical disruption of <i>in vitro</i> <i>S. sanguinis</i> biofilms.....	176
4.3.4.	SEM imaging of biofilms	180
4.3.5.	Time-kill assay with CPC \subset SNP	182
4.5.6.	The synergistic effect of ultrasonication and CPC \subset SNP on <i>S. sanguinis</i> biofilms	187
4.4.	Conclusion.....	193
4.5.	Appendix	195

4.6.	References	203
Chapter 5: Ultrasound-responsive Drug Release & Delivery of Ciprofloxacin Encapsulated Silica Nanoparticles207		
5.1.	Introduction	207
5.2.	Chapter outline	212
5.3.	Results & Discussion	214
5.3.1.	Development of CPX loaded SNPs.....	214
5.3.2.	Characterisation of CPX loaded NP's	216
5.3.3.	<i>In Vitro</i> drug release comparisons of CPX loaded NP's	222
5.3.4.	Determination of minimum inhibitory concentration and antimicrobial activity of CPX and formulations	225
5.3.5.	The antibacterial effect of CPX⊂SNP nanosystems against <i>S. sanguinis</i> biofilms.....	229
5.3.6.	The antibacterial effect of CPX⊂SNP nanosystems against <i>S. mutans</i> biofilms	232
5.4.	Conclusions.....	238
5.5.	Appendix	239
5.6.	References.....	262
Chapter 6: Conclusions & Future Work.....266		
6.1.	Conclusions.....	266
6.2.	Clinical relevance & Future work	268

6.3.	References	271
	List of Achievements	272

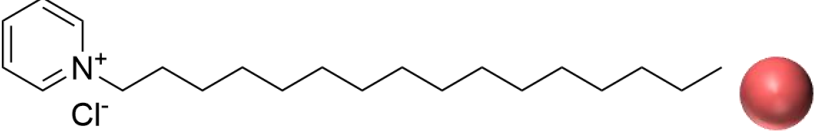
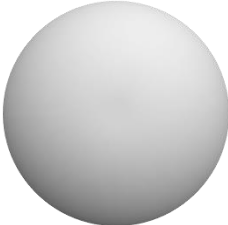
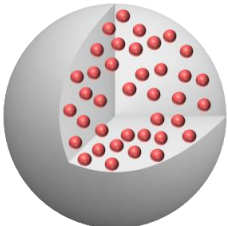

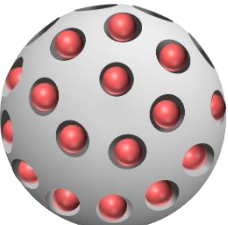
List of Abbreviations

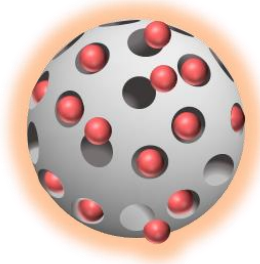
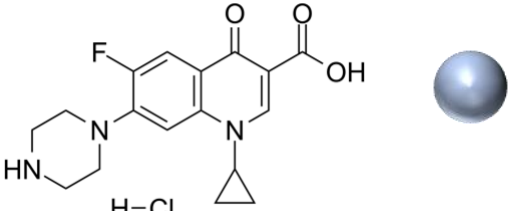
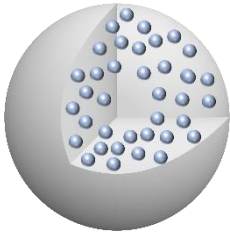
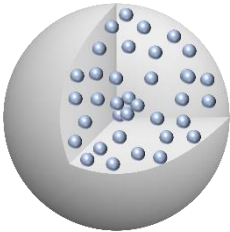
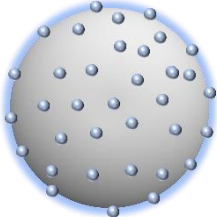
5-FC	5-Fluorocytosine
5-FU	5-Fluoruracil
AEMA	Amino ethyl methacrylate
AgNPs	Silver nanoparticles
AMF	Alternating magnetic field
APTES	(3-aminopropyl) triethoxysilane
Arg–Gly–Asp	Arginine-lysine-glycine
Au NBPs	Gold nanobipyridamids
BHI	Brain heart infusion
BNN6	N,N'-di-sec-butyl-N,N'- dinitroso-1,4-phenylenediamine
CD	Cytosine deaminase
CFUs	Colony forming units
CHCA	α -cyano-4-hydroxy-cinnamic acid
CHX	Chlorhexidine
CLSM	Confocal laser scanning microscopy
CMC	Critical micelle concentration
CPC	Cetylpyridinium chloride
CPT	Camptothecin
CPX	Ciprofloxacin
CS	Chitosan
CTAB	Cetyltrimethylammonium bromide
CUR	Curcumin
DAMO	N-(2-aminoethyl)-3-aminopropyltrimethoxy-silane
DLS	Dynamic light scattering
DNP	2,3 dihydroxynaphthalene
DOX	Doxorubicin
DSTNs	Dendritic silica/titania nanoparticles
EMA	European Medicines Agency
EPS	Extracellular polymeric substances

FA	Folic acid
FDA	Food and Drug Administration
Fe ₃ O ₄	Iron oxide
FT-IR	Fourier-transform infrared
Gd(DTPA) ²⁻	Gadopentetate dimeglumine
HAADF-STEM	High-annular dark field scanning TEM
HIFU	High intensity focused ultrasound
hMSNs	Hollow mesoporous silica nanoparticles
HR-TEM	High resolution transmission electron microscopy
IBU	Ibuprofen
LEVO	Levofloxacin
MALDI-TOF/TOF	Matrix-assisted laser desorption/ionization time-of-flight/time-of-flight
MIC	Minimum inhibitory concentration
MINO	Minocycline
MPTMS	(3-mercaptopropyl) trimethoxysilane
MSNs	Mesoporous silica nanoparticles
Nd:YAG	Neodymium-doped yttrium aluminium garnet
NIR	Near-infrared
NLCs	Nanostructured lipid carriers
NO	Nitric oxide
NPs	Nanoparticles
p(MEO ₂ MA-co-THPMA)	Poly(2-(2-methoxyethoxy) ethyl methacrylate-co-2-tetrahydropyranyl methacrylate)
PBS	Phosphate buffered saline
PCL	Poly (ε-caprolactone)
PDA	Polydopamine
PDI	Polydispersity index
PDMS	Poly(dimethylsiloxane)
PEG	Polyethylene glycol
PEI	Polyethyleneimine
PFH	Perflurohexane

PFOB	Perfluorooctyl bromide
PFP	Perfluoropentane
PI	Propidium iodide
PLGA	Poly(lactide-co-glycolide)
PNIPAM	Poly-N-isopropylacrylamide
PTT	Phototherapy
PTX	Paclitaxel
RhB	Rhodamine B
SA	Sodium alginate
SEM	Scanning electron microscope
SLNs	Solid lipid nanoparticles
SNPs	Silica nanoparticles
SNT	Silica nanotubes
SPIONs	Iron oxide nanoparticles
TEOS	Tetraethyl orthosilicate
TGA	Thermogravimetric analysis
US	Ultrasound
UV-Vis	Ultraviolet-visible
β -CD	β -cyclodextrin

List of Chemical Structures

CPC	
Plain SNP	
CPC \subset SNP	
Plain MSN	
CPX \subset MSN	

<p>CPC@MSN</p>	
<p>CPX</p>	
<p>CPX\subsetSNP_A</p>	
<p>CPX\subsetSNP_B</p>	
<p>CPX@SNP</p>	

Chapter 1: Introduction

1.1. An overview of the human oral microbiome

The oral microbiome is a complex ecological system which harbours over 700 species of bacteria, consisting of symbiotic, commensal, and pathogenic microorganisms.^{1–3} It is responsible for homeostasis, protecting the oral cavity, and preventing disease.^{4,5} All humans have a core microbiome in common, but depending on their lifestyle and physiological differences, variations can occur. The oral cavity is a gateway to the human body and is connected to the nose, throat, oesophagus, and trachea and to the ears via the eustachian tubes. There is constant exposure to dietary consumptions, saliva, and elements from the air.

The oral cavity is coated with bacteria forming biofilms. A biofilm is defined as ‘aggregates of bacterial microorganism that are embedded within a self-produced extracellular polymeric substances (EPS) matrix’.^{6,7} Typically, biofilms are adherent to any wet, non-sterile surface. They are widely used in the biotechnology industry for water filtration for safe drinking, biocatalysis and biofouling. However, biofilms are prevalent with plants, animals, and humans, as they are associated with persistent infection. Also, they cause contamination of medical devices and implants.^{6,8}

The surfaces in the oral cavity enable different microbes to accumulate at supragingival (above gumline) and subgingival (below gumline). Especially on the smooth, pitted or fissured surfaces of the tooth.⁹ The composition of biofilms can be influenced by various factors, which can lead to dental infections, such as caries (tooth decay), periodontitis (gum disease) and endodontic (root canal) infections.^{1,10} The presence of

bacteria has been linked to many systemic diseases⁴, such as cardiovascular disease¹¹, diabetes^{12,13} and pneumonia.^{14,15}

1.1.1. Biofilm formation in the oral cavity

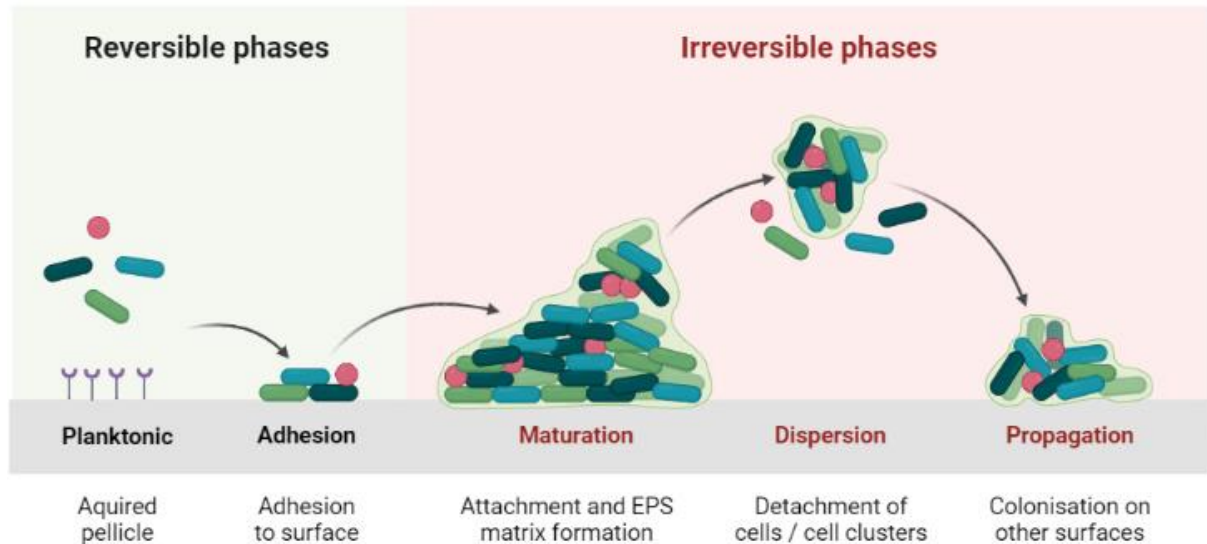


Figure 1. 1: Biofilm formation cycle. The reversible phase involves acquired enamel pellicle which forms a thin film on a surface, mediating attachment of planktonic bacterial species. Maturation of the biofilm enters an irreversible stage of adhesion and aggregation of microcolonies to the surface. Eventually some cells will detach and disperse to create new colonies on other surfaces. Adapted from Kolenbrander *et al.*¹⁸ and redrawn with BioRender.

The process of biofilm formation is highly complex and is difficult to replicate *in vitro* biofilm models.¹⁶ Generally biofilms develop by coaggregation and coadhesion of bacterial cells via cell-to-cell recognition and cell-to-surface attachment.¹⁷ The coaggregation and coadhesion are important mechanisms for growth and stability of multispecies biofilms in the oral cavity.¹⁸ There are two types of bacteria: Gram-positive and Gram-negative, which differ by their outer structure. Gram-negative have three layers, the outer membrane consisting of lipopolysaccharides, a thin peptidoglycan cell wall and an inner membrane. In comparison, Gram-positive bacteria have many layers of peptidoglycan creating a thick layer.^{19,20} Although both types can cause serious

infections, Gram-negative bacteria are a challenge to the healthcare sector due to the resistance to antibiotics. The fundamental double membrane structure provides extra protection.²¹

The formation of biofilms on the teeth (**Figure 1. 1**) is thought to begin from the attachment of acquired enamel pellicle, a thin-film of proteins and other macromolecules derived from salivary glycoproteins. The mechanism of initial attachment to the tooth surface may occur through several pathways, unique to each bacterium. For example, some attach by sensing physiochemical changes or adhere via bacterial appendages (flagella/pili), which enable hydrophobic to hydrophobic interactions or cell body attachment.^{22,23} Initial adhesion of planktonic (free-floating) bacteria occurs via their recognition and interaction with specific sequences of amino acids in the pellicle salivary proteins. Primary colonisers include Gram-positive facultative anaerobes *Streptococcus* and *Actinomyces* species with the salivary pellicle that natural form on the tooth surface. For example, *Streptococcus sanguinis* plays a key role in oral biofilm development, as it is an abundant and commensal bacterium that aids the attachment of succeeding organisms that can lead to pathogenicity given the opportunity. In such, promote secondary colonisers to allow coaggregation of bridging organisms, such as *Fusobacterium nucleatum*, *Corynebacterium* species together with *Porphyromonas gingivalis*. Both *F. nucleatum* and *P. gingivalis* are contributors to periodontal disease.^{3,18} As the biofilm formation progresses, certain species enable coaggregation of other bacteria to produce multispecies and the process becomes irreversible. Eventually, clusters of cells from the mature biofilm can break off and form new biofilms on other surfaces. It is this biofilm formation and dispersion process that can often lead to infection in the host.^{24–26}

An important feature of dental biofilm formation is the presence of extracellular polymeric substances (EPS) which surround the bacterial cells. This slime-like matrix is key for holding bacterial cells together, to provide a dense but highly porous biofilm network. It is mainly responsible for the architecture and integrity of the biofilm structure.^{22,27–29} Generally, the EPS is composed of three major components: extracellular polysaccharides, DNA and proteins.^{30,31} The structure of the biofilm can vary significantly, as can its functions. The EPS acts as a protective barrier for microbes to foreign materials, such as antimicrobial agents, but it is also stabilised by pH, retains water to prevent the biofilm from drying out, entraps nutrients and promotes bacterial cell adhesion and aggregation.^{32,33}

1.1.2. Tooth structure & dental infections

The human adult mouth contains 32 permanent teeth, classified into four types: incisors, canines, premolars, and molars. They differ in shape and size, which are related to their mechanical function of biting, tearing, and grinding. The tooth consists of the crown, which is visible in the mouth and the root buried below the gumline. The anatomised structure, shown in **Figure 1. 2A**, comprises of hard tissues: the enamel, cementum and dentine and soft tissue, the pulp. The dental enamel is the outer layer, covering the tooth crown. Enamel is the most highly mineralised substance in the human body and provides a hard resistant surface. Beneath the enamel is a thin layer of cementum covering the root and connected to the alveolar bone by periodontal ligament.³⁴ Dentine is a porous, hard, mineralised, connective tissue that contains dentinal tubules that range in diameter from 1 - 4 μm .³⁵ The microscopic channels run

through the dentine, radiating to the inner pulp canal. The pulp is in the centre of the tooth and includes a vascular and nerve supply.³⁶

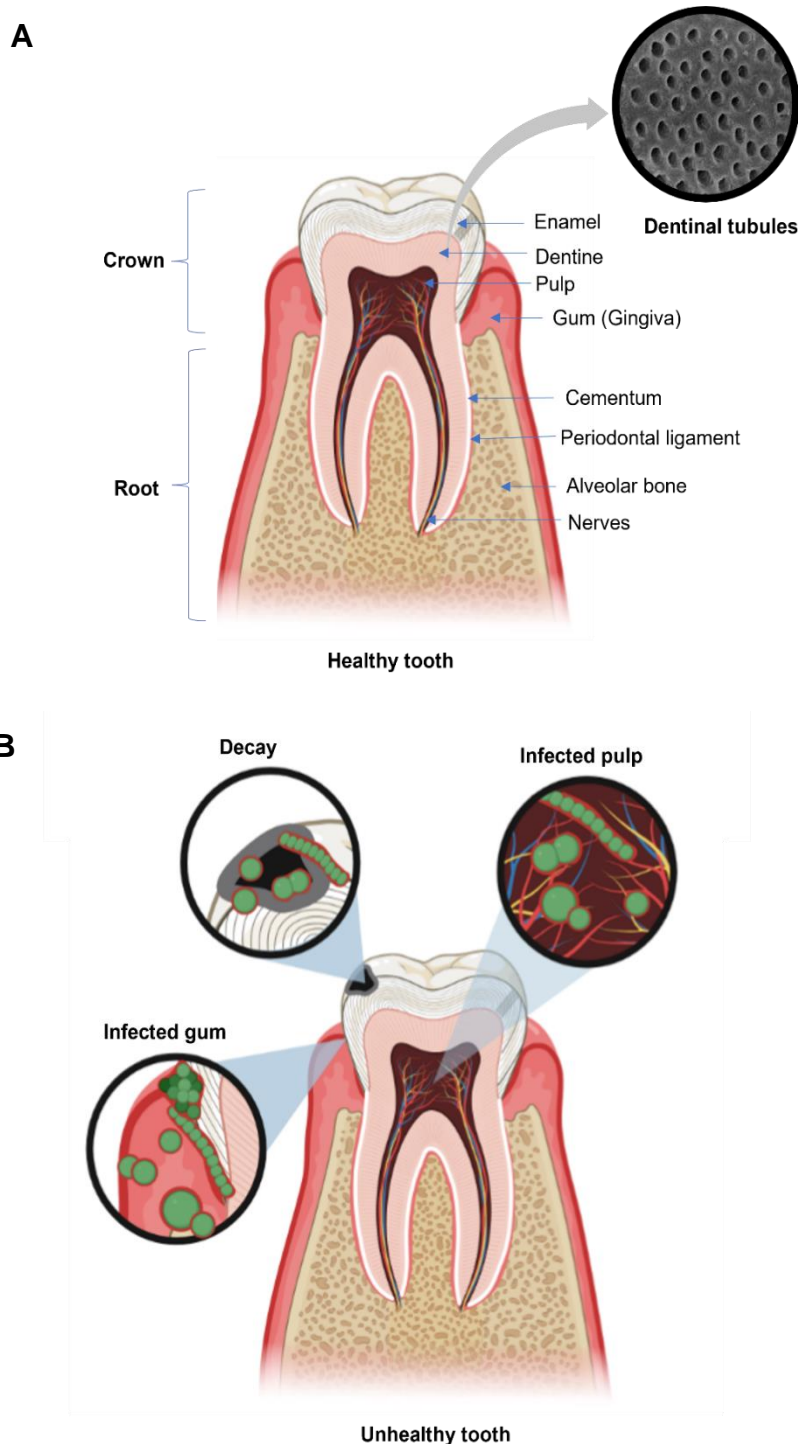


Figure 1. 2: A) Healthy tooth highlighting the key structures and features. **B)** Unhealthy tooth, showing potential areas susceptible to bacterial infections. *Created with BioRender.*

Dental caries and periodontal diseases are non-communicable chronic oral infections with increasing prevalence in the human global population.³⁷ Both infections occur due to a failure to readily remove pathogenic-associated biofilms. Periodontitis is caused by inflammatory and immune responses within the gingival (gum) and surrounding tissue (**Figure 1. 2B**). The secretion of proteolytic enzymes released from pathogenic bacteria in the dental plaque are predominately from Gram-negative anaerobes. Key periodontal pathogens include *Aggregatibacter actinomycetemcomitans*, *P. gingivalis*, *Tannerella forsythia* and *Treponema denticola*.³⁸ Gingivitis is caused by dental plaque accumulation between the teeth and the gingiva. By maintaining good oral health, such as daily tooth brushing, discourages biofilm aggregates from reforming. However, ineffective control can progress gingivitis into periodontitis, a non-reversible infection. The inflammation response causes damage to the connective tissue and supporting alveolar bone. Consequently, causing tooth loosening, pain and even tooth loss.^{39–42} Therefore, it is essential for biofilm removal or treatment to prevent chronic infections.

Dental caries is another chronic oral disease, affecting an estimated 90% of the world population at least once in their lifetime.³⁷ Caries is a result of localised destruction of the hard enamel tissue due to the acid-producing bacteria present in the dental plaque and fermentation of carbohydrates on the tooth surface (**Figure 1. 2**).⁴³ The most common caries-related bacteria are *Streptococcus mutans*, *Enterococcus faecalis* and *Lactobacillus species*.^{43–45} Overtime, the retention of dental plaque on the tooth surface for prolonged periods, facilitates the acids to demineralise the enamel and expose the underlying dentin, creating carious lesions. If enough dental plaque is reduced or removed, the tooth can remineralise and prevent the progression of caries. However, dental caries further advances due to risk factors that interfere with microenvironment

balance. Frequent sugar consumption, which encourages the growth of carcinogenic species, is responsible for low pH conditions (pH 5.5) and contributes towards salivary dysfunction.^{46,47} Saliva has an important role in protecting teeth, but if the pH falls then the mineral structure of the tooth will break down from this acid attack. Breach in the enamel integrity, allows bacteria to invade the dentine and diffuse through the dentinal tubules to the pulp. This can initiate an inflammatory response that leads to diseases of the pulp (pulpitis and necrosis), pain and potential tooth loss.^{48,49} Elimination of the invading bacteria is therefore essential to the prevention and treatment of dental caries.

1.2. Removal of biofilms in dentistry

Supragingival and subgingival plaque control is essential in the prevention of oral diseases. One main way to attain this is through antimicrobial agents or antiplaque agents that have been designed to prevent biofilm formation and or remove the established biofilm. For example, Chlorhexidine (CHX) and cetylpyridinium chloride (CPC) are two of the most frequently used antimicrobial agents in toothpaste and mouthwash formulations to inhibit bacterial plaque formation.⁵⁰ They both have a broad spectrum of bactericidal activity at killing both Gram-positive and Gram-negative bacteria.⁵¹ There are various mechanisms in which antimicrobial agents can affect the bacteria. This can be achieved by inhibiting the cell wall or inducing membrane permeability; blocking metabolic pathways; inhibiting the protein or nucleic synthesis.⁵² However, CPC containing mouth-rinses are often ineffective when used in conjunction with toothpaste, due to interactions with other ingredients.⁵³ Another reason includes, the hindered penetration of CPC into the biofilm matrix and retentiveness (substantivity) on the dental and mucosal surfaces.⁵⁴ Therefore, low concentrations of antimicrobial agent reaching the target site and preventing localised delivery.

Alternatively, the administration of prescribed antibiotics are used to kill bacteria (bactericidal) or prevent growth (bacteriostatic) of bacterial infections. The most commonly used antibiotics in dentistry are β -lactams, nitroimidazoles, macrolides, lincosamides, fluoroquinolones and tetracycline.^{55,56} Alarming, antibiotic resistance is surging and is one of the most significant, challenging, and urgent threats to public health. Antibiotic resistance can develop for several reasons. For example, the misuse and overuse of antibiotics can enable spontaneous genetic mutations to occur in bacteria.⁵⁵ Resistance can spread through horizontal gene transfer, by transferring plasmids between bacterial cells and species. As a result, bacteria are becoming less sensitive to antibiotic treatments.^{57,58} Another survival strategy is when bacteria cells are embedded within EPS matrix of biofilms. Biofilms are already highly tolerant to antibiotics, as it is difficult to penetrate their structure.⁵⁹ Resistance mechanisms of biofilms occur due to exporting the drug out faster than it can diffuse into the cell via efflux pumps. Also, antibiotics can be destroyed by chemical modifications from enzymes or even by reprogramming the target site.^{60–62} Therefore, it is becoming increasingly difficult to access bacteria communities within a biofilm using conventional antibiotics.

Furthermore, dental restoration materials are used in dentistry to restore, reduce infection and exposure to unwanted bacteria.⁶³ Demineralisation of the hard enamel and dentine tissue caused by dental caries are filled in with durable materials, such as composite resins. However, such materials have a resin base and can suffer from polymerisation shrinkage when cured, creating a gap between the filling and tooth structure.⁶⁴ Any roughness on the surface of the filling will provided an ideal surface for more bacteria to accumulate and grow. This in turn will lead to recurrent caries and

deterioration of the restorative material.⁶⁵ Furthermore, studies have been conducted for the incorporation of antimicrobial agents into resin composites to provide antibacterial activity.^{64,66} Unfortunately, modified resin composites with antimicrobial agents often influence the mechanical properties, resulting in the leakage of the antimicrobial agent. This will cause possible toxicity to surrounding tissues, reduction in the life of the filling due inadequate strength and toughness.^{67–69}

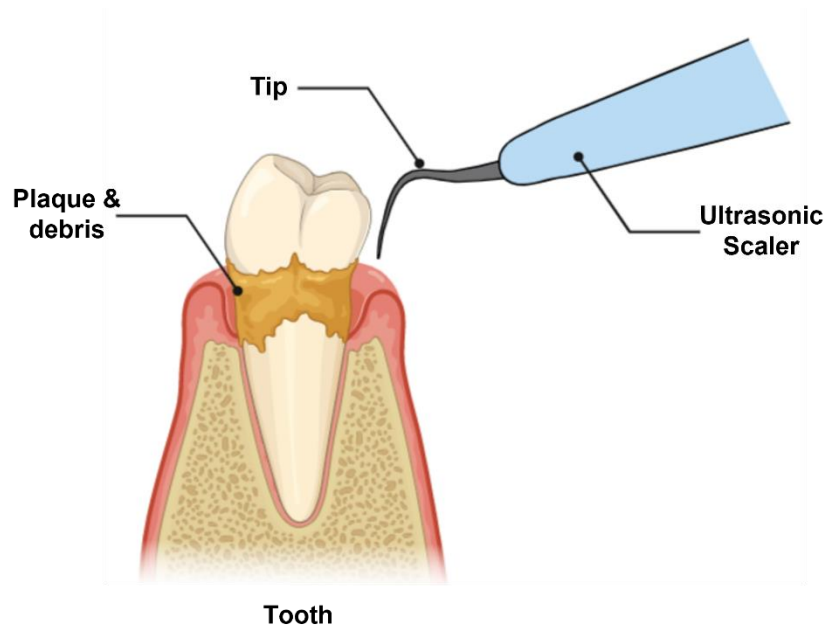


Figure 1. 3: Mechanical debridement for removal of plaque from the surface of the tooth with an ultrasonic scaler device. *Created with BioRender.*

Other clinical strategies involve the mechanical removal of biofilms from dental and implant surfaces, termed mechanical debridement.^{70,71} There are various procedures to clean the tooth surface. This may be done by hand or by the use of ultrasonic tips. The use of ultrasonic vibrations generated by a power-driven hand-held instrument can disrupt and dislodge plaque and calculus (calcified plaque), quicker than manual curettes and scalers.⁷² The ultrasonic scaler (**Figure 1. 3**) is often used by clinicians as an effective non-surgical device to remove supra and subgingival plaque, reducing

treatment times. Although there have been clinical studies on the efficiency for the removal of biofilms, it is more demanding from the subgingival, due to access and limited visibility. Therefore, it is difficult to eradicate bacteria that have reached and entered the dentinal tubules.^{73,74} It has been suggested treatment with antimicrobial agents and the ultrasonic scaler could enhance the biofilm removal strategy. However, antimicrobials can be washed away for clearance, by fluid in the oral cavity. Thus, diluting the concentration for any significant effect.⁷⁵ It has also been proposed ultrasonic scalers can have an antimicrobial effect on periodontal pathogenic bacteria, however there is limited evidence whether cell death is due to acoustic energy produced by the oscillating tip.^{76,77}

1.2.1. The effects of ultrasound

As mentioned previously, biofilm removal can be exploited by the effects of US, which can also be desirable for treatment and drug delivery applications. Ultrasound (US) waves have a frequency greater than 20 kHz and are pressure waves that are transmitted through the expansion and contraction of a liquid.⁷⁸ For example, ultrasonic scalers have a working tip that produce US waves at frequencies above 25-40 kHz and amplitude range between 10-100 μm .^{73,79} The ultrasonic energy is generated by either a magnetostrictive or piezoelectric transducer located in the hand-held piece of the ultrasonic scaler.^{80,81} A piezoelectric transducer converts alternating electric current directly into mechanical vibrations through the scaler tip. Magnetostrictive devices use a magnetic field, created by alternating electric current through a coil and ferromagnetic material, to transfer energy into mechanical energy. But the vibrational motion at the tip is elliptical and circular.^{78,82} Cooling water flows over the tip, which not only prevents frictional heating with the tip to surface contact, but assists with visibility

by debris clearance.^{83–85} The generation of high energy from the ultrasonic scaler can cause biological and physical effects, thermally and mechanically.⁷⁸

Thermal effects produced from US waves can occur when the energy from the US wave is transferred to cells in the form of heat. By increasing the pressure, the frequency of the wave increase, as a result a rise in temperature. If the temperature reaches above 43 °C, this can cause strong hyperthermia.⁸⁶ This is commonly used for tumour tissue ablation in the body with high intensity focused ultrasound (HIFU) rather than from dental ultrasonic scalers. The thermal effects can cause tissue damage by denaturing proteins leading to necrosis and allows for the tumour tissue to become more susceptible to chemotherapeutics.⁸⁷

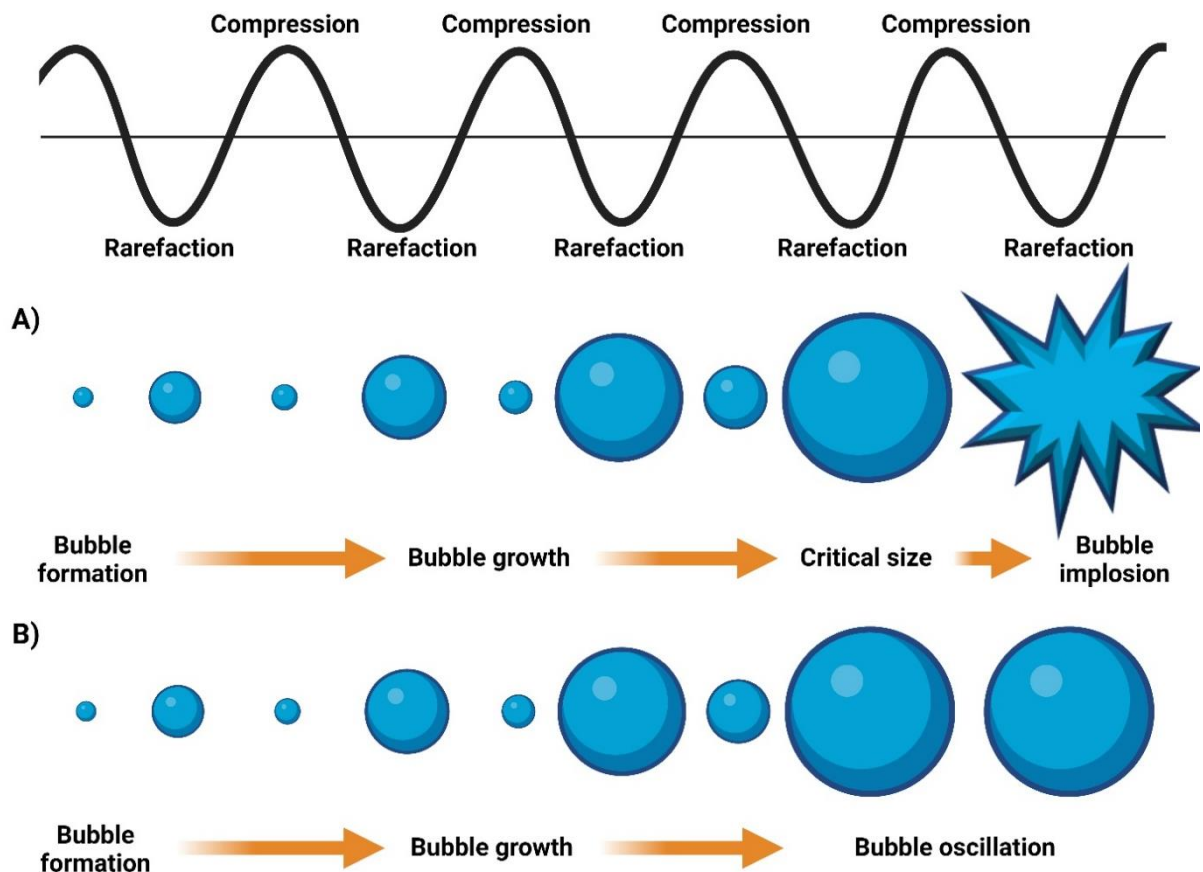


Figure 1. 4: Propagation of an ultrasound wave to show the bubble expansion and collapse at the rarefaction and compression phases of two types of cavitation: **A)** inertial cavitation and **B)** non-inertial cavitation. Bubbles not drawn to scale. Reproduced from Izadifar *et al.*⁹⁰ using *BioRender*.

Furthermore, mechanical effects from an ultrasonic scaler can occur from acoustic cavitation in a liquid. When US is applied in a liquid, acoustic cavitation occurs when the local pressure becomes lower than the saturated vapour pressure.^{88,89} It is this negative pressure that forms a cavity in the liquid, known as the cavitation threshold. During the US wave cycle (**Figure 1. 4**), a bubble grows from a small nuclei in the rarefaction phase. The bubble continues to grow with increasing pressure until it reaches the compression phase, which causes the bubble to oscillate. There are two types of cavitation: inertial and non-inertial.^{78,90}

In **Figure 1. 4A**, shows the inertial cavitation process, which involves the rapid rise and collapse of gas bubbles. Here bubbles can expand to twice its initial radius size and when the pressure increases above the critical threshold the bubbles violently implode, releasing high energy shockwaves and high velocity microjets upon release.^{89,91} These localised extreme conditions can lead to the emission of light bursts, known as sonoluminescence; disruption to tissues to enhance drug transport; and formation of reactive oxygen species.⁹² This latter occurs when the high pressure and temperature generated from the bubble implosion, release significant heat energy that can split water molecules into hydroxyl free radicals and oxygen.^{93,94} These extremely reactive species can cause a series of chain reactions, especially on a cellular level. For example, the formation of hydrogen peroxide that are damaging to cells and influence the cell membrane permeabilization.⁹⁵

Alternatively, non-inertial cavitation (**Figure 1. 4B**) is a stable form of gas bubbles. This happens when the bubble is forced to oscillate in the acoustic field, as a result of lower energy and amplitude. This creates a phenomena of acoustic microstreaming, which

have velocities and shear forces that can enhance the cleaning of dental biofilms, but can be damaging to surfaces.^{79,96,97}

1.3. Drug delivery systems

The prevalence of antimicrobial resistance is a consequence of antibiotic treatment. Often regimes involve a long course of therapy to ensure sufficient antibiotic exposure to eradicate pathogenic bacteria.⁹⁸ However, administration of antimicrobials can be inappropriately and over used leading to genetic alterations, such as gene expression and mutagenesis. Therefore, increasing frequent risk of bacterial antimicrobial resistance. Furthermore, delivery of antibiotics is not always localised to the infected site and are faced with challenges such as, solubility issues, lack of diffusion into biofilms and issues of rapid clearance from the target site. As a result, innovative strategies are crucial to combat the emergence of antimicrobial resistance to overcome the challenges of current antibiotic therapies.

Nanomedicine is a rapidly evolving field, although is under used for dental applications. The dentistry field would benefit from improved prevention, diagnosis, and therapy for oral and dental diseases.^{99,100} The use of nanomaterials offers an avenue to improve the effectiveness of existing therapeutics and better understand complex mechanisms underpinning infection. Also allow for the development of safer and effective treatments to overcome the fundamental limitations of conventional drug delivery.^{101,102}

Dental infections associated with biofilms are difficult to eradicate and is intrinsic to the resistance to antimicrobial agents and antibiotics. As previously mentioned, the complex architecture of the biofilm consists of bacteria colonies surrounded by an EPS

matrix. Therefore, traditional antibacterial agents lack the ability to penetrate the biofilm and kill the pathogenic bacteria.

Nanoparticles (NPs) have been extensively studied due to their excellent properties that can be utilised as nanomedicines and nano-delivery systems.^{103–105} In addition to being antibacterial agents, NPs can act as delivery systems to deliver agents by drug encapsulation or attachment for targeted delivery to the site of action and have a controlled drug release.^{106,107}

The design and synthesis of NPs is highly important, as each NP can present its own unique properties. The nanosize (1-100 nm) and sub-micron (100-900 nm) scales of NPs provides a high surface area-to-volume ratio, offering increased interaction with bacteria. This enhances membrane permeability of the bacterial cell that enables an increased accumulation of NPs (active agent) at the infected site.¹⁰⁸ Moreover, the nanostructure shape is a critical characteristic, as morphology and activity of NPs can improve the efficacy of treatment. Furthermore, NPs can be modified by providing a surface that can be functionalised with chemical groups and ligands to enhance the targeting to specific bacteria. The advantage of modifying NPs can help protect healthy bacteria and epithelial cells from cytotoxic and adverse effects. NPS will also shield drugs from enzymatic attack and drives interactions with the bacterial membrane to achieve an enhanced antimicrobial activity with control release of drugs.¹⁰⁴

The design of NPs can be optimised for stimuli-responsive drug release systems within the bacterial microenvironment. Internal stimuli can be fabricated to release the drug under physiological conditions dependant on the infection. Different types have been explored by releasing the drug from NPs under changes in pH, the presence of specific

enzymes or change in redox potential.^{109,110} Alternative systems have used external stimuli, where drug release has been achieved by magnetic, thermal, light and ultrasound applications.¹¹¹ Having a drug delivery system where the release of the drug can be controlled is a highly desirable function to enhance the antibacterial activity, reduce side effects and risk of drug resistance.

The NP platform is still a relatively new field and there are an increasing number of nanoformulations being successful approved by the Food and Drug Administration (FDA) and European Medicines Agency (EMA). Currently there are few antibacterial delivery nanosystems that remain in the clinical trials phases 1 to 3.^{101,112,113} For example ciprofloxacin and Amikacin loaded liposomes are two nanosized systems currently in phase 3 clinical trials for respiratory infections caused by *Pseudomonas aeruginosa*.^{114,115} The only dental product associated nanomedicine is of an antimicrobial peptide (C16G2) for prevention of dental caries caused by *Streptococcus mutans* in Phase 2.¹¹⁶

1.4. Nanoparticle drug delivery systems for antibacterial agents

NPs can be classified into two main categories (**Figure 1. 5**), organic nanoparticles, such as: liposomes, dendrimers, polymers, and micelles; and inorganic includes: silica, quantum dots, iron oxide and gold.¹⁰⁴

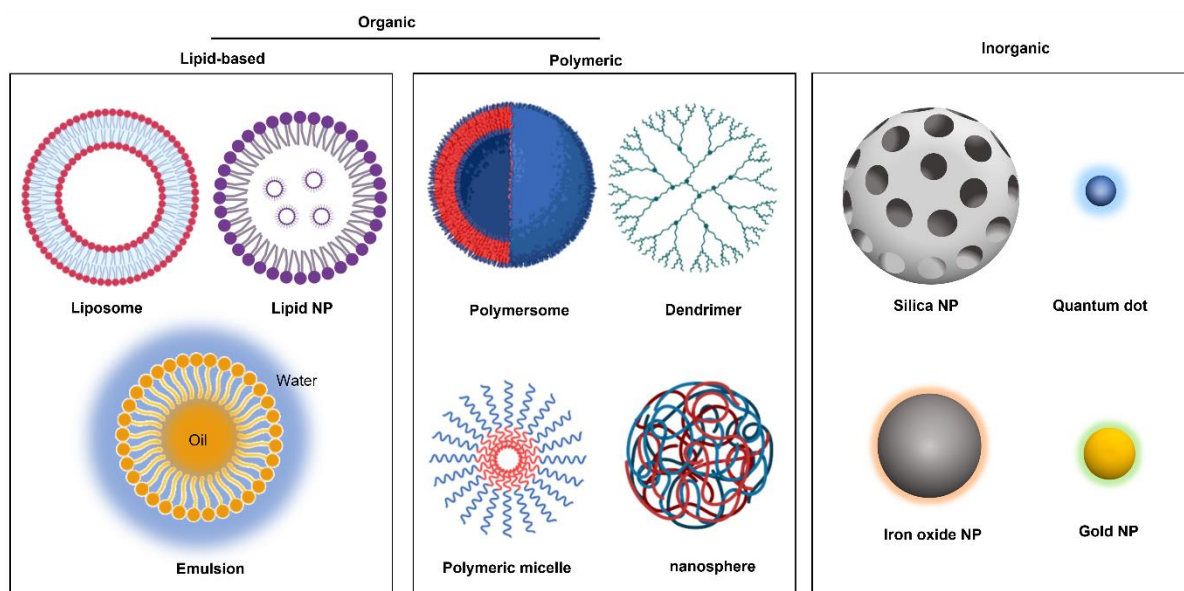


Figure 1. 5: Classes of Drug delivery systems, divided into two sub-sections: organic materials, including lipid-based and polymeric and organic materials. Redrawn from Mitchell *et al.*¹⁰⁴

1.4.1. Lipid-based nanoparticles

Lipid-based nanoformulations include liposomes, nanoemulsions, solid lipid nanoparticles (SLNs) and nanostructured lipid carriers (NLCs). Many liposomal formulations have been approved and with more in clinical development for the encapsulation and intention for the delivery of drugs. The first nano-carrier of the anticancer drug, doxorubicin was delivered using liposomes.^{117,118} They are well-investigated nano-carriers for improving the therapeutic index, enabling a targeted drug delivery and are considered non-toxic.¹¹⁹ Liposomes consist of phospholipids forming bilayers via self-assembly with the ability to entrap both hydrophilic and

hydrophobic drugs.¹²⁰ As a drug delivery system, liposomes are advantageous due to their biocompatibility and high drug loading capacity.

Despite liposome assisted drug delivery platforms showing many therapeutic advantages, they are heavily limited by their chemical stability, resulting in drug leakage or denaturing of the encapsulated drugs. A common strategy to overcome the barrier of instability includes, polymer coating with polyethylene glycol (PEG).¹²¹ Whilst PEGylation has improved NP stability and drug circulation times, it reduces the interaction with the target sites.¹²² Therefore, additional modifications with ligands and targeting moieties has led to more complex liposomal drug delivery systems. This creates more challenges often requiring multiple chemical synthetic steps. As a result, this can affect the biocompatibility, biodistribution and toxicological profiles, creating problems for scalability in industrial manufacturing processes and clinical translation.¹²³

1.4.2. Polymeric particles

Polymeric particles, made of natural and synthetic polymers have attracted much attention for delivery of a broad range of active agents, such as chitosan,¹²⁴ albumin,¹²⁵ poly(lactide-co-glycolide) (PLGA)¹²⁶ and poly (ϵ -caprolactone) (PCL)¹²⁷. Generally, drug molecules can be bonded to the polymer backbone or encapsulated within the polymer core. Polymeric materials present several advantages as drug carriers, as they are associated with high bioavailability and biodegradability.¹²⁸ There are a wide range of structures produced using a variety of techniques. Souto *et al.*¹²⁹ reviewed and discussed the methodologies for synthesising polymeric NPs for potential targeted delivery of drugs. Most require several synthetic and purification steps. Consequently, the use of organic solvents during the preparation of NPs can generate toxicity

problems in biological applications. Therefore, it is essential for the removal of any residual solvent from the final product. In addition, polymeric NPs are limited by chemical stability, although biodegradability is a valuable property. However, the breakdown NPs could have toxic properties. They are prone to particle aggregation and premature release of active substances.^{129–131}

1.4.3. Metal-based NPs

Metal-based NPs are inorganic materials that have been applied to various areas of dentistry because of the potent antimicrobial properties. Metals such as gold, silver, iron, copper, and zinc are some with valuable antibacterial activity. Generally, titania oxide is popular for its use for dental implants. Titania improves the implant surfaces by reducing bacterial adhesion and increasing the tensile properties. Similarly, zirconia lowers the bacterial adhesion and improves the mechanical properties of the tooth, utilised as a polishing agent.¹⁰⁰ The most extensively studied metal-based NPs are silver NPs (AgNPs).¹³² Silver has the advantages for being used as antimicrobial agent and in dental restorative materials, prosthetics and implants.

Though the mechanism of action of metal-based NPs is unclear, bactericidal activity is often attributed to electrostatic interactions between the cationic metal ions and negatively charged bacterial cell wall, leading to potential cell death and biofilm elimination. In addition, the small sized NPs usually increase the toxicity, as they can easily diffuse and accumulate into bacterial cells. Whilst these types of NPs show promising potent bactericidal activity, there are major concerns over toxicity.¹³³ For instance, the toxicity of AgNPs has been linked to the activity of free Ag⁺ ions in solution. There is no selectivity over mammalian or bacterial cells and AgNPs are susceptible to agglomeration. Also, at risk from oxidation and require surface

modification with agents, such as chitosan, thiols, or glucuronic acid for stabilisation. Furthermore, their non-specificity and small sizes risk crossing the blood brain barrier and accumulating in the brain via transsynaptic transport. Therefore, due to uncontrolled and unique toxicity mechanisms associated with metal-based NPs, further vigorous investigation is needed to evaluate their safety.^{134,135}

1.5. Silica NPs

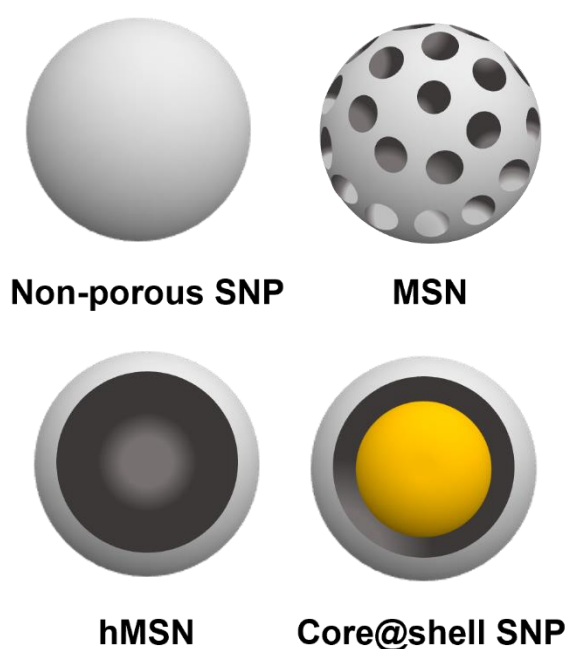


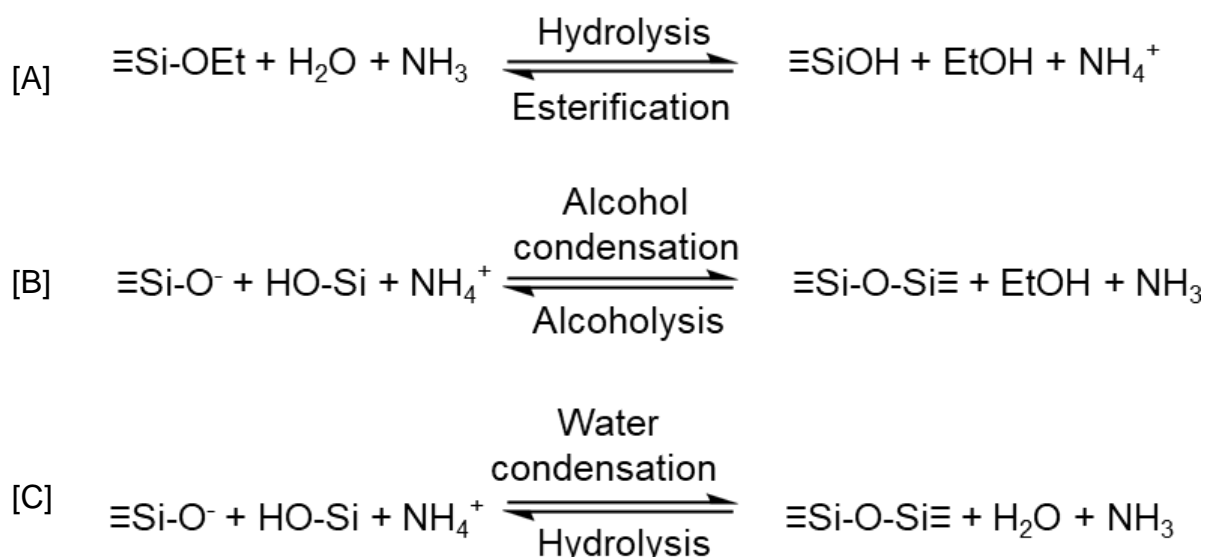
Figure 1. 6: Various structures of silica nanoparticles formed, depending on the synthetic procedure used. Reproduced from Selvarajan *et al.*¹³⁶

Amongst the wide range of NPs researched, silica NPs (SNPs) are a unique class of inorganic NPs that can offer a diverse range of advantages for combating bacterial infections. Colloidal silica is stable in aqueous medium and have varied range of uses, some of which are used in adhesives, fillers, food additives, drug-delivery systems and imaging agents. The most common types of amorphous silica particles include, non-

porous SNPs, mesoporous silica nanoparticles (MSNs), hollow MSNs (HMSNs) and core-shell SNPs.¹³⁶ The difference in their structures is shown in **Figure 1.6**.

1.5.1. Non-porous silica nanoparticles (SNPs)

The Stöber synthesis is a widely used procedure reported to yield non-porous SNPs, since 1968.¹³⁷ This method was first introduced to produce NPs of controlled monodisperse sizes of 50 nm to 2 μm with spherical morphology and tunable surface properties. The Stöber method has provided a foundation for several protocols designed and used in present research. The silica growth mechanism, responsible for SNPs produced using the Stöber method, has been described by several authors, such as Bruneau and Humbert *et al.*,¹³⁸ Van Blaaderen *et al.*,^{139,140} Giesche *et al.*¹⁴¹ and others.^{142–144} A general summary of the proposed synthetic route for non-porous SNPs is shown in **Equation 1A-C**.



Equation 1: The sol-gel process of synthesising SNPs using TEOS precursor. The reaction proceeds in stages of hydrolysis and condensation reactions driven by a base catalyst to form Si-O-Si bonds. Also producing ethanol and water as side products.

The standard silica precursor used is tetraethyl orthosilicate (TEOS), which undergoes a series of hydrolysis and alcohol and water condensation reactions, in which the ethoxy groups (-Si-OEt) are replaced with silanol groups (-Si-OH), as shown in **Equation 1A**. Unreacted -Si-OEt can also undergo condensation reactions with silanol monomers to contribute to the nucleation and growth of the NPs in **Equation 1B**. Finally, condensation between two silanol groups create clusters of siloxanes forming the predominate structure in silica NPs, in **Equation 1C**. The addition of 28% ammonia in a co-solvent mixture of ethanol: water, acts as a base catalyst, which is important for the rate of hydrolysis and condensation reactions that occur.

Due to SNPs desirable physicochemical qualities, fine-tuning of the synthesis has led to the encapsulation and conjugation of various cargos, such as small drug molecules and organic dyes, for various drug loading and delivery applications. Particularly, the surface of SNPs is rich in silanol groups, which can act as an anchor for modifications with coupling groups, such as (3-aminopropyl) triethoxysilane (APTES) and (3-mercaptopropyl) trimethoxysilane (MPTMS), thus enabling the loading and adsorption of various cargos. Surface modification have been particularly utilised for anticancer agents in light-based nanomedicines and photo-theranostics.^{145–149} A review by Cheng *et al.*,¹⁵⁰ also addressed the attractive nature of employing non-porous silica NPs in the field of nanotechnology for biomedical applications, which will be discussed later in this chapter.

1.5.2. Mesoporous silica nanoparticles (MSNs)

Of the silica structures, MSNs have been extensively researched and utilised as a drug delivery system.¹⁵¹ In **Figure 1. 7**, MSNs are synthesised by adapting the sol-gel method used to make non-porous SNPs.^{152,153} Upon addition of an amphiphilic surfactants or block copolymers, they can act as structure-directing agents during NP synthesis. Cetyltrimethylammonium bromide (CTAB) is a widely used cationic surfactant to template a porous structure.¹⁵⁴ Often, removal of the surfactant material is achieved with additional steps to the procedure via calcination or chemical extraction to expose the porous structure. Much attention to MSNs has been owed to its advantages of achieving NPs with increased surface area-to-volume ratio and tunable pore sizes from 2 to 50 nm, leading to higher drug or other therapeutic agents loading.¹⁵¹ Furthermore, the size and morphology are easily controlled through varying

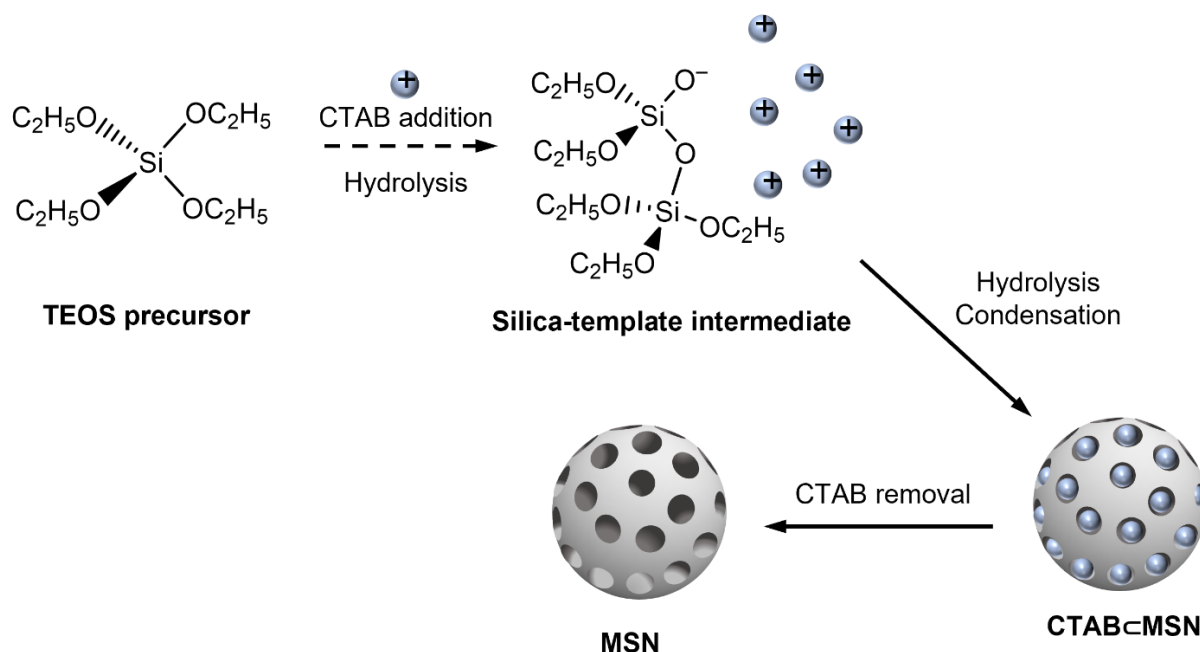


Figure 1. 7: General mesoporous silica nanoparticle (MSN) synthetic route, showing the interaction with the silica precursor and templating agent to form a surfactant templated MSN. Upon surfactant removal processes, the MSN structure remains. Based on Varache *et al.*¹⁵²

conditions, such as reactant concentrations, reaction temperature and pH. However, altering these parameters is often challenging to produce NPs smaller than 100 nm. Synthetic procedures have since been adapted to achieve MSNs smaller than 100 nm. In light of this, NPs have suffered from monodispersed and uniform sizes. Therefore, more complex methods are being used for modification before or after the template removal stage.^{155–157}

1.5.3. Stimuli-responsive MSNs for bacterial infections

As a drug delivery system, MSNs can be engineered to encapsulate various agents through the conventional drug loading approach by absorption to the particle surface or modification of the internal pore structure. This is usually achieved by chemical modification, methods of which have been extensively reported in the literature,¹⁵¹ and has been used because open pores have often resulted in uncontrolled and leakage of drug molecules. Therefore, to overcome such drug release issues, additional functionalisation steps are required.^{151,158} To achieve a controlled drug release, it is common to have a stimuli-trigger responsive system incorporated into the design of MSNs to act as gate-keepers to block the release from the mesopores and to have an on-demand release.^{159–161}

1.5.3.1. Triggered release in the presence of bacteria

There are various approaches to aid drug delivery, majority have focused on decorating the surface of MSNs with chemical moieties. One strategy aims to target bacteria in biofilms by functionalising the surface of MSNs with positively charged polymers, shown in **Figure 1. 8**. Interestingly, Martínez-Máñez and co-workers¹⁶² were the first to report a stimuli-responsive system for antimicrobials.

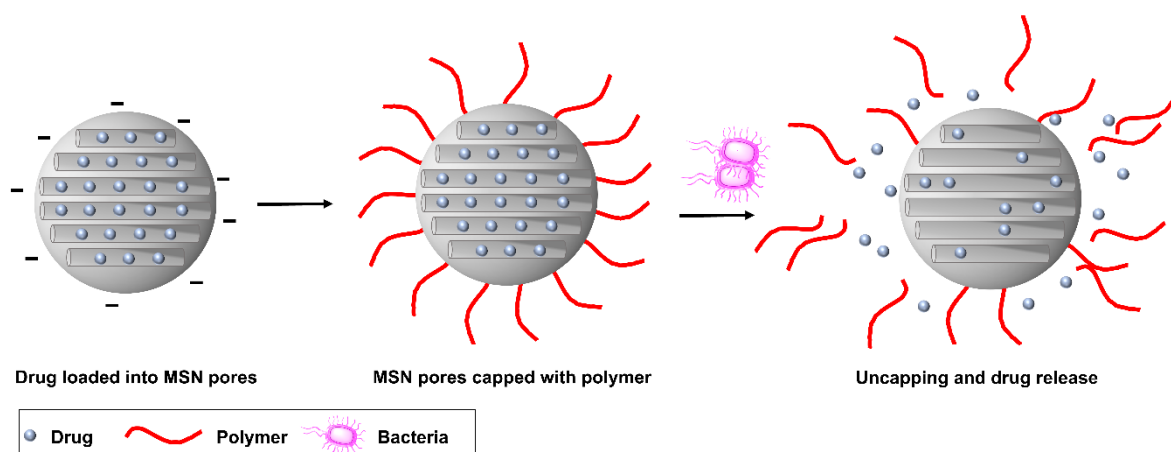


Figure 1. 8: Internal-stimuli, bacterial triggered drug release. MSNs loaded with drug and coated with positively charged polymer. Release is triggered upon contact with bacterial species. Note that bacteria cells and nanoparticles are to scale. Based on Velikova *et al.*¹⁶²

Until then no one had achieved a zero-release drug delivery system that could not only deliver the drug and release it in the presence of bacteria but show that MSNs could enhance the efficacy of antimicrobials. The work provided a platform to load vancomycin and then functionalise the surface with an anchoring ligand for ϵ -poly-L-lysine. The positively charged polymer, ϵ -poly-L-lysine, was attached to the exterior of MSNs to cap the pores loaded with vancomycin. The final product showed particles sizes of 100 nm, positive charge of 23.6 mV and drug loading of 0.01 mmol/g. Vancomycin selectively targets Gram-positive bacteria, but in a nanoformulation with ϵ -poly-L-lysine a significant synergistic effect against Gram-negative bacteria *E. coli* was achieved. The polymer has antibiotic characteristics towards Gram-negative and can damage the cell wall. This can bind to the bacteria and uncaps from the MSN pores to enable vancomycin to access the cell. Therefore, it was demonstrated by MSNs loaded with vancomycin higher toxicity, showing a lower minimum inhibition concentration (MIC) of 0.75 $\mu\text{g/mL}$ compared to free drug (>15 $\mu\text{g/mL}$).

Subsequently, Martínez-Máñez *et al.* have continued to expand nanoformulations using MSNs as a promising carrier for delivery of other agents, such as histidine kinases and linezolid. As well as, surface modification by pores capped with ϵ -poly-L-lysine, in efforts to achieve a synergistic effect and overcome resistance against Gram-negative bacteria.^{163,164}

Other studies have taken advantage of bacterial responsiveness to the MSN surface functionalisation. For example, Vallet-Regí and co-workers¹⁶⁵ describe the development of a “nanoantibiotic”. This involves loading antimicrobial drug levofloxacin (LEVO) by adsorption into the MSN pores. Then modification to the exterior surface of MSNs with cationic polymers. Attachment of positively charged polymer N-(2-aminoethyl)-3-aminopropyltrimethoxy-silane (DAMO) or third generation polycation dendrimer (G3) created nanosystems that were able to load 5 and 7.8 wt% of LEVO (L) into MSN-DAMO-L and MSN-G3-L internal pores, respectively. MSN-DAMO-L and MSN-G3-L produced average particle diameter sizes of 140 nm with a stable colloidal positive charge above 31 mV. Both nanosystems were able to penetrate Gram-positive *S. aureus* biofilms. Evidence of MSN-DAMO-L and MSN-G3-L internalisation was examined with confocal microscopy imaging by labelling the lipid cell membrane and MSNs. However, the surface functionalisation with G3 provided a highly dense branched network of positive charges to allow for the internalisation by binding to the negatively charged membrane of Gram-negative *E. coli* and cause some permeability. Therefore, positively charged polymers combined with the antimicrobial agent produced a synergistic effect and showed sustained drug release via diffusion for antimicrobial efficacy.

Pathogen-selectively and detection is receiving much attention, with recent studies designing more complex systems, with attachment of aptamers and antibodies.^{166–168} Although having a targeting nanosystem that can fulfil multiple goals, the synthesis stages and time increases and becomes more difficult, requiring more in-depth characterisations and purification steps to obtain a system that is suitable for biological testing.

1.5.3.2. pH responsive MSNs

Another smart drug delivery system where release is triggered by an environmental stimulus, is pH. Usually, pH-responsive nanosystems are stable in physiological conditions (pH 7.4) and change under acidic pH environments. Dental caries is an oral infection that is prone to having a low pH of 5.5, as a result of acid production by the oral biofilm, such as *S. mutans* bacteria.

Fawzy et al.,^{169,170} developed a pH-dependent delivery system to tackle challenges of current durability and leakage of adhesive restorations, which can result in secondary caries. The surface of MSNs was modified by grafting synthetic polypeptide PLGA containing carboxyl groups, known for its pH-responsive behaviour and degradability of PLGA matrix in low pH. The antimicrobial agent, CHX was loaded into the pores and adsorbed on the external surface after PLGA modification. The final CHX-loaded/MSN-PLGA formulation achieved a drug encapsulation efficiency of 95%, this was 10% greater than unmodified MSNs and a total drug loading of 24%. The drug release was tested at pH 7.4 and 5.0, both showed an initial burst release then constant release over a 24 h period. However, the release was faster and greater in acidic conditions. Therefore, the antimicrobial activity on *S. mutans* biofilms significantly reduced in viability upon exposure to CHX-loaded/MSN-PLGA examined at 24 h and after 30

days. Despite the remarkable antimicrobial activity, 20-30% of the biofilm remained viable. This still leaves the opportunity for pathogenic bacteria to continue to grow and cause infections.

To improve the bactericidal activity and achieve a synergistic effect, Zhou and co-workers¹⁷¹ developed a pH-responsive co-delivery system with AgNPs and CHX for a pH triggered drug release for antibacterial applications. The MSN structure was functionalised with amino groups to enable the surface to be decorated with nanosilver and then modified with carboxylate groups to introduce CHX through electrostatic interactions. Therefore, in higher pH, it was thought deprotonation of the carboxylate group prevents CHX from releasing. Within 12 h, 39 % more CHX was released at pH 5.0 compared to pH 7.4, a similar accelerated release was observed with Ag. The antibacterial activity of Ag-MSNs@CHX was tested on Gram-positive *S. aureus* and Gram-negative *E. coli*, which showed inhibition of 25 and 12.5 µg/mL, respectively. The study showed promising initial findings, however the nanosystem was only investigated on planktonic bacteria in a liquid culture, whereas bacterial species embedded in biofilm would require a much higher antimicrobial efficacy.

Similarly, Ag-MSNs@CHX were further improved with the introduction of disulfide bridges into the silica framework, by Tang and co-workers.¹⁷² Organo-silica bridges has already been investigated for cancer therapy, but has not yet been applied as nanoantiseptics to therapeutically effect biofilms.¹⁷³ In addition to two therapeutic agents, the system was a dual redox/pH stimuli-responsive for periodontal diseases, shown in **Figure 1. 9**. The introduction of disulfide-bridges in MSNs enables a biodegrade structure in the presence of glutathione. Glutathione can cleave the disulfide bond. A 21% of CHX loading was achieved, and release was accelerated at

pH 5.5 and in the presence of GSH. Almost all drug was released after 96 h. The inhibitory effects of Ag-MSNs@CHX showed a MIC of 12 $\mu\text{g/mL}$ and minimum biofilm inhibitory concentration of 50 $\mu\text{g/mL}$. The activity of Ag-MSNs@CHX on *S. mutans* biofilms showed the viability to decrease in 24 h, however increases from 20 to 40% after 72 h. This may be problematic, as continued use of CHX for prolonged periods can induce unwanted side effects, as well as failure eradication of biofilm can lead to recurrence in infection.

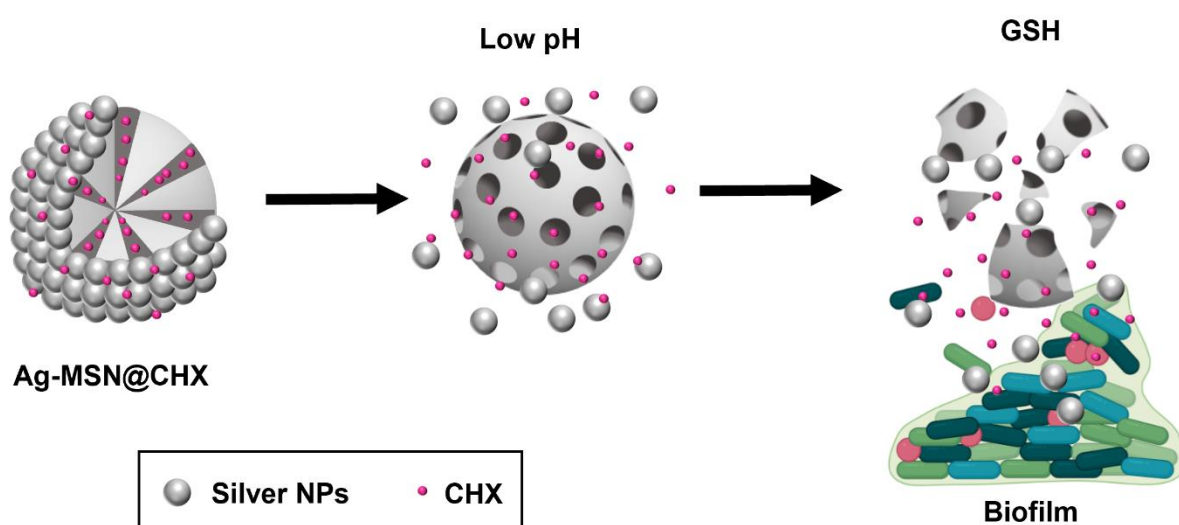


Figure 1. 9: The pH-responsiveness of Ag-MSNs@CHX shows the release of CHX at low pH. Followed by disintegration of the MSN structure by the presence of GSH due to disulfide bridges. Reproduced from Lu *et al.* and Yue *et al.*^{172,173}

1.5.3.3. Photothermal triggers of NPs

There are few drug release systems to target bacterial infections, especially those used in the clinic. As a result, Lin *et al.*¹⁷⁴ developed a near-infrared (NIR) responsive system constructed of gold nanobipyridamids, (Au NBPs) in the core of MSNs encapsulated by a polymer hydrogel (GelMA) containing minocycline (MINO) to form MINO-GelMA-AuNBPs@SiO₂. Au NBPs is a photothermal reagent with strong surface plasmon resonance. The gold structure can provide a photothermal element to the

system activated by NIR to cause photo-induced heat. Phototherapy (PTT) is a non-invasive technique and can effectively kill bacteria reaching areas mechanical debridement for periodontal treatments do not. Although, the antibacterial efficacy against *P. gingivalis* was enhanced by Au NBPs when NIR light-irradiation was applied, the hydrogel used is highly soluble in presence of phosphate buffer solution at pH 7.4 and enzyme solution of collagenase. This resulted in a rapid release behaviour of MINO and no control of drug release. The thermal effects from NIR were only applied to induce more MINO release after the initial burst.

More recently, the Vallet-Regí group,¹⁷⁵ showed the reduction of *S. aureus* biofilms by 90%. A multifunctional nanosystem was developed to enhance the bactericidal activity. Gold nanorods were used as the core of MSNs and loaded with LEVO. The core@shell-type of nanoparticles, shown in **Figure 1. 10**, were thiolated on the silica surface to allow the modification with nitrosothiol groups (-SNO). These groups were heat-labile linkers that release nitric oxide (NO) upon irradiation with NIR. NO has been considered a key regulator of biofilm disruption. Therefore, the studies of AuNR@MSN-SNO+LEVO triggered with NIR showed a three-fold increase at disrupting *S. aureus* biofilms compared to only applying AuNR@MSN to bacteria. The use of PTT can offer an avenue for a triggered release at locally infected sites. However, sophisticated chemistry to modify NPs would be required to achieve targeted photothermal killing and precise NIR irradiation to the infected site.^{176,177} In addition, PTT has been used for cancerous tumours, which are orders of magnitude larger than bacterial infections.¹⁷⁸ Therefore, much harder to achieve precision NIR and non-

localised heat into healthy tissues may cause collateral tissue damage when eliminating biofilms compared to larger tumours.

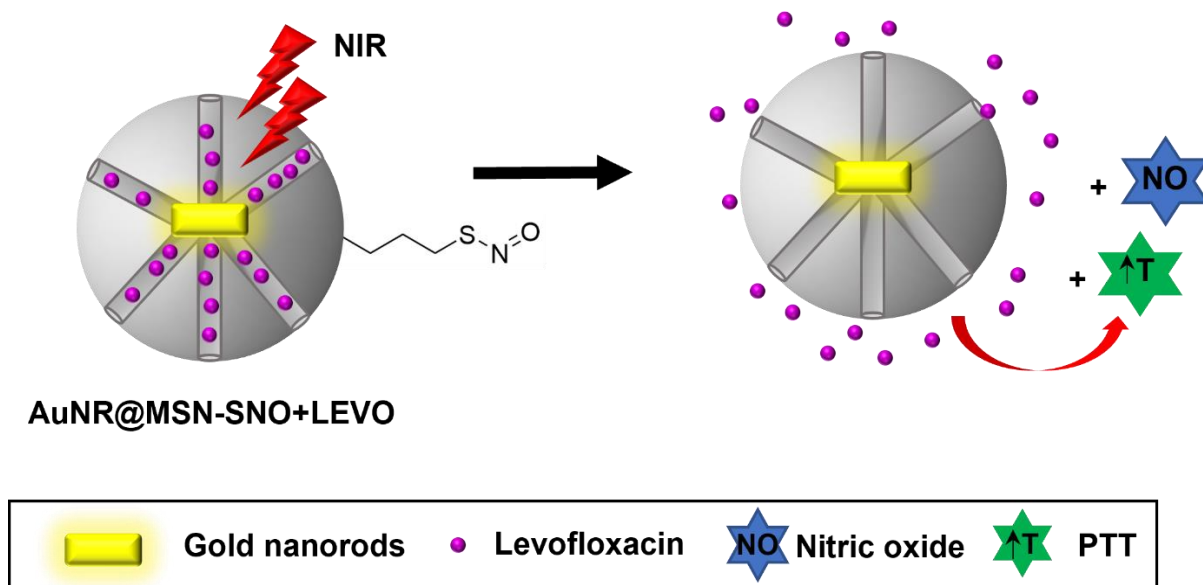


Figure 1. 10: Schematic of core@shell designed AuNR@MSN-SNO+LEVO nanosystem showing the triggered drug release from NIR laser. Reproduced from Garcia *et al.*¹⁷⁵

1.5.3.4. Magnetic stimulated NPs

Incorporation of iron oxide into MSNs is relatively new and few publications for antimicrobial therapies, especially to treat oral biofilms, have been reported. Majority of research has focused on magnetic hyperthermia to treat cancer, *in vivo* imaging agents or management of infections.^{179,180}

The Vallet-Regí group,¹⁸¹ expanded their silica research to include iron oxide-based magnetic NPs. They used mesoporous silica first coated with PEG and followed by a thermosensitive poly-N-isopropylacrylamide (PNIPAM) polymer, then superparamagnetic iron oxide NPs (SPIONs) were coated and antibacterial agent, LEVO was loaded (**Figure 1. 11**). SPIONs have shown to be effective as heating

materials for local hyperthermia by applying an alternating magnetic field (AMF). Usually, electromagnetic radiation is adsorbed upon exposure to high frequency fields, converting into heat energy.^{179,180} The amount of heat released is dependent on the size, shape and composition of the NPs.¹⁸² The SPION-PNIPAM/PEG-MSN@LEVO nanosystem formed particles with diameters 255 nm and surface charges of - 6 mV. The thermal-triggered drug release was tested with increasing the temperature to 50 °C. This resulted in release of 7.87 µg/mL in 6 h and also showed 3.5 µg/mL premature drug at 37 °C in 80 min. Additionally, the magnetic-triggered drug release resulted in 9.44 ug/mL at 37 °C in 60 min. The nanosystem exhibited a 4 log₁₀ CFU/mL reduction in *E. coli* biofilm viability, upon exposure to a magnetic field for 16 h. However, the nanosystem that was drug free also showed a decrease in the biofilm viability by 2 log₁₀ CFU/mL. This maybe an interesting SPION- based system with dual triggered drug release for potential of targeting zones directly on biofilms, but the number of

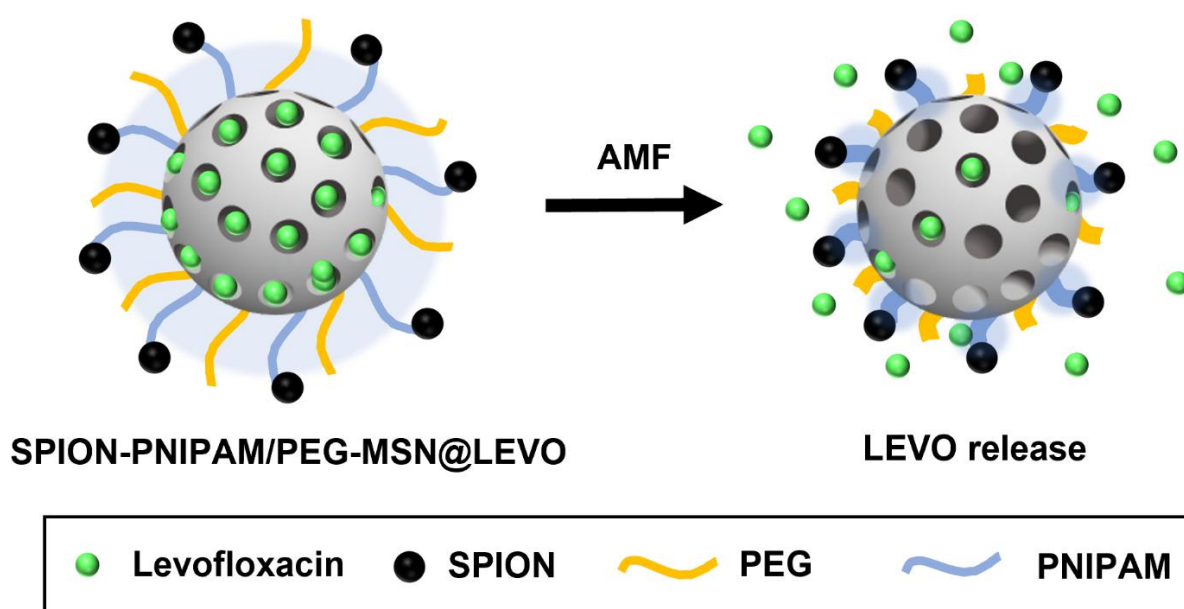


Figure 1. 11: Schematic depiction of SPION-PNIPAM/PEG-MSN@LEVO nanosystem triggered by an alternating magnetic field. Modified from Álvarez *et al.*¹⁸¹

synthetic steps to achieve the nanosystem and the long times needed for drug release are not feasible for oral infections.

1.5.4. Ultrasonic-stimulated silica NPs for drug release

Ultrasound (US) has been used in a variety of medical applications, especially for imaging, increasing blood flow, tumour ablation, kidney stone disruption and dentistry.^{80,90} Mainly low intensity frequency ultrasound has been used for diagnostics purposes, as the low frequencies allow for continuous application and minimal thermal effects.¹⁸³ On the other hand, high intensity focused ultrasound (HIFU) produces thermal (temperatures of 65 to 85 °C) and mechanical effects useful for tumour ablation.⁸⁶ HIFU can also be combined with imaging techniques, such as US and magnetic resonance imaging (MRI) for increased precision and accuracy. In addition, US is a non-invasive technique and can be focused for localisation and controlled with transducers and phase arrays. For these reasons, there has been increased researched of US for its ability to permeabilise cell membranes, enhance the delivery of drugs and release of drugs from nanoparticles by thermal and mechanical effects.

92,184,185

US-triggered drug release from silica nanoparticles has been investigated as one of the most promising external triggers. The introduction of focused US has shown to substantially increase the drug release by carefully altering frequency, power and time of application. Generally, hMSNs, MSNs and core-shell MSNs have been used to load anticancer drugs into the porous channels and then coated with materials that block the pores to prevent drug leakage and can undergo removal upon US irradiation.¹⁸⁶

The most common are polymer coated MSNs and one of the earlier reports was from Honma and co-workers.¹⁸⁷ In this work, MSNs were loaded with 15 wt% ibuprofen (IBU) and the silica surface was modified with poly(dimethylsiloxane) (PDMS) polymer to form PDMS@MSN-IBU (**Figure 1. 12**). PDMS has been used in microfluidics, so was an ideal implantable material. Without PDMS or US trigger, a very fast release of IBU occurs in 3 h. However, PDMS restricted the release of IBU by providing a thick film barrier. In **Figure 1. 12A**, when exposed to 10 min pulses of US (28 kHz, 1.5 Wcm⁻²), PDMS@MSN-IBU released 10% IBU over 100 min. US showed to enhance the drug release kinetics dramatically compared to PDMS@MSN-IBU with no US.

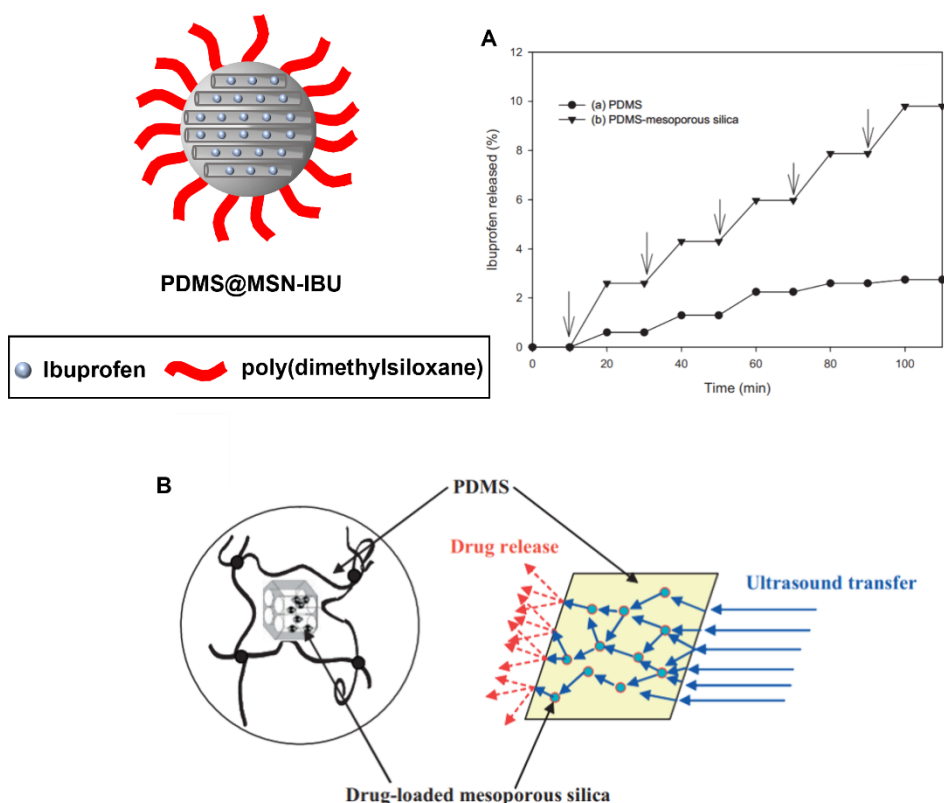


Figure 1. 12: PDMS-MSN@IBU schematic **A)** US-triggered drug release from PDMS polymer compared to polymer and MSN. **B)** Representation of the release mechanism of IBU from nanostructure stimulated by US. Reproduced from Kim *et al.*¹⁸⁷

It was reported that there was no damage to the polymer by scanning electron microscopy and assumed the polymer expands reversibly, as illustrated in **Figure 1.12B**. However, there must have been some disruption to the polymer due to the mechanical and thermal effects produced from US. Possibly, a similar effect to when US is applied to cells, where cavitation can cause small pores in the cell membrane, called sonoporation. In this case, the polymer could behave the same, resulting in the release of IBU.

Alternatively, chitosan (CS) can block the pores of MSNs loaded with IBU. Depan *et al.*,¹⁸⁸ developed CS-SBA-15@IBU system that upon US irradiation, at a frequency of 33 kHz, the polymer matrix permeability could be altered to allow the release of IBU. The flexibility of CS chains enabled the absorption of water and swelling causing the hydrogen bonds between IBU and the polymer chains to weaken and dissociate. Therefore, cavitation effects generated by US enhanced the drug release, reporting pulsing the US increased the drug release than continuous application.

Li *et al.*,¹⁸⁹ built-upon the previous US-triggered drug release systems by coating the MSN surface with a polydopamine (PDA) film with a 3 nm thickness. The anticancer drug, doxorubicin (DOX) was not only adsorbed into the silica mesopores, but was present in the PDA network, possibly due to π - π conjugation or hydrogen bonding interactions. The obtained MSN@DOX-PDA nanosystem showed diameter sizes of ~100 nm and 13.6 wt% drug loading. Interestingly, the drug delivery system was responsive to both pH and HIFU, creating a dual release system. In acidic conditions, the PDA polymer was prone to partial degradation, weakening the interaction with DOX causing its release. In addition, MSN@DOX-PDA was activated with HIFU (1.1 MHz, 100 W) by on/off switching, showing the pulsatile DOX-release behaviour. At pH 5.5

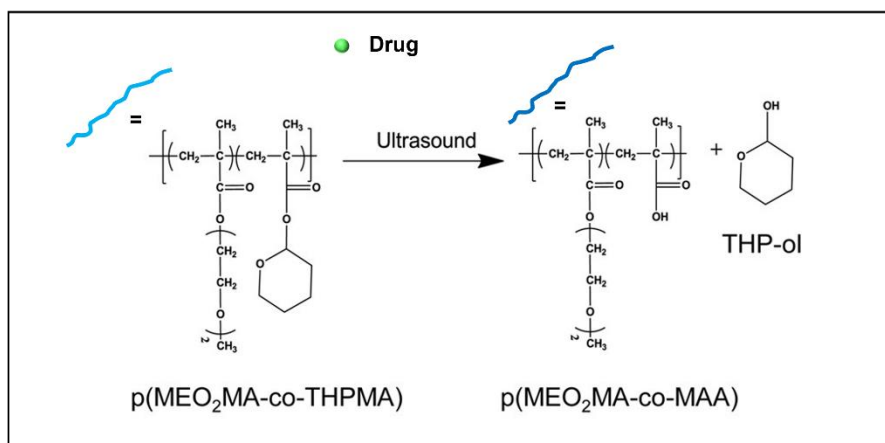
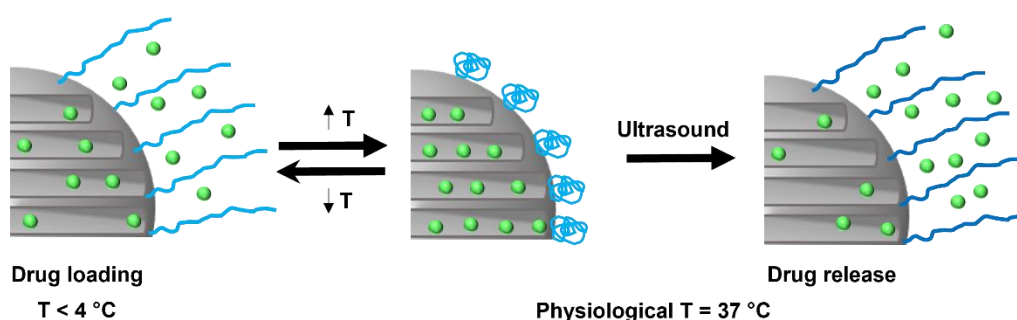
and 10 min HIFU the drug release was accelerated by 4% each time. Furthermore, the cytotoxicity of MSN@DOX-PDA's was tested on HeLa cells, which revealed cell viability was not affected by concentrations of MSN or PDA up to 60µg/mL and the killing effect came from free DOX.

More sophisticated systems were developed by using co-polymers to graft on the surface of MSNs to achieve a dual responsiveness for cancer treatments. An example was demonstrated by the Vallet-Regí group.¹⁹⁰ Demonstrated in **Figure 1. 13A**, MSNs were functionalised with co-polymer poly(2-(2-methoxyethoxy) ethyl methacrylate-co-2-tetrahydropyranyl methacrylate p(MEO₂MA-co-THPMA) to act as gatekeepers for the pore entrances loaded with drugs. The THPMA monomer contains a labile acetal group that could be cleaved with US. In addition, p(MEO₂MA) was included as the thermo-responsive polymer to aid loading and retention of the drug. At a low critical temperature of 4 °C in aqueous solution, the polymer adopts a linear confirmation to allow the drug molecules to enter the pores and increasing the temperature above 10 °C the polymer shows hydrophilic behavioural changes to form coil-like structures. However, aggregation problems due to the hydrophobic surface and lack of targeting moieties of the nanosystem resulted in Vallet-Regí and co-workers¹⁹¹ modifying the drug delivery system further, as displayed in **Figure 1. 13B**.

Firstly, the US-responsive co-polymer p(MEO₂MA-co-THPMA), termed PUS, was modified with PEG chains to provide stability to the NPs and prevent aggregation. The PEGylated polymer contained a maleimide group on one end to enable conjugation to the MSN surface via APTES carboxylic acid groups. Secondly, two different targeting agents were attached to the other end of the PEG chain. One included biotin (vitamin B7), as there is overexpression of biotin receptors in various cancer cells, hence a

desirable targeting moiety to increase cellular uptake of nanoparticles. The other included a peptide consisting of a Arg–Gly–Asp (RGD) sequence, which is selectively recognised by the $\alpha_v\beta_3$ integrin receptor. However, to evaluate the complex and versatile MSN@PUS-PEG-Biotin and MSN@PUS-PEG-RGD systems, fluorescein, ruthenium compound $[\text{Ru}(\text{bipy})_3]^{2+}$ and Rhodamine B (RhB) were used as model molecules to load into the pores and test the release profiles with US. Generally, the

A) Co-polymer conformation for loading & release



B) Modified drug delivery system with US trigger and targeting moiety

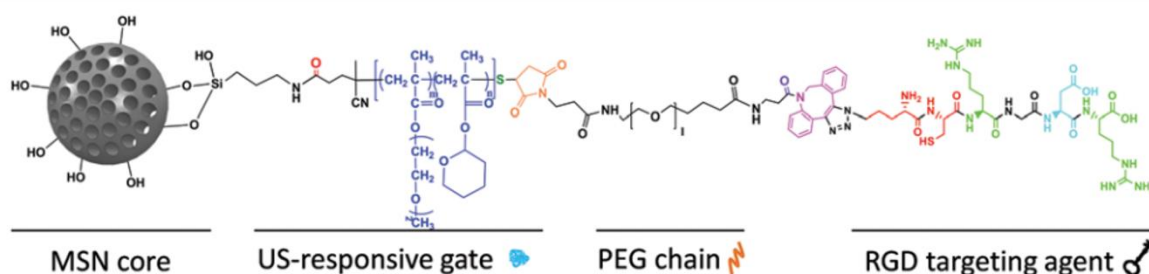


Figure 1. 13: A) Schematic of thermal and US responsive co-polymer functionalised on MSN and **B)** further modifications with PEG and targeting moiety to form MSN@PUS-PEG-RGD. Adapted from Paris *et al.* 190-192

synthesised particles produced sizes of 250 nm with 2 nm pores and surface charge between -31 and -45 mV. A high drug loading of 30 % was possible and was shown to be consistent with all fluorescent molecules. Also 10 min US irradiation (1.3 MHz, 100 W) demonstrated a triggered response with release reaching up to ~95 % after 24 h, almost a 4-fold increase compared to no US irradiation.

In 2019, Vallet-Regí and co-workers,¹⁹² expanded their polymer US-responsive system to carry both an anticancer drug DOX and plasmid encoding suicide genes, cytosine deaminase (CD) or uracil phosphoribosyl transferase (UPRT). In this case, MSN@PUS was engineered by coating with polyethyleneimine (PEI) to include nucleic acids for gene transfection. Therefore, non-toxic pro-drug 5-fluorocytosine (5-FC), when injected, could be converted into toxic 5-Fluoruracil (5-FU) by activation through US-released suicide genes from MSN@PUS. Hence, the plasmids combined with anticancer agents had the potential for inducing cell death in mesenchymal stem cells.

Co-polymers p(MEO₂MA-co-THPMA) have become highly popular to graft onto MSNs amongst researchers, especially taking advantage of THPMA monomer's critical US-responsive properties and acting as gatekeepers for controlled drug release. Nair *et al.*,¹⁹³ despite using a different co-polymer comprised of amino ethyl methacrylate (AEMA) to form p(AMEA-co-THPMA), the functionality remained the same by being sensitive to temperature and US. Their system differed to other reported MSNs, by their application purpose of transdermal drug delivery of 5-FU instead of intravenous administration. This was to avoid direct entry into the bloodstream and prevent unwanted side effects. The chemotherapeutic drug loaded MSN@p(AMEA-co-THPMA) produced particles sizes of 340 nm, much larger than previously reported and positive surface charge of 32 mV. They showed sensitivity to 15 min US (1.3 MHz, 100

W), releasing 42% of 5-FU after 24h and surprisingly by SEM imaging showed changes in morphology. Post-US exposure the surface of the NPs appeared disrupted and looked aggregated, a result not reported by previous polymer-coated-MSNs.

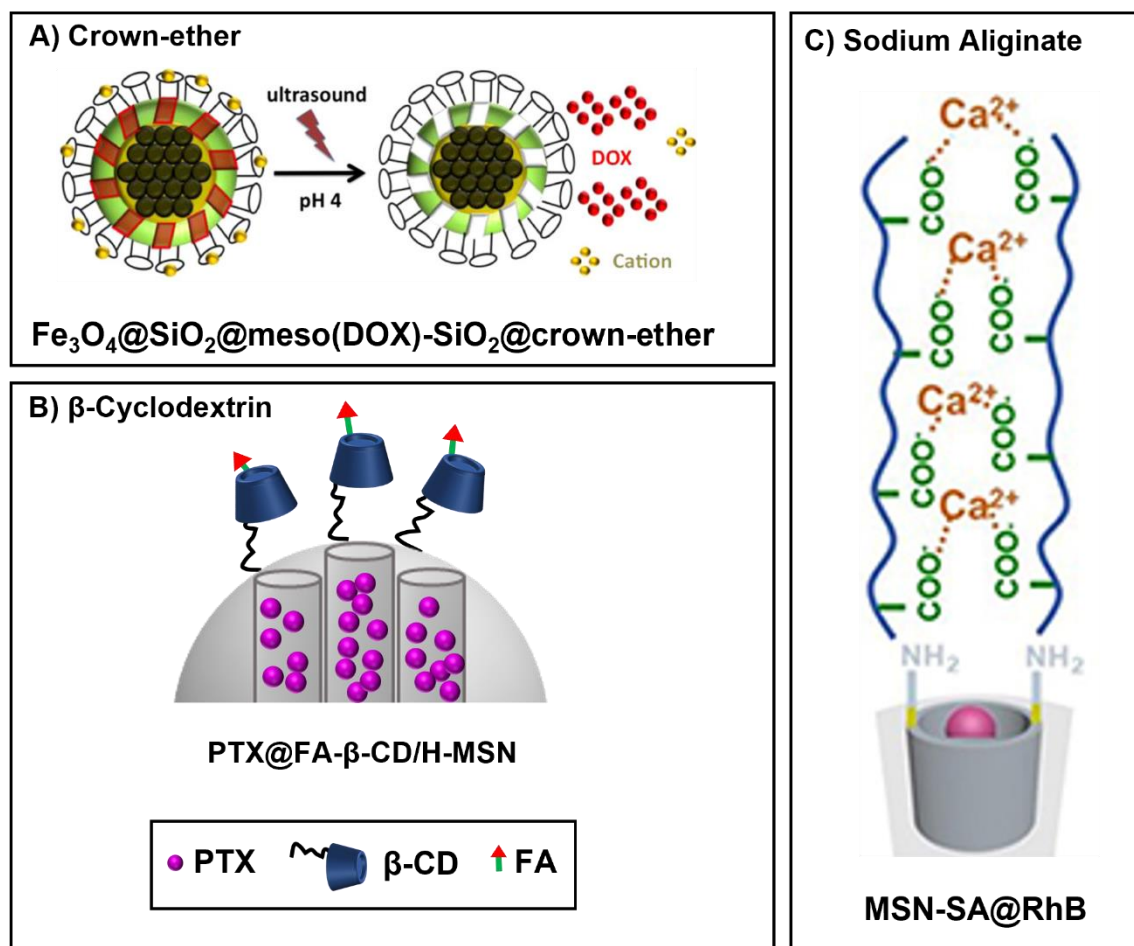


Figure 1. 14: MSN capping with nanomachines **A)** crown-ether, **B)** cyclodextrin and **C)** Sodium alginate. Reproduced from Lee *et al.*; Wang *et al.*; Li *et al.*¹⁹⁷⁻¹⁹⁹

Alternative to polymer-based capped MSNs, supramolecular nanomachines has been employed to provide large bulky constructs to block prevent drug release. Zink and co-workers, have already established ground-breaking work in developing stimuli-responsive gate-keepers on MSNs for antibiotic and cancer drug delivery.^{194–196}. However, US has been a less studied concept for drug release from silica. Therefore, in 2013, Zink and co-workers¹⁹⁷ loaded DOX into MSNs with an iron oxide (Fe_3O_4) core

and attached a dibenzo-crown ether via amide linkages, illustrated in **Figure 1. 14A**. Cationic ions, such as Na^+ or Cs^+ were used as capping agents to coordinate to the crown ether to act as the nano-valve gatekeeper and formed $\text{Fe}_3\text{O}_4@\text{SiO}_2@\text{meso}(\text{DOX})-\text{SiO}_2@\text{crown-ether}$. The release was tested in various pH conditions and pH 4 was chosen to mimic the conditions in tumour environments, which showed minimal premature drug release with no US. However, US (20 kHz, 130 W) irradiation at a pH 4, showed controlled and immediate release within the first 10 mins by dissociation of the metal ions from the crown ether, by 5-fold compared to the other crown-ether also studied.

In comparison, the works of Wang *et al.*,¹⁹⁸ focused on low intensity frequency US to trigger the release of loaded anticancer drug paclitaxel (PTX) from the hydrophobic modified internal channels of MSNs. The PTX loaded MSNs were coated with folic acid (FA) and β -cyclodextrin (β -CD) designed for active targeting to folic acid receptors overexpressed on cancer cells and cap the pores of MSNs, demonstrated in **Figure 1. 14B**. Cavitation effects produced from low energy US (1 MHz, 1.0 W cm^{-2}) on $\text{PTX}@\text{FA}-\beta\text{-CD}/\text{H-MSN}$, degenerated the alkyl bond between the MSNs and $\text{FA}-\beta\text{-CD}$, rapidly releasing PTX and showed to efficiently inhibit tumour growth.

Other supramolecular interactions were also explored by Li *et al.*,¹⁹⁹ by incorporating metal coordination bonds with a sodium alginate (SA) polymer coated of the surface of MSNs. As shown in **Figure 1. 14C**, this created a reversible on/off US system, where carboxyl (COO^-) and calcium ions (Ca^{2+}) interactions formed from the crossed linked SA polymer could break and reform. RhB was loaded into the MSN pores to produce $\text{MSN-SA}@\text{RhB}$ nanosystem with sizes of 147 nm and achieved a loading of 14% RhB.

The on-off releasing profiles of RhB with 5 min total HIFU (1.1 M Hz, 80 W) irradiation showed 98 % release.

To boost the US activity, enhancing agents, such as perfluorohexane (PFH) have been entrapped into silica structures alongside therapeutic agents. Fluorocarbons increase the microbubble volume formation, intensifying the cavitation effect produced from US.²⁰⁰ Therefore, US sensitive and hydrophobic PHF has been included into several silica nanosystems and has been mainly reported to enhance tumour ablation, whilst releasing anticancer agents at the targeted site. An early example by Shi and co-workers²⁰¹ encapsulated hydrophobic camptothecin (CPT), hydrophilic DOX and PFH into a hollow interior of mesoporous shell. Fabrication of the porous silica shell and hollow core is usually achieved through an etching process that entails -O-Si-O- bonds to be broken under basic conditions, following the general steps in **Figure 1. 15A**. However, resulted in large diameters of 300 nm and encapsulation of 35% CTP. US-triggered CPT release from CPT/DOX/PFH@hMSN was accelerated upon HIFU (150 W cm^{-2}) irradiation by cleavage of the hollow stricture. However, CPT release was also apparent when no US applied aqueous solution, but slow due to its hydrophobicity. The combined effect of DOX and CPT co-encapsulated hMSNs showed significantly higher cytotoxicity on DOX-resistant MCF-7/ADR cells than single drug in hMSNs or drug alone. Thus, showing promising syngenetic effects for overcoming potential drug-resistance issues.

Similarly, in **Figure 1. 15B** silica nanoparticles were formulated with CPT and perfluorooctyl bromide (PFOB), another US-sensitive agent.²⁰² Although in this design, CPT and PFOB were first loaded into a polymer (PLGA) before coating with an ultrathin layer of silica (4 nm thickness) using a nanoemulsion process. This formed

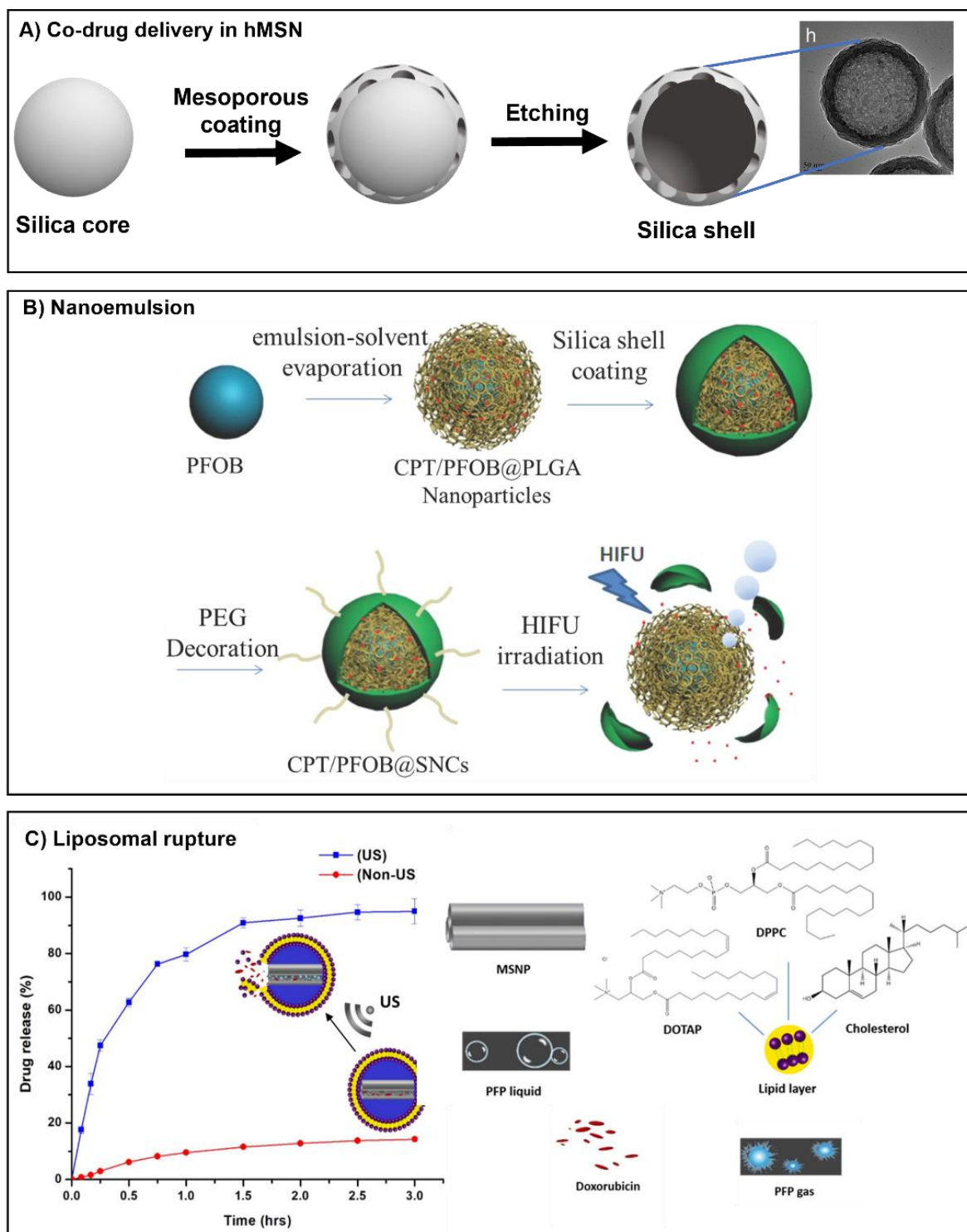


Figure 1. 15: Schematic representation of silica nanosystems including US enhancing agents **A)** synthesis of hollow MSNs (hMSNs) for co-delivery of DOX and CPT. **B)** CPT/PFOB@SNCs nanocapsules activated by US. **C)** Drug loaded liposome. Adapted from Chen *et al.*, Ma *et al.* and Amin *et al.* ^{201,202,204}

nanocapsules CPT/PFOB@SNCs of 200 nm sizes and almost a 4-fold higher drug loading was achieved compared to hMSNs, due to the hydrophobicity of PLGA core. The intact silica shell acted as a barrier to reduce drug release and structural collapse was dependant on the shell thickness to allow rapid drug release induced by HIFU (3.5 MHz, 80W) irradiation expelling PLGA and silica segments. On demand HFIU was highly favourable to produce a synergistic effect in breast cancer cells.

More recently, hydrogels and liposomes have been utilised to coat SNPs to add multifunctionality to the nanosystem, such as for US imaging, HIFU therapy, and prevent uncontrolled release.²⁰³ As a result, Bakowsky and co-workers²⁰⁴ took advantage of the high loading capabilities and fabricated a US-responsive drug release system. A liposome coating on the MSN surface was filled with DOX and perfluoropentane (PFP). The electrostatic interaction played a key role between the MSNs, liposome, and DOX to facilitate drug entrapment of 48%. Interestingly, drug release was stimulated by a HIFU (12 MHz, 351.37 W cm⁻²), which showed complete drug release after 3h and minimal leakage (10%) with no US. Therefore, incorporating PFP into the MSNs favoured the production of large volumes of gas bubbles by vaporisation PFP upon exposure to US irradiation. The combined mechanical and thermal effects increased internal pressure rupturing the lipid structure, forcing the rapid release of DOX, shown by transmission electron microscopy.

Besides MSNs other silica structures have been utilised for drug delivery and release with a US-trigger. For example, Kapoor *et al.*,²⁰⁵ deviated from the typical MSN spherical shape and synthesised silica nanotubes (SNT). The internal structure of SNT remained like MSNs, containing porous channels created by a sol-gel templating method. However, in terms of morphology SNTs were much larger in size with lengths

of 10 μm and inner and outer diameters of 200 and 300 nm, respectively. The SNTs were coated in 2,3 dihydroxynaphthalene (DN) to prevent the escape of 25% loaded IBU. The drug release kinetics of IBU from SNT-DN: IBU were conducted in simulated body fluid (SBF) at 25 °C with and without a US-trigger. In absence of US, 20% of IBU was released after 30 h, compared to the control MSNs loaded with IBU, which showed ~80%. Furthermore, US-irradiation (33 kHz) exhibited release kinetics that were more favourable with 0.5 min impulses and 2 min rest times rather than continuous US, displaying higher IBU yields of 37%. Additionally, the shorter impulse times with US resulted in far less debris formed, which could have unknown and unwanted cytotoxicity effects.

The next few fabricated silica US-responsive systems have been based on hollow MSNs. The hollow interior is an excellent feature for enhanced drug loading capabilities and the composition is desirable to improve bio-safety issues. The porous hMSN shell provides a reservoir for both hydrophobic and hydrophilic drugs by diffusion and encapsulation via the pore channels.

Qian et al.,²⁰⁶ synthesised hMSN with a chemical alkaline etching process and loaded with anticancer drug, PTX forming large sizes of 450 nm and drug encapsulation of 90.9 mg/g (**Figure 16A**). No additional surface modifications were reported to block or slow the release of PTX, which lead to 60% uncontrolled release within 12 h with no US irradiation. Although with three pulses of US-irradiation (1 MHz, 1.5 Wcm^{-2}), 82% of IBU had been release in 5.5 h, a 3-fold increase. Hence, the π - π supramolecular interactions of silica framework with drug were US-sensitive, triggering IBU release. In other works, He and co-workers²⁰⁷ developed and demonstrated a combined tumour-targeting, image guidance for precision gas therapy and US-stimuli drug release

nanosystem. For MRI guidance, image contrast agent iron oxide NPs (SPIONs) were used as the core to hMSNs (**Figure 16B**).

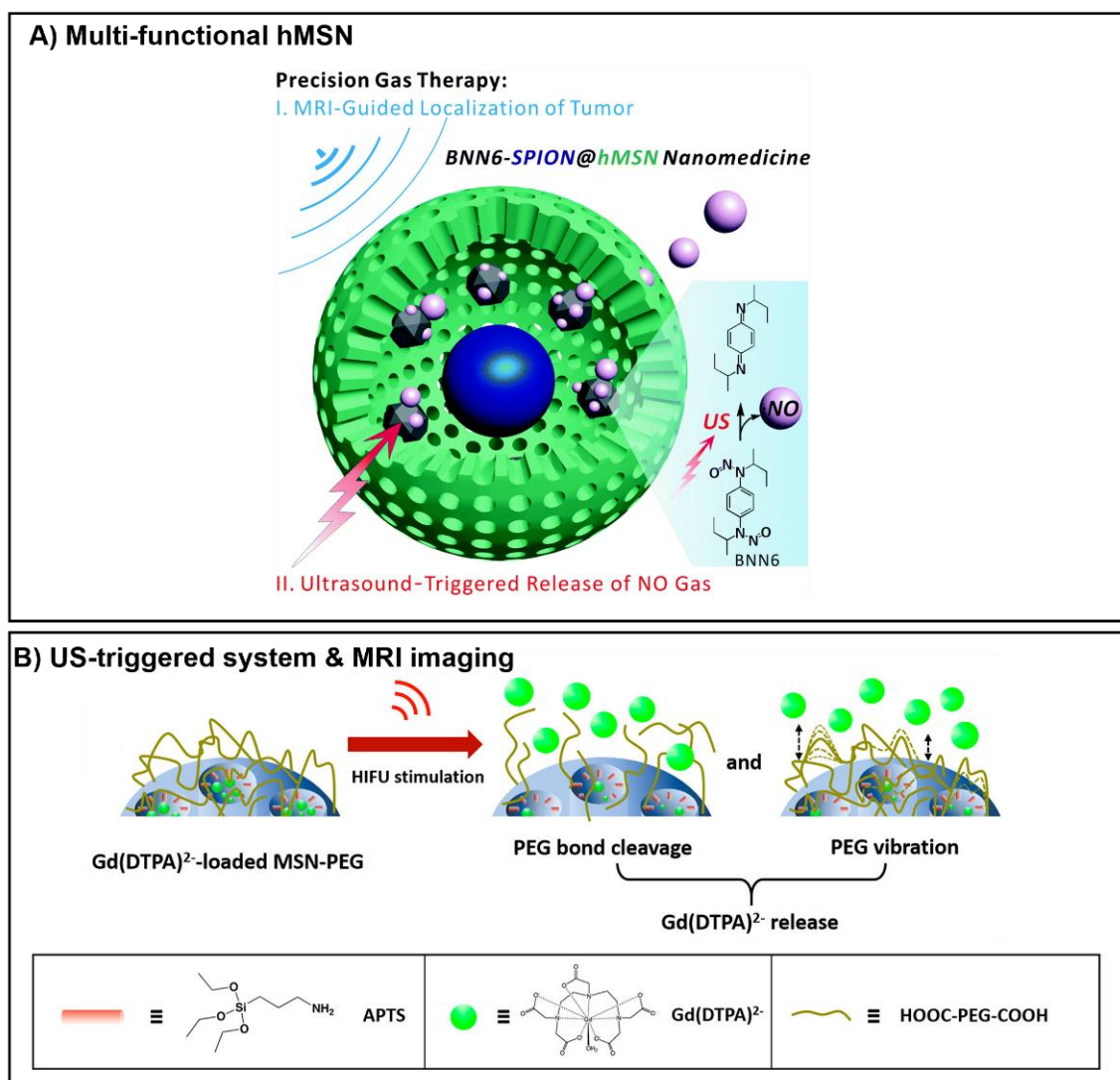


Figure 1. 16: **A)** schematic of BNN6-SPION@hMSN for triggered release of nitric oxide and **B)** PEG cleavage from MSN surface to release (Gd(DTPA)²⁻) with US. Adapted from Jin *et al.* and Chen *et al.*²⁰⁶⁻⁷

The mesoporous silica coating was formed layer-by-layer with etching methods to load a highly hydrophobic drug, N,N'-di-sec-butyl-N,N'- dinitroso-1,4-phenylenediamine (BNN6). The high loading capacity of hMSNs provided efficient loading of 623 mg BNN6 per gram silica by a nano-casting method, driven by degassing under vacuum

to form BNN6-SPION@hMSN (**Figure 1. 16A**). Importantly, BNN6 prodrug structure is stable in aqueous conditions and is responsible for liberating nitric oxide (NO) to inhibit the growth of tumours. US induced the release of $\cdot\text{NO}$ free radicals caused by decomposition of BNN6 by removal of two nitrosyl groups. Adjusting the powered settings of the US applied, increased the amount of NO generated. For biological studies, the highest power setting of US (0.5 MHz, 1.5 Wcm^{-2}) caused greater cytotoxicity, reducing the cell viability by 94% with $200 \mu\text{g mL}^{-1}$ BNN6-SPION@hMSN concentration. Zink and co-workers,²⁰⁸ employed MRI contrast agent gadopentetate dimeglumine ($\text{Gd}(\text{DTPA})^{2-}$) into amine functionalised MSNs. The surface was modified with HOOC-PEG-COOH designed seal the MSN pores and cleave when stimulated by HIFU, as exhibited in **Figure 1. 16B**. Even though, this system focused on the release of an MRI imaging agent, a good loading of 24% was achieved with a positively charged compound and showed a 62% release efficacy with 30 min US irradiation (20 kHz, 75 Wcm^{-2}).

A very unique silica designed US-responsive nanosystem was established by Malekmohammadi *et al.*²⁰⁹ Dendritic silica mesoporous particles were prepared by the traditional MSNs synthesis, but modified with a titanium precursor to form titanium dioxide layers on the surface of the silica nanoparticles. This formed dendritic silica/titania nanoparticles (DSTNs), which were functionalised with PEI-FA through electrostatic interactions to act as gatekeepers to block the loaded anticancer drug, curcumin (CUR). The fabricated particles had diameters of 173 nm, a drug loading capacity of 25% and encapsulation efficient of 43%, similar to other reported MSN structures. Titania was included for its sonosensitiser properties, important for inducing reactive oxygen species. Therefore, US (1 MHz, 2 Wcm^{-2}) triggered release of CUR

was stimulated by titania, which generated free radicals (OH^\bullet and O_2^\bullet) that cleaved PEI from the surface of MSNs. The new system showed accelerated drug release with only 120s US and overall, 78% CUR in 48h. In addition, US-triggered CUR@PEI-FA-DSTN showed the enhanced cytotoxic activity on HeLa cells. A remarkable 5-fold cell death was shown compared to 200 $\mu\text{g/mL}$ free CUR (18% inhibition).

1.6. Research aims

To summarise, there is a need for localised delivery and controlled release of antimicrobial agents to improve the prevention and eradication of dental biofilms, responsible for infections. Current NP methods that involve drug loading and a controlled triggered drug release, are complex. They require several synthetic, characterisation and purification steps to overcome problems of stability, drug loading and ensuring the release of the drug with an internal or external stimuli. The effect of nanotechnology on dentistry remains limited and more research is required to investigate the efficacy of nanomaterials. In addition, SNPs have been recognised for their ability to load drugs, provide protection and enhance the bactericidal activity.

Furthermore, the combination of US and nanoparticles has substantial potential to enhance the drug release and delivery. To-date US-stimulated antimicrobial release from SNPs has not been investigated before for dental applications.

Therefore, the overall aim of the PhD project is to develop a simple SNP drug delivery system to incorporate antimicrobial agents. The drug will be released on-demand by ultrasonication for treatment of biofilms. This will contribute towards dental infections and SNP stimuli-responsive drug delivery fields. To achieve this, the project has been divided into three areas:

- Firstly, to design and synthesise a one-pot method to create SNPs that can encapsulate antimicrobial agents without any additional steps and modifications. Optimisation of the synthetic process will be evaluated and analysed by various characterisation techniques. This information will give conditions that affect the particle formation and confirmation of drug loading. In addition, an ultrasonic scaler

(clinical dental tool) will be used to assess the drug release behaviour from the SNPs with and without US activation. After establishing a proof-of-concept model this can be tested for its antimicrobial efficacy.

- The optimised drug loaded SNP system will be investigated for its effectiveness against oral strains of bacteria. A single-species biofilm model will be developed to study the antimicrobial efficacy in combination with US.
- Finally, the SNP drug delivery model will be investigated if it can be applied to other antimicrobial agents and evaluated for its bactericidal activity.

1.7. References

- 1 F. E. Dewhirst, T. Chen, J. Izard, B. J. Paster, A. C. R. Tanner, W.-H. Yu, A. Lakshmanan and W. G. Wade, *J. Bacteriol.*, 2010, **192**, 5002–5017.
- 2 B. J. Paster, S. K. Boches, J. L. Galvin, R. E. Ericson, C. N. Lau, V. A. Levanos, A. Sahasrabudhe and F. E. Dewhirst, *J. Bacteriol.*, 2001, **183**, 3770–3783.
- 3 J. L. Mark Welch, B. J. Rossetti, C. W. Rieken, F. E. Dewhirst and G. G. Borisy, *Proc. Natl. Acad. Sci.*, 2016, **113**, E791–E800.
- 4 M. Lu, S. Xuan and Z. Wang, *Food Sci. Hum. Wellness*, 2019, **8**, 8–15.
- 5 M. Kilian, I. L. C. Chapple, M. Hannig, P. D. Marsh, V. Meuric, A. M. L. Pedersen, M. S. Tonetti, W. G. Wade and E. Zaura, *Br. Dent. J.*, 2016, **221**, 657–666.
- 6 H.-C. Flemming, J. Wingender, U. Szewzyk, P. Steinberg, S. A. Rice and S. Kjelleberg, *Nat. Rev. Microbiol.*, 2016, **14**, 563–575.
- 7 J. W. Costerton, P. S. Stewart and E. P. Greenberg, *Science (80-.)*, 1999, **284**, 1318–1322.
- 8 R. M. Donlan, *Emerg. Infect. Dis.*, 2002, **8**, 881–890.
- 9 P. N. Deo and R. Deshmukh, *J. Oral Maxillofac. Pathol.*, 2019, **23**, 122–128.
- 10 E. Karatan and P. Watnick, *Microbiol. Mol. Biol. Rev.*, 2009, **73**, 310–347.
- 11 M. V. Martin, L. P. Longman, M. P. Forde and M. L. Butterworth, *Br. Dent. J.*, 2007, **203**, 2006–2008.
- 12 R. J. Genco, S. G. Grossi, A. Ho, F. Nishimura and Y. Murayama, *J. Periodontol.*, 2005, **76**, 2075–2084.
- 13 W. S. Borgnakke and P. Poudel, *Front. Dent. Med.*, 2021, **2**, 1–13.
- 14 S. Awano, T. Ansai, Y. Takata, I. Soh, S. Akifusa, T. Hamasaki, A. Yoshida, K. Sonoki, K. Fujisawa and T. Takehara, *J. Dent. Res.*, 2008, **87**, 334–339.
- 15 M. Son, S. Jo, J. S. Lee and D. H. Lee, *Sci. Rep.*, 2020, **10**, 1–9.
- 16 N. Wake, Y. Asahi, Y. Noiri, M. Hayashi, D. Motooka, S. Nakamura, K. Gotoh, J. Miura, H. Machi, T. Iida and S. Ebisu, *npj Biofilms Microbiomes*, 2016, **2**, 16018.
- 17 V. Zijge, M. B. M. van Leeuwen, J. E. Degener, F. Abbas, T. Thurnheer, R. Gmür and H. J. M. Harmsen, *PLoS One*, 2010, **5**, e9321.
- 18 P. E. Kolenbrander, R. J. Palmer, S. Periasamy and N. S. Jakubovics, *Nat. Rev. Microbiol.*, 2010, **8**, 471–480.
- 19 T. J. Silhavy, D. Kahne and S. Walker, *Cold Spring Harb Perspect Biol*, 2010, **2**, 1–16.

- 20 P. Clarke and M. D. Lilly, *Nature*, 1962, **195**, 516–517.
- 21 R. M. Epand, C. Walker, R. F. Epand and N. A. Magarvey, *Biochim. Biophys. Acta - Biomembr.*, 2016, **1858**, 980–987.
- 22 L. Hall-Stoodley and P. Stoodley, *Curr. Opin. Biotechnol.*, 2002, **13**, 228–233.
- 23 A. H. Nobbs, H. F. Jenkinson and N. S. Jakubovics, *J. Dent. Res.*, 2011, **90**, 1271–1278.
- 24 D. Berger, A. Rakhamimova, A. Pollack and Z. Loewy, *High-throughput*, 2018, **7**, 1–8.
- 25 R. Huang, M. Li and R. L. Gregory, *Virulence*, 2011, **2**, 435–444.
- 26 G. M. Abebe, *Int. J. Oral Dent. Heal.*, 2021, **7**, 1–11.
- 27 O. Y. A. Costa, J. M. Raaijmakers and E. E. Kuramae, *Front. Microbiol.*, 2018, **9**, 1–14.
- 28 P. Di Martino, *AIMS Microbiol.*, 2018, **4**, 274–288.
- 29 H. C. Flemming, T. R. Neu and D. J. Wozniak, *J. Bacteriol.*, 2007, **189**, 7945–7947.
- 30 M. Pan, L. Zhu, L. Chen, Y. Qiu and J. Wang, 2016, **11**, 8092–8115.
- 31 T. Ramirez-Mora, C. Retana-Lobo and G. Valle-Bourrouet, *PLoS One*, 2018, **13**, 1–12.
- 32 H. C. Flemming and J. Wingender, *Nat. Rev. Microbiol.*, 2010, **8**, 623–633.
- 33 R. M. Donlan and J. W. Costerton, *Clin. Microbiol. Rev.*, 2002, **15**, 167–193.
- 34 S. Kamakura, in *Advances in Metallic Biomaterials: Tissues, Materials and Biological Reactions*, 2015, vol. 3, pp. 99–122.
- 35 R. Schilke, J. A. Lisson, O. Bauß and W. Geurtsen, *Arch. Oral Biol.*, 2000, **45**, 355–361.
- 36 G. W. Marshall, S. J. Marshall, J. H. Kinney and M. Balooch, *J. Dent.*, 1997, **25**, 441–458.
- 37 P. E. Petersen, D. Bourgeois, H. Ogawa, S. Estupinan-day and C. Ndiaye, *Bull World Heal. Organ.*, 2005, **83**, 661–669.
- 38 S. S. Socransky, A. D. Haffajee, M. A. Cugini, C. Smith and R. L. Kent, *J. Clin. Periodontol.*, 1998, **25**, 134–144.
- 39 A. O. Arigbede, B. O. Babatope and M. K. Bamidele, *J. Indian Soc. Periodontol.*, 2012, **16**, 487–491.
- 40 F. Q. Bui, C. L. C. Almeida-da-Silva, B. Huynh, A. Trinh, J. Liu, J. Woodward, H. Asadi and D. M. Ojcius, *Biomed. J.*, 2019, **42**, 27–35.

- 41 B. L. Pihlstrom, B. S. Michalowicz and N. W. Johnson, *Lancet*, 2005, **366**, 1809–1820.
- 42 L. M. Sedghi, M. Bacino and Y. L. Kapila, *Front. Cell. Infect. Microbiol.*, 2021, **11**, 1–26.
- 43 C. M. L. Bollen, P. Lambrechts and M. Quirynen, *Dent. Mater.*, 1997, **13**, 258–269.
- 44 W. M. Mcshan, R. E. Mclaughlin, G. Savic, J. Chang, M. B. Carson, C. Primeaux, R. Tian, S. Kenton, H. Jia, S. Lin, Y. Qian, S. Li, H. Zhu, F. Najjar, H. Lai, J. White, B. A. Roe and J. J. Ferretti, *PNAS*, 2002, **99**, 14434–14439.
- 45 D. Kim, J. P. Barraza, R. A. Arthur, A. Hara, K. Lewis, Y. Liu, E. L. Scisci, E. Hajishengallis, M. Whiteley and H. Koo, *Proc. Natl. Acad. Sci.*, 2020, **117**, 12375–12386.
- 46 P. D. Marsh, *Dent. Clin. North Am.*, 2010, **54**, 441–454.
- 47 R. H. Selwitz, A. I. Ismail and N. B. Pitts, *Lancet*, 2007, **369**, 51–59.
- 48 N. Takahashi and B. Nyvad, *J. Dent. Res.*, 2011, **90**, 294–303.
- 49 W. H. Bowen, R. A. Burne, H. Wu and H. Koo, *Trends Microbiol.*, 2018, **26**, 229–242.
- 50 B. M. Eley, *Br. Dent. J.*, 1999, **186**, 286–296.
- 51 V. García, M. Rioboo, J. Serrano, A. O'Connor, D. Herrera and M. Sanz, *Int. J. Dent. Hyg.*, 2011, **9**, 266–273.
- 52 G. M. S. Soares, L. C. Figueiredo, M. Faveri, S. C. Cortelli, P. M. Duarte and M. Feres, *J. Appl. Oral Sci.*, 2012, **20**, 295–309.
- 53 S. Sheen, M. Eisenburger and M. Addy, *J. Clin. Periodontol.*, 2003, **30**, 255–260.
- 54 P. D. Marsh, *J. Dent.*, 2010, **38**, S11–S15.
- 55 H. Ahmadi, A. Ebrahimi and F. Ahmadi, *Int. J. Dent.*, 2021, **2021**, 1–10.
- 56 K. Lewis, *Nat. Rev. Drug Discov.*, 2013, **12**, 371–387.
- 57 C. L. Ventola, *P T*, 2015, **40**, 277–283.
- 58 I. Roca, M. Akova, F. Baquero, J. Carlet, M. Cavaleri, S. Coenen, J. Cohen, D. Findlay, I. Gyssens, O. E. Heur, G. Kahlmeter, H. Kruse, R. Laxminarayan, E. Liébana, L. López-Cerero, A. MacGowan, M. Martins, J. Rodríguez-Baño, J. M. Rolain, C. Segovia, B. Sigauque, E. Taconelli, E. Wellington and J. Vila, *New Microbes New Infect.*, 2015, **6**, 22–29.
- 59 H. Wu, C. Moser, H.-Z. Wang, N. Høiby and Z.-J. Song, *Int. J. Oral Sci.*, 2015, **7**, 1–7.

- 60 D. Davies, *Nat. Rev. Drug Discov.*, 2003, **2**, 114–122.
- 61 C. Walsh, *Nature*, 2000, **406**, 775–781.
- 62 D. Sharma, L. Misba and A. U. Khan, *Antimicrob. Resist. Infect. Control*, 2019, **8**, 76.
- 63 S. Of and M. Covered, in *Craig's Restorative Dental Materials*, Elsevier, 2019, pp. 1–3.
- 64 S. Kasraei, L. Sami, S. Hendi, M.-Y. Alikhani, L. Rezaei-Soufi and Z. Khamverdi, *Restor. Dent. Endod.*, 2014, **39**, 109–14.
- 65 M. Gharechahi, H. Moosavi and M. Forghani, *J. Biomater. Nanobiotechnol.*, 2012, **03**, 541–546.
- 66 S. J. Ahn, S. J. Lee, J. K. Kook and B. S. Lim, *Dent. Mater.*, 2009, **25**, 206–213.
- 67 N. Beyth, I. Yudovin-Farber, A. Basu, E. I. Weiss and A. J. Domb, in *Emerging Nanotechnologies in Dentistry*, Elsevier, Second Edi., 2018, pp. 41–58.
- 68 S. Gupta, P. Saxena, V. Pant and A. Pant, *Toxicol. Int.*, 2012, **19**, 225–234.
- 69 J.-S. Kim and D.-H. Shin, *Restor. Dent. Endod.*, 2013, **38**, 36.
- 70 A. D. Walmsley, *Ultrasound Med. Biol.*, 1988, **14**, 7–14.
- 71 B. DeSpain Eden, *Prev. Clin. Oral Heal. Care*, 2008, 213–229.
- 72 I. Ioannou, N. Dimitriadis, K. Papadimitriou, D. Sakellari, I. Vouros and A. Konstantinidis, *J. Clin. Periodontol.*, 2009, **36**, 132–141.
- 73 S. Oda, H. Nitta, T. Setoguchi, Y. Izumi and I. Ishikawa, *Periodontol. 2000*, 2004, **36**, 45–58.
- 74 G. Greenstein, *J. Am. Dent. Assoc.*, 2000, **131**, 1580–1592.
- 75 G. Greenstein and M. Tonetti, *J. Periodontol.*, 2000, **71**, 125–140.
- 76 G. Schenk, T. F. Flemmig, S. Lob, G. Ruckdeschel and R. Hickel, *J. Clin. Periodontol.*, 2000, **27**, 116–119.
- 77 G. J. Petersilka, B. Ehmke and T. F. Flemmig, *Periodontol. 2000*, 2002, **28**, 56–71.
- 78 W. R. E. Laird and A. D. Walmsley, *J. Dent.*, 1991, **19**, 14–17.
- 79 S. C. Lea, G. J. Price and A. D. Walmsley, *Ultrason. Sonochem.*, 2005, **12**, 233–236.
- 80 Y.-L. Chen, H.-H. Chang, Y.-C. Chiang and C.-P. Lin, *J. Formos. Med. Assoc.*, 2013, **112**, 659–665.
- 81 A. D. Walmsley, *Phys. Procedia*, 2015, **63**, 201–207.

- 82 A. D. Walmsley, W. R. E. Laird and P. J. Lumley, *J. Dent.*, 1992, **20**, 11–17.
- 83 N. Vyas, E. Pecheva, H. Dehghani, R. L. Sammons, Q. X. Wang, D. M. Leppinen and A. D. Walmsley, *PLoS One*, 2016, **11**, 2–13.
- 84 R. P. Howlin, S. Fabbri, D. G. Offin, N. Symonds, K. S. Kiang, R. J. Knee, D. C. Yoganantham, J. S. Webb, P. R. Birkin, T. G. Leighton and P. Stoodley, *J. Dent. Res.*, 2015, **94**, 1303–1309.
- 85 A. D. Walmsley, S. C. Lea, B. Felver, D. C. King and G. J. Price, *Clin Oral Investig.*, 2013, **17**, 1227–1234.
- 86 J. L. Roti Roti, *Int. J. Hyperth.*, 2008, **24**, 3–15.
- 87 I. V. Larina, B. M. Evers, T. V. Ashitkov, C. Bartels, K. V. Larin and R. O. Esenaliev, *Technol. Cancer Res. Treat.*, 2005, **4**, 217–226.
- 88 N. Vyas, K. Manmi, Q. Wang, A. J. Jadhav, M. Barigou, R. L. Sammons, S. A. Kuehne and A. D. Walmsley, *Ultrasound Med. Biol.*, 2019, **45**, 1044–1055.
- 89 F. R. Young, *Cavitation*, 1999.
- 90 Z. Izadifar, P. Babyn and D. Chapman, *J. Med. Biol. Eng.*, 2019, **39**, 259–276.
- 91 T. Y. Wu, N. Guo, C. Y. Teh and J. X. W. Hay, *Chem. Eng. J.*, 2013, **2**, 5–9.
- 92 P. Tharkar, R. Varanasi, W. S. F. Wong, C. T. Jin and W. Chrzanowski, *Front. Bioeng. Biotechnol.*
- 93 B. Felver, D. C. King, S. C. Lea, G. J. Price and A. Damien Walmsley, *Ultrason. Sonochem.*, 2009, **16**, 692–697.
- 94 G. J. Price, T. J. Tiong and D. C. King, *Ultrason. Sonochem.*, 2014, **21**, 2052–2060.
- 95 M. Wang, Y. Zhang, C. Cai, J. Tu, X. Guo and D. Zhang, *Sci. Rep.*, 2018, **8**, 3885.
- 96 B. S. Khambay and A. D. Walmsley, *J. Periodontol.*, 1999, **70**, 626–636.
- 97 N. Vyas, Q. X. Wang and A. D. Walmsley, *Ultrason. Sonochem.*, 2021, **70**, 105338.
- 98 L. R. Pizzolato-Cezar, N. M. Okuda-Shinagawa and M. Teresa Machini, *Front. Microbiol.*, 2019, **10**, 1–5.
- 99 A. Das and I. Nasim, *J. Adv. Pharm. Educ. Res.*, 2017, **7**, 43–45.
- 100 S. Priyadarsini, S. Mukherjee and M. Mishra, *J. Oral Biol. Craniofacial Res.*, 2018, **8**, 58–67.
- 101 S. Hua, M. B. C. de Matos, J. M. Metselaar and G. Storm, *Front. Pharmacol.*, 2018, **9**, 1–14.

- 102 P. V. Baptista, M. P. McCusker, A. Carvalho, D. A. Ferreira, N. M. Mohan, M. Martins and A. R. Fernandes, *Front. Microbiol.*, 2018, **9**, 1–26.
- 103 J. K. Patra, G. Das, L. F. Fraceto, E. V. R. Campos, M. D. P. Rodriguez-Torres, L. S. Acosta-Torres, L. A. Diaz-Torres, R. Grillo, M. K. Swamy, S. Sharma, S. Habtemariam and H. S. Shin, *J. Nanobiotechnology*, 2018, **16**, 1–33.
- 104 M. J. Mitchell, M. M. Billingsley, R. M. Haley, M. E. Wechsler, N. A. Peppas and R. Langer, *Nat. Rev. Drug Discov.*, 2021, **20**, 101–124.
- 105 T. L. Doane and C. Burda, *Chem. Soc. Rev.*, 2012, **41**, 2885–2911.
- 106 D. Lombardo, M. A. Kiselev and M. T. Caccamo, *J. Nanomater.*, 2019, **2019**, 1–26.
- 107 T. J. Webster and Taylor, *Int. J. Nanomedicine*, 2011, **6**, 1463.
- 108 H. Zazo, C. I. Colino and J. M. Lanao, *J. Control. Release*, 2016, **224**, 86–102.
- 109 H. Chen, Y. Jin, J. Wang, Y. Wang, W. Jiang, H. Dai, S. Pang, L. Lei, J. Ji and B. Wang, *Nanoscale*, 2018, **10**, 20946–20962.
- 110 N. Devnarain, N. Osman, V. O. Fasiku, S. Makhathini, M. Salih, U. H. Ibrahim and T. Govender, *Wiley Interdiscip. Rev. Nanomedicine Nanobiotechnology*, 2021, **13**, 1–38.
- 111 Y. C. Yeh, T. H. Huang, S. C. Yang, C. C. Chen and J. Y. Fang, *Front. Chem.*, 2020, **8**, 1–22.
- 112 D. Bobo, K. J. Robinson, J. Islam, K. J. Thurecht and S. R. Corrie, *Pharm. Res.*, 2016, **33**, 2373–2387.
- 113 A. C. Anselmo and S. Mitragotri, *Bioeng. Transl. Med.*, 2019, **4**, 1–16.
- 114 D. Bilton, I. Fajac, T. Pressler, J. P. Clancy, D. Sands, P. Minic, M. Cipolli, I. Galeva, A. Solé, A. L. Quittner, Z. Jumadilova, M. Ciesielska and M. W. Konstan, *J. Cyst. Fibros.*, 2021, **20**, 1010–1017.
- 115 C. S. Haworth, D. Bilton, J. D. Chalmers, A. M. Davis, J. Froehlich, I. Gonda, B. Thompson, A. Wanner and A. E. O'Donnell, *Lancet Respir. Med.*, 2019, **7**, 213–226.
- 116 C. W. Kaplan, J. H. Sim, K. R. Shah, A. Kolesnikova-Kaplan, W. Shi and R. Eckert, *Antimicrob. Agents Chemother.*, 2011, **55**, 3446–3452.
- 117 Y. (Chezy) Barenholz, *J. Control. Release*, 2012, **160**, 117–134.
- 118 Y.-M. Ning, K. He, R. Dagher, R. Sridhara, A. T. Farrell, R. Justice and R. Pazdur, *Oncology (Williston Park)*, 2007, **21**, 1503–8; discussion 1511, 1513, 1516 passim.
- 119 M. Ferreira, M. Ogren, J. N. R. Dias, M. Silva, S. Gil, L. Tavares, F. Aires-da-Silva, M. M. Gaspar and S. I. Aguiar, *Molecules*, 2021, **26**, 2047.

- 120 D. B. Fenske and P. R. Cullis, *Expert Opin. Drug Deliv.*, 2008, **5**, 25–44.
- 121 Z. Shen, A. Fisher, W. K. Liu and Y. Li, in *Engineering of Biomaterials for Drug Delivery Systems*, Elsevier, 2018, pp. 1–26.
- 122 A. L. Klibanov, K. Maruyama, V. P. Torchilin and L. Huang, *FEBS Lett.*, 1990, **268**, 235–237.
- 123 L. Sercombe, T. Veerati, F. Moheimani, S. Y. Wu, A. K. Sood and S. Hua, *Front. Pharmacol.*, 2015, **6**, 1–13.
- 124 F. Khan, D. T. N. Pham, S. F. Oloketuyi, P. Manivasagan, J. Oh and Y.-M. Kim, *Colloids Surfaces B Biointerfaces*, 2020, **185**, 110627.
- 125 I. Hassanin and A. Elzoghby, *Cancer Drug Resist.*, 2020, 930–946.
- 126 A. F. Radovic-Moreno, T. K. Lu, V. A. Puscasu, C. J. Yoon, R. Langer and O. C. Farokhzad, *ACS Nano*, 2012, **6**, 4279–4287.
- 127 N. Alhusein, P. A. De Bank, I. S. Blagbrough and A. Bolhuis, *Drug Deliv. Transl. Res.*, 2013, **3**, 531–541.
- 128 M. Xiong, Y. Bao, X. Yang, Y. Zhu and J. Wang, *Adv. Drug Deliv. Rev.*, 2014, **78**, 63–76.
- 129 A. Zielińska, F. Carreiró, A. M. Oliveira, A. Neves, B. Pires, D. N. Venkatesh, A. Durazzo, M. Lucarini, P. Eder, A. M. Silva, A. Santini and E. B. Souto, *Molecules*, 2020, **25**, 3731.
- 130 H. Le, C. Karakasyan, T. Jouenne, D. Le Cerf and E. Dé, *Appl. Sci.*, 2021, **11**, 10695.
- 131 V. A. Spirescu, C. Chircov, A. M. Grumezescu and E. Andronescu, *Polymers (Basel)*, 2021, **13**, 724.
- 132 E. Sánchez-López, D. Gomes, G. Esteruelas, L. Bonilla, A. L. Lopez-Machado, R. Galindo, A. Cano, M. Espina, M. Ettcheto, A. Camins, A. M. Silva, A. Durazzo, A. Santini, M. L. Garcia and E. B. Souto, *Nanomaterials*, 2020, **10**, 1–39.
- 133 M. G. Correa, F. B. Martínez, C. P. Vidal, C. Streitt, J. Escrig and C. L. de Dicastillo, *Beilstein J. Nanotechnol.*, 2020, **11**, 1450–1469.
- 134 V. T. Noronha, A. J. Paula, G. Duran, A. Galembeck, K. Cogo-Muller, M. Franz-Montan and N. Duran, *Dent. Mater.*, 2017, **33**, 1110–1126.
- 135 J. M. Corrêa, M. Mori, H. L. Sanches, A. D. da Cruz, E. Poiate and I. A. V. P. Poiate, *Int. J. Biomater.*, 2015, **2015**, 1–9.
- 136 V. Selvarajan, S. Obuobi and P. L. R. Ee, *Front. Chem.*, 2020, **8**, 1–16.
- 137 W. Stober, A. Fink and E. Bohn, *J. Colloid Interface Sci.*, 1968, **26**, 62–69.
- 138 A. Burneau and B. Humbert, *Colloids Surfaces A Physicochem. Eng. Asp.*, 1993,

- 75**, 111–121.
- 139 A. van Blaaderen and A. P. M. Kentgens, *J. Non. Cryst. Solids*, 1992, **149**, 161–178.
 - 140 A. Van Blaaderen, J. Van Geest and A. Vrij, *J. Colloid Interface Sci.*, 1992, **154**, 481–501.
 - 141 H. Giesche, *J. Eur. Ceram. Soc.*, 1994, **14**, 189–204.
 - 142 L. Jelinek, P. Dong and H. Tai, 1992, 2152–2164.
 - 143 T. Matsoukas and E. Gulari, *J. Colloid Interface Sci.*, 1989, **132**, 13–21.
 - 144 T. Matsoukas and E. Gulari, *J. Colloid Interface Sci.*, 1988, **124**, 252–261.
 - 145 M. Nakamura and K. Ishimura, *Langmuir*, 2008, **24**, 5099–5108.
 - 146 M. Nakamura and K. Ishimura, *Langmuir*, 2008, **24**, 12228–12234.
 - 147 W. Arap, R. Pasqualini, M. Montalti, L. Petrizza, L. Prodi, E. Rampazzo, N. Zaccheroni and S. Marchio, *Curr. Med. Chem.*, 2013, **20**, 2195–2211.
 - 148 W. Borzęcka, T. Trindade, T. Torres and J. Tomé, *Curr. Pharm. Des.*, 2016, **22**, 6021–6038.
 - 149 S. Santra, in *Cancer Nanotechnology: Methods and Protocols*, eds. S. R. Grobmyer and B. M. Moudgil, Humana Press, Totowa, NJ, 2010, pp. 151–162.
 - 150 L. Tang and J. Cheng, *Nano Today*, 2013, **8**, 290–312.
 - 151 V. Mamaeva, C. Sahlgren and M. Lindén, *Adv. Drug Deliv. Rev.*, 2013, **65**, 689–702.
 - 152 G. Buchel, M. Grun, K. K. Unger, A. Matsumoto and K. Tsutsumi, *Supramol. Sci.*, 1998, **5**, 253–259.
 - 153 M. Grün, K. K. Unger, A. Matsumoto and K. Tsutsumi, *Microporous Mesoporous Mater.*, 1999, **27**, 207–216.
 - 154 Q. Cai, W. Y. Lin, F. S. Xiao, W. Q. Pang, X. H. Chen and B. S. Zou, *Microporous Mesoporous Mater.*, 1999, **32**, 1–15.
 - 155 G. Newham, R. K. Mathew, H. Wurdak, S. D. Evans and Z. Y. Ong, *J. Colloid Interface Sci.*, 2021, **584**, 669–683.
 - 156 F. Lu, S. H. Wu, Y. Hung and C. Y. Mou, *Small*, 2009, **5**, 1408–1413.
 - 157 S. H. Wu and H. P. Lin, *Chem. Soc. Rev.*, 2013, **42**, 3862–3875.
 - 158 M. Varache, I. Bezverkhyy, L. Saviot, F. Bouyer, F. Baras and F. Bouyer, *J. Non. Cryst. Solids*, 2015, **408**, 87–97.
 - 159 M. Frascioni, Z. Liu, J. Lei, Y. Wu, E. Strekalova, D. Malin, M. W. Ambrogio, X.

- Chen, Y. Y. Botros, V. L. Cryns, J. P. Sauvage and J. Fraser Stoddart, *J. Am. Chem. Soc.*, 2013, **135**, 11603–11613.
- 160 X. Wu, Z. Wang, D. Zhu, S. Zong, L. Yang, Y. Zhong and Y. Cui, *ACS Appl. Mater. Interfaces*, 2013, **5**, 10895–10903.
- 161 X. Li, T. Tang, Y. Zhou, Y. Zhang and Y. Sun, *Microporous Mesoporous Mater.*, 2014, **184**, 83–89.
- 162 N. Mas, I. Galiana, L. Mondragón, E. Aznar, E. Climent, N. Cabedo, F. Sancenón, J. R. Murguía, R. Martínez-Máñez, M. D. Marcos and P. Amorós, *Chem. - A Eur. J.*, 2013, **19**, 11167–11171.
- 163 G. G. Kaya, S. Medaglia, V. Candela-Noguera, M. Á. Tormo-Mas, M. D. Marcos, E. Aznar, H. Deveci and R. Martínez-Máñez, *Pharmaceutics*, 2020, **12**, 1–14.
- 164 N. Velikova, N. Mas, L. Miguel-Romero, L. Polo, E. Stolte, E. Zaccaria, R. Cao, N. Taverne, J. R. Murguía, R. Martinez-Manez, A. Marina and J. Wells, *Nanomedicine Nanotechnology, Biol. Med.*, 2017, **13**, 569–581.
- 165 B. González, M. Colilla, J. Díez, D. Pedraza, M. Guembe, I. Izquierdo-Barba and M. Vallet-Regí, *Acta Biomater.*, 2018, **68**, 261–271.
- 166 B. Ruehle, D. L. Clemens, B. Y. Lee, M. A. Horwitz and J. I. Zink, *J. Am. Chem. Soc.*, 2017, **139**, 6663–6668.
- 167 M. Kavruk, O. Celikbicak, V. C. Ozalp, B. A. Borsa, F. J. Hernandez, G. Bayramoglu, B. Salih and M. Y. Arica, *Chem. Commun.*, 2015, **51**, 8492–8495.
- 168 S. K. Alsaiani, M. A. Hammami, J. G. Croissant, H. W. Omar, P. Neelakanda, T. Yapici, K. V. Peinemann and N. M. Khashab, *Adv. Healthc. Mater.*, 2017, **6**, 1–9.
- 169 Z. Akram, U. Daood, S. Aati, H. Ngo and A. S. Fawzy, *Mater. Sci. Eng. C*, 2021, **122**, 111894.
- 170 Z. Akram, S. Aati, H. Ngo and A. Fawzy, *J. Nanobiotechnology*, 2021, **19**, 43.
- 171 M. M. Lu, Q. J. Wang, Z. M. Chang, Z. Wang, X. Zheng, D. Shao, W. F. Dong and Y. M. Zhou, *Int. J. Nanomedicine*, 2017, **12**, 3577–3589.
- 172 M. M. Lu, Y. Ge, J. Qiu, D. Shao, Y. Zhang, J. Bai, X. Zheng, Z. M. Chang, Z. Wang, W. F. Dong and C. B. Tang, *Int. J. Nanomedicine*, 2018, **13**, 7697–7709.
- 173 J. Yue, S. zhong Luo, M. meng Lu, D. Shao, Z. Wang and W. fei Dong, *Chem. Biol. Drug Des.*, 2018, **92**, 1435–1444.
- 174 J. Lin, Z. He, F. Liu, J. Feng, C. Huang, X. Sun and H. Deng, *Int. J. Nanomedicine*, 2020, **15**, 5377–5387.
- 175 A. García, B. González, C. Harvey, I. Izquierdo-Barba and M. Vallet-Regí, *Microporous Mesoporous Mater.*, 2021, **328**, 111489.

- 176 X. Ren, R. Gao, H. C. Van Der Mei, Y. Ren, B. W. Peterson and H. J. Busscher, *ACS Appl. Mater. Interfaces*, 2020, **12**, 34610–34619.
- 177 D. Hu, H. Li, B. Wang, Z. Ye, W. Lei, F. Jia, Q. Jin, K. F. Ren and J. Ji, *ACS Nano*, 2017, **11**, 9330–9339.
- 178 J. Cummins and M. Tangney, *Infect. Agent. Cancer*, 2013, **8**, 1.
- 179 K. Maier-Hauff, F. Ulrich, D. Nestler, H. Niehoff, P. Wust, B. Thiesen, H. Orawa, V. Budach and A. Jordan, *J. Neurooncol.*, 2011, **103**, 317–324.
- 180 X. Liu, Y. Zhang, Y. Wang, W. Zhu, G. Li, X. Ma, Y. Zhang, S. Chen, S. Tiwari, K. Shi, S. Zhang, H. M. Fan, Y. X. Zhao and X. J. Liang, *Theranostics*, 2020, **10**, 3793–3815.
- 181 E. Álvarez, M. Estévez, A. Gallo-Cordova, B. González, R. R. Castillo, M. D. P. Morales, M. Colilla, I. Izquierdo-Barba and M. Vallet-Regí, *Pharmaceutics*, 2022, **14**, 163.
- 182 J. G. Ovejero, I. Armenia, D. Serantes, S. Veintemillas-Verdaguer, N. Zeballos, F. López-Gallego, C. Grüttner, J. M. De La Fuente, M. Del Puerto Morales and V. Grazu, *Nano Lett.*, 2021, **21**, 7213–7220.
- 183 F. Nakonechny and M. Nisnevitch, *Adv. Funct. Mater.*, 2021, **31**, 2011042.
- 184 S. Gopalakrishnan, A. Gupta, J. M. V. Makabenta, J. Park, J. J. Amante, A. N. Chattopadhyay, D. Matuwana, C. J. Kearney and V. M. Rotello, *Adv. Healthc. Mater.*, 2022, **2201060**, 1–8.
- 185 K. Entzian and A. Aigner, *Pharmaceutics*, 2021, **13**, 1–31.
- 186 M. Manzano and M. Vallet-Regí, *Chem. Commun.*, 2019, **55**, 2731–2740.
- 187 H. J. Kim, H. Matsuda, H. Zhou and I. Honma, *Adv. Mater.*, 2006, **18**, 3083–3088.
- 188 D. Depan, L. Saikia and R. P. Singh, *Macromol. Symp.*, 2010, **287**, 80–88.
- 189 X. Li, C. Xie, H. Xia and Z. Wang, *Langmuir*, 2018, **34**, 9974–9981.
- 190 J. L. Paris, M. V. Cabanas, M. Manzano and M. Vallet-Regí, *ACS Nano*, 2015, **9**, 11023–11033.
- 191 J. L. Paris, G. Villaverde, M. V. Cabañas, M. Manzano and M. Vallet-Regí, *J. Mater. Chem. B*, 2018, **6**, 2785–2794.
- 192 J. L. Paris, P. de la Torre, M. V. Cabañas, M. Manzano, A. I. Flores and M. Vallet-Regí, *Acta Biomater.*, 2019, **83**, 372–378.
- 193 T. S. Anirudhan and A. S. Nair, *J. Mater. Chem. B*, 2018, **6**, 428–439.
- 194 F. C. Lin, Y. Xie, T. Deng and J. I. Zink, *J. Am. Chem. Soc.*, 2021, **143**, 6025–6036.

- 195 W. Chen, C. A. Glackin, M. A. Horwitz and J. I. Zink, *Acc. Chem. Res.*, 2019, **52**, 1531–1542.
- 196 C. A. Cheng, T. Deng, F. C. Lin, Y. Cai and J. I. Zink, *Theranostics*, 2019, **9**, 3341–3364.
- 197 S. F. Lee, X. M. Zhu, Y. X. J. Wang, S. H. Xuan, Q. You, W. H. Chan, C. H. Wong, F. Wang, J. C. Yu, C. H. K. Cheng and K. C. F. Leung, *ACS Appl. Mater. Interfaces*, 2013, **5**, 1566–1574.
- 198 J. Wang, Y. Jiao and Y. Shao, *Materials (Basel)*, 2018, **11**, 2041.
- 199 X. Li, Z. Wang and H. Xia, *Front. Chem.*, 2019, **7**, 1–11.
- 200 L. C. Phillips, C. Puett, P. S. Sheeran, P. A. Dayton, G. Wilson Miller and T. O. Matsunaga, *J. Acoust. Soc. Am.*, 2013, **134**, 1473–1482.
- 201 Y. Chen, Y. Gao, H. Chen, D. Zeng, Y. Li, Y. Zheng, F. Li, X. Ji, X. Wang, F. Chen, Q. He, L. Zhang and J. Shi, *Adv. Funct. Mater.*, 2012, **22**, 1586–1597.
- 202 M. Ma, H. X. Xu, H. R. Chen, X. Q. Jia, K. Zhang, Q. Wang, S. G. Zheng, R. Wu, M. H. Yao, X. J. Cai, F. Q. Li and J. L. Shi, *Adv. Mater.*, 2014, **26**, 7378–7385.
- 203 X. Wang, L. Qiao, X. Yu, X. Wang, L. Jiang and Q. Wang, *ACS Biomater. Sci. Eng.*, 2019, **5**, 5888–5896.
- 204 M. U. Amin, S. Ali, I. Tariq, M. Y. Ali, S. R. Pinnapreddy, E. Preis, C. Wölk, R. D. Harvey, G. Hause, J. Brüßler and U. Bakowsky, *Pharmaceutics*, 2021, **13**, 1396.
- 205 S. Kapoor and A. J. Bhattacharyya, *J. Phys. Chem. C*, 2009, **113**, 7155–7163.
- 206 X. Qian, W. Wang, W. Kong and Y. Chen, *J. Nanomater.*, 2014, **2014**, 1–8.
- 207 Z. Jin, Y. Wen, Y. Hu, W. Chen, X. Zheng, W. Guo, T. Wang, Z. Qian, B. L. Su and Q. He, *Nanoscale*, 2017, **9**, 3637–3645.
- 208 C. A. Cheng, W. Chen, L. Zhang, H. H. Wu and J. I. Zink, *J. Am. Chem. Soc.*, 2019, **141**, 17670–17684.
- 209 S. Malekmohammadi, H. Hadadzadeh, S. Rezakhani and Z. Amirghofran, *ACS Biomater. Sci. Eng.*, 2019, **5**, 4405–4415.

Chapter 2: General Methods & Procedures

2.1. Synthesis of SNPs with Cetylpyridinium Chloride

All general reagents were purchased from commercial suppliers without any additional purification needed. N-cetyltrimethylammonium bromide ($C_{16}TAB \geq 99.0\%$), cetylpyridinium chloride monohydrate (CPC), concentrated hydrochloric acid (HCl, 37%), tetraethyl orthosilicate ($TEOS \geq 99.0\%$), sodium hydroxide (NaOH) and ethanol (EtOH) were all obtained from Sigma-Aldrich (Merck). Ammonium hydroxide (NH_4OH , 28.0-30.0% NH_3) was obtained from Fisher Scientific.

2.1.1. Synthesis of plain non-porous SNP (Plain SNP)

The Stöber method with modifications was used to synthesis non-porous SNPs.^{1,2} First a solution containing EtOH (26.66 mL), ammonia (1.88 mL, 0.93 M), water (1.57 mL, 2.9 M) and TEOS (2.4 mL) were added together. The reaction mixture was kept at 25 °C for 12 h under stirring (150 rpm). The **plain SNPs** were isolated by centrifugation (15 min, 7830 rpm) and washed with water three times. After three cycles of the centrifugation-washing procedures, the **plain SNPs** were dried under *vacuo* to yield a white solid powder.

2.1.2. Synthesis of encapsulated CPC inside SNP (CPC \subset SNP)

For CPC loaded SNPs, the same procedure was followed for **plain SNPs** with the addition of CPC solution (3mL of 155 mg mL⁻¹ at 3 h. The reaction mixture was kept at 25 °C for a total of 12 h under stirring (150 rpm). The **CPC \subset SNP** particles were isolated by centrifugation (15min, 7830 rpm) and washed with water three times to

ensure removal of excess reactant and drug. After three cycles of the centrifugation-washing procedures, **CPC \subset SNP** were dried under *vacuo* to yield a white solid powder.

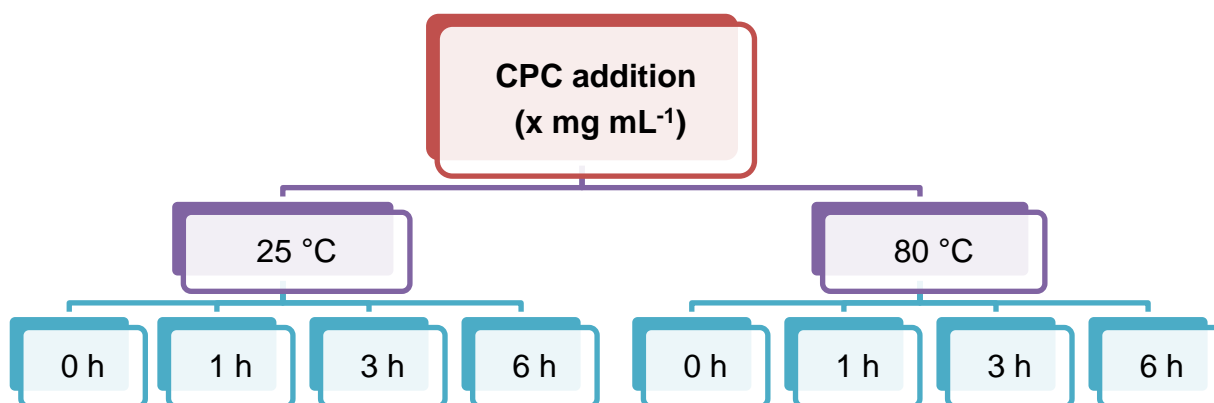


Figure 2. 1: Flow diagram to represent CPC concentration added to reaction at 25 or 80 °C and time of addition 0, 1, 3 or 6 h.

Preparations of **SNP1** to **SNP6** followed **CPC \subset SNP** method, changing the CPC concentration: 0.05, 0.2, 0.5, 2, 82 and 115 mg mL⁻¹. The drug was added after 3 h, dissolved in 3 mL H₂O.

Other preparations **SNP7** to **SNP13** followed **CPC \subset SNP** method, but the CPC concentration was kept at 155 mg mL⁻¹ and time of addition 0, 1, 3 and 6 h were changed and examined at 25 and 80 °C.

2.1.3. Preparation of MCM-41 type MSN's

Mesoporous silica nanoparticles were synthesised according to methods by Wu *et al.*³ and Varache *et al.*⁴ with slight alterations. C₁₆TAB (0.25 g, 0.68 mmol) and NaOH (12.5 mM, 1.5 mmol) were dissolved in ultrapure H₂O (120 mL), then TEOS (1.25 mL, 5.6 mmol) was added dropwise over 10 min. The solution was stirred at 750 rpm and

heated to 80 °C for 2 h. The white precipitate formed in the reaction was isolated by centrifugation (15min, 7830 rpm) and washed with water three times. For the removal of the surfactant template (CTAB), the isolated white solid was calcinated at 600°C for 8 h. Alternatively to remove CTAB, the particles are centrifuged and washed with MeOH. The nanoparticles are then heated in MeOH (50 mL) and concentrated hydrochloric acid (3 mL) under reflux for 24h. The nanoparticles are centrifuged and washed with MeOH. The nanoparticles were dried under *vacuo* to yield a white solid powder, **plain MSNs**.

2.1.4. Synthesis of adsorbed drug loaded particles (CPC@MSN)

The previously synthesised **plain MSNs** were added to a solution of CPC dissolved in H₂O (2 mg mL⁻¹). The mixture was stirred at room temperature for 24 h. After **CPC@MSN** was isolated by centrifugation (15 min, 7830 rpm) and dried under *vacuo* to yield a white solid powder.

2.1.5. Synthesis of templated drug loaded particles (CPC<MSN)

CPC (250mg) was dissolved in ultrapure H₂O (120 mL) with NaOH (12.5 mM, 0.15 mmol), then TEOS (1.25 mL, 5.6 mmol) was added dropwise over 10 min. The solution was stirred at 750 rpm and heated to 80 °C for 2 h. The **CPC<MSN** particles were washed and isolated by centrifugation (15 min at 7830 rpm) then dried under *vacuo* to yield a pale-yellow solid powder.

2.2. Synthesis of SNPs with Ciprofloxacin Hydrochloride

All general reagents were purchased from commercial suppliers without any additional purification needed. Ciprofloxacin hydrochloride (CPX, purity 95%, CAS 8639-32-0, Fluorochem Ltd.), tetraethyl orthosilicate (TEOS, ≥ 99.0%, CAS 78-10-4,

Sigma-Aldrich), sodium hydroxide (NaOH, $\geq 98\%$, pellets (anhydrous), CAS 1310-73-2, Fisher Scientific) and ethanol (EtOH), Ammonium hydroxide (NH₄OH, 28.0-30.0% NH₃, from Fisher Scientific).

2.2.1 Synthesis of drug encapsulated CPX \subset SNPs via method A

For CPX encapsulated silica nanoparticles, a solution containing EtOH (26.66 mL), ammonia (1.88 mL, 0.93 M), water (1.57 mL, 2.9 M) and TEOS (2.4 mL) were added together. The reaction mixture was kept at 25 °C under stirring (150 rpm). After 3 h, a prepared CPX solution (3 mL) was added to the reaction and continued to stir for a total reaction time of 12 h. The **CPX \subset SNP_A** particles were isolated by centrifugation (15 min, 7830 rpm) and washed with water (20 mL) three times. After three cycles of the centrifugation-washing procedures, the **CPX \subset SNP_A** particles were dried under *vacuo* to yield a white solid powder.

2.2.2. Synthesis of drug encapsulated CPX \subset SNPs via method B

Method B CPX encapsulated silica nanoparticles were prepared by adding a mixture of EtOH (25 mL), NH₄OH (1.5 mL) and CPX (3 mL) to a fast-stirring (>750 rpm) solution of TEOS (2 mL) and EtOH (5 mL). The reaction was mixed vigorously for 5 mins at 750 rpm and then left to stir for 3 h at 25 °C. The **CPX \subset SNP_B** particles were isolated by centrifugation (15 min, 7830 rpm) and washed three times with water (20 mL). After three cycles of the centrifugation-washing procedures, the **CPX \subset SNP_B** particles were dried under *vacuo* to yield a white solid powder.

2.2.3. Synthesis of adsorbed drug loaded CPX@SNPs via method A or B

First **Plain SNPs** were synthesised via method A or method B without drug addition and all other conditions and reagents were kept the same. The **Plain SNPs** were

isolated by centrifugation (15 min, 7830 rpm) and washed with water three times. After three cycles of the centrifugation-washing procedures, the **Plain SNPs** were dried under *vacuo* to yield a white solid powder.

Plain SNPs (100 mg) were added to a solution of CPX (200 mg) dissolved in H₂O (35 mL). The mixture was stirred (150 rpm) at room temperature for 24 h. After **CPX@SNP_A** and **CPX@SNP_B** were isolated by centrifugation (15min, 7830 rpm) and dried under *vacuo* to yield a white solid powder.

2.3. General procedures for nanoparticle characterisation

Dynamic light scattering (DLS) and Zeta (ζ)-potential measurements were performed on a Zetasizer Nano ZS (Malvern Instruments Ltd, UK) at 25°C in ultrapure water. For DLS, each was repeated 5 times combining 11 runs per measurement. ζ -potentials were recorded in triplicates with 100 runs per measurement at 140 V.

The size and morphology of all samples were prepared by mounting onto a carbon coated aluminium stub before sputter coating with gold (Quorum Emitech K550X sputter coater). A scanning electron microscope (SEM), XL30 ESEM-FEG (Philips) was used under high vacuum, at 20 kV electron beam and 20,000- 25000x magnification. All images for particle-size were analysed by ImageJ software.

Several spectroscopic techniques were performed for chemical and structural characterisation. Mass spectrometry (MS) analyses were performed on a Bruker ultrafleXtreme instrument. A pulsed Nd: YAG laser at a wavelength of 355 nm was operated at a 100 Hz frequency. The course was operated in positive mode with a delayed extraction time of 30 ns. Data was acquired and processed with the Flex Analysis 3.10 software. Samples (1 mg) prepared for matrix-assisted laser

desorption/ionization time-of-flight/time-of-flight (MALDI-TOF/TOF) MS were added to a matrix (100 μL) α -cyano-4-hydroxy-cinnamic acid (CHCA) 10 mg mL^{-1} in MeOH: ACN + 1% formic acid + 100 μL MeOH) and 20 μL was spotted on a steel MTP384 anchor chip plate. Fourier-transform infrared (FT-IR) spectroscopy was performed on samples using the Varian 640-IR spectrometer (Agilent Technologies). Solid-state emission spectra were acquired using Edinburgh Instruments FLS900 equipped with a 450 W Xenon lamp, double excitation, and emission monochromators. Wavelengths were controlled using Edinburgh Instruments v6.8 PC software. All spectra were corrected for Photomultiplier tube and instrument response. Solid-state UV-Vis absorption spectra were recorded using a Varian Cary 5000 dual beam spectrometer (Agilent Technologies) in reflectance mode with solid-state attachment.

High resolution transmission electron microscopy (HR-TEM) was carried out on a Jeol 1400 BioTEM and FEI TECNAI F20 (Philips). All images for particle-size were analysed by ImageJ software.

2.3.1. Sample preparation for imaging of CPC \subset SNP

For SEM imaging, **CPC \subset SNP** were immersed in either MeOH or H₂O and cavitation was applied using the ultrasonic scaler device. The total time of cavitation was 10 min, after the particles were centrifuged for 5 min at 7830 rpm and washed once before drying under *vacuo*. The dried particles were then sputter coated with gold before imaging.

Sample preparation for HR-TEM:

- 1) **CPC \subset SNP** no US
- 2) **CPC \subset SNP** with US applied in H₂O (2 mg mL^{-1}) for 2 min.

3) **CPC-SNP** stirred in MeOH (1.5 mg mL⁻¹ stirred at 400 rpm) for 72 h.

The solutions were then centrifuged for 5 min at 7830 rpm and washed once before drying under *vacuo*. After drying the powder was transferred to a carbon-film copper mesh grid for imaging.

2.4. Drug loading entrapment measurement

The drug concentration was measured from absorbance using UV-Vis spectroscopy with a Varian Cary 5000 dual beam spectrometer (Agilent Technologies). The drug loading entrapment was calculated by using the following equation:

% **Drug loading entrapment**

$$= \frac{\text{initial amount of drug (mg)} - \text{Amount of free drug in supernatant (mg)}}{\text{Total amount of drug (mg)}} \times 100$$

In general, all supernatants after reaction and subsequent washings were collected and 1 mL was used to record the remaining drug in solution. This was then subtracted from the initial amount of drug added to the reaction and divided by the total amount of drug added, multiplied by 100 to determine the drug loading entrapment percentage.

Thermogravimetric analysis coupled with FT-IR (TGA-FTIR) was performed using TGA 8000™ Thermogravimetric Analyzer (PerkinElmer, UK) at a heating rate of 10 °C min⁻¹ from 30 to 800°C under a nitrogen atmosphere. TGA was used to calculate the drug loading, determined by the weight loss curve and expressed as drug (ug) per **drug-SNP** (mg) (μg_{drug} mg_{drug-SNP}⁻¹).

2.5. *In Vitro* drug-release studies

2.5.1. General drug release measurements

For all samples, dry solid particles were immersed in the release media of ultrapure H₂O (10 mg mL⁻¹) at pH 7.4, 37°C. For a measurement of release, 1 mL of the particle suspension was removed and centrifuged for 5 min at 7830 rpm. The supernatant was collected and analysed by UV-Vis spectrometry by monitoring drug absorbance at the wavelength maximum (λ_{max}). The concentration of drug was calculated by its calibration curve that determined the absorption coefficient (ϵ , M⁻¹cm⁻¹). The amount of drug (μg) per drug loaded silica NP (mg) could be determined. Then the drug solution was then returned to the stock media.

2.5.2. Ultrasound-responsive triggered drug release in short intervals

To confirm the drug release from the silica NP structure with an external trigger the ultrasonic scaler (P5 Newton XS, Satelec, Acteon, France) with tip 10P was used for mechanical cavitation at low, medium, or maximum power (P=10, 15 or 20 respectively). It should be noted power settings are reference of the dial control on the ultrasonic scaler. The power is not representative of the power output and cannot be measured accurately due to tip shape. The set-up of the ultrasonic scaler handheld piece was positioned inside a 50 mL centrifugal tube, immersed in 10mL release media, and fixed at distance of 10 mm above the SNPs. Subsequently, cavitation was applied in 2 min intervals using the tip of the hand-held piece. After each cycle, the 1 mL of the particle suspension was removed and the measurement procedure from **section 2.4.** was followed.

2.5.3. Investigation of drug leakage in static conditions

For the stability studies, the static release was run in parallel to the US-triggered release experiments to monitor the leakage of CPC via passive diffusion. The same method for measurements to determine the drug concentration was followed as in **section 2.3.1.**

2.5.4. Continuous ultrasound with ultrasonic bath

To maximise drug release, cavitation was applied to the NPs over a continuous period using an ultrasonic bath (frequency 30 kHz). First, the foil test was implemented to find the hot spots for zones of cavitation. Subsequently, the 50 mL centrifugal tube containing the NP solution was positioned and fixed in the same place. Cavitation was applied continuously, and measurements were taken at predetermined intervals of 0, 10, 20, 30, 60, 90 and 180 min. This procedure was conducted in both MeOH and H₂O. The drug release was monitored by following measurement procedure in **section 2.4.**

2.6. Biological studies

2.6.1. General procedure & chemicals

Brain heart infusion (BHI, CM1135, Oxoid, Dorset, UK) broth and agar (BHI, CM1135, Oxoid, Dorset, UK) were used to culture *Streptococcus sanguinis* (ATCC 10556), *Streptococcus mutans* (3209), *Pseudomonas aeruginosa* (PA14), *P. aeruginosa* (PAO1-N) and *Enterococcus faecalis* (ATCC 29212) from frozen stocks stored at -80°C and obtained from Professor Paul Williams, University of Nottingham.

All bacterial overnight cultures were prepared by bacteria from frozen stock were streaked on BHI agar and incubated overnight (37 °C, 5 % CO₂ environment). Liquid

cultures were prepared with a single colony in 5 mL BHI broth before incubating for 20 h in the orbital shaker (37 °C, 100 rpm).

To prepare artificial saliva a modified method described by Prattern *et al.*⁵ was used. To ultrapure water (1 L) the following were added sequentially, accurately to 0.001g: Sodium chloride (NaCl, 0.35 g, VWR 102415K), potassium chloride (KCl, 0.2 g, Sigma 60129), calcium chloride (CaCl₂, 0.2 g, WVR 007103020), yeast extract (2 g, Oxoid LP0021), lab lemco powder (1 g, Oxoid L29), hog gastric mucin (type III, partially purified) (2.5 g, Sigma M177) and protease peptone (5 g, Oxoid L85). The mixture was left to stir for 1 h, then autoclaved. After sterilisation 40 % sterile urea (1.25 mL, 0.5 g urea, Oxoid SR20, in 1.25 mL ultrapure H₂O) was added using a 0.22 µm filter. Once the urea was added the media was wrapped in aluminium foil to exclude light and prevent protein degradation and stored at 4 °C.⁶

For biofilm BHI medium: 1 % sucrose was added to sterilised BHI broth. First the sucrose (3.5 g, Sigma S0389) was mixed with sterilised filtered ultrapure H₂O (3.5 mL) then added to BHI broth (350 mL) with a sterile syringe.

Phosphate buffered saline (PBS, Dulbecco A, Sigma P4417) solution was prepared by dissolving one tablet in ultrapure H₂O (200 mL) and autoclaved for sterilisation.

2.6.2. Minimum inhibitory concentration (MIC) assay

The MIC of antimicrobial agent or particles was determined using one bacterial strain at a time. Overnight cultures were prepared in BHI broth (5 mL) from bacteria previously streaked on BHI agar plates. The overnight cultures were incubated for 20 h at 37 °C, 100 rpm. A stock solution of bacteria was made by adjusting the OD₆₀₀ to 0.1 by diluting the bacterial inoculum with fresh BHI broth. A 2-fold dilution series of

antibiotic or particles in BHI broth was made (note in the first well of the plate the drug concentration will be halved, for example the concentration of CPC desired was $80 \mu\text{g mL}^{-1}$, so made an initial concentration of $160 \mu\text{g mL}^{-1}$). In a 96-well plate, $200 \mu\text{L}$ of the first concentration in the dilution series of drug was added to $200 \mu\text{L}$ of diluted culture into the well. Then $100 \mu\text{L}$ of the drug and bacteria medium was added to $100 \mu\text{L}$ in the next well. This step was repeated 8 times, so each well had a total volume of $200 \mu\text{L}$. The 96-well plate was incubated for 24h under anaerobic conditions. For controls: 1:1 ratio of bacteria to BHI broth to make sure bacteria growth is maintained, BHI broth was used to show no contamination and empty well to obtain background reading of the well plate. The growth and no growth were determined visually and by measuring the OD600 using the microplate reader (ELx800, BIO-TEK instruments Inc.) in triple triplicates (N=9) with the Gen5 data analysis software for all measurements.

Table 2. 1: Concentration range used for MIC assay in Chapter 4.

	<i>S. sanguinis</i>	<i>S. mutans</i>	<i>E. faecalis</i>
CPC	80-0.16 $\mu\text{g mL}^{-1}$	80-0.16 $\mu\text{g mL}^{-1}$	80-0.16 $\mu\text{g mL}^{-1}$
Plain SNP	16-0.3 mg mL^{-1}	-	-
Plain MSN	16-0.3 mg mL^{-1}	-	-

Table 2. 2: Concentration range used for MIC assay in Chapter 5.

	CPX
<i>S. sanguinis</i>	80-0.08 $\mu\text{g mL}^{-1}$
<i>S. mutans</i>	80-0.08 $\mu\text{g mL}^{-1}$
<i>P. aeruginosa</i> (PA14)	80-0.08 $\mu\text{g mL}^{-1}$
<i>P. aeruginosa</i> (PAO1N)	80-0.08 $\mu\text{g mL}^{-1}$
<i>E. faecalis</i>	80-0.08 $\mu\text{g mL}^{-1}$

2.6.3. Antimicrobial activity against planktonic *S. sanguinis*

Overnight bacterial stocks were prepared in 5 mL BHI broth and incubated at 37 °C, under orbital shaking at 100 rpm. After overnight growth, 3 mL of the turbid culture was diluted with 7 mL BHI broth and pre-weighed samples were added (see **Table 2.3**). Samples had no US applied or US was applied for 2 min, then all samples were incubated at 37 °C, 100 rpm. After 3 h, a serial dilution was performed for all samples in a 96-well plate. Each sample was prepared in triplicate. 180 µL aliquots of BHI broth were added to each well with 20 µL of samples for the first dilution (1×10^{-1}). Subsequently, 20 µL was taken from the first dilution and added to the next well with BHI broth. This was repeated 7 more times. For each dilution, 20 µL aliquots were spotted onto BHI agar plates three times, which were divided into four segments. This was repeated for each sample. Once dry, all plates were incubated in a CO₂ environment at 37 °C overnight. Following this, the number of colonies were counted and the colony forming unit was calculated for each sample and its dilution. The serial dilution was repeated for samples taken at 8, 24 and 48 h.

Table 2. 3: Concentration of sample used to test antimicrobial activity on planktonic bacteria with and without US (P10, 10s).

	Concentration / mg mL ⁻¹
Bacteria	-
CPC	0.5
Plain MSN	10

2.6.4. Agar Diffusion Assay

Overnight bacterial stocks were prepared as mentioned in **section 2.4.1**. The inhibition of growth on bacteria from samples were tested using an agar diffusion

assay. BHI agar plates were inoculated by swabbing with an overnight culture of bacteria to create an evenly distributed lawn of bacteria. In each agar plate, five wells of 6 mm in diameter were cut with the larger end of a sterile pipette tip, approximately equal distances apart. Each well was loaded with 50 μL of sample from stock solutions. Afterwards the plates were incubated at 37 °C in 5% CO_2 for 20 h in static conditions. At the end of incubation time the bacterial growth was confluent on the agar surface, except at areas of growth inhibition where there was a clear zone surrounding the well. The zones of inhibition were measured using a millimetre ruler. All experiments and measurements were performed in triplicates and the mean and standard deviations were obtained. All samples were dispersed in ultrapure water and was used as negative control.

The inhibition of growth of *S. sanguinis* was tested using an agar diffusion assay using the following samples:

Table 2. 4: Concentration added to well of agar plate.

Concentration in 50 μL	
CPC	500 $\mu\text{g mL}^{-1}$
Plain SNP	2 mg mL^{-1}
CPC\subsetSNP	2/5/10 mg mL^{-1}
Plain MSN	2 mg mL^{-1}
CPC\subsetMSN	2 mg mL^{-1}
CPC@MSN	2 mg mL^{-1}

The inhibition of growth of *S. sanguinis*, *S. mutans*, *P. aeruginosa* (PA14), *P. aeruginosa* (PAO1N) and *E. faecalis*. This was tested using an agar diffusion assay using the following samples:

Table 2. 5: Concentration added to well of agar plate.

Concentration in 50 μL	
CPX	2 mg mL ⁻¹
Plain SNP	10 mg mL ⁻¹
CPX\subsetSNP_A2	10 mg mL ⁻¹
CPX@SNP A	10 mg mL ⁻¹

2.6.5. Development of single-species biofilm model

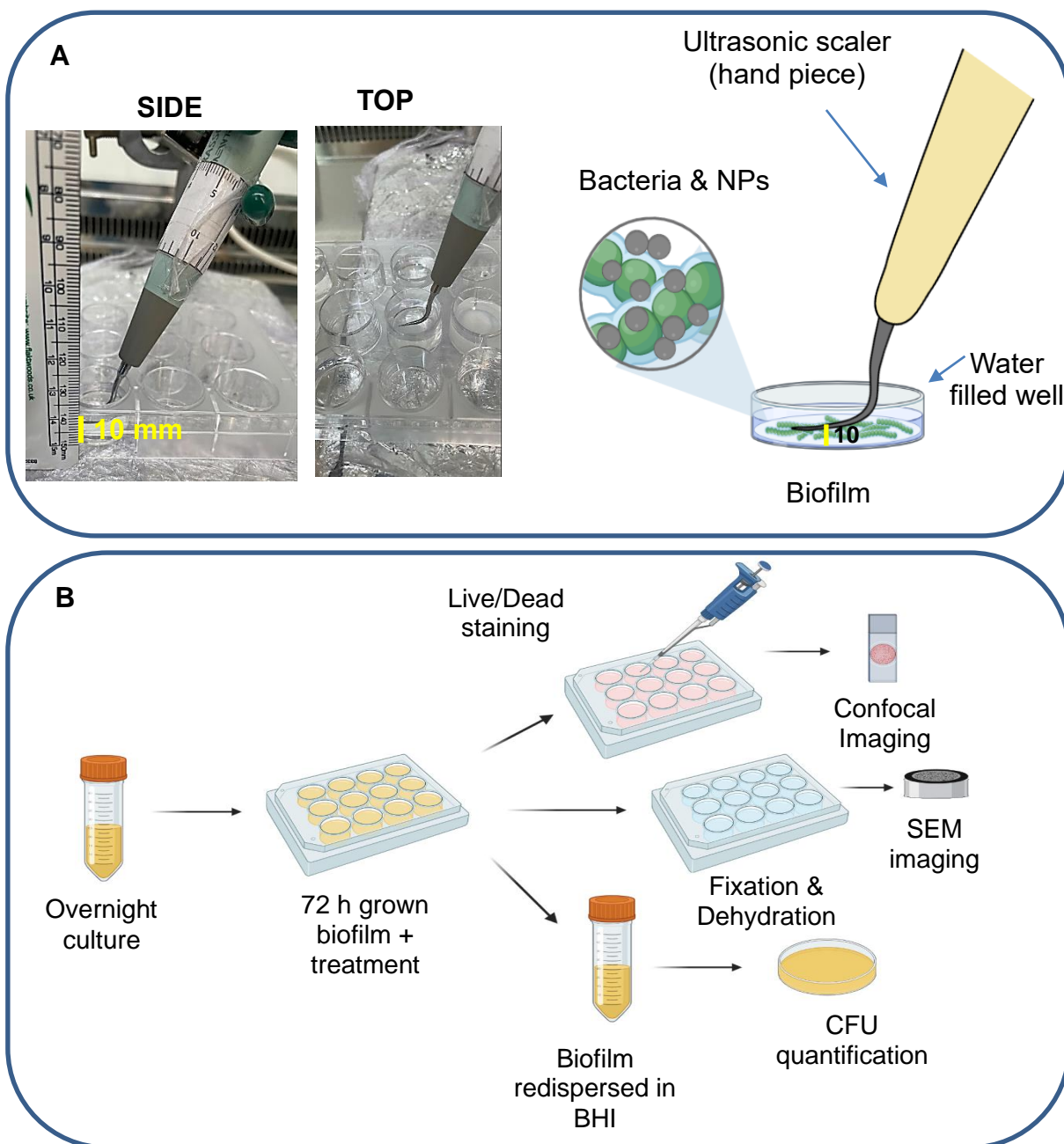


Figure 2. 2: Photographs and schematic representation of experimental set-up of the ultrasonic scaler for biofilm viability assay. A 12-well plate with 72 h grown biofilm covered Thermanox coverslip (13 mm diameter) was placed inside a well and secured with double sided tape to ensure the slip remains in position during cavitation. A solution (3 mL) containing the treatment was pipetted into the well plate. The ultrasonic scaler (Satelec P5 Newtron XS scaler, Acteon Group, USA) with tip 10P was fixed parallel and 10 mm away from the biofilm using a clamp stand to aid the positioning. The scaler was operated at a power setting of 10 (medium power) for 10s.

The chosen bacteria used in the study to form a single species biofilm model for treatment with nanoparticles and ultrasonic scaler. An overnight bacterial culture in BHI broth was prepared from bacteria, as mentioned in **section 2.6.1.** Firstly, Thermo Scientific™ Nunc™ Thermanox™ Coverslips (13 mm diameter, cell culture-treated one side) were added to a 24-well plate and primed with artificial saliva for 15 min (described in general methods section).⁵ The artificial saliva was removed and the overnight bacterial suspension was diluted to $\times 10^3$ in fresh BHI medium with 1% sucrose and 1 mL was added to each coverslip. The 24-well plate was incubated at 37°C, 100 rpm for 24 h. Afterwards the medium was removed and replaced with 2 mL fresh medium. This was repeated to obtain biofilms grown for 72 h.

The Gram-positive *Streptococcus sanguinis* (ATCC 10556) was used in the current study to form a single-species biofilm model for treatment with nanoparticles and ultrasonic scaler.

Table 2. 6: Sample concentrations of samples added to the biofilm, testing incubation time with sample after release with US (P10, 10s).

	Incubation time / min	Concentration / mg mL ⁻¹
Cavitation only	30	-
CPC	30	0.5
CPC⊂SNP	5	10
CPC⊂SNP	15	10
CPC⊂SNP	30	10

Table 2. 7: Antimicrobial activity against *S. sanguinis* biofilms. Sample concentrations used for live/dead staining and CFU-methods. CPC, **Plain SNP** and **CPC \subset SNP** without and with US (P10, 10s) incubated at 37°C

	Incubation time / min	Concentration
Bacteria	30	-
CPC	30	13 $\mu\text{g mL}^{-1}$
Plain SNP	30	10 mg mL^{-1}
CPC\subsetSNP	30	10 mg mL^{-1}

Two Gram-positive strains *S. sanguinis* and *S. mutans* was used in the current study to form a single-species biofilm model for treatment with nanoparticles and ultrasonic scaler.

Table 2. 8: Antimicrobial activity against *S. sanguinis* and *S. mutans* biofilms. Sample concentrations used for live/dead staining, without and with US (P10, 10s) incubated at 37°C

	Incubation time / min	Concentration
Bacteria	30	-
CPX	30	0.68 $\mu\text{g mL}^{-1}$
CPX\subsetSNP_A2	30	10 mg mL^{-1}
CPX\subsetSNP_B5	30	10 mg mL^{-1}

2.6.6. Determination of CPC release from CPC \subset SNP for biofilm studies

CPC \subset SNP particles were immersed in the release media of ultrapure H₂O (10 mg mL^{-1}). Then US was applied for 10s at power setting P10 on the ultrasonic scaler. Then incubated in a water bath at 37°C for 30 min. For a measurement of release, 1 mL of the particle suspension was removed and centrifuged for 5 min at 7830 rpm. The

supernatant was collected and analysed by UV-Vis spectrometry by CPC absorbance at the wavelength maximum of 259 nm. The concentration of CPC released was calculated by its absorbance and absorption coefficient ($\epsilon = 4191 \text{ M}^{-1} \text{ cm}^{-1}$). The amount of drug (μg) per drug loaded SNP (mg) could be determined. This was repeated three times and the amount of CPC released was averaged. This was the concentration used for biofilm studies.

2.6.7. Determination of CPX release from CPX-SNP for biofilm studies

CPX-SNP particles were immersed in the release media of ultrapure H_2O (10 mg mL^{-1}). Then US was applied for 10s at power setting P10 on the ultrasonic scaler. Then incubated in a water bath at 37°C for 30 min. For a measurement of release, 1 mL of the particle suspension was removed and centrifuged for 5 min at 7830 rpm. The supernatant was collected and analysed by UV-Vis spectrometry by CPX absorbance at the wavelength maximum of 275 nm. The concentration of CPX released was calculated by its absorbance and absorption coefficient ($\epsilon = 43060 \text{ M}^{-1} \text{ cm}^{-1}$). The amount of drug (μg) per drug loaded SNP (mg) could be determined. This was repeated three times and the amount of CPX released was averaged. This was the concentration used for biofilm studies.

2.6.8. Biofilm viability studies & ultrasonic scaler experimental set-up

In a 12-well plate, the Thermanox coverslips were either treated with the sample solution and no cavitation or with sample solution and cavitation and then incubated at 37°C , 100 rpm for 30 min. The biofilm treatment process achieved using a Satelec P5 Newtron XS scaler (Acteon Group, USA) with a 10P tip in all experiments. The handpiece of the scaler was fixed with manual clamp stand and adjusted to 10 mm

from the biofilm surface and the orientation of the tip was kept in a horizontal position relative to the biofilms. The biofilm coverslips were stuck to the surface of 12-well plate using double-sided tape and wells were filled with H₂O (3 mL) to completely immerse the tip surface of the scaler (note the cooling water flow unit part of the scaler was not used in these experiments). The ultrasonic scaler was operated at low (P10) or high (P20) power for 10 seconds.

2.6.9. Live/dead staining assay

Filmtracer™ LIVE/DEAD® Biofilm Viability Kit (Invitrogen, California, USA) was used to stain the biofilms. A stock solution of the stain prepared with SYTO® 9 stain (3 µL) and propidium iodide (3 µL) in filter-sterilised ultrapure H₂O (1 mL), this was enough to stain 5 biofilms. After the biofilms had been treated, they were washed with PBS solution and the staining solution (~200 µL) was added gently to the biofilm. The biofilms were incubated for 20-30 min at room temperature and protected from light exposure with foil. The stain was removed, and biofilms were washed by rinsing gently once with PBS to remove all excess stain. To fix the biofilms, the coverslips were placed onto microscope slides (biofilm facing up) and a drop of Invitrogen™ ProLong™ Gold Antifade Mountant (ThermoFisher Scientific, Massachusetts, USA) was added before putting a 22 x 26 mm cover glass on top. The slides were left to solidify and dry for 24 h and were stored in the dark to preserve fluorescence.⁷

2.6.10. Confocal laser scanning microscopy (CLSM) imaging

The biofilms viability was imaged with confocal laser scanning microscope (LSM 700, Carl Zeiss GmbH, Germany). The images were obtained with the Zeiss Zen lite 2011 software. A x40 oil immersion objective (Zeiss Objective EC Plan-Neofluar

40x/1.30 Oil DIC M27, FWD = 0.21 mm) in combination with an immersion oil (Immersol™ 518F) was used. The emission/excitation wavelengths for the stains were 488 nm/<550 nm for SYTO® 9 and 555 nm/>550 nm for propidium iodide. Both the green and red channels were imaged together with an image size of 1024 x 1024 pixels. Five random locations were scanned on each biofilm sample and 2-3 Z-stacks of 10-30 µm optical thickness separated by 1.30 µm increments from the surface were obtained for each condition. Z-stacks were examined to calculate the biofilm thickness and for 3D visualisation analysis.

2.6.11. Image analysis of single-species biofilms

The percentage of live and dead bacteria in each image was determined from the CLSM images. An automated computation method developed and described by S. E. Mountcastle *et al.*⁸ was used to evaluate the cell viability. The macro created was a method carried out using the ImageJ software (version 2.1.0). This was achieved by splitting the CLSM images into two different channels (green and red) and converted into an 8-bit image. A series of erosion, reconstruction and dilation steps had been incorporated into the script to perform on each channel (element size 3). The total bacteria were calculated by number of pixels in the image (green and red), differentiating between background noise depending on intensity values. A Gamma command (set at 1.5) was used to correct for uneven fluorescence intensities and allowed for detection of faint bacteria. Then segmentation and thresholding were performed by using the Otsu's threshold. The output was presented as white pixels, which the number of pixels corresponding to the dead (red) bacteria was calculated. This was used to determine the area of dead bacteria, followed by the total number of white pixels, which were used to calculate the total area of all bacteria. Finally, the

percentage of viable cells (green) were calculated from the total area of bacteria and red bacteria. The macro is used based on the assumption that the image contains a single-species biofilm and output is a percentage of live cell area.

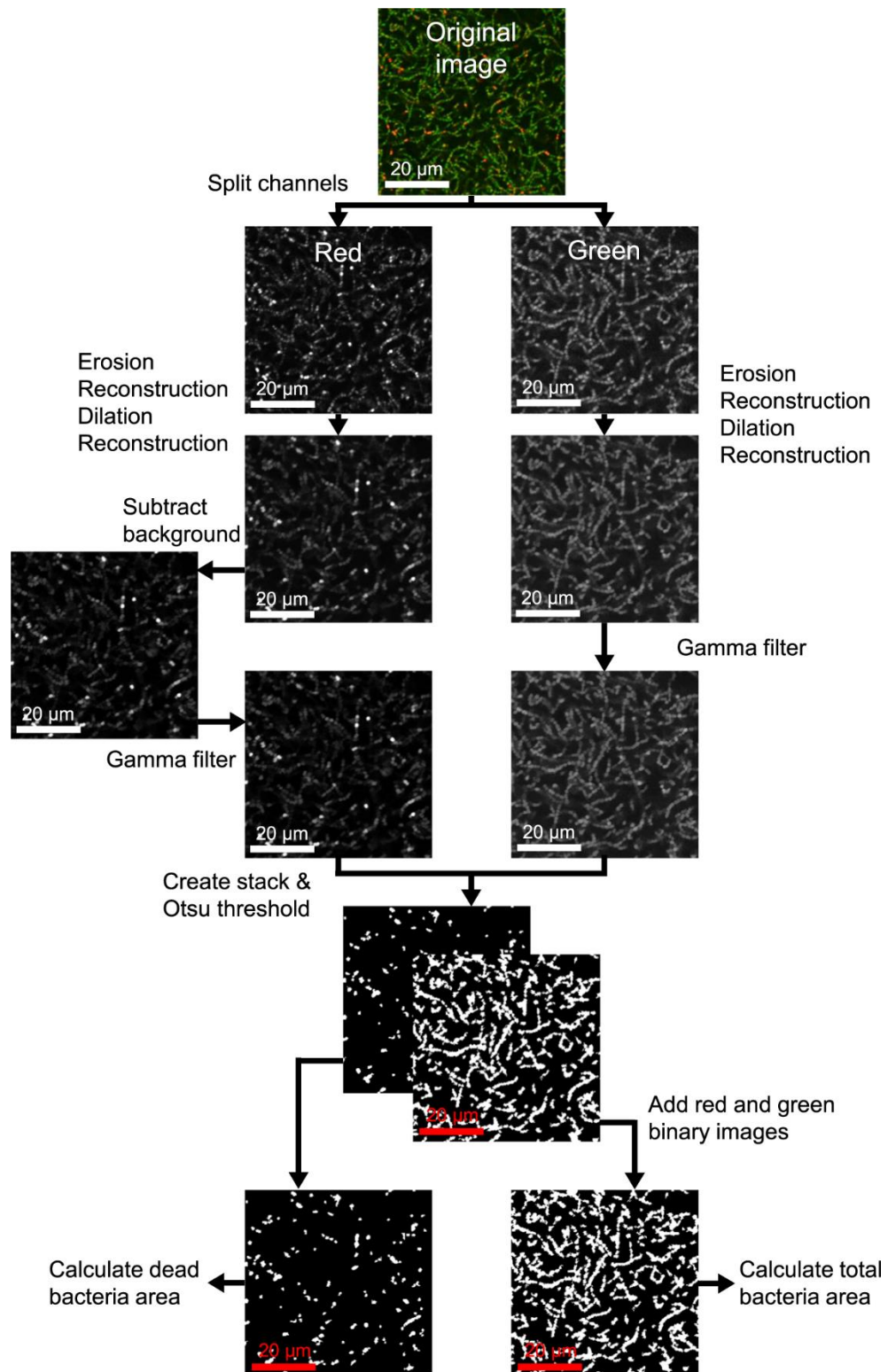


Figure 2. 3: Example of image analysis steps used in ImageJ to calculate bacterial viability from a confocal image of biofilm with LIVE/DEAD stain. Images show *S. sanguinis* biofilm cultured for 48 h (20 µm scale bar). Figure taken from Mountcastle *et al.*⁴

2.6.12. Colony counting method – colony forming units (CFUs)

An alternative quantification method to determine bacterial growth was conducted by counting the number of colony forming units in a bacterial suspension, a well-known procedure known as the Miles and Misra method.⁹ After treatment the biofilms were removed from each well and coverslip and redispersed by using the vortex for 2 min in fresh BHI broth (3 mL). A serial dilution was performed using the Miles and Misra method to count the number of CFUs. BHI broth (180 µL) was aliquoted into each well with 20 µL of samples for the first dilution (1×10^{-1}). Subsequently, 20 µL was taken from the first dilution and added to the next well with BHI broth, repeating the process to 1×10^{-8} dilution. For each dilution, 20 µL aliquots were spotted onto BHI agar plates three times. This was repeated for each sample and all plates were incubated at 37 °C in a 5 % CO₂ environment overnight. Following this, the number of CFU/mL was determined for each sample prepared in triplicate.

2.6.13. Scanning electron microscopy (SEM) imaging of biofilms

For further visualisation of bacterial biofilms, samples were prepared for SEM imaging by a fixation and dehydration procedure described by Dysktra *et al.*¹⁰ The biofilms were rinsed with three times with PBS to remove the culture medium.

1. For fixation: the samples were immersed in 2.5% EM grade glutaraldehyde in 0.1 M sodium cacodylate buffer, pH 7.3 for 10 min. Note the fixative must be prepared fresh but can be kept up to 1 week in the fridge. For a 10 mL stock solution of the fixative, ultrapure H₂O (4 mL), 0.2 M sodium cacodylate buffer pH 7.3 (5 mL, prepare in advance, pH with sodium hydroxide, the pH is

important) and 25% EM grade glutaraldehyde (1 mL, CAS 111-30-8, Sigma-Aldrich) were mixed.

2. Dehydration of each specimen was performed by removing water slowly in ethanol solutions of increasing concentration, for at least 10 min in each %: 20, 30, 40, 50, 60, 70, 90, 95 (twice) and 100 % (twice). The ethanol (100 %) was completely removed and hexamethyldisilane (HMDS, CAS 999-97-3, Sigma-Aldrich) was added quickly to cover the surface before the sample could dry out and left to evaporate overnight in a fume cupboard.

After the fixation and dehydration process the biofilms were prepared for imaging with the SEM. The biofilm coated coverslips were adhered onto aluminium stubs using 12 mm carbon adhesive tabs (Agar Scientific) and secured with single-sided conductive copper tape. All samples were sputter coated with gold (Quorum Emitech K550X, Kent, UK) before insertion into the SEM. The morphology and changes to the bacteria before and post treatment were examined using a Zeiss Evo MA-10 SEM (Carl Zeiss Jena GmbH, Germany) and SmartSEM software. Imaging was performed at x10-25 k magnifications with a working distance of 8-10.5 mm and accelerating electron beam voltage of 20 kV.

2.7. Bacteria viability statistical analysis

2.7.1. Biofilms treated with CPC in Chapter 4

All statistical analyses were performed in GraphPad Prism (v. 5.03). In biofilm viability studies the percentages of live and dead *S. sanguinis*, were represented by the mean with standard deviation for each group. Normality tests were performed to determine the distribution of data in each group using Kolmogorov-Smirnov, D'Agostino &

Pearson and Shapiro-Wilk tests for comparison. The graph showing the mechanical disruption of US in **section 4.3.3.**, used the Mann Whitney U, unpaired t-test (two-tailed, non-parametric) to compare cavitation times to bacterial control. For the time-kill assay with CPC \leq SNP (and synergetic effect of **CPC \leq SNP**, to determine the significance, one-way ANOVA non-parametric was employed with the Kruskal-Wallis test. Followed by a post-test conducted with the Dunn's test multiple comparison test. A value of $P \leq 0.05$ was considered significant.

2.7.2. Biofilms treated with CPX in Chapter 5

Statistical analysis was performed on percentage viability of *in vitro* *S. sanguinis* and *S. mutans* biofilms. The bacterial viability was determined from the automatic image analysis software used in ImageJ and then statistics were calculated in GraphPad Prism (v. 5.03). Data presented in bar graphs were shown as mean and standard deviation (SD) for sample sizes between 7-14. The significance level was set at $p < 0.05$. Kolmogorov-Smirnov was used to access data normality and homogeneity of variance. Firstly, two groups were compared by the non-parametric Mann-Whitney U test. The test was used to show the effect of biofilms treated with CPX, **CPX \leq SNP_A2**, **CPX \leq SNP_B5** or nothing at all compared to with the addition of cavitation. One-way ANOVA, non-parametric Kruskal-Wallis test was performed followed by the post hoc test, Dunn's Multiple Comparison Test to compare all factors categorically. A value of $P \leq 0.05$ was considered significant.

2.8. References

- 1 W. Stober, A. Fink and E. Bohn, *J. Colloid Interface Sci.*, 1968, **26**, 62–69.
- 2 D. Zhang, Z. Wu, J. Xu, J. Liang, J. Li and W. Yang, *Langmuir*, 2010, **26**, 6657–6662.
- 3 S. Wu, Q. Deng, X. Huang and X. Du, *ACS Appl. Mater. Interfaces*, 2014, **6**, 15217–15223.
- 4 M. Varache, I. Bezverkhyy, L. Saviot, F. Bouyer, F. Baras and F. Bouyer, *J. Non. Cryst. Solids*, 2015, **408**, 87–97.
- 5 J. Pratten, A. W. Smith and M. Wilson, *J. Antimicrob. Chemother.*, 1998, **42**, 453–459.
- 6 M. Lodovici, L. Raimondi, F. Guglielmi, S. Gemignani and P. Dolara, *Toxicology*, 2003, **184**, 141–147.
- 7 L. F. Dawson, E. Valiente, A. Faulds-Pain, E. H. Donahue and B. W. Wren, *PLoS One*, 2012, **7**, e50527.
- 8 S. E. Mountcastle, N. Vyas, V. M. Villapun, S. C. Cox, S. Jabbari, R. L. Sammons, R. M. Shelton, A. D. Walmsley and S. A. Kuehne, *npj Biofilms Microbiomes*, 2021, **7**, 1–12.
- 9 B. Y. A. A. Miles and S. S. Misra, 1931, 732–749.
- 10 M. J. Dykstra, P. C. Mann, M. R. Elwell and S. V. Ching, *Toxicol. Pathol.*, 2002, **30**, 735–743.

Chapter 3: The Synthesis, Optimisation & Characterisation of Cetylpyridinium Chloride Loaded Silica Nanoparticles

3.1 Introduction

A critical challenge for dental infections and diseases is the restricted delivery of antimicrobial agents to achieve an effective therapeutic efficacy at the site of action.¹ The research into SNPs, as drug delivery systems have provided a platform to enhance the delivery of therapeutic agents, by fine tuning their properties and functions.² Most importantly, SNPs have been recognised for its ability to achieve a high drug loading and ease of modification capabilities to provide value properties. Of the classes of SNPs, MSNs have demonstrated their porous structures can incorporate antimicrobial agents.³ Although porosity has shown to induce premature drug leakage from the MSN framework, which many researchers have investigated functionalisation of the silica surface with coatings or internal pore modifications to block and prevent uncontrolled release.^{3,4} As a result, the drug release can be controlled by internal-stimuli, triggered by bacterial contact, change in pH or redox conditions. Also with external-stimuli; by applying light, temperature changes, magnetic fields and ultrasound.⁵⁻⁷

The combination of a stimuli-responsive drug loaded MSNs have shown many advantages for release and delivery of antimicrobial agents.⁸ Notably, nanosystems have showed to enhance the bactericidal activity compared to free antimicrobial agent alone. Synergistic effects were demonstrated by both drug and nanoparticle

together.^{9,10} Furthermore, SNPs provide protection for the drug to be delivered into biofilms, some triggered release mechanisms achieving deeper drug penetration and activity.¹¹ However, US-stimulated antimicrobial release from non-porous SNPs has not been investigated before, especially for dental applications. So far, anticancer agents have been studied for a controlled release, from SNPs.^{12–14} The focus has been attaching polymers to the silica surface to act as gatekeepers that can be removed with an US trigger and protect the entrapped drug.^{15–18} Even more, nanomachinery has provided capping ligands on MSN porous channels to prevent the drug escaping. The supramolecular molecules contain liable bonds that are cleavable to US.^{17,19,20} Recent developments have advanced to cater for multifunctional purposes and increased use of hollow MSNs to include imaging agents, US microbubble enhancers, modifications for specific targeting moieties and dual drug release.^{21–24} Although, attaching US liable ligands may resolve the undesired release to an extent, the increasing number of synthesis steps to control drug release reduces the ease of synthesis. This results in longer synthesis times, additional characterisation, and increased costs.²⁵

To eliminate additional synthesis stages, one-pot syntheses have been attempted to encapsulate metal complexes or template antimicrobial agents within the mesoporous structure to increase the drug efficiency and retention. Examples in the literature have been based on templating agents typically used in the synthesis of organised materials to form MSNs.^{26–32} Commonly ionic surfactants, such as CTAB are used as they have the fundamental physical properties of self-assembling into micelles above its critical micelle concentration (CMC). This has assisted in the formation of a uniform porous silica network. However, CTAB is well known to be

cytotoxic to healthy cells and undesirable for biological work if not removed after NP synthesis.^{33–35} Instead, antibacterial agents have been studied for encapsulation. For example, Stewart *et al.*³⁶ incorporated octenidine dihydrochloride, a surfactant-like drug, into a MSN type structure, as shown in **Figure 3. 1A**. The NPs produced large sizes of 500 nm and showed slow drug diffusion from MSNs. In comparison, Dubovoy *et al.*³⁷ templated benzalkonium chloride, a bactericidal drug, into the MSN structure, demonstrated in **Figure 3. 1B**. However, formed even larger particles of 650-850 nm and the release kinetics were enhanced slightly in lower pH conditions. Similarly, both one-pot examples explored diffusion of the drug from the silica as the release trigger and the antimicrobial activity was only studied on bacteria in planktonic conditions.

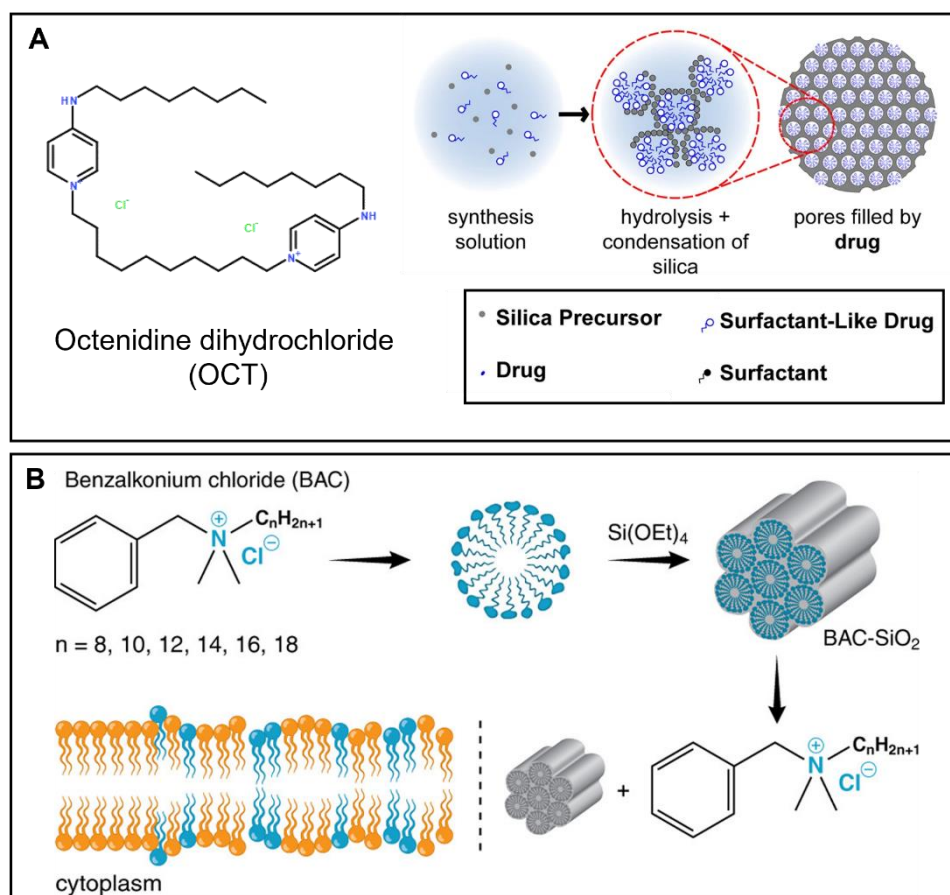


Figure 3. 1: One-pot synthesis examples of templated drug within a mesoporous silica nanoparticle structure of **A)** Octenidine dihydrochloride and **B)** Benzalkonium chloride. Adapted from Stewart *et al.* and Dubovoy *et al.*^{36,37}

Non-porous SNPs have found use in biomedical applications and this offers new and exciting platform for drug delivery.³⁸ Commonly, non-porous SNPs have been utilised for molecular imaging and less so for drug delivery. One-pot syntheses with positively charged dye complexes has been previously reported by Lewis *et al.*, Rossi *et al.*, and Zhang *et al.*^{39–41} to produce luminescent nanoparticles for imaging purposes. Zhang and co-workers⁴¹ used this process by reporting encapsulation of a ruthenium dye within the silica network with no additional modification. Notably, the effect of adding the ruthenium complex at different time points throughout the reaction, changed the emission intensity of ruthenium. In **Figure 3. 2**, showed the proposed silica growth stages and the difference in drug encapsulation. The tetraethyl orthosilicate (TEOS) consumption was monitored during the reaction and the luminescent properties of the NPs post-synthesis were examined. Zhang *et al.*⁴¹ found addition of the dye at 3 h exhibit greater emission intensity from dye loaded particles, due to a balance in the silica nucleation and aggregation.

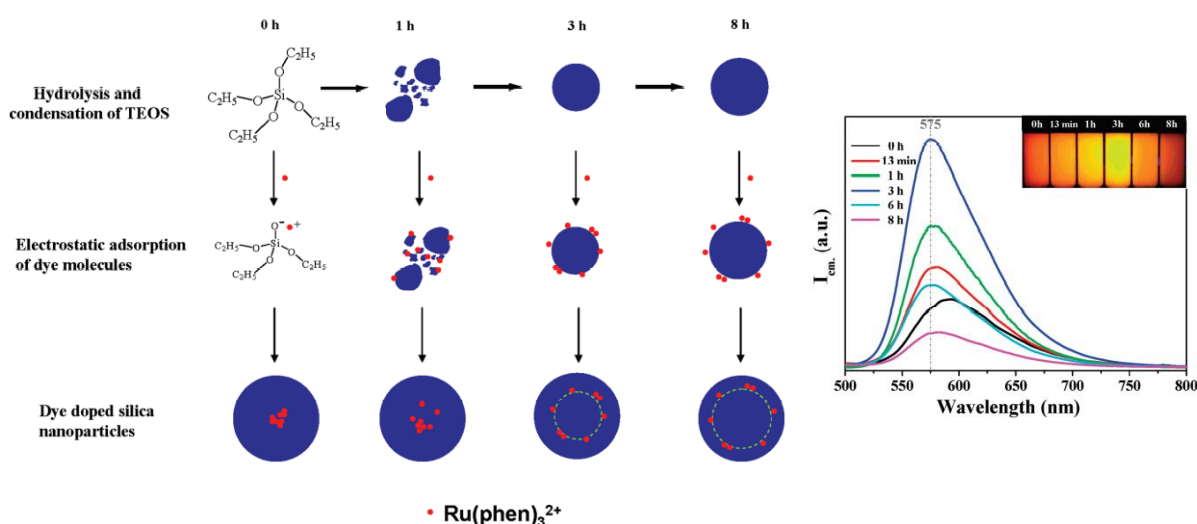


Figure 3. 2: Schematic illustration to show the different stages of silica growth with the addition of Ru(Phen)_3^{2+} dye molecule and emission spectra, Adapted from Zhang *et al.*⁴¹

In addition to drug loading, the delivery of submicron silica particles can be effectively deposited on the surface of the tooth. This was demonstrated by Claire *et al.*,⁴² in **Figure 3. 3A**. The luminescence produced from encapsulated ruthenium complex within the silica particles, was shown using confocal imaging. This promising work led to the successful rapid delivery of sub-micron particles to occlude and penetrate inside the dentinal tubules from the acoustic cavitation behaviour produced from an ultrasonic scaler, reported by Vyas *et al.*⁴³ **Figure 3. 3B**, showed potential effects of cavitation with sub-micron silica particles was advantageous to infiltrate the tubules ~185 μM in depth, over double the distance without cavitation. However, there has been little research into the use and effectiveness of the ultrasonic scaler to release drugs from SNPs. Therefore, combining drug loaded non-porous SNP with US would be a novel and desirable delivery system.

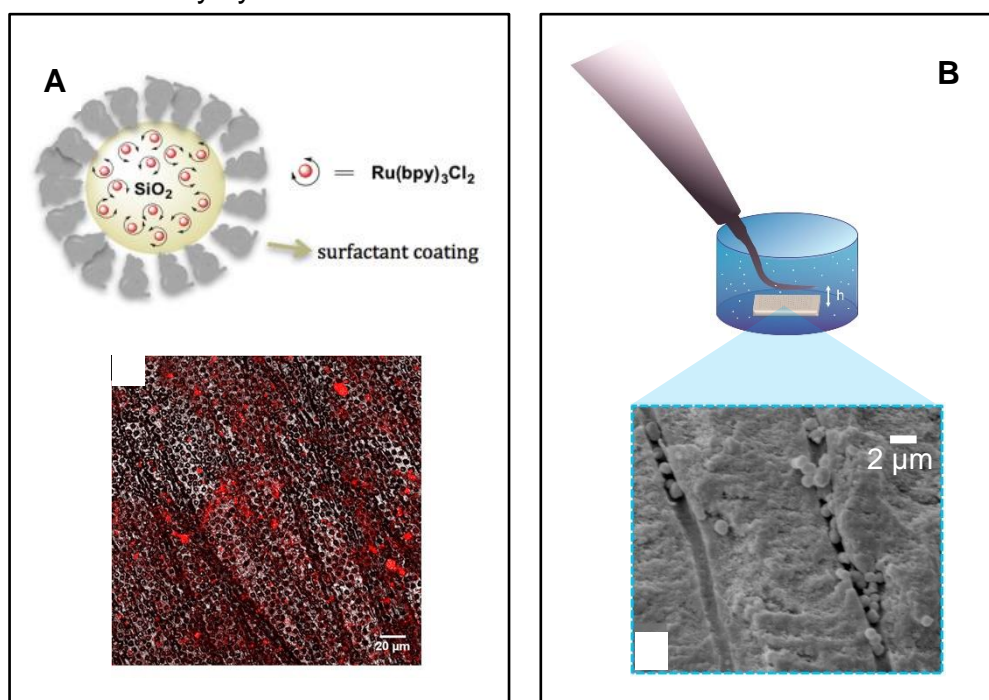


Figure 3. 3: The delivery of sub-micron silica particles **A)** schematic of silica particles with encapsulated luminescent ruthenium and image of deposition on tooth surface. **B)** shows particle penetration into the dentinal tubules in water with cavitation applied of depths of 185 μM with cavitation from ultrasonic scaler. Adapted from Claire *et al.* and Vyas *et al.*^{42,43}

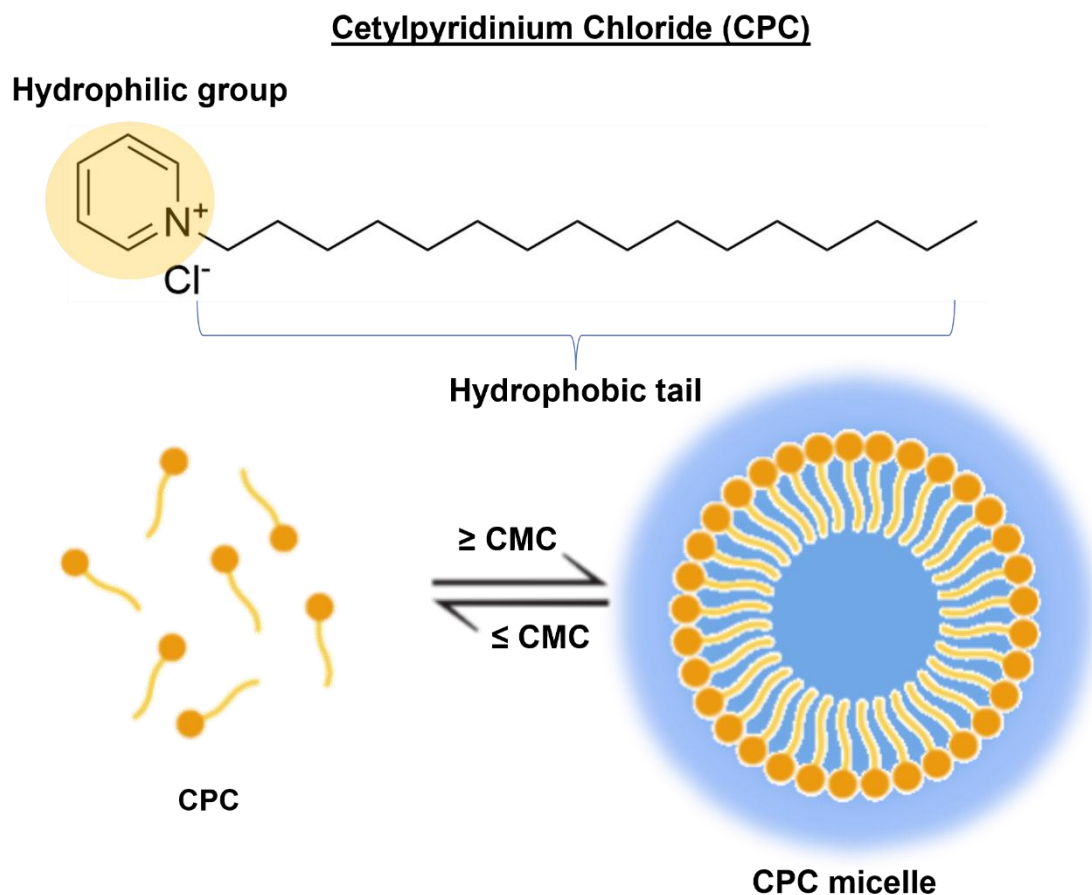


Figure 3. 4: Structure of cetylpyridinium chloride (CPC), showing the formation of micelles above its critical micelle concentration (CMC) in aqueous conditions. *Created with BioRender.*

The desirable property of drug loading could potentially be useful in encapsulating CPC into a non-porous SNP and triggered by an external stimulus for release. Cetylpyridinium chloride (CPC) is a commercially available cationic surfactant with potent antimicrobial properties against a broad range of bacteria.⁴⁴ The drug was approved by the food and drug administration (FDA) and is an active ingredient found in many medicines and commonly found in mouthwashes due to its potent and broad-spectrum of antimicrobial properties.^{45–47} It has been found to alleviate plaque-induced infections to promote a healthy oral microbiota environment. The mechanism of action

has been reported to proceed by the positive charged head group interacting with the negative bacterial membrane. CPC causes disruption to the lipid bilayer allowing the hydrophobic tail to permeabilise the cell membrane, resulting in the leakage of its intracellular contents.^{48,49} Additionally, CPC can inhibit the action of the extracellular enzymes, which are responsible for synthesising a polysaccharide, sucrose, well known to be important for the development of dental caries. Therefore, CPC can limit the biofilm formation on the surface of the tooth, to prevent oral disease such as gingivitis and periodontitis (gum diseases) and dental caries.^{50,51} Due to CPC's chemical structure, which contains a pyridine ring and a 16-carbon chain, its hydrophilic head group and lipophilic tail permits the formation of micelles (**Figure 3.4**) in aqueous and low alcoholic solutions at its CMC value of ~0.99 mM.^{52–55}

3.2 Chapter Outline

The design, synthesis, and characterisation of CPC encapsulated SNP (**CPC \subset SNP**) is reported for a potential application contributing towards improving dental diseases. This is a new approach to develop a drug delivery system based upon non-porous SNPs aiming to produce a silica shell to delay the drug release. This will be the first one-pot synthesis to incorporate an antimicrobial agent into the silica network that can be activated by cavitation produced from an ultrasonic scaler (**Figure 3. 5**). The **CPC \subset SNP** will be a proof-of-concept model with the purpose to tackle challenges associated with uncontrolled drug leakage, improve the pharmacokinetics and activity of antibiotics, and protect the drug until released to reduce the risk of antimicrobial resistance. Additionally, provide a platform for US-triggered drug release from SNPs that could be beneficial for encapsulation of other antimicrobial agents and improve treatment of dental diseases.

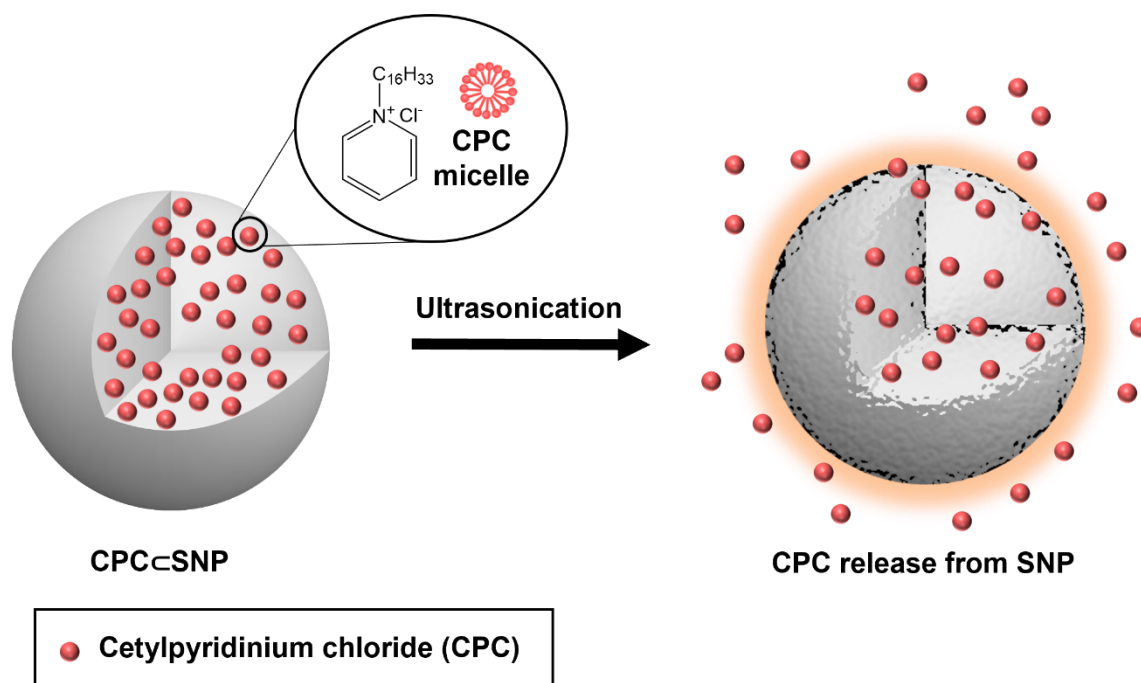


Figure 3. 5: Schematic representation of US triggered drug release from **CPC \subset SNP**.

3.3 Results & Discussion

3.3.1. Synthesis & optimisation of CPC loaded SNPs

To develop a one-pot synthetic route for encapsulation of CPC, the Stöber method was adapted, which has been used to produce non-porous SNPs (**SNPs**).⁴¹ First **plain SNPs** were prepared with no drug, yielding a white precipitate and would be used as a control NP in these studies for comparison to drug loaded SNPs.

The procedure for **plain SNPs** was further adapted to incorporate CPC into the reaction. To obtain the optimal CPC loaded into **SNPs**, the reaction conditions, such as, the drug concentration and reaction temperature were investigated. Initially, the concentration of CPC added was attempted between 0.05 to 155 mg mL⁻¹. This range was chosen based on the solubility limit of CPC in solution, the limit of quantification using UV-Visible spectroscopy and to determine the maximum drug loading. UV-Visible spectroscopy was a suitable technique to determine the loaded CPC in a sample. In water, CPC shows an intense absorption peak in the region of 230-280 nm, which is characteristic of the π - π^* transitions of the aromatic pyridine ring system. Whereas silica materials do not adsorb light in the UV-Visible region. As a result, the absorbance of CPC at different concentrations was used in the Beer's Lambert law to obtain the molar absorptivity (ϵ) of $4190 \pm 5.6 \text{ M}^{-1} \text{ cm}^{-1}$ at a wavelength (λ_{maxima}) of 260 nm. The absorbance could then be used to determine the entrapped drug in the NP samples. This was calculated by **Equation 2**, using the remaining CPC in solution post-synthesis and subsequent washes to subtract from the initial amount of CPC.

Equation 2:

% *Drug loading entrapment*

$$= \frac{\text{initial amount of CPC (mg)} - \text{Amount of free CPC in supernatant (mg)}}{\text{Total amount of CPC (mg)}} \times 100$$

Table 1: Summary of drug loading entrapment percentage of different CPC concentration preparations. determined by UV-Vis absorbance of CPC at $\lambda_{\text{max}} = 260$ nm, $\epsilon = 4190 \pm 5.6 \text{ M}^{-1} \text{ cm}^{-1}$ and observed drug release.

Sample	Drug concentration added to reaction (3 mL) / mg mL ⁻¹	Drug loading entrapment / %	Drug release observed in H ₂ O
SNP1	0.05	0	No
SNP2	0.2	33	No
SNP3	0.5	51	No
SNP4	2	52	No
SNP5	82	70	No
SNP6	155	83	Yes

Table 1 shows a summary of the drug loading entrapment percentages obtained from samples **SNP1-6** prepared with CPC. The addition of CPC to the reaction mixture after 3 h and total length of reaction was kept the same for **SNP1-6**. By increasing the initial CPC concentration added to the reaction, it resulted in a greater drug loading efficiency from 0 to 83%. It is possible during the SNP growth process, using tetraethyl orthosilicate (TEOS) enabled a crosslinked network of negatively charged silanol groups (Si-OH) that can interact with the positive charge on CPC. The higher drug concentrations increased the presence of positive charges creating more opportunity for electrostatic interactions to occur. Therefore, **Table 2** highlighted there was a

positive correlation between CPC concentration and drug loading entrapment with **SNP6** exhibiting a high loading efficiency of 83%. Furthermore, **SNP6** was the only drug delivery system to show drug release in water with use of applying US (discussed later in this chapter). The initial concentration studies were a beneficial starting point to change other reaction parameters.

To further examine conditions, the reaction temperature was altered to 25 °C and 80 °C to confirm the maximum drug loading. In addition, the concentration of CPC (155 mg mL⁻¹) remained consistent, but was added at different times during the reaction, at 0, 1 and 6 h to compared to addition at 3 h. The purpose of changing the time of CPC addition was to also observe any changes to the drug loading efficiency.

Table 2 shows a summary of prepared **SNP6-13** samples with their calculated drug loading entrapment percentages. The comparison between 25 and 80°C showed displayed no significant changes to the loading entrapment nor did the time of the CPC addition. Although, **SNP13** did exhibit a higher loading efficiency of 87% with CPC addition at 6 h and temperature of 80°C than **SNP6**. However, upon further characterisations studies, shown in the next section, **SNP13** was not a suitable candidate for drug delivery.

In this case, CPC additions before 3 h showed lower efficiencies than at 3 h, possibly affecting the silica's nucleation process. Also, in agreement with studies from Zhang *et al.*⁴¹, who showed a stronger emission from a ruthenium dye at 3 h into the reaction. For these reasons, CPC inclusion at 3 h at 25 °C seemed the most promising. For subsequent characterisations of **SNP7-13** drug loaded particles developed see **Appendix section 3.5**.

Based on the various SNPs synthesised, the most optimum particles were achieved with the **SNP6** method. The particles produced from this method has been renamed as **CPC \subset SNP** for the rest of this chapter. This decision was made based on the promising initial results of the drug loading efficiency and comparisons made to the other **SNPs**.

Table 2: The drug addition time (*t*), reaction temperature (*T*) and drug loading efficiency measured by UV-Vis absorbance of CPC at $\lambda_{\text{maxima}} = 260 \text{ nm}$, $\epsilon = 4190 \pm 5.6 \text{ M}^{-1} \text{ cm}^{-1}$.

Sample	Drug addition, <i>t</i> / h	Reaction temperature, <i>T</i> / °C	Drug loading efficiency / %
SNP7	0	25	65
SNP8	1	25	65
SNP6	3	25	83
SNP9	6	25	25
SNP10	0	80	26
SNP11	1	80	33
SNP12	3	80	83
SNP13	6	80	87

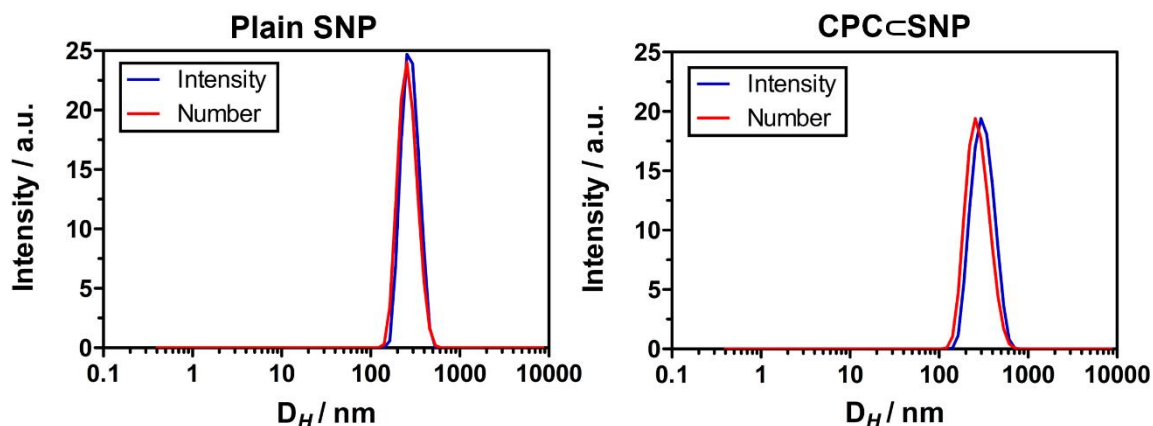
3.3.2. Characterisation of CPC \subset SNP drug delivery system

3.3.2.1. Size & morphology

The chosen **CPC \subset SNP** was first characterised by dynamic light scattering (DLS). DLS measurements uses estimations to obtain the hydrodynamic size of particles in solution. The NP diameter size is usually displayed by intensity, volume or number, based on the Stokes Einstein equation.⁵⁶

In addition, a polydispersity index (PDI) value provided information on the size distribution of how well the particles were dispersed in solution. **Figure 3. 6A** shows the diameter sizes of **CPC-SNP** compared to **Plain SNP**. The average diameter measured by intensity of **CPC-SNP** when dispersed in water was 420 ± 49 nm. This was much larger than the diameter obtained for **Plain SNPs** of 238 ± 61 nm. The low PDI values of 0.308 and 0.233 for **Plain SNP** and **CPC-SNP** respectively, also suggested a narrow particle size distribution and uniform diameter size. It was evident there was a clear size difference between particles with no drug loaded and drug incorporated into the NPs. The **SNP** method generally produced large diameters possibly due to a long reaction time of 12 h, resulting in continued nucleation growth of the silica network. However, the size of **CPC-SNP** were still considered a suitable size for delivery into the dentinal tubules, which have diameters of approximately 2-4 μ m.⁵⁷

A) Particle size and surface charge



Sample	D _H by Intensity / nm	D _H by Number / nm	PDI	ζ / mV
Plain SNP	283 ± 61	267 ± 64	0.308	-45 ± 6
CPC-SNP	420 ± 49	418 ± 64	0.233	-32 ± 6

B) SEM images

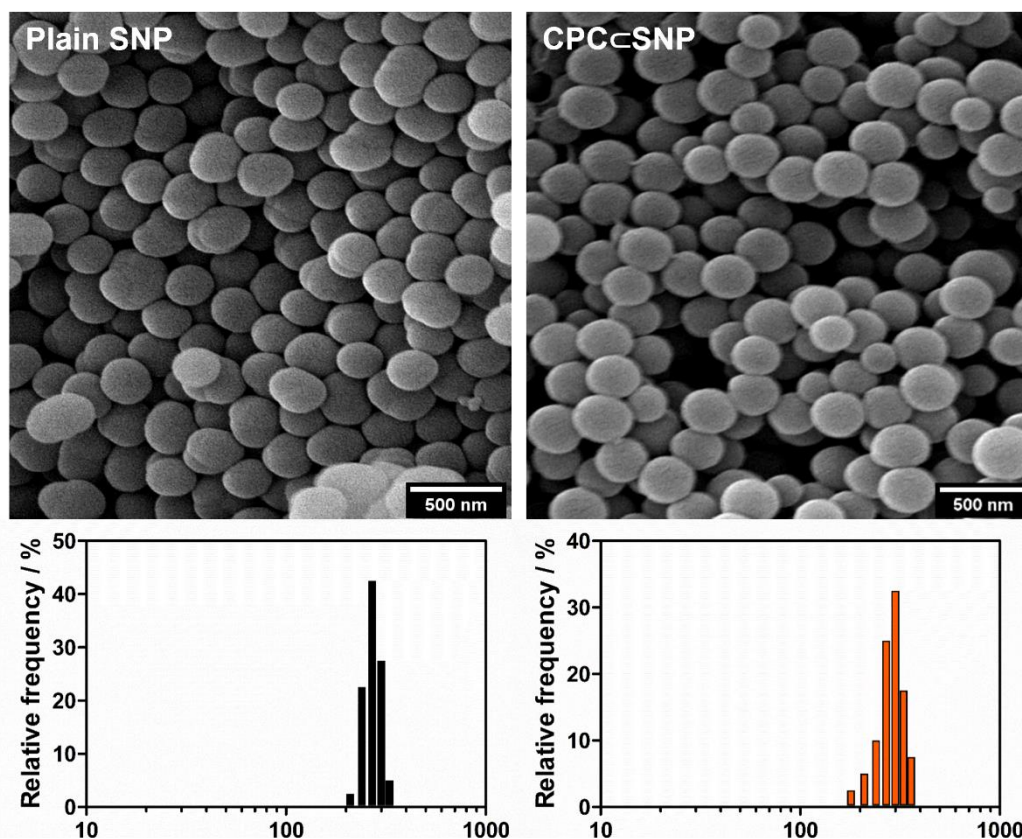


Figure 3. 6: Comparison of **Plain SNP** and **CPC-SNP** by **A)** DLS graphs showing size distributions by intensity and number. Hydrodynamic sizes are summarised in the table with surface charge reported by the zeta potential. **B)** SEM images and analysis of measured physical sizes.

Additionally, the surface charge was measured and determined by the zeta potential in an aqueous solution, also displayed in **Figure 3.6A**. **Plain SNP** was used as control to show unmodified silica has a highly negative and stable charge of -45 ± 9 mV. This is due to the abundant Si-OH groups available on the particle surface and dense silica network. Upon incorporation of drug, **CPC-SNP** showed a slight decrease in the zeta value to -32 ± 6 mV but remained stable after drug inclusion. The overall negative charge of the silica system supports that CPC has been integrated into the silica network and the slight increase in charge is due to remaining CPC on or near the surface. This was further supported by comparison to a control method that used mesoporous silica to incorporate CPC to form **CPC-MSNs**. The **CPC-MSNs** sample showed high positive charge of $+36 \pm 5$ mV (**Appendix: Figure S3.32**). This indicated the cationic nature of CPC, which dominates the surface and pores of the silica bulk particles. Hence, **CPC-MSNs** would not be an ideal drug delivery system for CPC without further modifications. On the other hand, **SNP13** had previously shown a high drug loading efficiency of 87 %, showed a more positive surface charge of -21 ± 4 mV than **CPC-SNP**. Not only did this indicate a system with less colloidal stability, but the addition of CPC later to the reaction suggested more drug interactions to the surface of the particle rather than encapsulated, indicated also by the smaller size diameter of less than 200 nm. For these reasons **CPC-SNP** remained the more suitable method for synthesising drug loaded particles with CPC.

In addition, scanning electron microscopy (SEM) was a complimentary technique to DLS analysis to determine the shape and size of **SNPs**. The images shown in **Figure 3. 6B** illustrated both **Plain SNP** and **CPC-SNP** methods had produced particles of uniform and spherical shapes. The particles looked well dispersed and correlated to

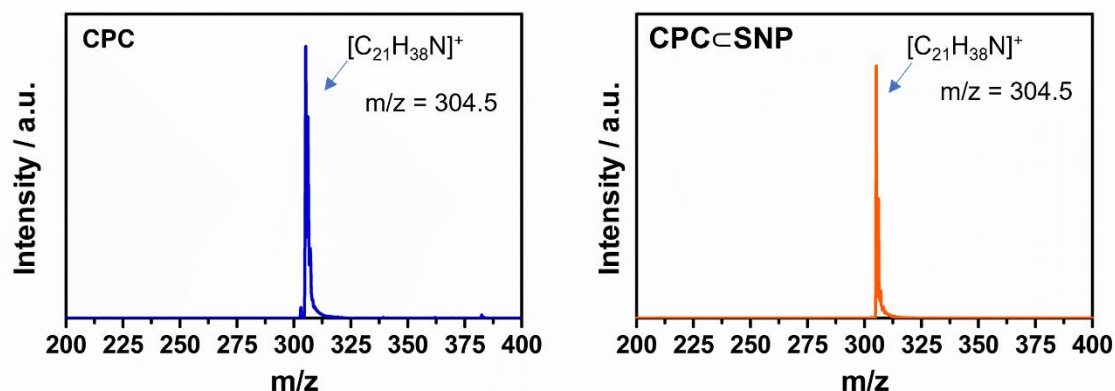
the low PDI values obtained by DLS. Furthermore, after image analysis the physical diameters of particles had an average of 272 ± 25 and 289 ± 39 nm for **Plain SNP** and **CPC \subset SNP**, respectively. There was variation in measured diameters of SNPs, the **Plain SNP** seems coherent between DLS and SEM measurements, however **CPC \subset SNP** revealed smaller diameters with SEM. The hydrodynamic diameter is often influenced by interactions between particles and the media used for dispersion. In this case, the DLS averages were higher for **CPC \subset SNP** because of possible water hydration included into the NP and the entrapment of CPC. Whereas the sample preparation for SEM was of dry particles and were not affected by water or solvents.

3.3.2.2. Structural analysis of CPC \subset SNP

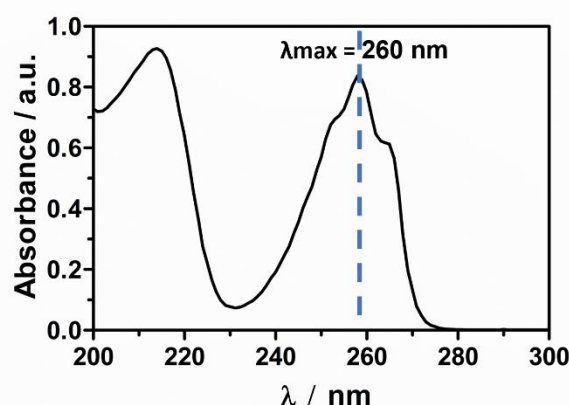
Further analysis of **CPC \subset SNP** was conducted and compared to **plain SNP** by MALDI-TOFMS, FT-IR and solid-state UV-Vis and fluorescence. These techniques were important to confirm the presence of CPC and reveal any changes to the silica structure.

MALDI-TOF mass spectrometry is a relatively simplistic and high-resolution analytical technique and can be used for detection of CPC. The instrument was used in positive mode to indicate the presence of CPC in the SNPs. In **Figure 3. 7A**, a spectrum of pure CPC monohydrate was obtained and indicated a m/z peak at 304. This attributed to the cetylpyridinium ion and loss of the chloride salt. The spectrum of CPC alone was compared to the formulation of **CPC \subset SNP**. The spectrum for drug loaded SNP also showed the same peak at 304 m/z, which reflected the presence of CPC in its ion form, confirming the presence of CPC. This finding is in agreement with studies shown by Morrow *et al.*,⁵⁸ in which they observe spectra of quaternary ammonium compounds from mouth-rinse formulations and their fragmentation under MALDI conditions.

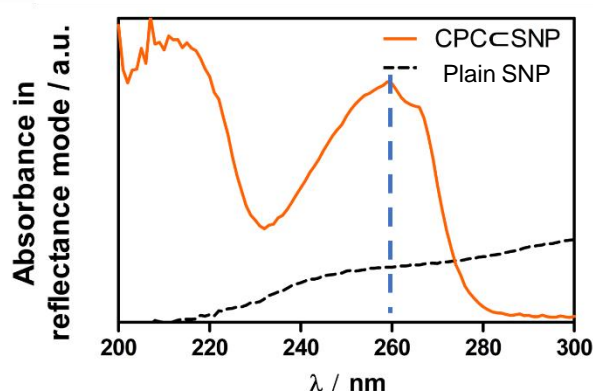
A) MALDI-TOFMS



B) CPC in solution



C) Solid-state UV-Vis



D) Solid-state emission

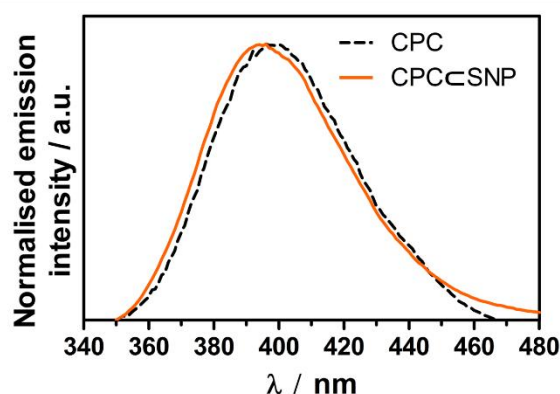


Figure 3. 7: A) MALDI-TOFMS of CPC monohydrate and **CPC@SNP** prepared in α -Cyano-4-hydroxycinnamic acid (CHCA), acetonitrile (ACN) and formic acid in MeOH in 1:1 ratio. **B)** UV-Visible absorption spectrum of CPC in H_2O ($\epsilon_{4190} M^{-1} cm^{-1}$) and **C)** Solid-state UV-Visible spectra shows the absorbance in reflectance mode for detection of CPC powder (λ_{260nm}) from **plain SNP** and **CPC@SNP**. **D)** Solid-state emission spectra of CPC and **CPC@SNP** $\lambda_{exc}=260$ nm and $\lambda_{em}=340-480$ nm. Spectra were corrected for PMT response.

Therefore, MALDI-TOFMS demonstrated its versatility at detecting a low molecular weight compound for analysis and by the mode of ionisation of cationic surfactants, CPC presence could be confirmed in **CPC@SNP**.

The drug loaded **SNPs** were examined using FT-IR spectroscopy, the spectra can be found in the **Appendix Figure S3.14-15**. It is clear in **plain SNP** and **CPC@SNP** spectra, they both had the characteristic formation of Si-O-Si and Si-OH vibrational bands at 1051, 950 and 794 cm^{-1} (highlighted in red), which indicated silica was the dominant material. With FT-IR spectroscopy, it was thought changes to the spectra would confirm the modification of the silica with CPC. CPC monohydrate has C-H stretching of alkyl chain at 2922 and 2852 cm^{-1} , weaker bands are observed at approximately 2158, 1635, 680 cm^{-1} , which are characteristic of the aromatic nitrile stretch, C=C bend and C-H bend respectively (highlighted in blue). However, no vibrational bands correlated to CPC for the spectra for **CPC@SNP**, probably due to CPC's weak transmission bands and the strong intensity of the silyl bands making it difficult to distinguish the CPC bands.

An alternative method was employed to confirm the presence of CPC by exploiting its photophysical properties. The characteristic absorbance spectrum of CPC in solution was displayed in **Figure 3. 7B**, indicating a λ_{max} at 260 nm. Due to scattering of silica NPs in solution, diffuse reflectance was employed to measure the absorbance of CPC when incorporated into the silica system in its solid form, shown in **Figure 3. 7C**. As expected, the **plain SNP** in the absence of drug showed no absorbance peaks corresponding to CPC and showed light scattering instead. Whereas **CPC@SNP** showed adsorption at approximately $\lambda_{\text{max}} = 260 \text{ nm}$ consistent with CPC. This

reinforced CPC is present in the NPs but should be noted the amount of drug was not quantifiable in its solid form.

Furthermore, pure CPC, although not emissive in water at pH 7.4, is luminescent in its solid form when excited at its λ_{max} at 260 nm. The emission spectrum in **Figure 3. 7D** was collected between 340-480 nm. The result of a strong emission peak at approximately at λ_{max} at 396 nm also implies the presence of CPC loaded silica. The reason for luminescence of CPC in its solid phase is unknown, it could be attributed to the possibility of π - π^* stacking of the aromatic rings or the interaction between the drug and silica influencing an enhanced emission from **CPC@SNP**. Although solid-state UV-Visible and emission techniques confirmed the CPC in the silica structure, it was not a suitable technique to quantify drug loading or to provide information if the drug was on the surface or encapsulated within the SNP structure, hence further characterisation was required.

3.3.2.3. Drug loading content

The total drug loading amount was quantified by using thermogravimetric analyser coupled with FT-IR and gas chromatography-mass spectroscopy (TGA-FT-IR-GCMS). TGA is commonly used to characterise materials based on their thermal stability.⁵⁹ The weight change is monitored in real-time as the sample is heated at a constant rate. The thermal curves obtained in **Figure 3. 8**, indicated the weight loss percentage due to the decomposition of volatile organic compound, CPC monohydrate with increasing temperature. Silica is well known to be thermally stable at high temperatures, hence was ideal to use TGA to determine the amount of CPC present.

First, the decomposition of **plain SNP** was tested, the thermal curve showed no significant weight loss, supporting silica's stability under high temperatures.

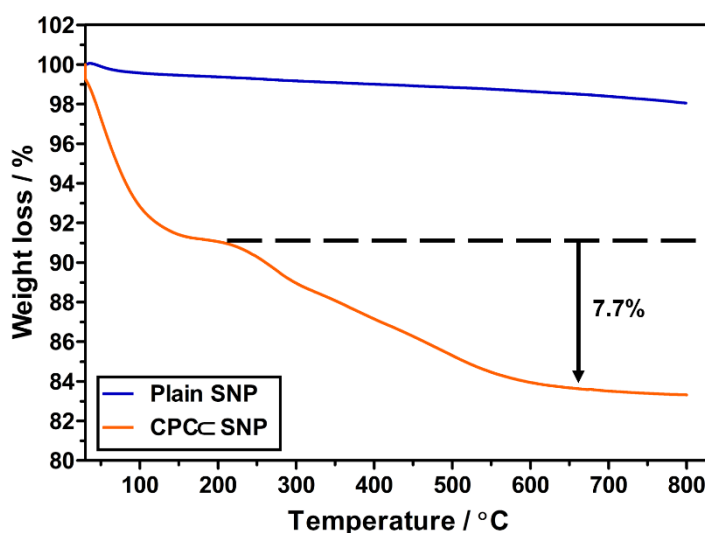


Figure 3. 8: Thermogravimetric analysis curves of **plain SNP** (10 mg) and **CPC-SNP** (10 mg), showing the overall weight loss with increasing temperature.

The overall weight loss was <2%, due to the loss of water and was deemed negligible. The drug decomposition of CPC occurred at 234 °C, in agreement with the literature values.^{60,61} The decomposition profile of **CPC-SNP** displayed two steps. The initial step attributed to the loss of water <180 °C and the other analogous to the pyrolysis of CPC occurring between 233-476 °C (5% error), which gradually declined. Although the TGA can be coupled with FT-IR to obtain spectra in real time, in this case CPC was too weak and previously been shown that FT-IR was unable to detect CPC peaks with **SNP** prepared drug loaded samples. However, previous studies from other preparation methods, samples such as: **adsorbed CPC@MSN** and **templated CPC@MSN** did reveal comparable bands associated to that from CPC (clearly shown in **Appendix S3.39**). It supported that the main weight loss step between 280 and 500 °C was due to the pyrolysis of CPC, by strong characteristic peaks attributed to the CH₂ and CH₃

vibrational stretches and bends. In addition, at the inflection points (IP) of **CPC@MSN** and **CPC \subset MSN** curves, the sample was vaporised and run through a GC column. Retention peaks from the fragmentation of the organic material were detected by mass spectroscopy. This was achieved by holding the temperature at 300 °C and 510 °C to allow separation of the two main decomposition stages. The retention peaks at 2 and 11 min corresponded to the pyridine ring and alkyl chain of CPC, respectively. Therefore, coupling all three techniques strengthened that the major weight loss was due to CPC. The sample principles could be applied to the **SNP** prepared samples with CPC, as the same starting materials were used. Therefore, the TGA-FT-IR-GCMS could determine quantitatively the amount of CPC loaded.

The overall weight loss due to CPC decomposition from **CPC \subset SNP** was calculated to be 7.7%. Therefore, it was calculated the drug loading per mg of **CPC \subset SNP** was 77 $\mu\text{g}_{\text{CPC}} \text{mg}_{\text{CPC}\subset\text{SNP}}^{-1}$. In addition to the drug loading value, the entrapped drug was derived from the initial amount of CPC and the free CPC in solution after the reaction and subsequent washes measured by UV-Vis absorbance, which was calculated to be 83% of CPC encapsulated into **CPC \subset SNP**. The level of drug loading of **CPC \subset SNP** was comparable to the literature and was sufficient.^{20,62–67} It was difficult to compare the loading because majority of drug delivery systems are MSNs based, where the drug has been adsorbed to the surface or included within the pore after the NP has been synthesised making it straightforward to calculate the loading amount. Determination of drug loading through encapsulation into a supposedly non-porous SNP system is difficult to quantify and normally aided by fluorescent molecules. However, for the purposes of this research, this was not explored here. From the drug

loading quantification acquired by the TGA, this was used for the drug release studies with examination with and without US.

3.3.3. *In Vitro* drug release studies of CPC=SNP

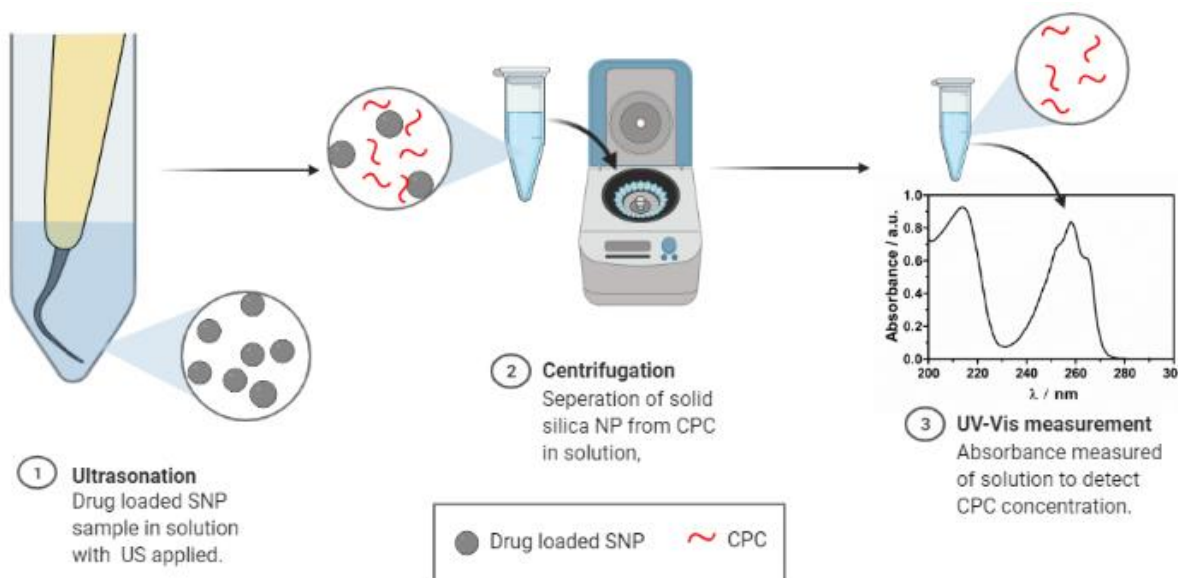


Figure 3. 9: Illustration of US triggered release of CPC from drug loaded SNP and separation method to achieve CPC absorbance in solution. *Created with BioRender.*

After successful preparation of **CPC=SNP**, the drug release behaviour with and without US was investigated. First, **CPC=SNP** was dispersed in water (2 mg mL^{-1}) and the temperature was maintained at 37°C . A temperature probe was used to monitor the temperature of the water bath that surrounded the universal tube containing the sample. The ultrasonic scaler tip was directly immersed into the NP solution. As shown in **Figure 3. 9**, the drug release was measured in the same way the drug loaded entrapment studies were conducted, using the UV-Vis absorbance of CPC ($\lambda=260 \text{ nm}$) to calculate the concentration of drug. The release profiles of CPC from **CPC=SNP** are shown in **Figure 3. 10**. **CPC=SNP** was exposed to 2 min pulses of ultrasound (US) at three different power settings. The ultrasonic scaler was applied at low (P10),

medium (P15) and high (P20) at a frequency of 28-36 kHz. It is clearly seen from **Figure 3. 10A and B** that CPC release was dramatically enhanced by US.

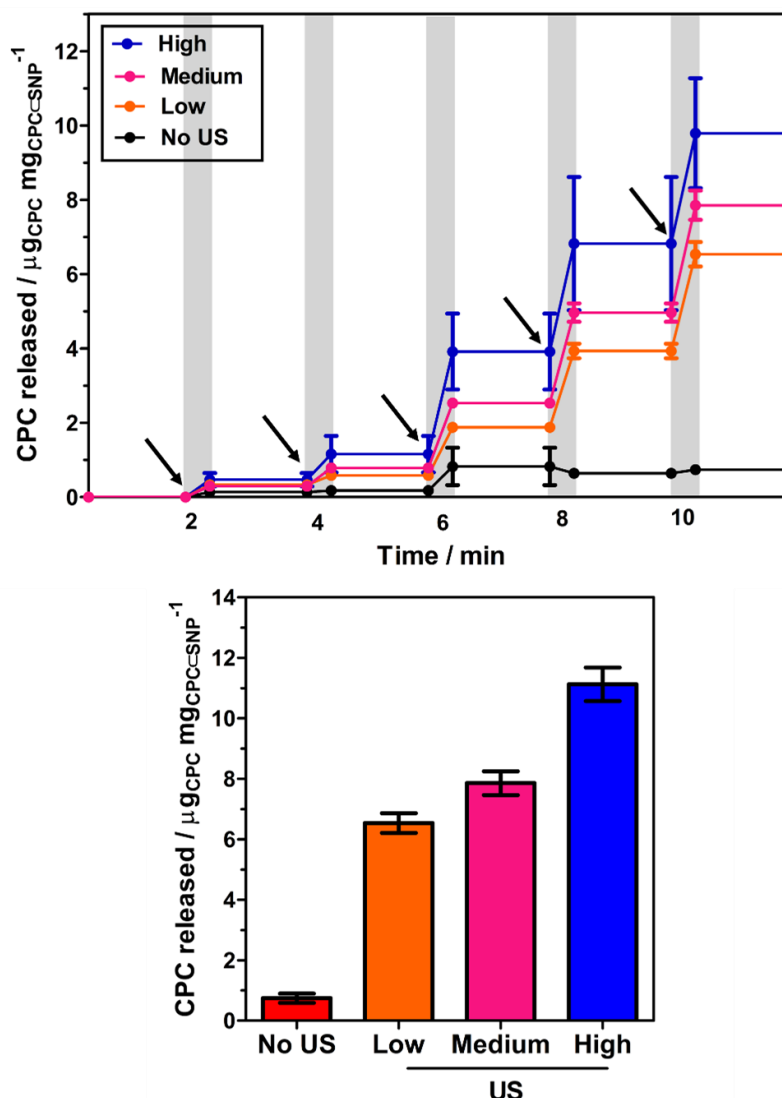


Figure 3. 10: Drug release profiles of **CPC_CSNP** (2 mg mL⁻¹, H₂O, 37 °C, pH 7.4). The natural release profile with no ultrasound and different power setting on the ultrasonic scaler (low- P10, medium-P15, high-P20) were compared. **CPC_CSNP** was exposed to ultrasound for 2 min pulses for a total of 10 min. The release was monitored by UV-Vis absorbance at λ_{max} 260 nm. **A)** mass of CPC release and **B)** overall percentage of CPC release with 10 min.

The profiles showed drug release could reach up to 6, 8 and 13 μgCPC mgCPC_CSNP⁻¹ at output power setting low, medium and high, respectively. By applying 2 min US each time, stimulated the CPC release. There are several reasons to rationalise the release

mechanism with US. It is well known that thermal and mechanical effects are a consequence of US waves generated in a fluid.⁶⁸ These effects can have an impact on the silica surface upon interaction. The US vibrations from the tip attenuated by the particles can be converted into other forms of energy, such as heat. A rise in temperature could force the release of CPC and cause damage to the surface of **CPC@SNP**, especially at the highest power setting. However, US was used for short periods of time, the solution was maintained at 37 °C and silica is a material that is stable under high temperatures. In the literature, most of the US-responsive silica-based NP drug delivery systems are coated with materials that are affected by US, rather than the silica NP. For example, functionalisation with polymer chains, which are more prone to degradation or disruption by heat.⁶⁹ Therefore, it was thought thermal effects were not a major contributor to release.

The main mechanism of US that is most likely to influence the release of CPC was acoustic cavitation. The mechanical effects due to the rise and collapse of gas bubble in the solution could have a profound impact on the silica⁷⁰. By increasing the power setting, this may have led to high pressures in the water causing bubbles that have formed to become unstable. This can result in violent bubble implosion, releasing high energy shockwaves or even microjets, that can destroy **CPC@SNP**'s surface to induce release.⁷¹ Alternatively, if non-inertial cavitation was produced by the US tip then US could have had a milder impact on **CPC@SNP**.

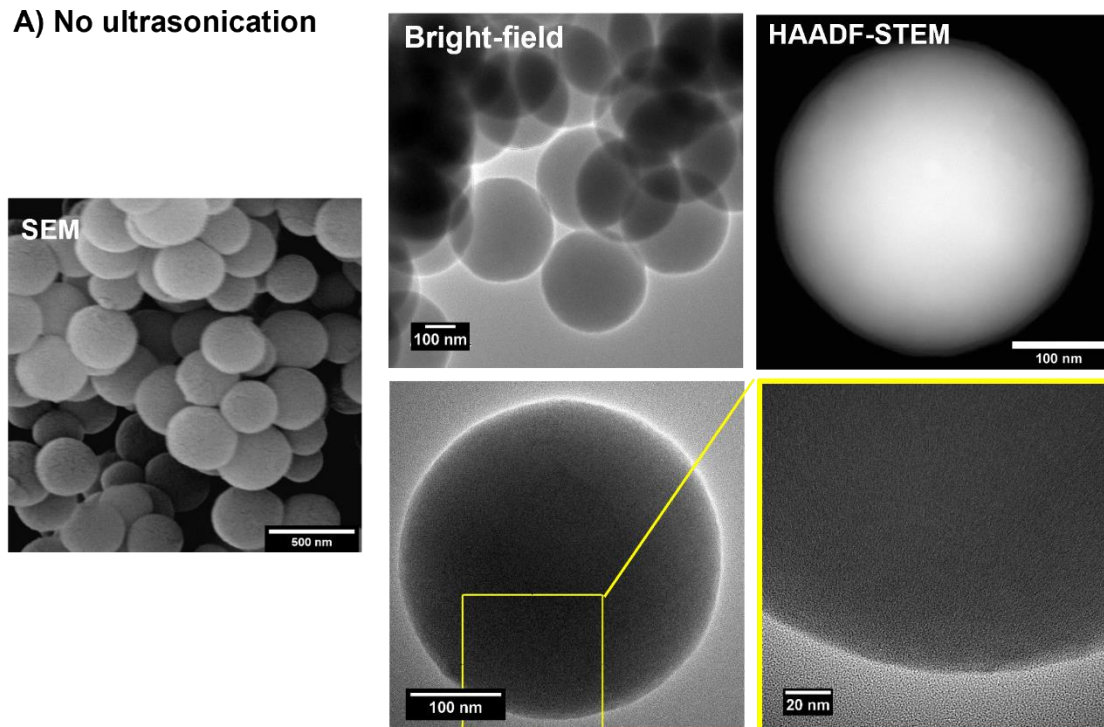
Furthermore, the production of cavitation could be impacted by **CPC@SNP** in solution. Reports in the literature have mentioned SiO₂ NPs delay cavitation by reducing the bubble growth rate. Others believe strong hydrogen bonds are formed in solution with silica. On the other hand, other researchers have suggested NPs promote

cavitation.^{72,73} It is unclear from these studies how the phenomenon of cavitation affects CPC \subset SNP, but also the mechanism of NP's acting on cavitation.

To further the understanding of CPC release with US, **CPC \subset SNP** samples were observed with two different imaging techniques, SEM and HR-TEM in **Figure 3.11**. The images of no US (**Figure 3. 11A**) were compared to the effects of 10 min of US (**Figure 3. 11B**) **CPC \subset SNP**. Firstly, SEM had previously been used to assess the morphology and sizes of **CPC \subset SNP** after synthesis and was used again to reveal any structural changes to the NPs. The uniform and spherical nature of the particles was preserved with no US in water. Even when US was applied, the **CPC \subset SNPs** remained unchanged in the size and shape. However, due to the limitations of the SEM resolution, it would be difficult to detect small changes to the individual particles.

Despite this, **CPC \subset SNP** particles were evaluated using HR-TEM instead. The HR-TEM instrument has a high magnification range to observe defects that can be resolved on the atomic scale. The use of a high-powered electron beam, up to 300 kV, is valuable for high resolution images of nanomaterials and is more suitable than TEM. Normal TEM uses a weaker electron beam, has lower resolution and is limited to thin specimens for the electrons to pass through to create a projection image.^{74–77} The bright-field HR-TEM micrographs showed **CPC \subset SNP** particles had a dark contrast and smooth-like textures attributing to a solid and high mass density before exposure to US in **Figure 3. 11A**. Highlighted by the yellow outlines and increasing the magnification from ~100 kx to 295 kx, emphasised the solid structure of **CPC \subset SNP**, which had no porous channels. This possibly indicated that the particles have a silica shell thick enough to entrap the drug within the structure.

A) No ultrasonication



B) With Ultrasonication

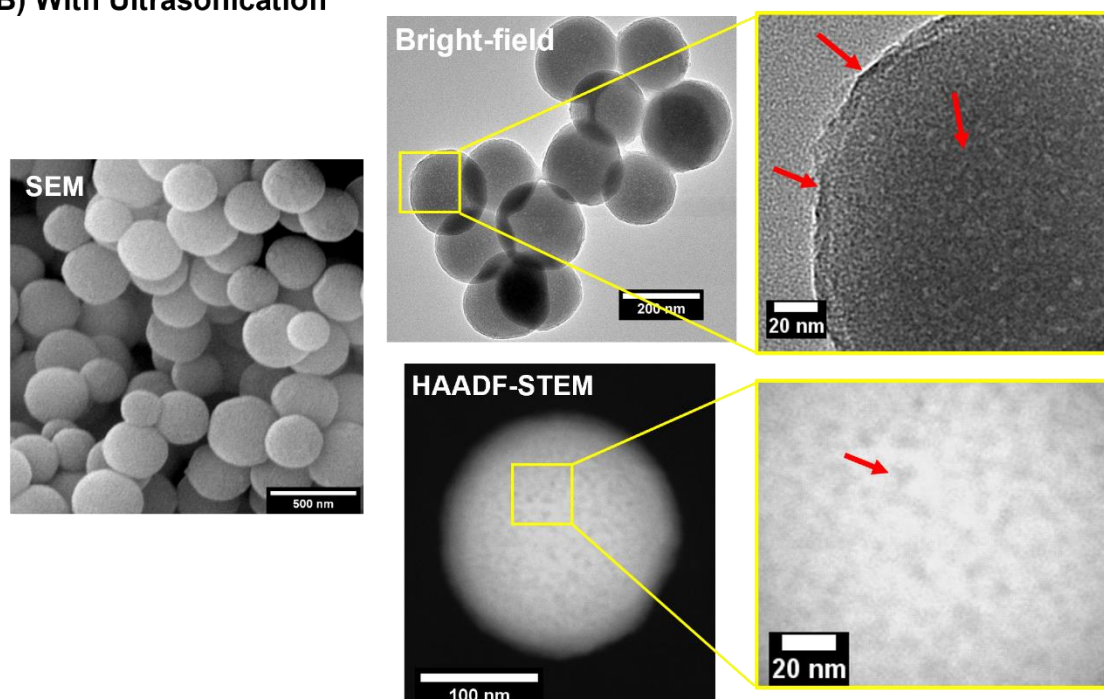


Figure 3. 11: SEM and HR-TEM micrographs of CPC@SNP **A)** without US and **B)** with 10 min US. SEM magnification 35 kx, 20.0 kV electron beam; Bright-field HR-TEM magnification 49-295 kx, 300 kV electron beam; HAADF-STEM magnification from 190 to 540 kX. 300 kV electron beam.

The HR-TEM images could help explain the delayed response of drug releases from **CPC@SNP** when no US had been applied.

To support these findings, high-annular dark field scanning TEM (HAADF-STEM) was employed. HAADF-STEM is a powerful and complementary technique to other imaging methods and was used to enhance the contrast of the particles, by reversing their appearance. This further corroborated **CPC@SNP** dense nature and loaded with CPC.

Furthermore, bright-field HR-TEM, revealed alterations to the surface of **CPC@SNP** with US applied for 10 min in aqueous solution. Indicated by the red arrows in **Figure 3. 11B**, the roughness to exterior of the silica shell is visible. Remarkably with HAADF STEM, dark and small circular features were apparent. In addition, the shape of **CPC@SNP** appeared to have deformed slightly with US. In the literature, application of US has been responsible for the breakage of covalent bonds, non-covalent π - π , metal coordination and hydrogen bonds.⁷⁸ Some researchers have shown US induces flexibility to polymer coating and in some cases causing damage to the drug delivery system and breaking them apart.¹⁶ As a result, all have led to an accelerated expulsion of drugs. In this case, the HR-TEM images can support the assumption of mechanical and thermal effects produced from US, which could contribute to weakening the electrostatic interaction between positively charged CPC and the negative silica network. Therefore, operating the US at maximum power (P20) promotes disruption to the silica shell releasing CPC.

More studies were conducted to support the drug release from **CPC@SNP** with the ultrasonic scaler. The release media conditions were changed to methanol and continuous US was applied using an ultrasonic bath. The US bath was used instead

of the ultrasonic scaler tip, to observe the effect to the drug delivery system over a longer period. The solvent was changed to methanol, as it is less polar than water, meaning CPC would have a higher solubility and increase the detection. Depicted in **Figure 3. 12**, **CPC \subset SNP** displayed rapid release kinetics in methanol, showing an initial burst release within the first 10 min. By this point majority of CPC ($30 \mu\text{g}_{\text{CPC}} \text{mg}_{\text{CPC}\subset\text{SNP}}^{-1}$) had been release. Thereafter, CPC release remained slow and steady, reaching up to $45 \mu\text{g}_{\text{CPC}} \text{mg}_{\text{CPC}\subset\text{SNP}}^{-1}$. In comparison, the gradual release kinetics in water amounted to 40% less than in methanol after 180 min.

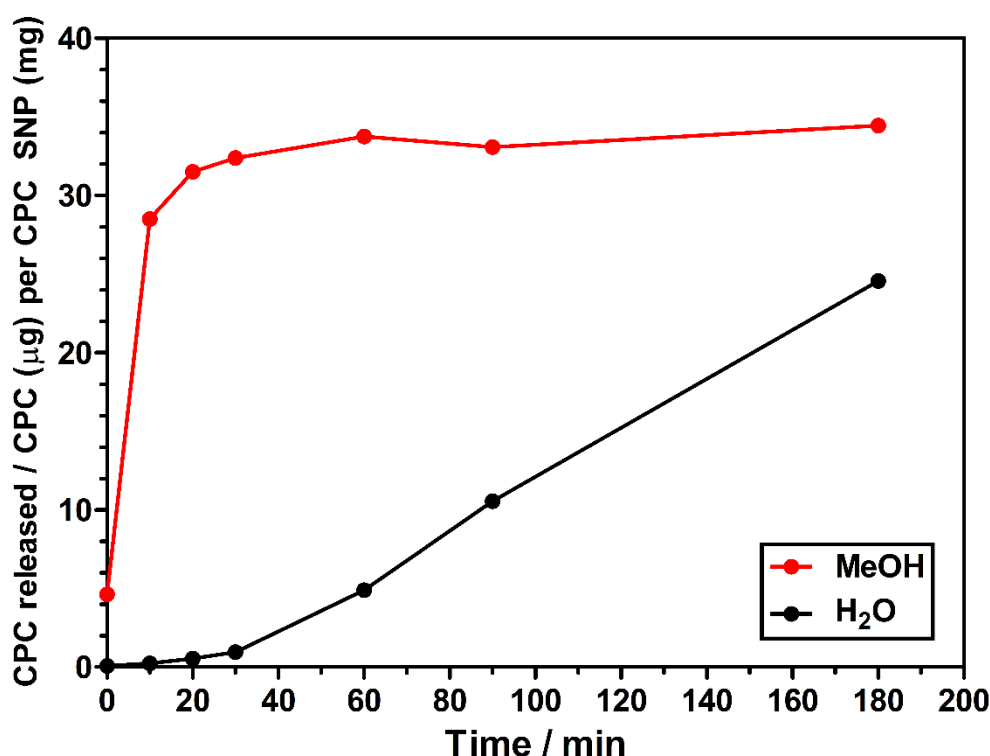


Figure 3. 12: Drug release profiles of **CPC \subset SNP** (2 mg mL^{-1} , 37°C , pH 7.4) with continuous cavitation from ultrasonication bath for 180 min in MeOH and H₂O.

Interestingly, CPC was found to be more soluble in methanol than water, hence the difference in release rates. Previously, it has been proposed the structure integrity of **CPC \subset SNP** is based on the formation of CPC micelles encapsulated into the silica

framework by weak electrostatic interactions of positively charged CPC and negatively charged Si-O⁻ groups. Introduction of methanol into the drug delivery system can increase the repulsion between head groups of CPC molecule when in its micelle form.⁵² Rafati *et al.*, reported a conductometric technique to show that by increasing the alcohol concentration, causes the destabilisation of micelles and increases the degree of dissociation of molecules.⁵² Therefore, is possible methanol lowers the CPC CMC to below ~0.99 mM in water,⁵⁴ enhancing release of CPC in methanol when exposed to US. Unfortunately, not all the expected drug was released in this time and is thought more drug could be trapped within the silica network and may not release with US or methanol.

To verify the effect of methanol on **CPC@SNP**, a sample was stirred in methanol for 72 h. More images were taken to visualise any structural changes with SEM and HR-TEM. In **Figure 3. 13**, the SEM images, indicated by the arrows, the surface appears to have a crinkled like texture, but the overall shape and size was unaltered. In bright-field HR-TEM mode, bright circular features with darker ringed outlines were strikingly obvious. At a higher magnification of 295 kx the diameters were measured, averaging 20 nm in size. Even more, the features were still evident with HAADF-STEM, showing dark circular holes. The development of structural changes to **CPC@SNP** is more likely due to the effect of MeOH, not Us. Instead, the indicated how CPC micelles/aggregates formed during the synthesis could have been incorporated into the internal silica particles system. Therefore, encapsulating CPC in a one-pot process has most likely produced silica shell to protect and prevent diffusion of CPC.

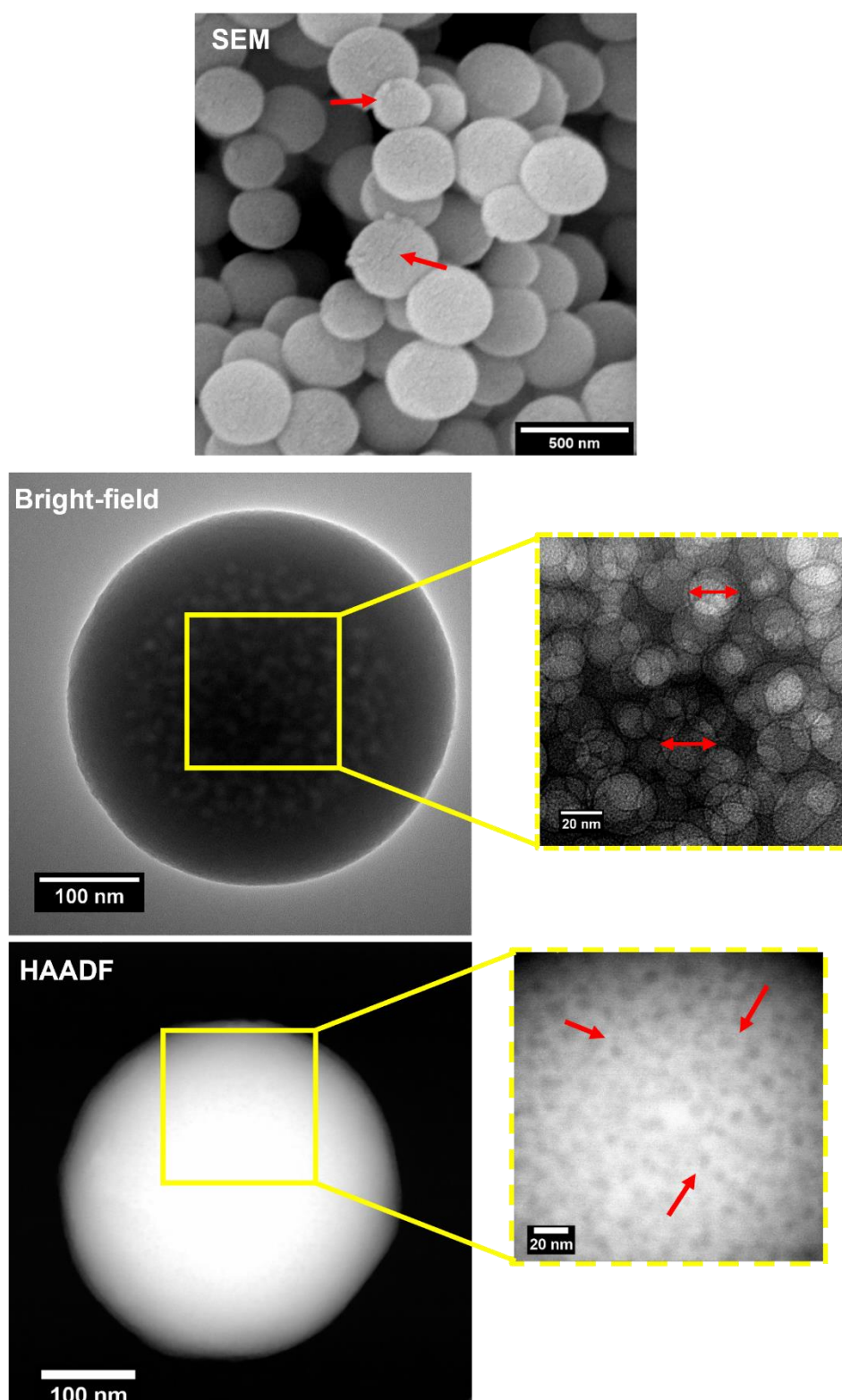


Figure 3. 13: SEM and HR-TEM micrographs of **CPC-SNP** in MeOH (1.5 mg mL^{-1} stirred at 400 rpm, 72 h. SEM magnification 35 kx, 20.0 kV electron beam; Bright field images with magnification from 48 to 295 kx; HAADF STEM with magnification from 190 to 540 kx. 300 kV electron beam

3.4 Conclusions

In this study, a model drug delivery system, **CPC@SNP**, has been developed and optimised by loading the drug, CPC. The antimicrobial drug was successfully encapsulated into the SNP framework through a one-pot process and found that introducing CPC at 3 h into the reaction mixture, was ideal for efficient drug entrapment. Various characterisation techniques provided sufficient evidence that **CPC@SNP** had been successfully achieved. Complimentary techniques were utilised to determine the uniform and spherical size and shape, as well as the presence of CPC in **CPC@SNP**.

Furthermore, **CPC@SNP** was responsive to US at frequencies between 28-36 kHz showing enhanced drug release. Importantly, **CPC@SNP** showed minimal leakage with no US when compared to other conventional drug loaded silica systems with CPC, such as templated **CPC@MSN** and adsorbed **CPC@MSN** methods. On-demand and controlled release was successfully achieved by applying US produced from an ultrasonic scaler. The release kinetics were enhanced with US and suggestions of the mode of release. Release was thought to be induced by thermal and mechanical effects of US. However, HR-TEM analysis was a good indicator to show the structural damage that could have been caused by cavitation effects. This also indicated a core-shell type of drug delivery system had been created, responsible for preventing uncontrolled release.

Although methanol was used to help understand the release of CPC with US, instead provided more insight of how CPC could be loaded into the silica NP. This revealed

noticeable pore like structures and the potential drug incorporation into the silica network.

Even though it has been strongly suggested cavitation is responsible for the release of CPC. This work could benefit from experiments that can detect and visualise cavitation bubbles, such as sonochemiluminescence or high speed imaging

CPC@SNP will be the first reported antimicrobial-SNP drug delivery system triggered by US. The new drug delivery system has the potential for future clinical applications and the proposed one-pot processes reduces the need for multi-step and complicated reactions. Also, subsequent characterisation and purification stages. Finally, this work presents **CPC@SNP** as US-responsive model drug delivery system that can be utilised for the encapsulation of other antimicrobial agents.

.

3.5. Appendix

3.5.1. Synthesis and Characterisation of CPC loaded NPs

Sample	Molar Equivalence				
	TEOS	H ₂ O	CPC	NH ₄ OH	EtOH
SNP	1	23	0	154	39.8
SNP1	1	23	3.71×10^{-5}	154	39.8
SNP2	1	23	1.49×10^{-4}	154	39.8
SNP3	1	23	3.71×10^{-4}	154	39.8
SNP4	1	23	6.19×10^{-4}	154	39.8
SNP5	1	23	6.08×10^{-2}	154	39.8
SNP6	1	23	1.16×10^{-1}	154	39.8

Figure S3. 1: The ratio of starting materials using in the reaction for SNP-6 presented by their molar equivalences.

Sample	Drug Concentration / mg/mL	CPC Moles in reaction / mmol	CPC Concentration in reaction / mM
SNP	0	0	0
SNP1	0.05	0.004	0.01
SNP2	0.2	0.0017	0.05
SNP3	0.5	0.0042	0.12
SNP4	2	0.0070	0.2
SNP5	82	0.6860	20.58
SNP6	155	1.3034	39.10

Figure S3. 2: Table to show the initial CPC drug concentration before added to total reaction volume compared to concentration and number of moles of CPC when added to total volume of 30 mL after 3 h , 25 °C.

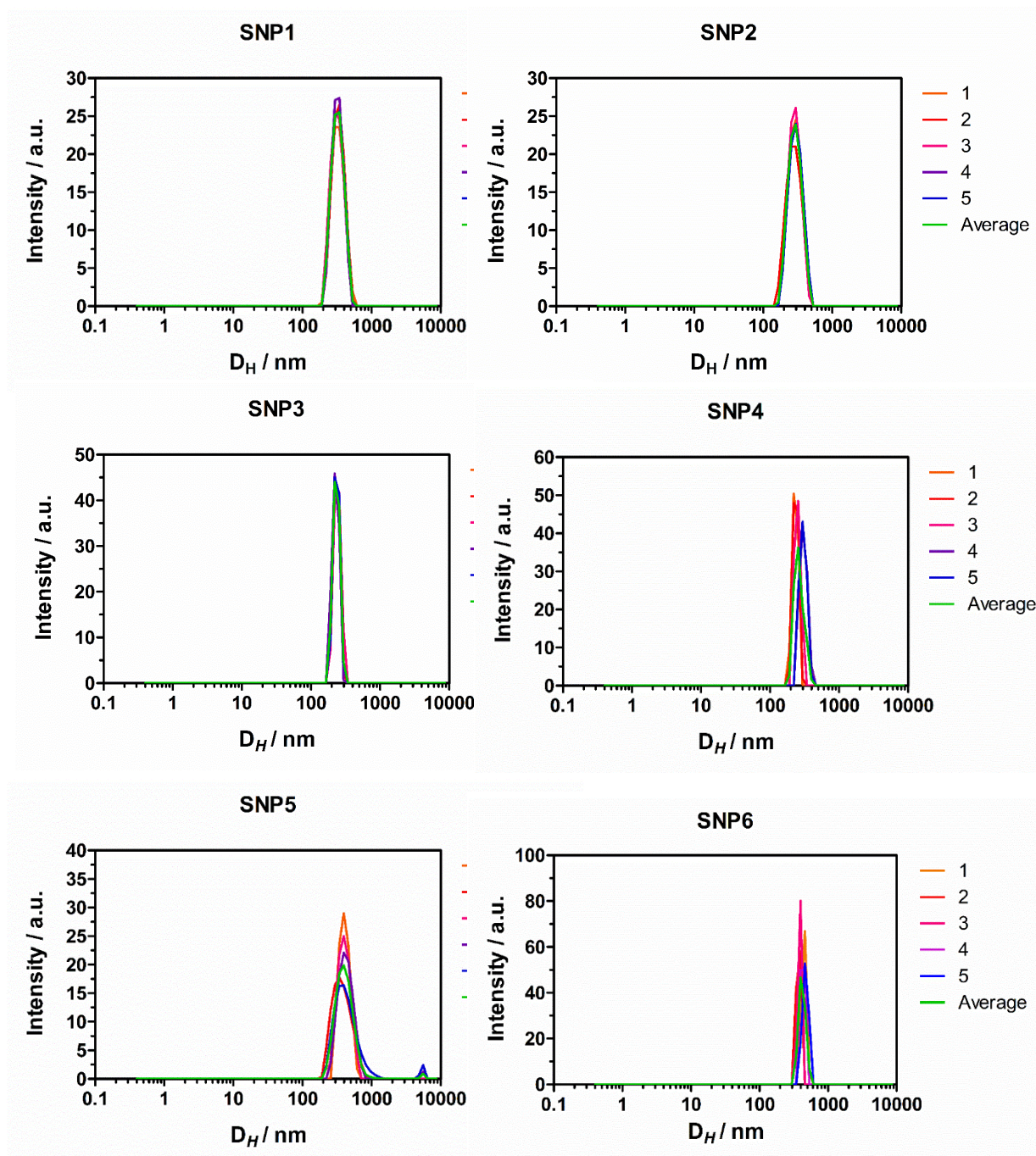


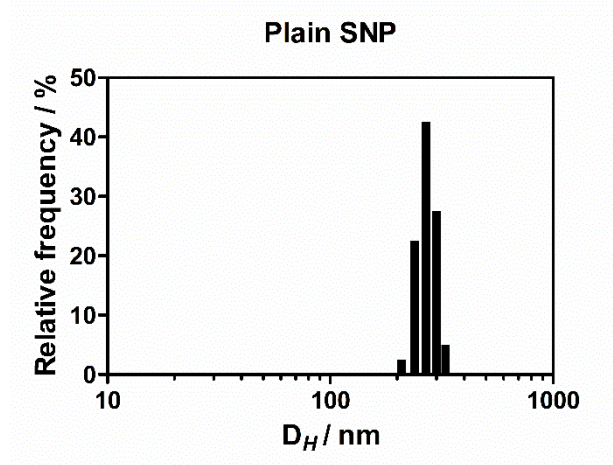
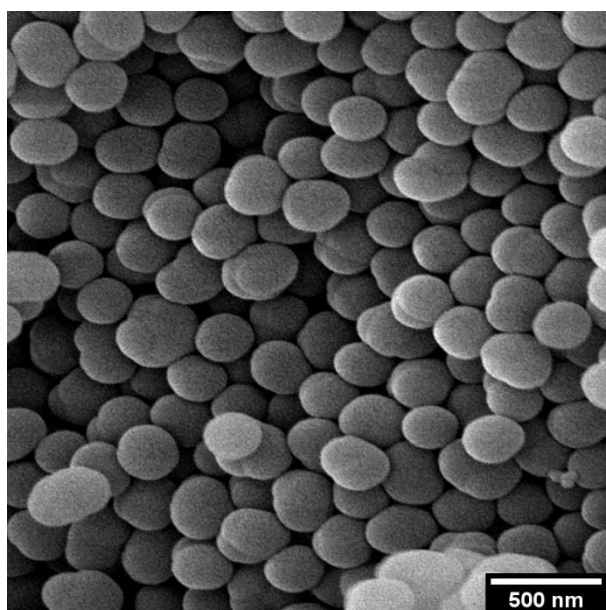
Figure S3. 3: DLS analysis of **SNP1-6** in H₂O, showing their size distribution by intensity graph.

3.5.1.2. Investigation of drug addition and temperature of CPC loaded SNPs

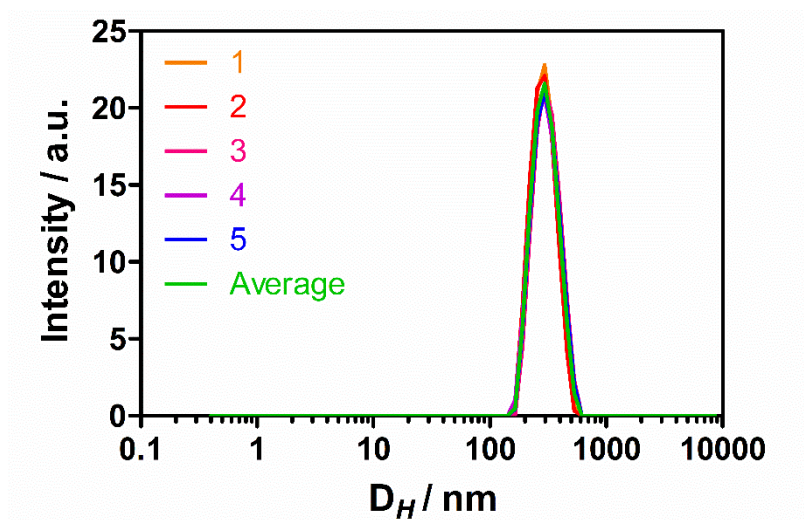
Sample	Temperature of Reaction / °C	Molar Equivalence				
		TEOS	H ₂ O	CPC	NH ₄ OH	EtOH
SNP7	25	1	23	1.16 x 10 ⁻¹	154	39.8
SNP8	25	1	23	1.16 x 10 ⁻¹	154	39.8
SNP6	25	1	23	1.16 x 10 ⁻¹	154	39.8
SNP9	25	1	23	1.16 x 10 ⁻¹	154	39.8
SNP10	80	1	23	1.16 x 10 ⁻¹	154	39.8
SNP11	80	1	23	1.16 x 10 ⁻¹	154	39.8
SNP12	80	1	23	1.16 x 10 ⁻¹	154	39.8
SNP13	80	1	23	1.16 x 10 ⁻¹	154	39.8

Figure S3. 4: The ratio of starting materials used in the reaction for SNP6-13, the table highlights molar equivalences of reaction mixture testes at 25 and 80 °C.

A



B



C

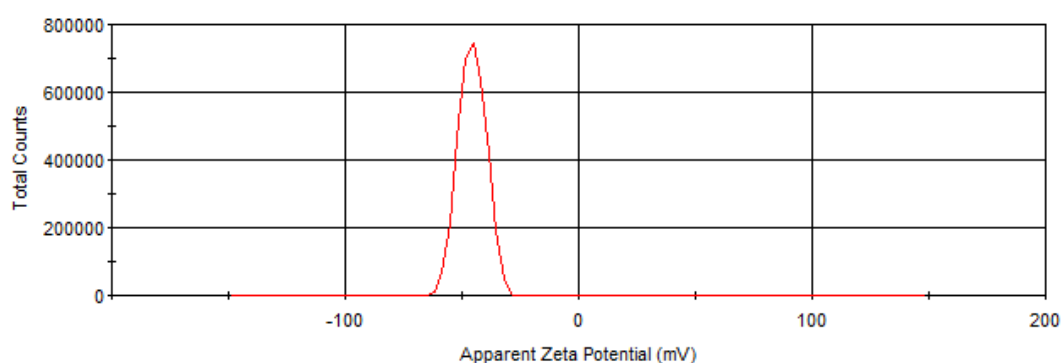


Figure S3. 5: Plain SNP **A)** SEM image and size distribution graph. Magnification 25,000x, 20.0 kV electron beam and analysed using ImageJ (Version 2.1.0). **B)** DLS analysis in H₂O, showing size distribution by intensity graph: 238 ± 61 nm, PDI: 0.308 and **C)** zeta potential charge: -46 ± 6 mV.

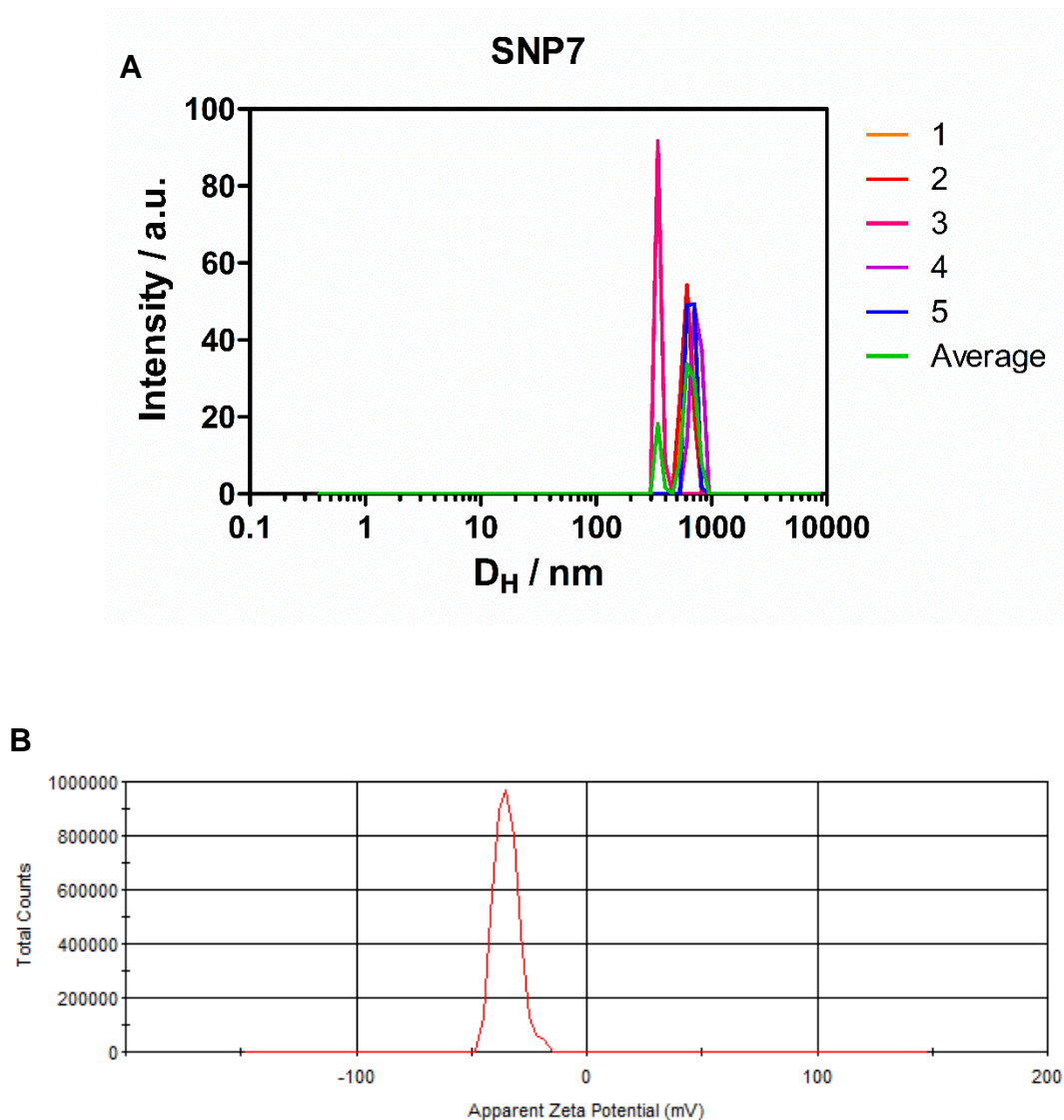


Figure S3. 6: DLS analysis of **SNP7** in H_2O , showing size distribution by intensity graph: 308 ± 42 nm, PDI: 0.811 and zeta potential charge: -36 ± 7 mV.

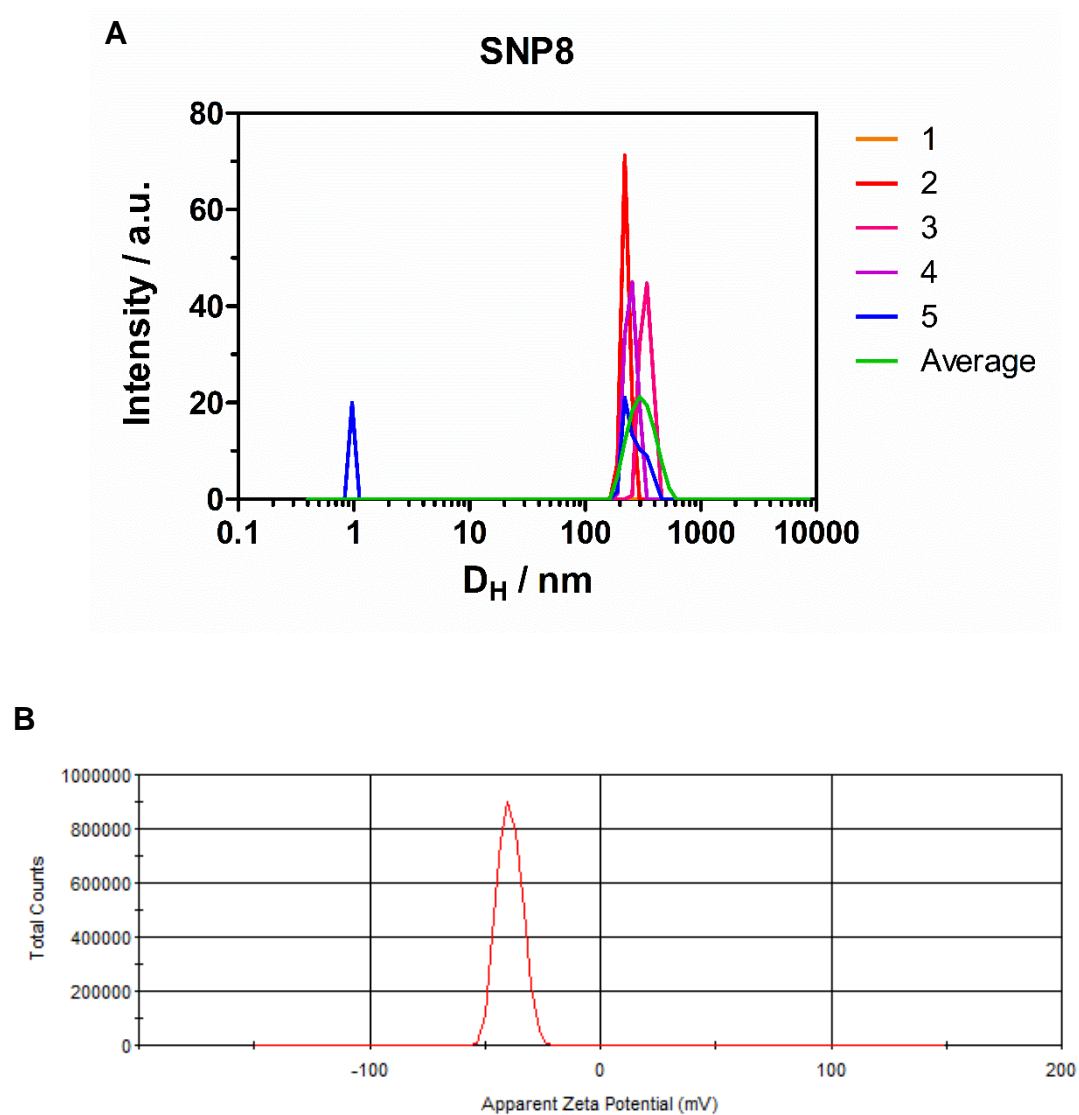


Figure S3. 7: DLS analysis of **SNP8** in H₂O, showing size distribution by intensity graph: 167 ± 39 nm, PDI 0.277 and zeta potential charge: -39 ± 5 mV.

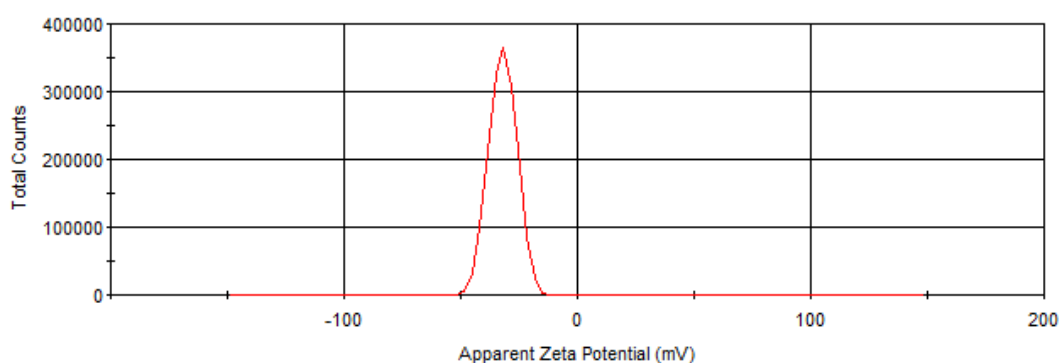
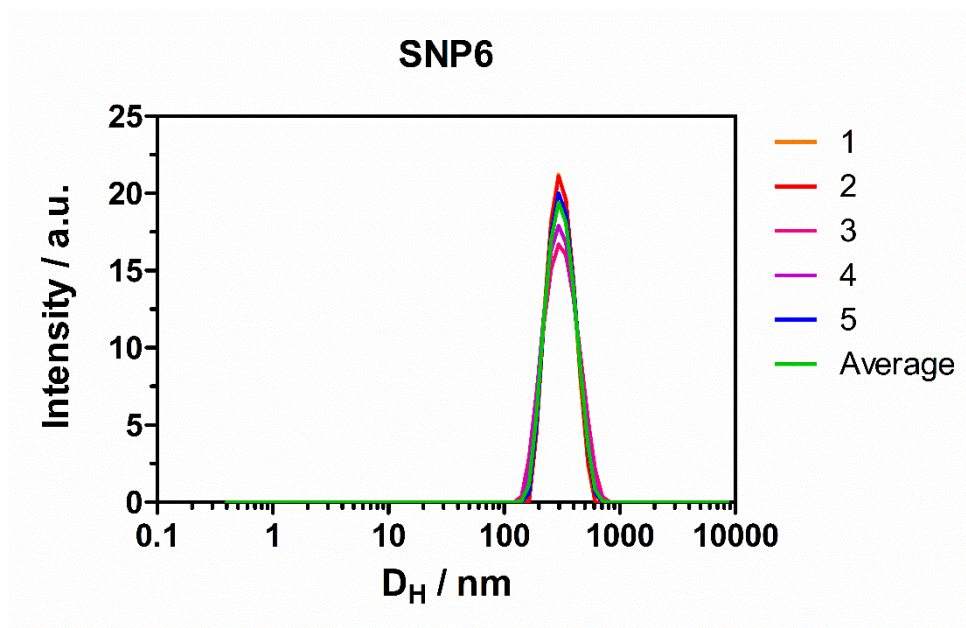


Figure S3. 8: DLS analysis of **SNP6** in H₂O, showing size distribution by intensity graph: 420 ± 49 nm PDI: 0.233 and zeta potential charge: -32 ± 6 mV.

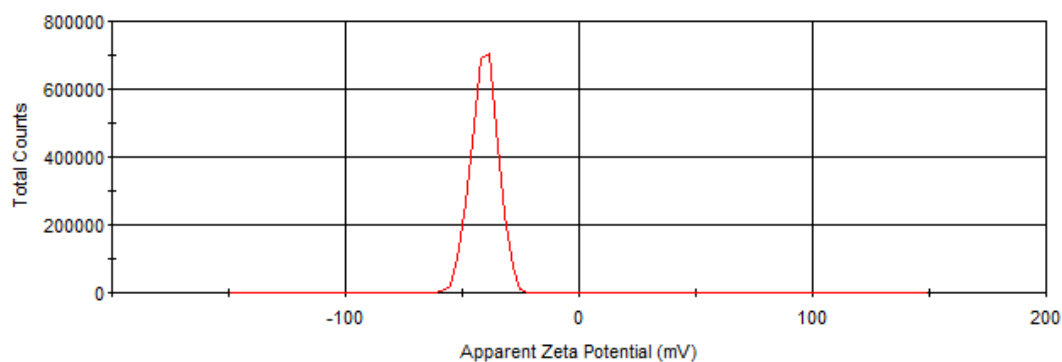
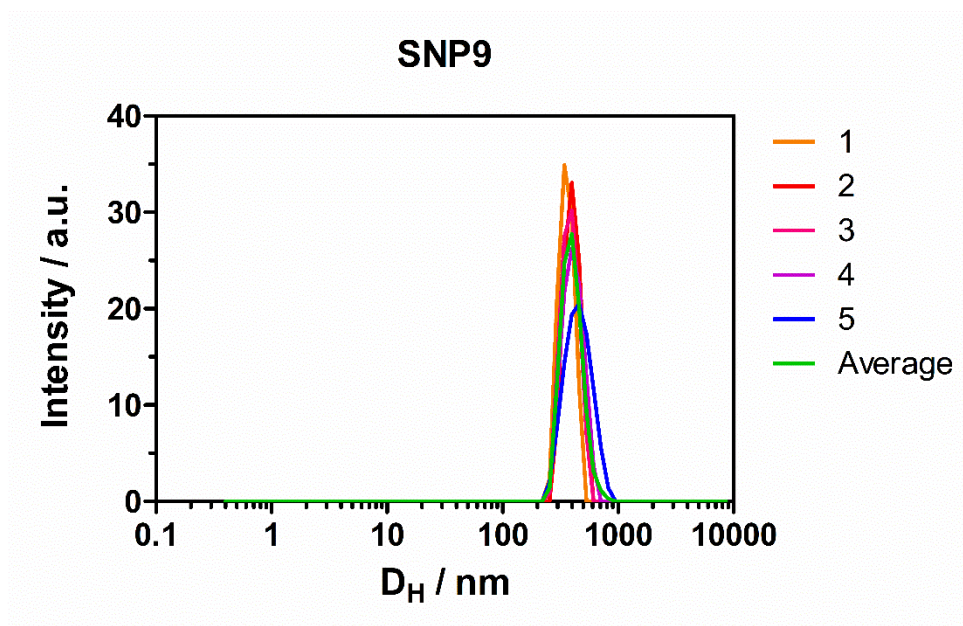


Figure S3. 9: DLS analysis of **SNP9** in H₂O, showing size distribution by intensity graph: 341 ± 60 nm and Zeta potential charge: -40 ± 6 mV.

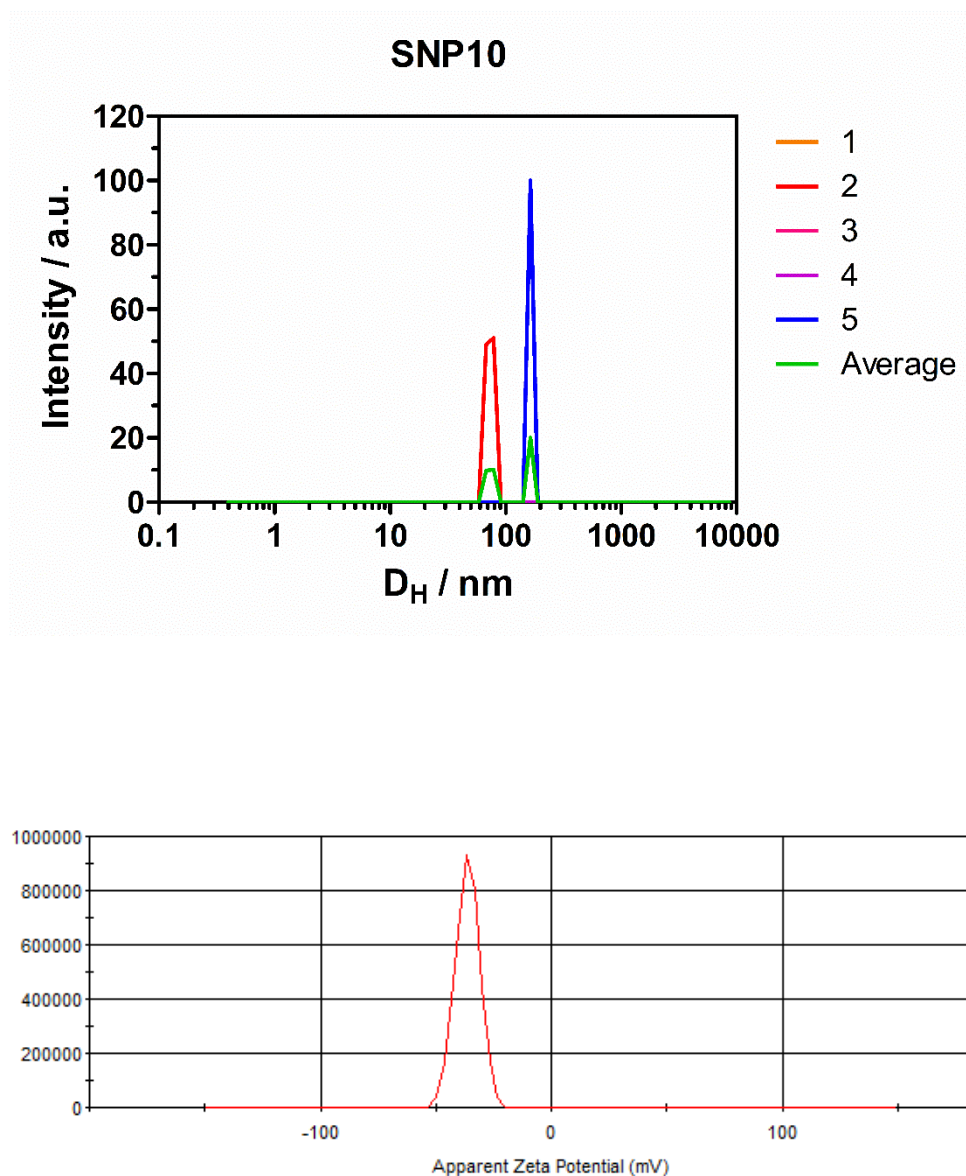


Figure S3. 10: DLS analysis of **SNP10** in H₂O, showing size distribution by intensity graph: 376 ± 32 nm (26 %), PDI: 1.000 and zeta potential charge: -36 ± 5 mV.

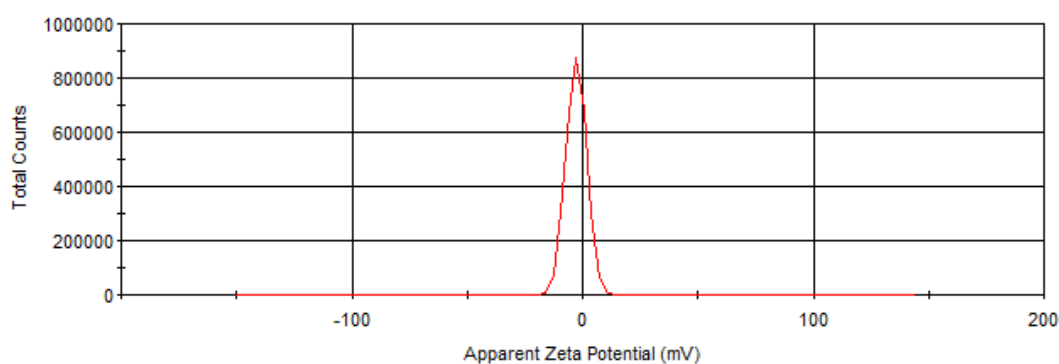
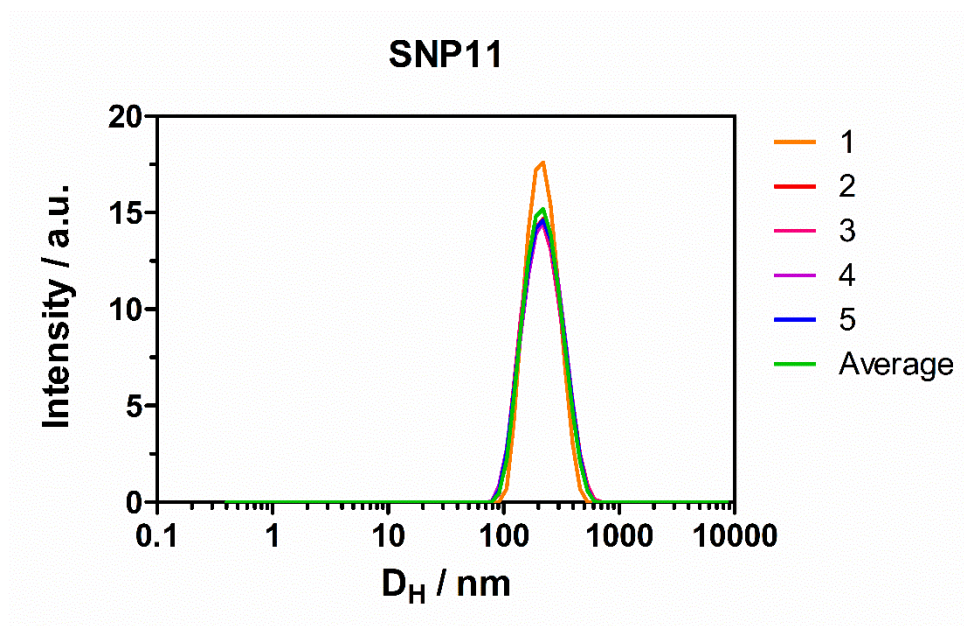


Figure S3. 11: DLS analysis of **SNP11** in H₂O, showing size distribution by intensity graph: 231 ± 83 nm, PDI: 0.120 and zeta potential charge: -3 ± 4 mV.

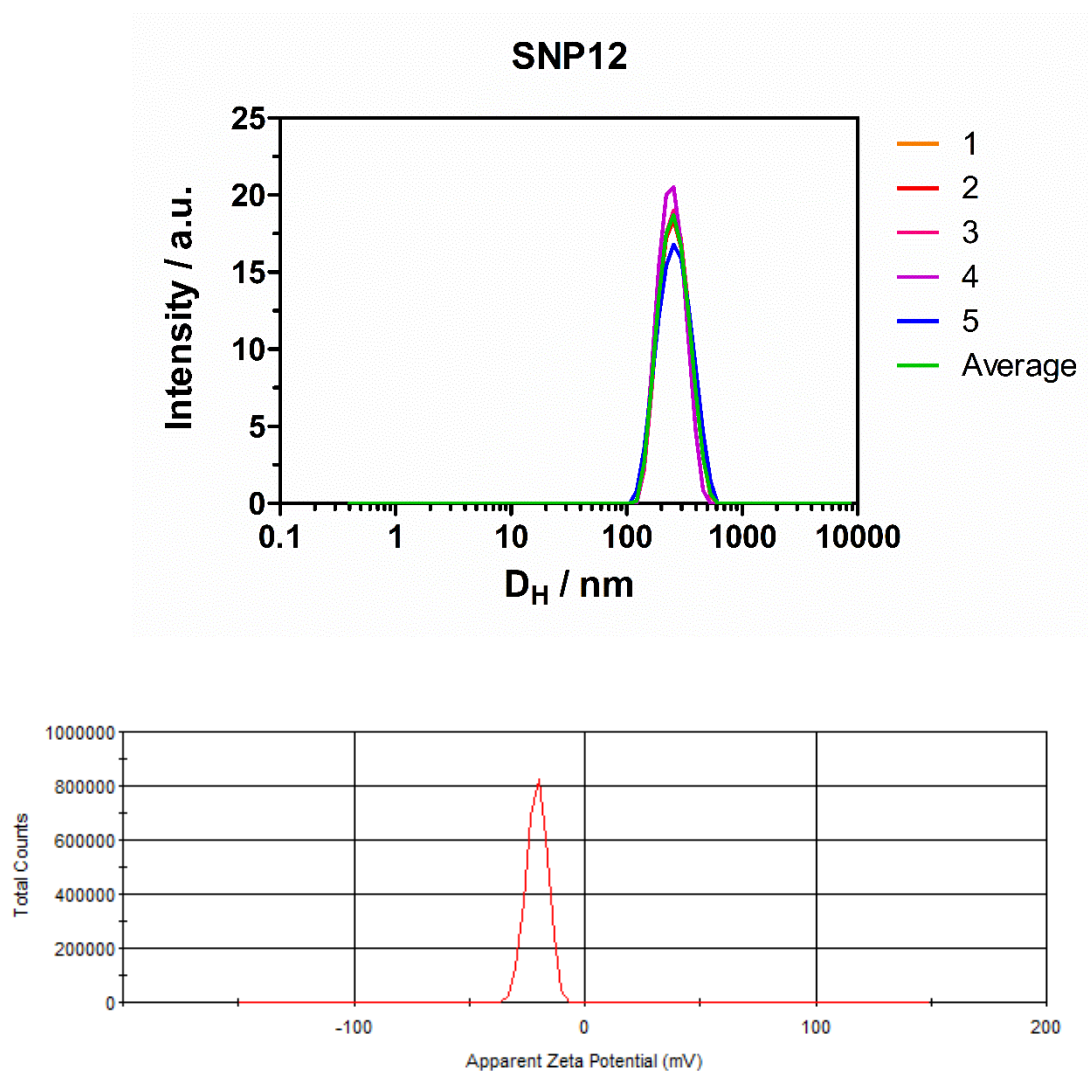


Figure S3. 12: DLS analysis of **SNP12** in H₂O, showing size distribution by intensity graph: 266 ± 77 nm, PDI: 0.123 and zeta potential charge: -21 ± 5 mV.

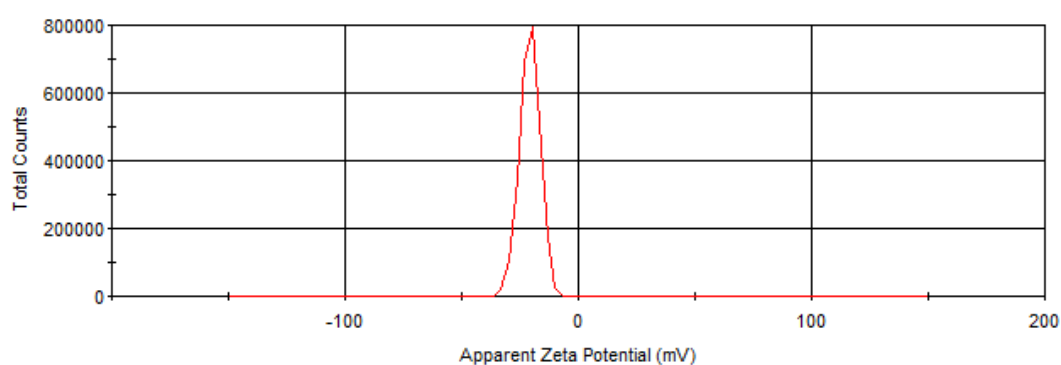
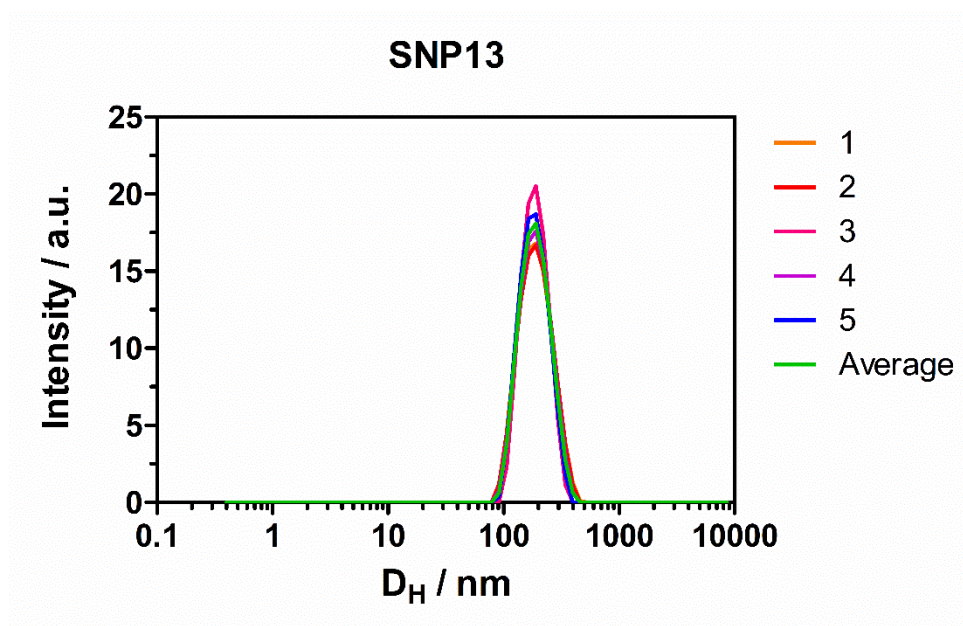


Figure S3. 13: DLS analysis of **SNP13** in H₂O, showing size distribution by intensity graph: 194 ± 59 nm, PDI: 0.076 and zeta potential charge: -21 ± 4 mV.

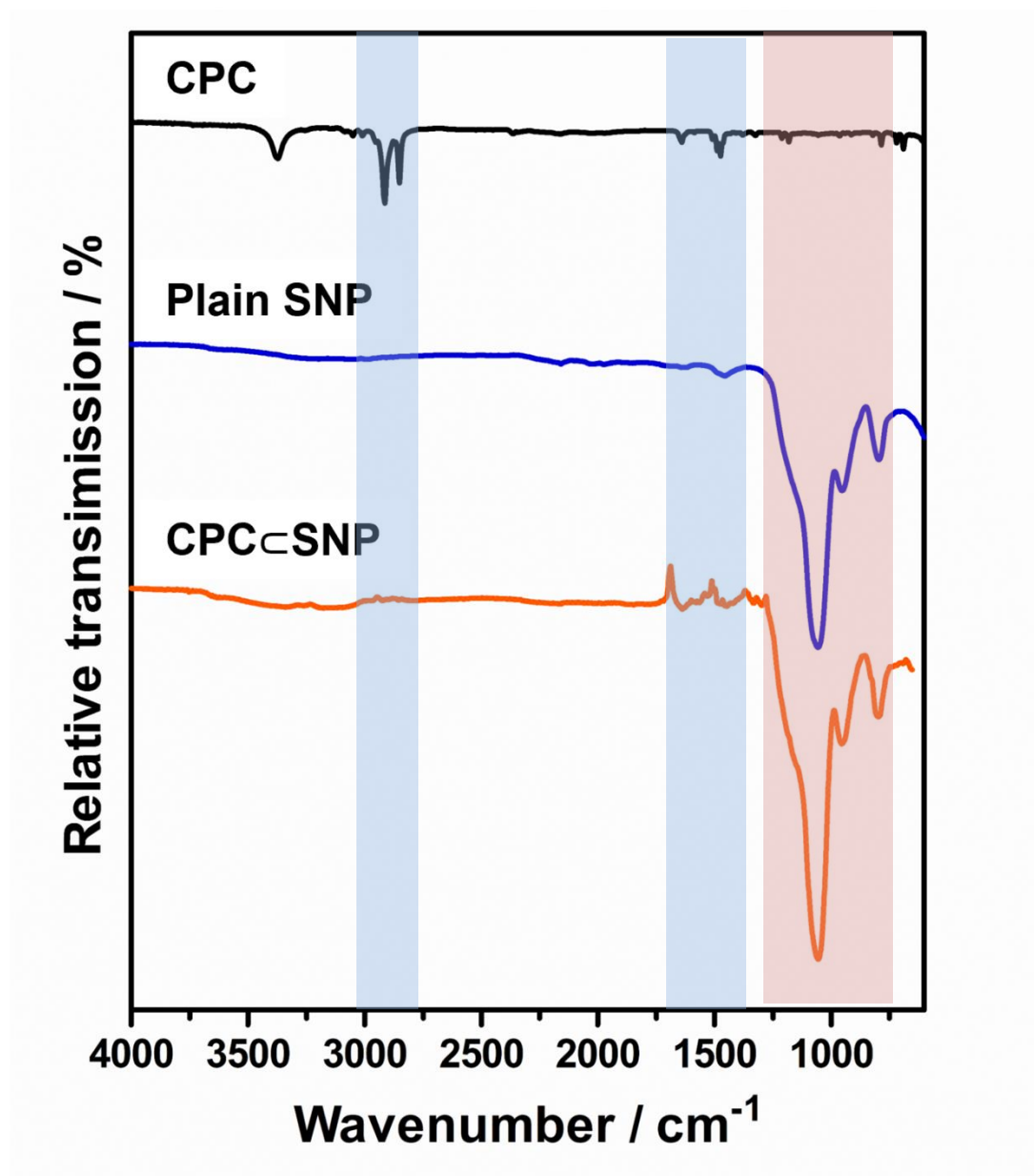


Figure S3. 14: Structural analysis with FT-IR spectroscopy of CPC, plain SNP and CPC@SNP post synthesis. Blue indicates peaks found in CPC And red indicates silica formation.

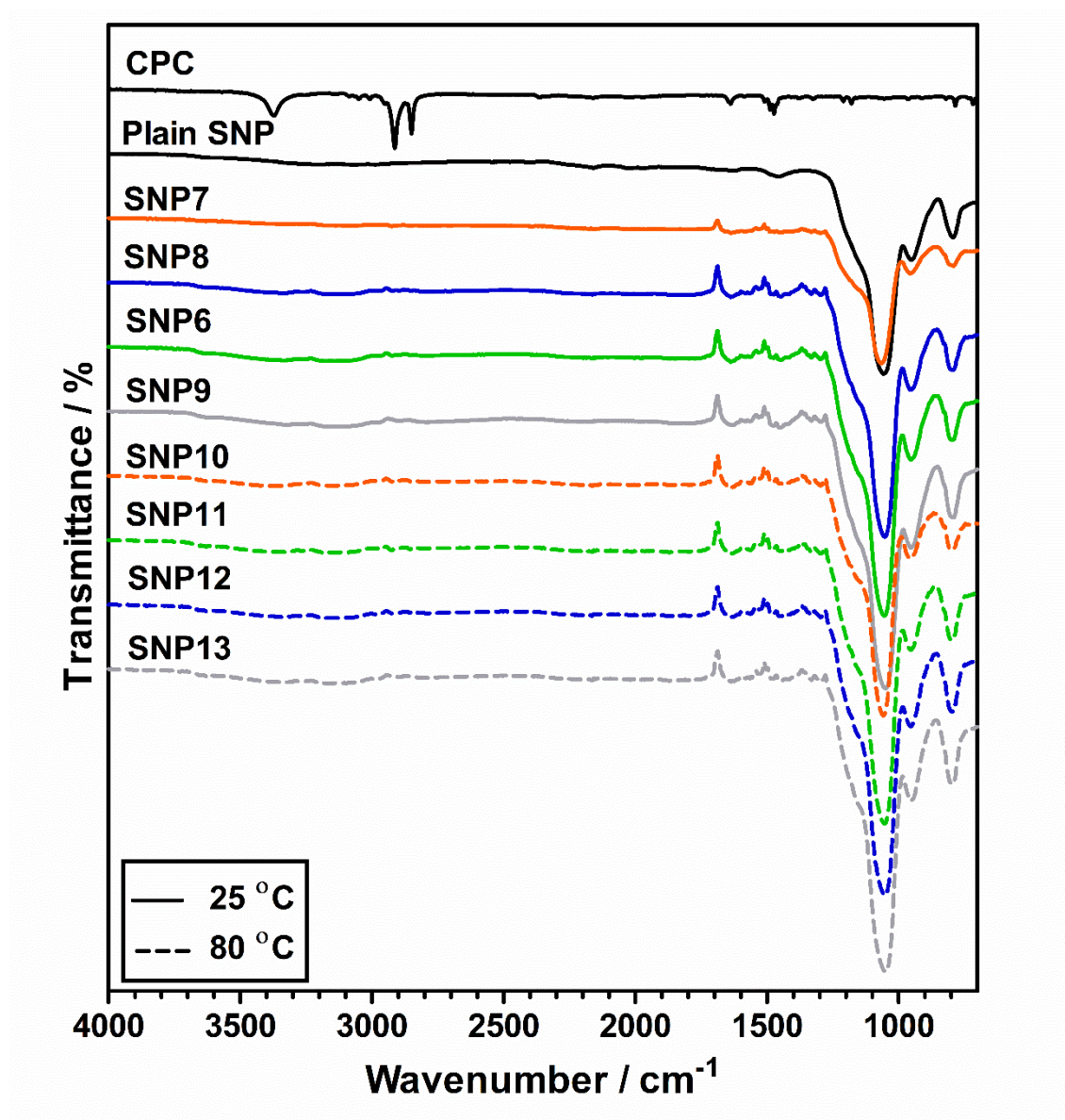


Figure S3. 15: Structural analysis with FT-IR spectroscopy of **CPC**, **plain SNP** and **CPC loaded SNPs** post synthesis (**SNP7-13**).

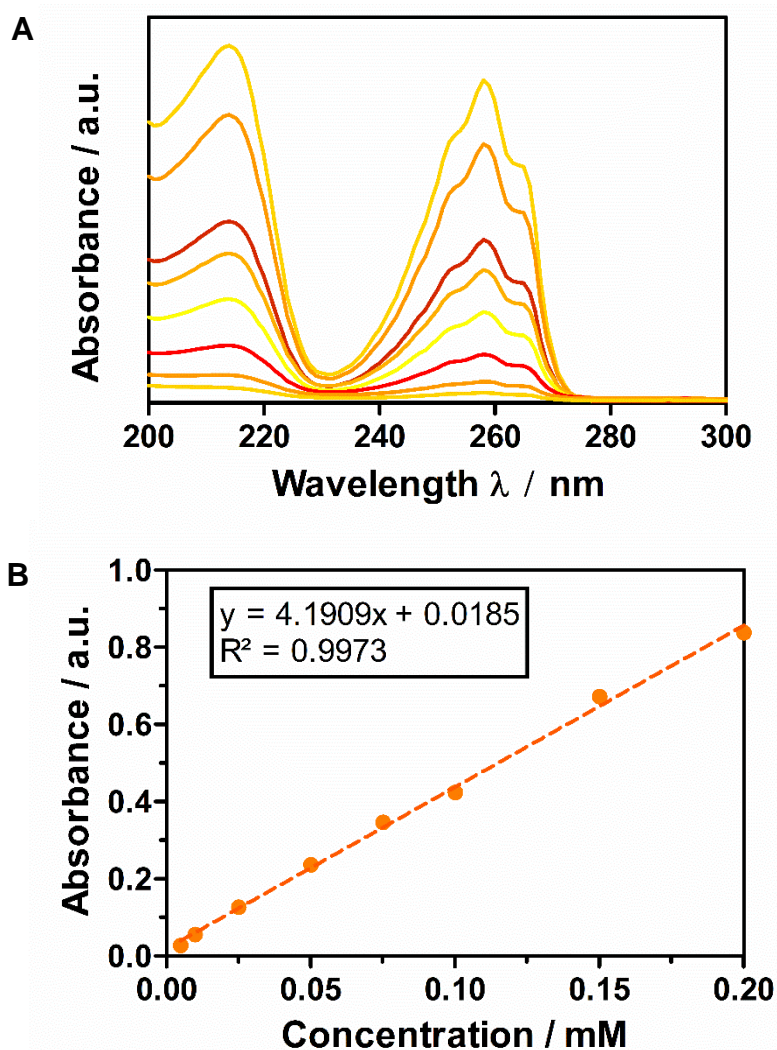


Figure S3. 16: **A)** UV-Vis absorption spectra of CPC in H₂O at different concentrations (0.005, 0.01, 0.025, 0.05, 0.075, 0.1, 0.15 and 0.2 mM). **B)** Calibration curve of CPC to calculate the absorption coefficient (ϵ) using the Beer Lamberts Law. Concentration plotted against absorbance at $\lambda_{\text{max}}=260$ nm to determine $\epsilon = 4191 \pm 5 \text{ M}^{-1}\text{cm}^{-1}$ (mean and standard deviation, $n=3$).

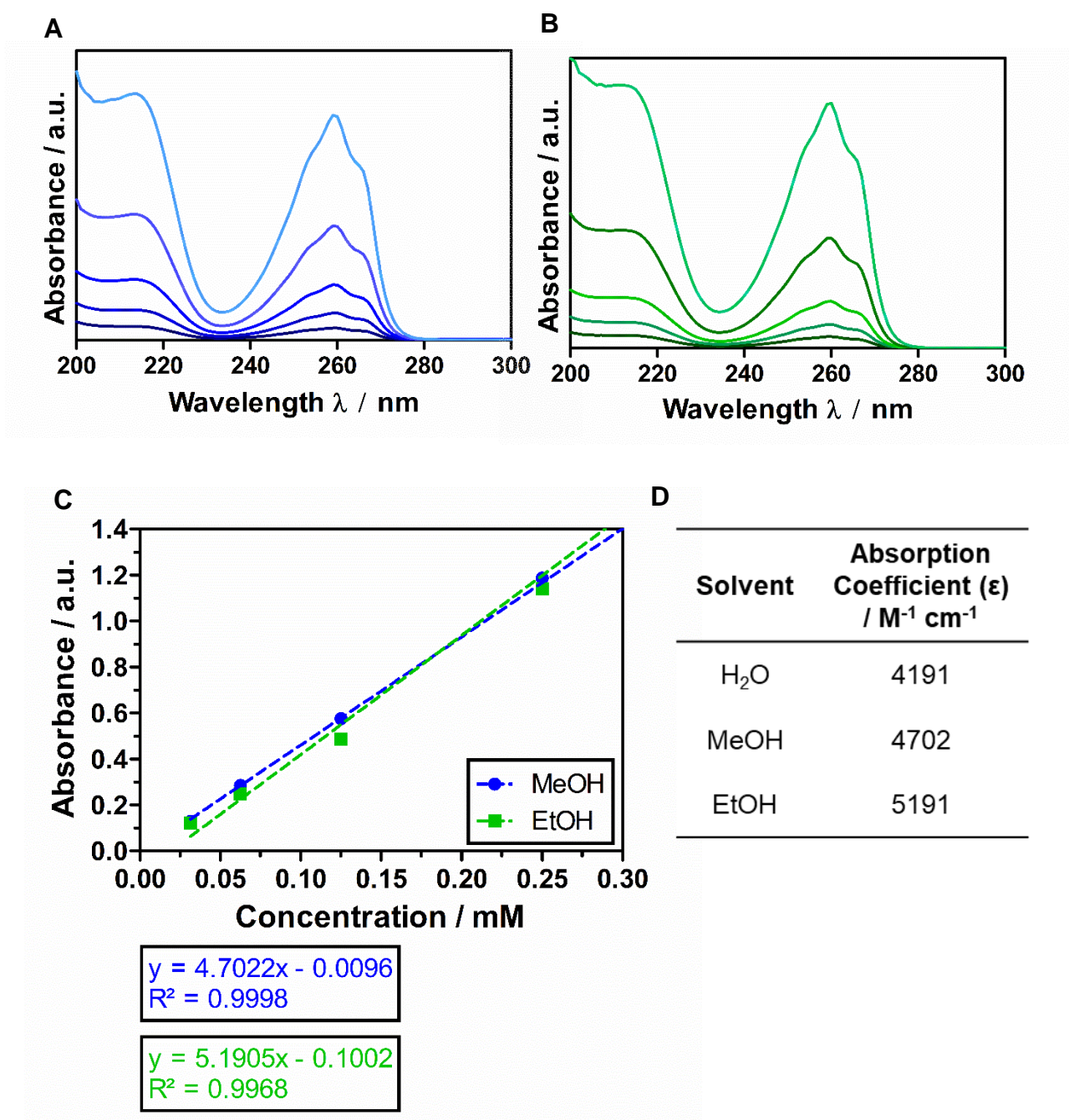
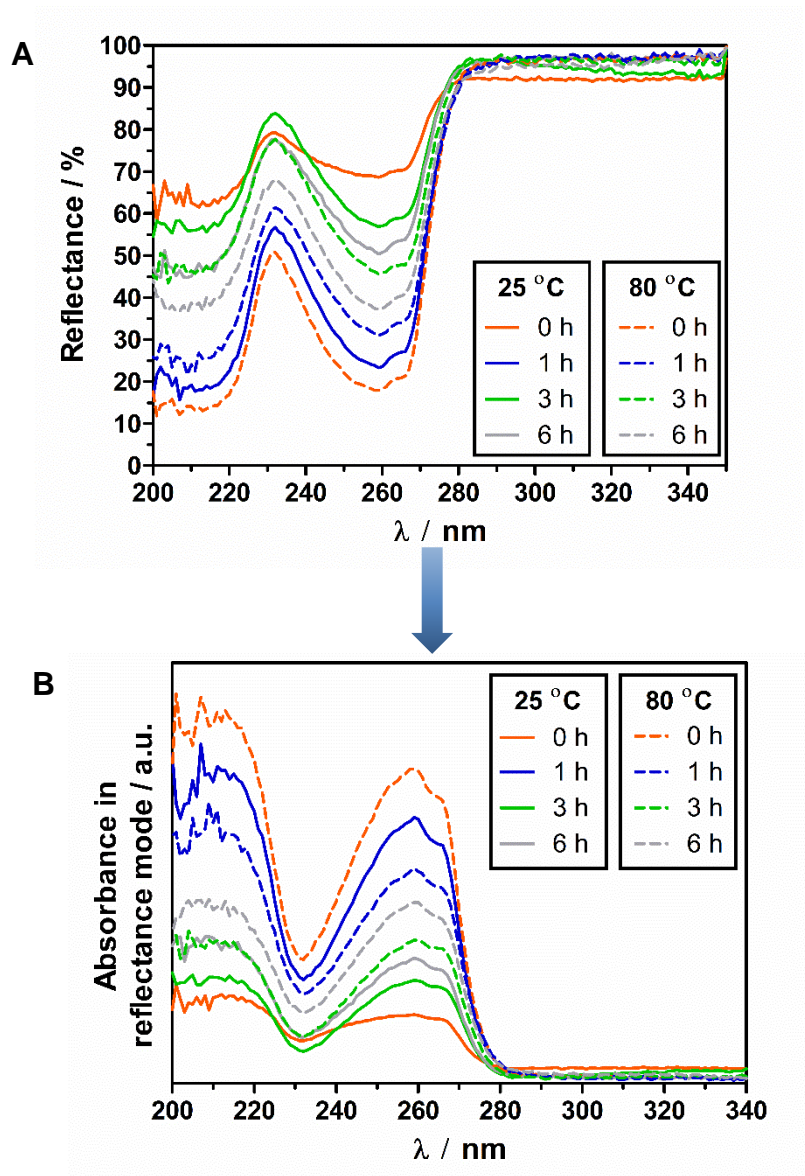


Figure S3. 17: UV-Vis absorption spectra of CPC in **A)** MeOH and **B)** EtOH (0.03, 0.06, 0.13, 0.25, 0.5 mM). **C)** Calibration curve of CPC to calculate the absorption coefficient (ϵ) using the Beer Lamberts Law. Concentration plotted against absorbance at $\lambda_{max}=260$ nm **D)** Table of determined ϵ values.



$$[1] \quad \text{Transmission} (t) = \frac{I_t}{I_0}$$

$$[2] \quad \text{Absorbance} (A) = \epsilon Cl \quad I_t = I_0 \times 10^{-\epsilon Cl}$$

Rearrangement of absorbance and transmission equations:

$$[3] \quad A = -\log(t) = -\log \frac{I_t}{I_0}$$

$$A = -\log I_t - \log I_0 = \log I_0 - \log I_t = \log(100) - \log I_t$$

Absorbance can be expressed as:

$$[4] \quad A = 2 - \log I$$

Figure S3. 18: Solid-state UV-Vis **A)** DRA spectra for **SNP6-13** presented as **B)** absorbance using the derived equation shown.

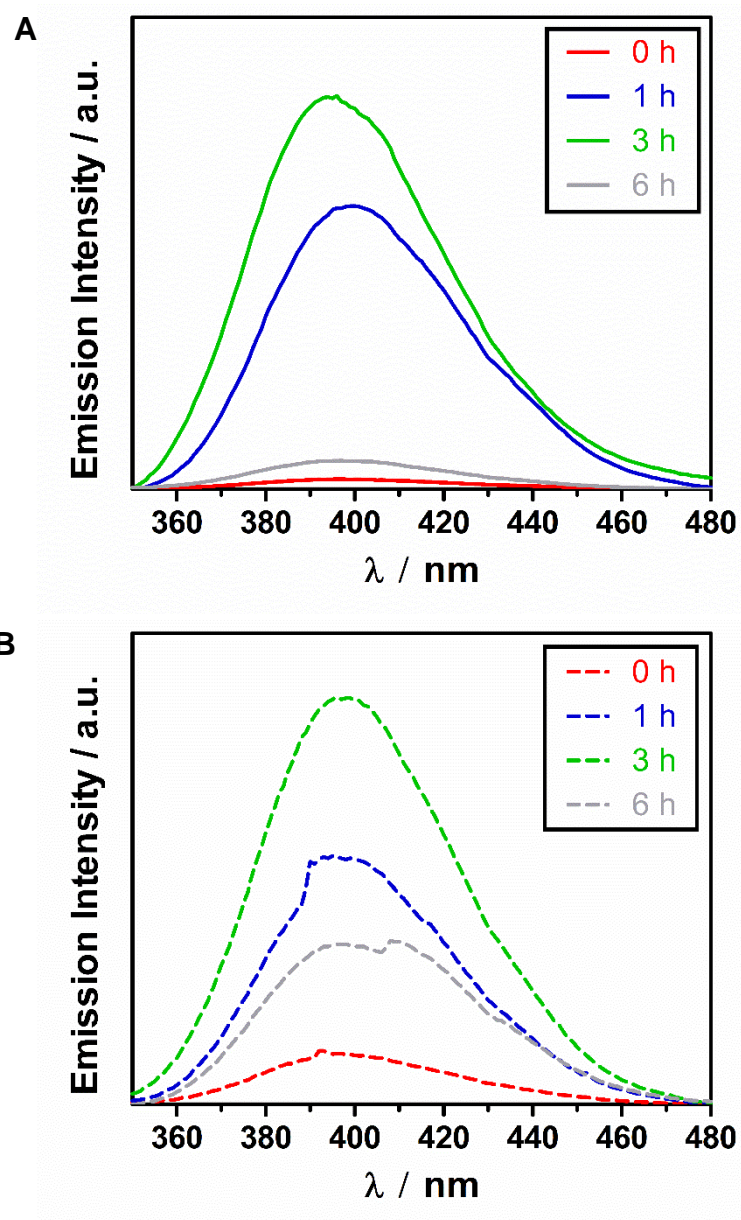
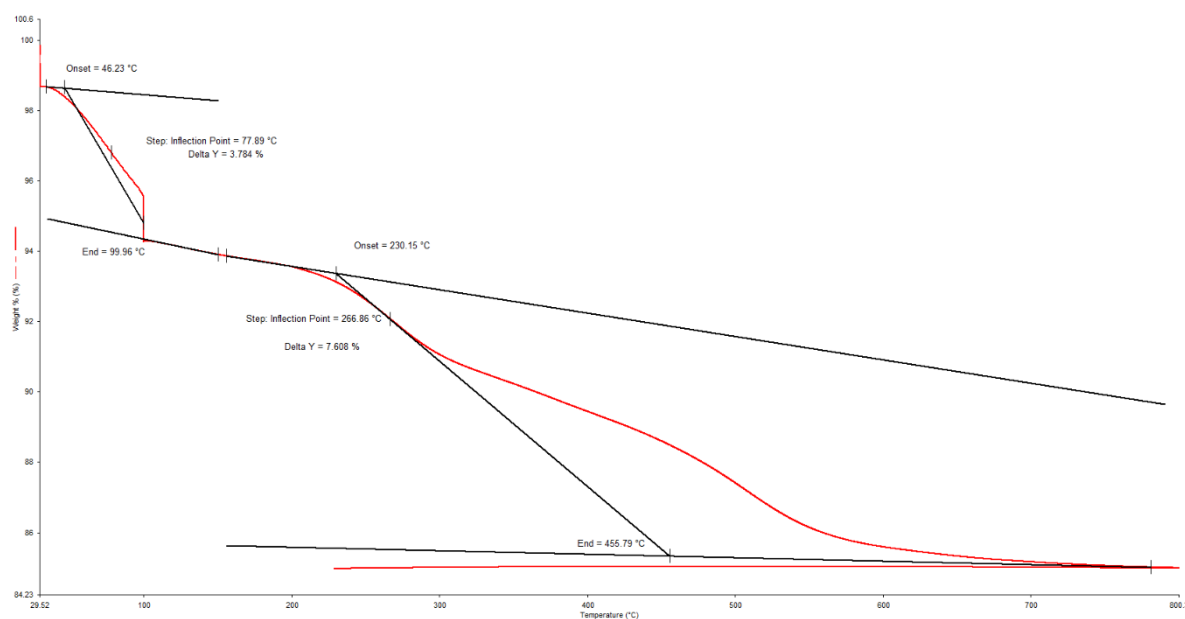
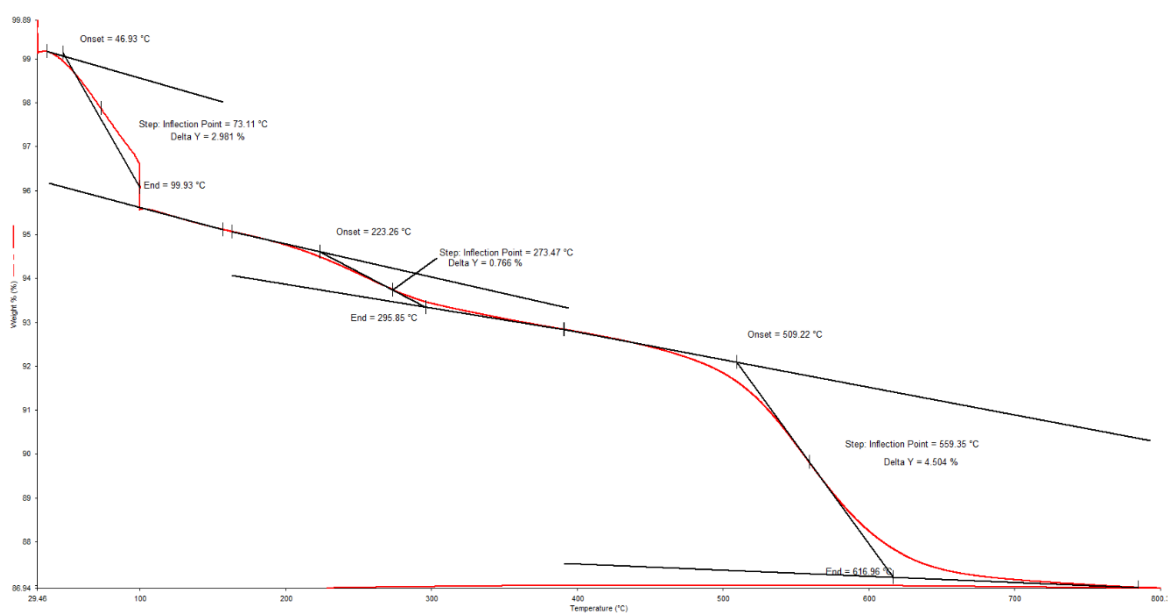


Figure S3. 19: Solid-state Emission spectra of **A) SNP6-9** and **B) SNP10-13**. λ_{ex} at 260 nm, λ_{em} = 395-398 nm, λ_{em} range collected from 350-480 nm, slit width 8 nm.. Corrected for PMT response.

3.6.1.3. Drug loading content

Sample	Initial CPC / mg	Included CPC / mg	Total CPC loaded SNPs / mg	Loading efficiency / %	TGA determined drug loading / %	Absolute drug content / $\mu\text{g mg}^{-1}$	
25 °C	0 h	466.45	302	717	65	7.9	79
	1 h	466.48	303	544	65	8.8	88
	3 h	466.29	386	603	83	8.9	89
	6 h	466.45	115	687	25	5.0	50
80 °C	0 h	465.93	123	775	26	8.5	85
	1 h	466.48	152	524	33	8.2	82
	3 h	466.29	388	614	83	8.0	80
	6 h	465.93	406	569	87	6.7	67

Figure S3. 20: Drug entrapment of CPC determined from UV-Vis spectroscopy, from initial and remaining CPC in solution. Absolute drug loading derived from TGA weight loss percentage of CPC and displayed as CPC in μg per drug loaded SNP in mg.



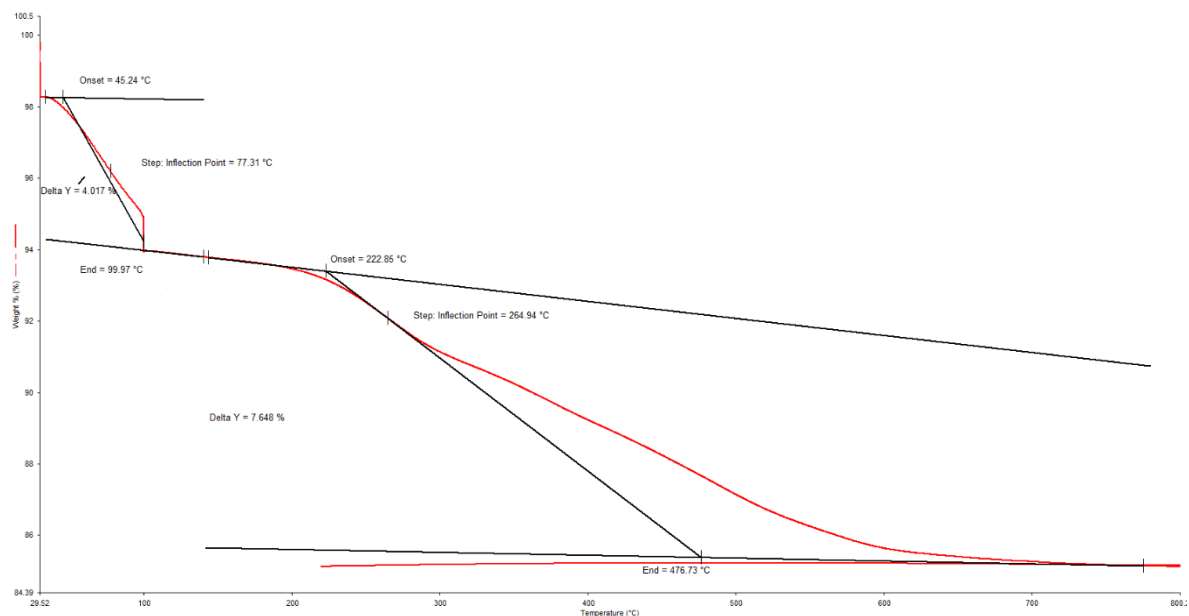


Figure S3. 23: TGA curve of **SNP6**, Showing the overall weigh loss with increasing temperature.

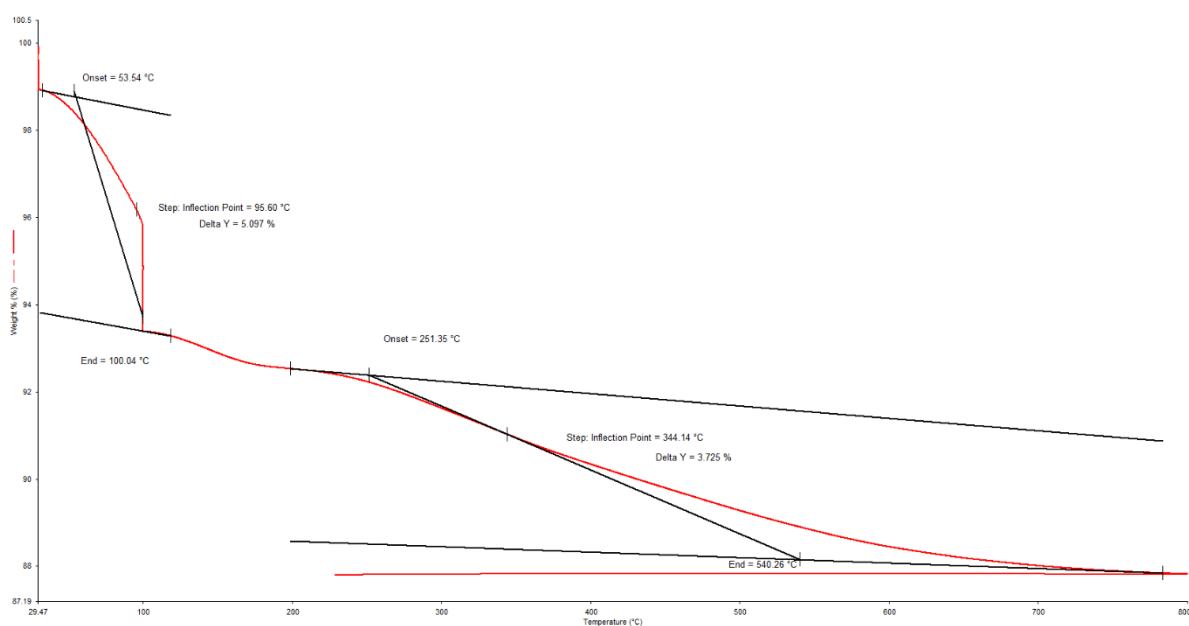


Figure S3. 24: TGA curve of **SNP9**, Showing the overall weigh loss with increasing temperature.

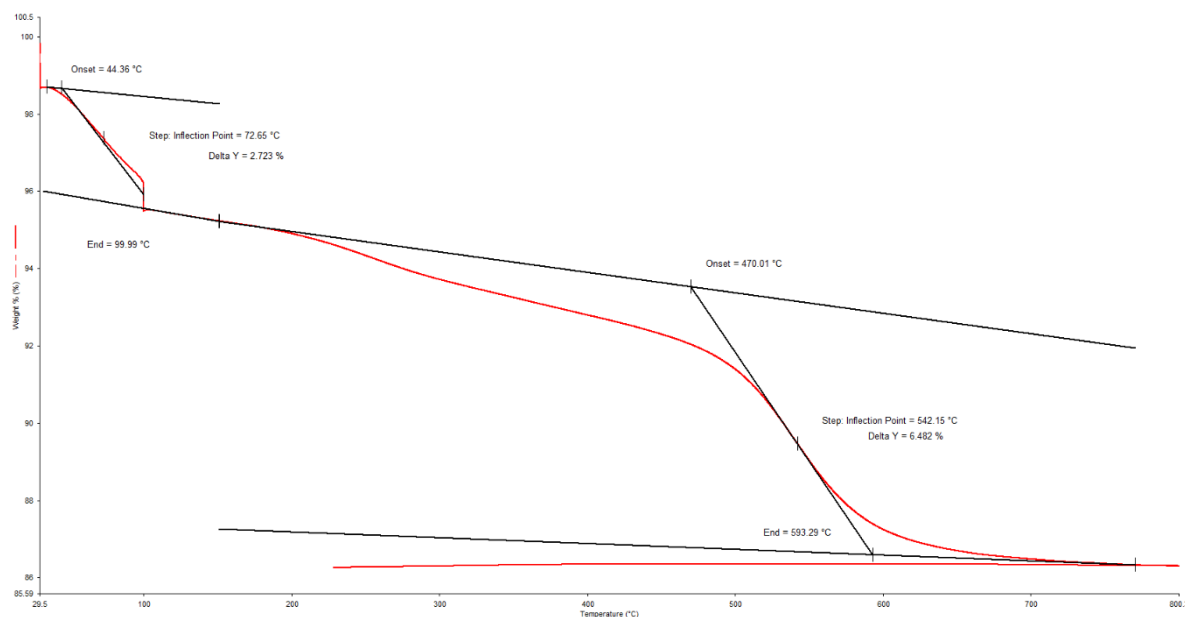


Figure S3. 25: TGA curve of **SNP10**, Showing the overall weigh loss with increasing temperature.

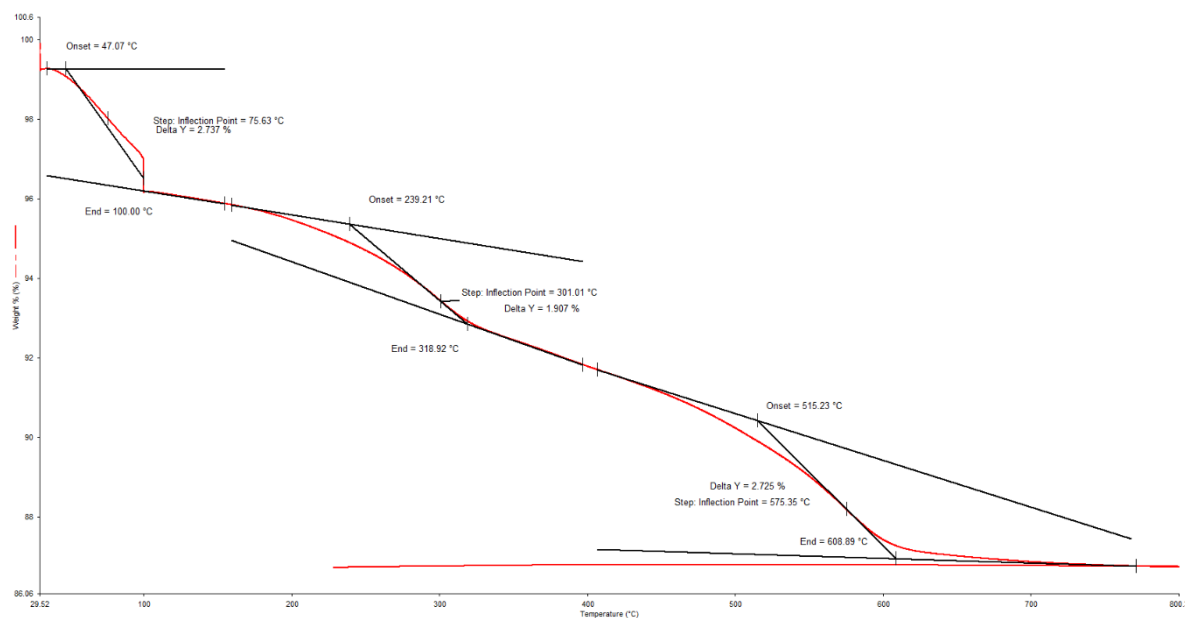


Figure S3. 26: TGA curve of **SNP11**, Showing the overall weigh loss with increasing temperature.

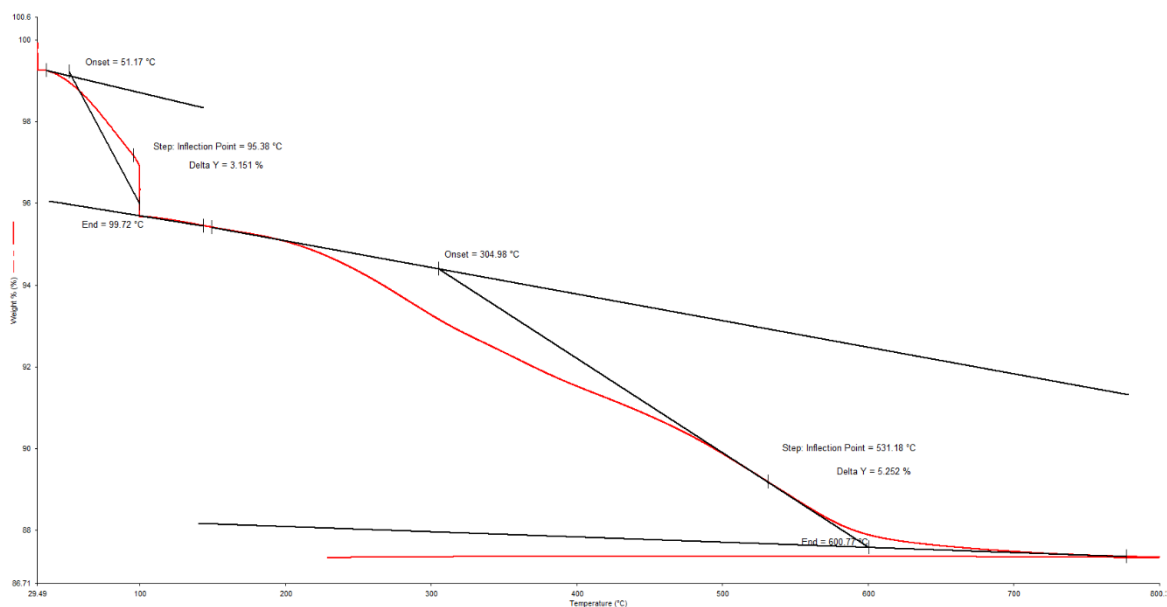


Figure S3. 27: TGA curve of **SNP12**, Showing the overall weigh loss with increasing temperature.

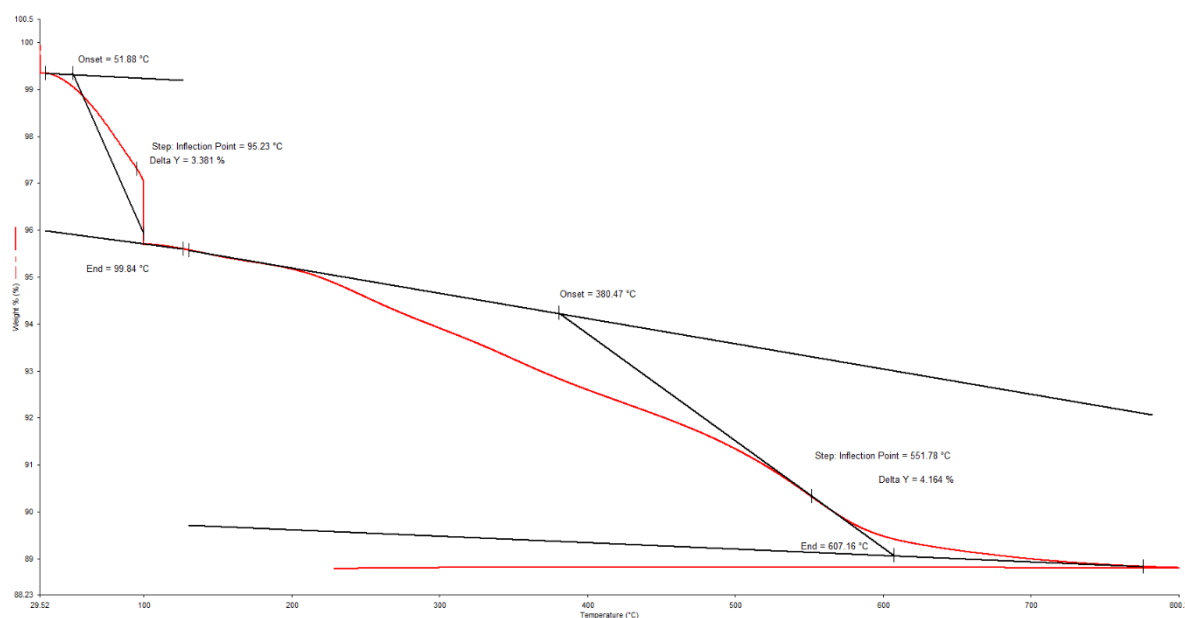


Figure S3. 28: TGA curve of **SNP13**, Showing the overall weigh loss with increasing temperature.

Step assignment				
Sample	H ₂ O		CPC	
	Region / °C	Weight loss / %	Region / °C	Weight loss / %
SNP7	<180	3.0	223 – 617	5.3
SNP8	<180	3.8	230 – 458	7.6
SNP6	<180	4.0	223 – 476	7.7
SNP9	<180	5.1	251 – 540	3.7
SNP10	<180	2.7	470 – 593	6.5
SNP11	<180	2.7	239 – 319	4.6
SNP12	<180	3.2	305 – 601	5.3
SNP13	<180	3.4	380 – 607	4.1

Figure S3. 29: Summary table of TGA data, showing the weight loss percentages of samples **SNP6-13** at different temperature ranges due to water and CPC loss.

3.5.2. Other CPC loaded SNPs

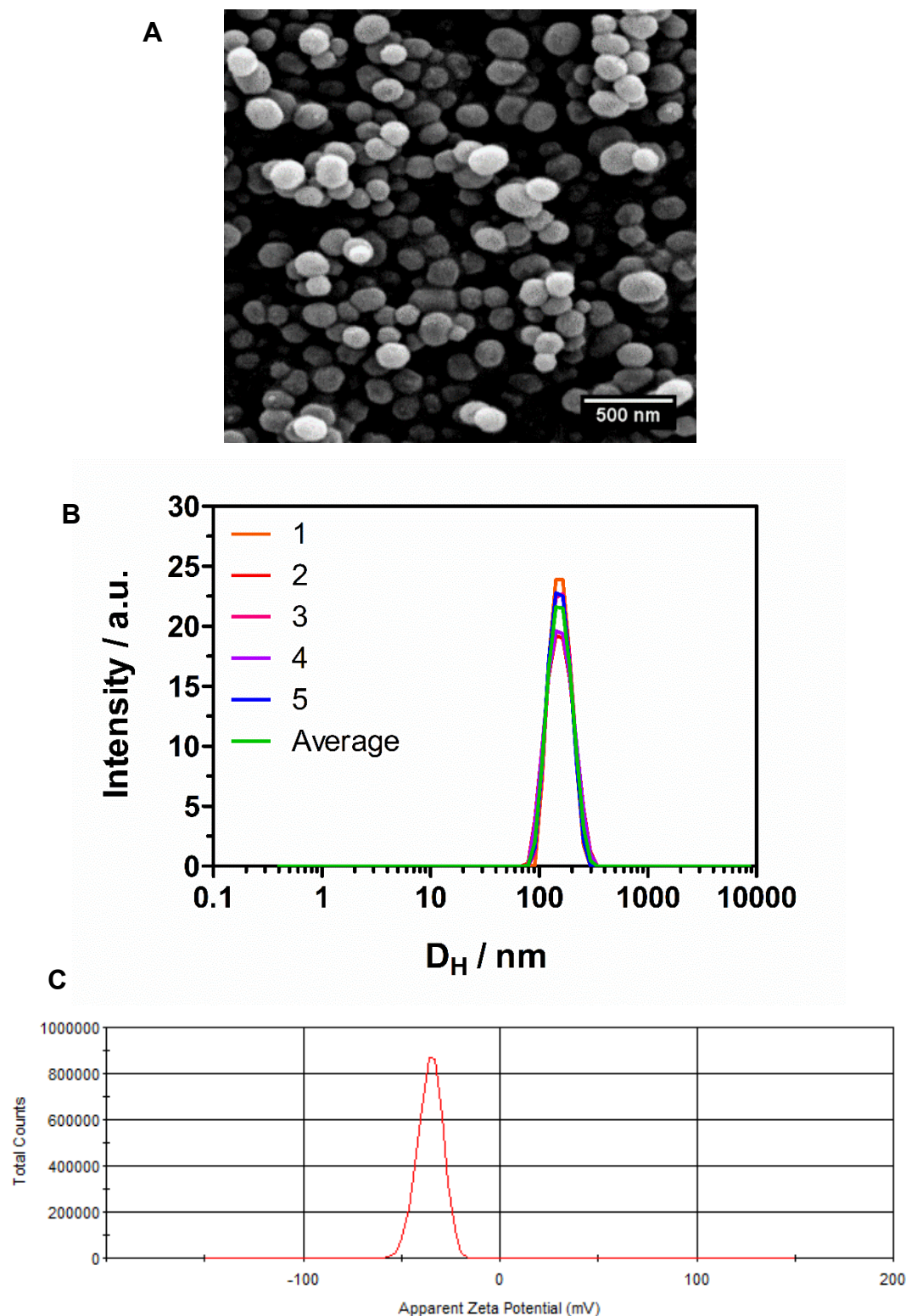


Figure S3. 30: Plain MSN: A) SEM imaging, magnification, electron beam 20 kV, analysed with ImageJ. **B)** DLS analysis showing size by intensity: 201 ± 28 nm and **C)** Zeta potential charge -35.4 ± 6.32 mV.

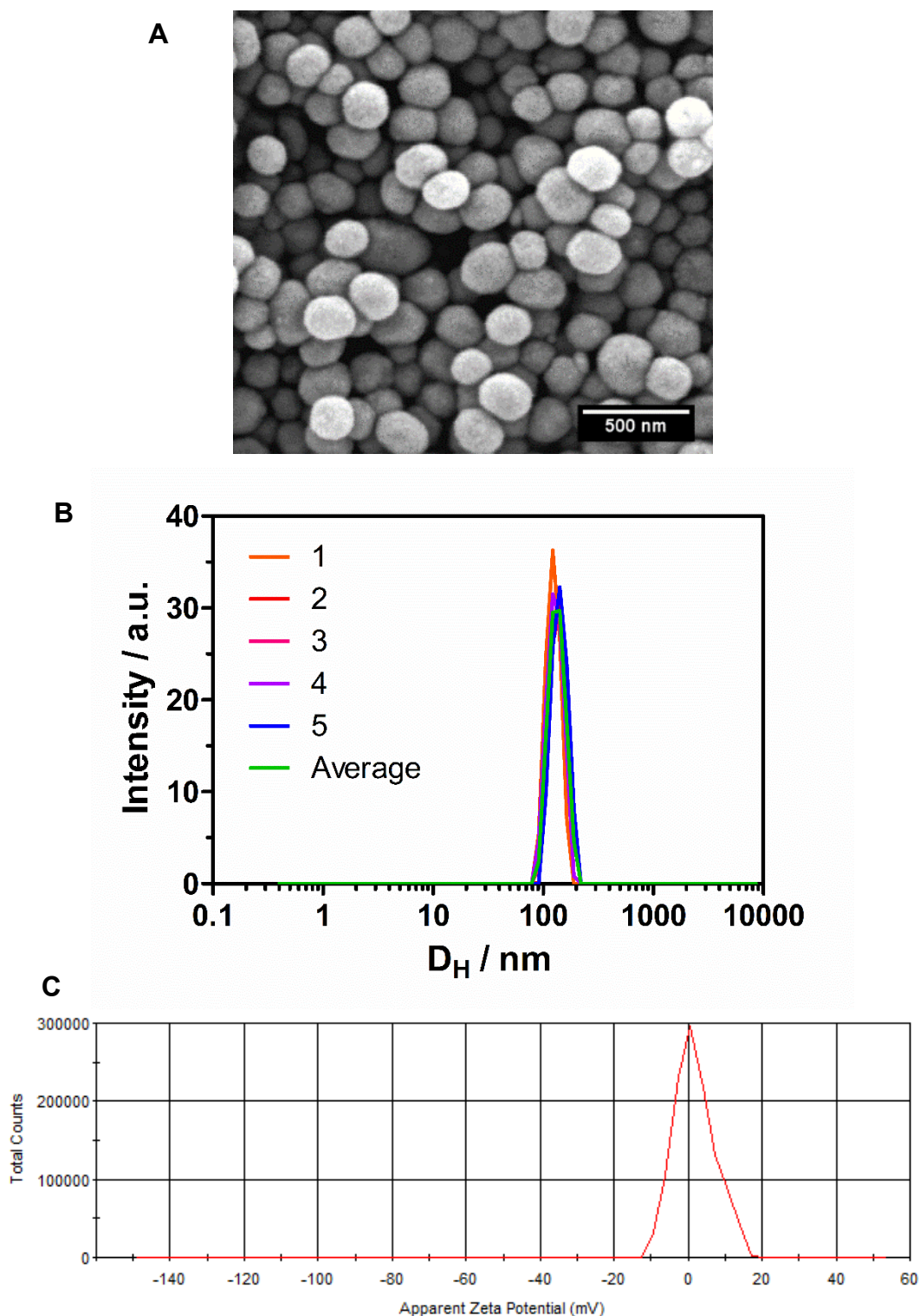


Figure S3. 31: Adsorbed CPC@MSN A) SEM imaging, magnification, electron beam 20 kV, analysed with ImageJ . **B)** DLS analysis showing size by intensity: 234 ± 24 nm and **C)** Zeta potential charge 2.03 ± 10.09 mV.

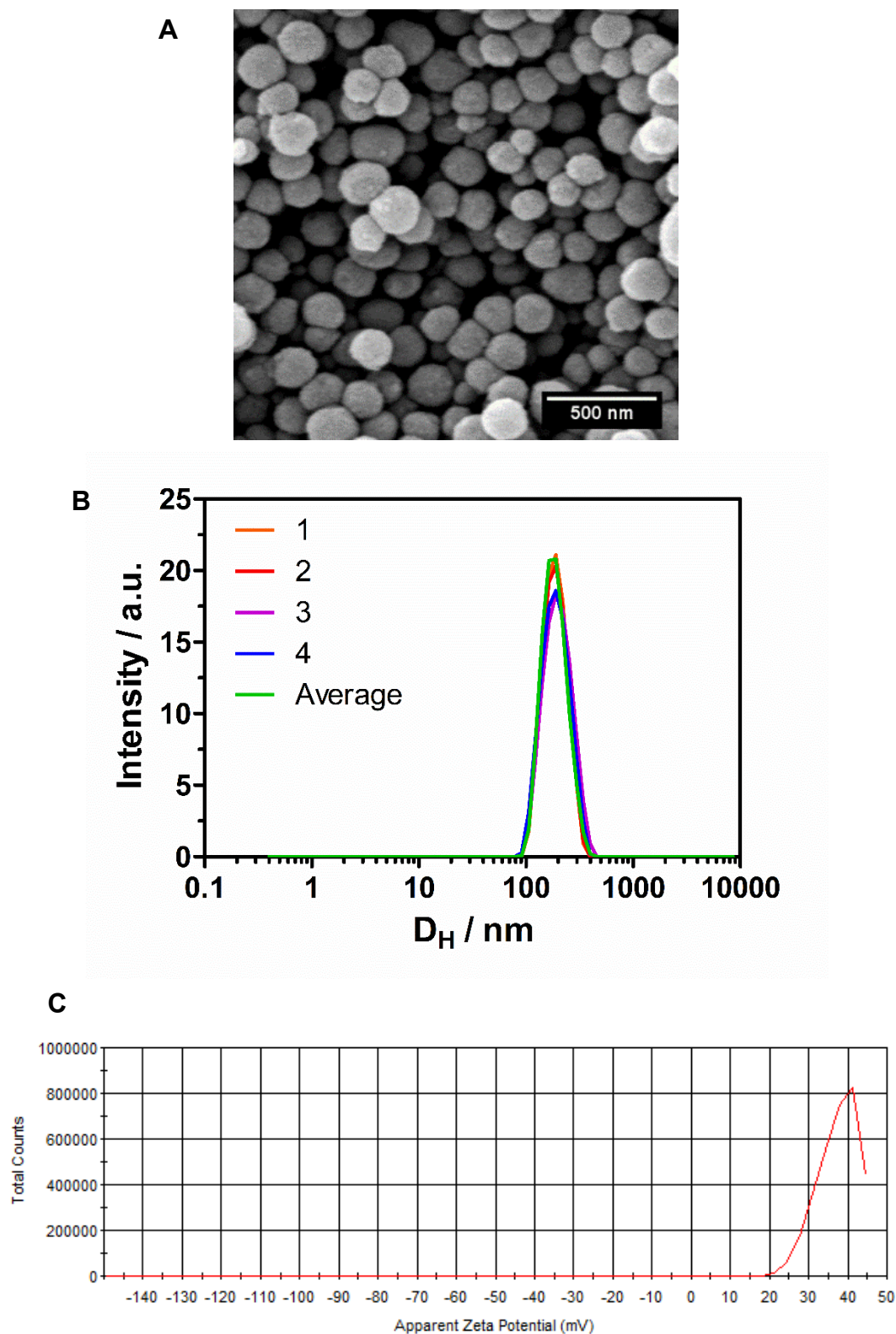


Figure S3. 32: Templated CPC-MSN: A) SEM imaging, magnification, electron beam 20 kV, analysed with ImageJ. **B)** DLS analysis showing size by intensity: 217 ± 26 nm and **C)** Zeta potential charge: $+36 \pm 5$ mV.

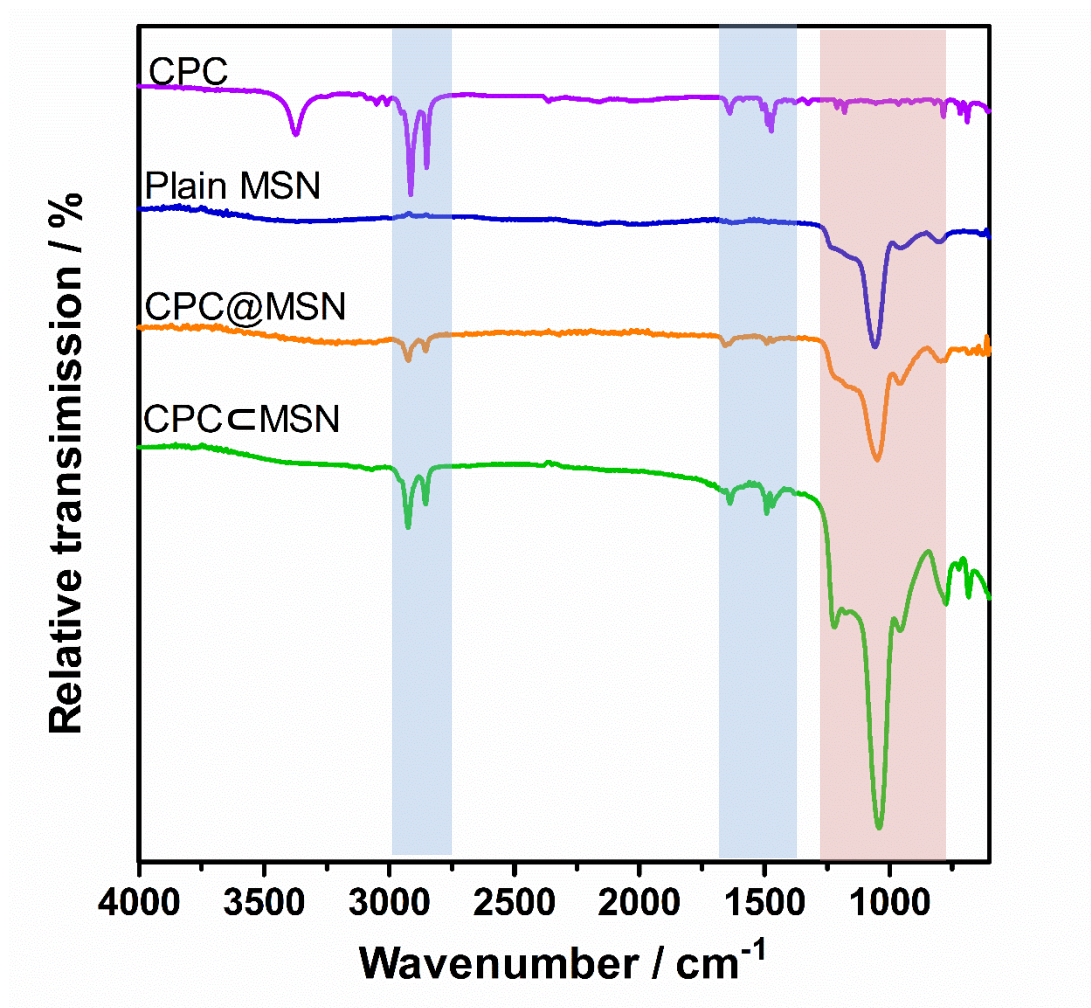


Figure S3. 33: FT-IR spectra of **CPC**, **plain MSN**, **adsorbed CPC@MSN** and **templated CPC⊂MSN**. The blue bands show peaks related to CPC and red related to silica bonds.

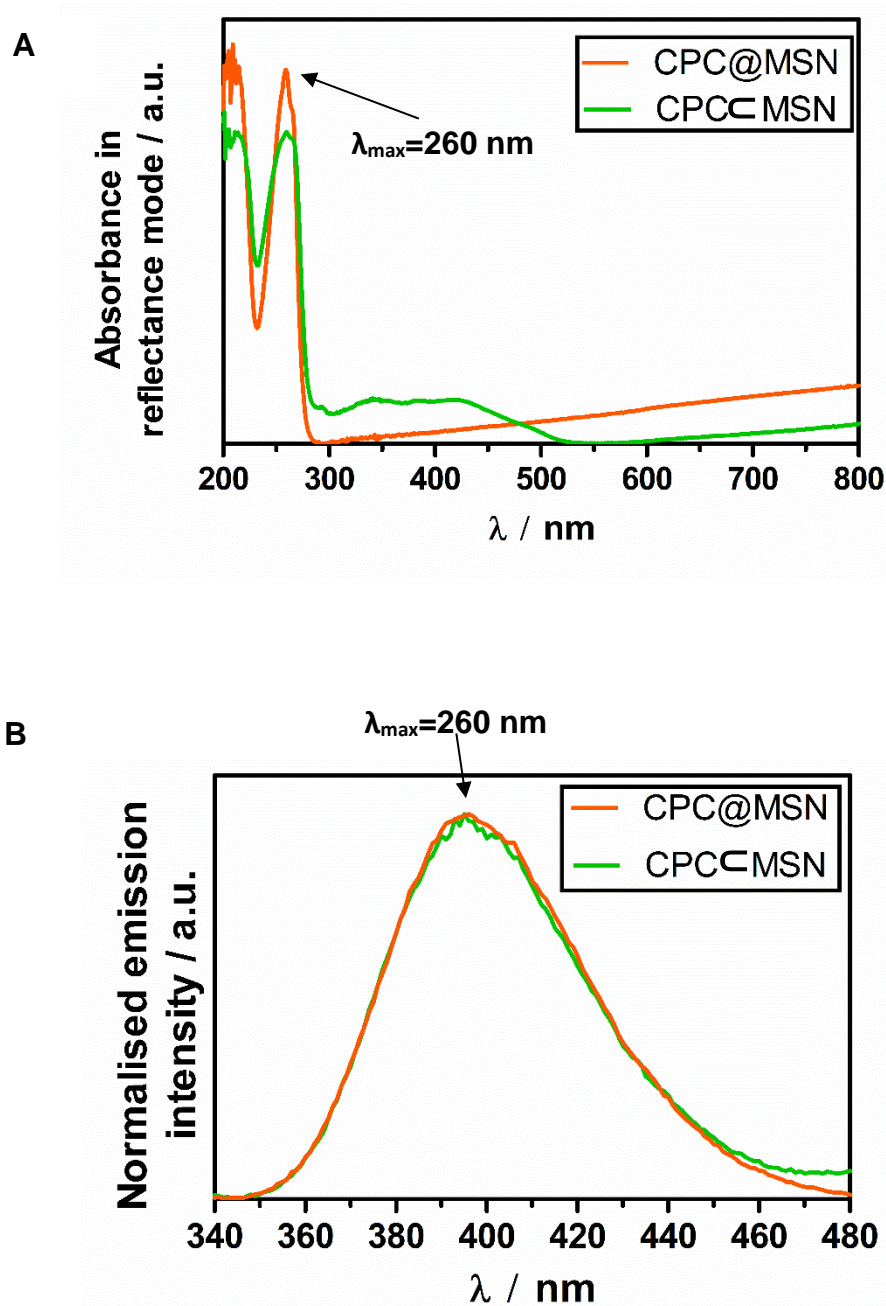


Figure S3. 34: Confirmation of CPC presence using **A)** Solid-state UV-Vis spectroscopy, showing shows the absorbance in reflectance mode for detection of CPC ($\lambda_{\max}= 295$ nm). **B)** Solid-state emission spectra of CPC $\lambda_{\text{exc}}=260$ nm and $\lambda_{\text{em}}=340\text{-}480$ nm, spectra were corrected for PMT response.

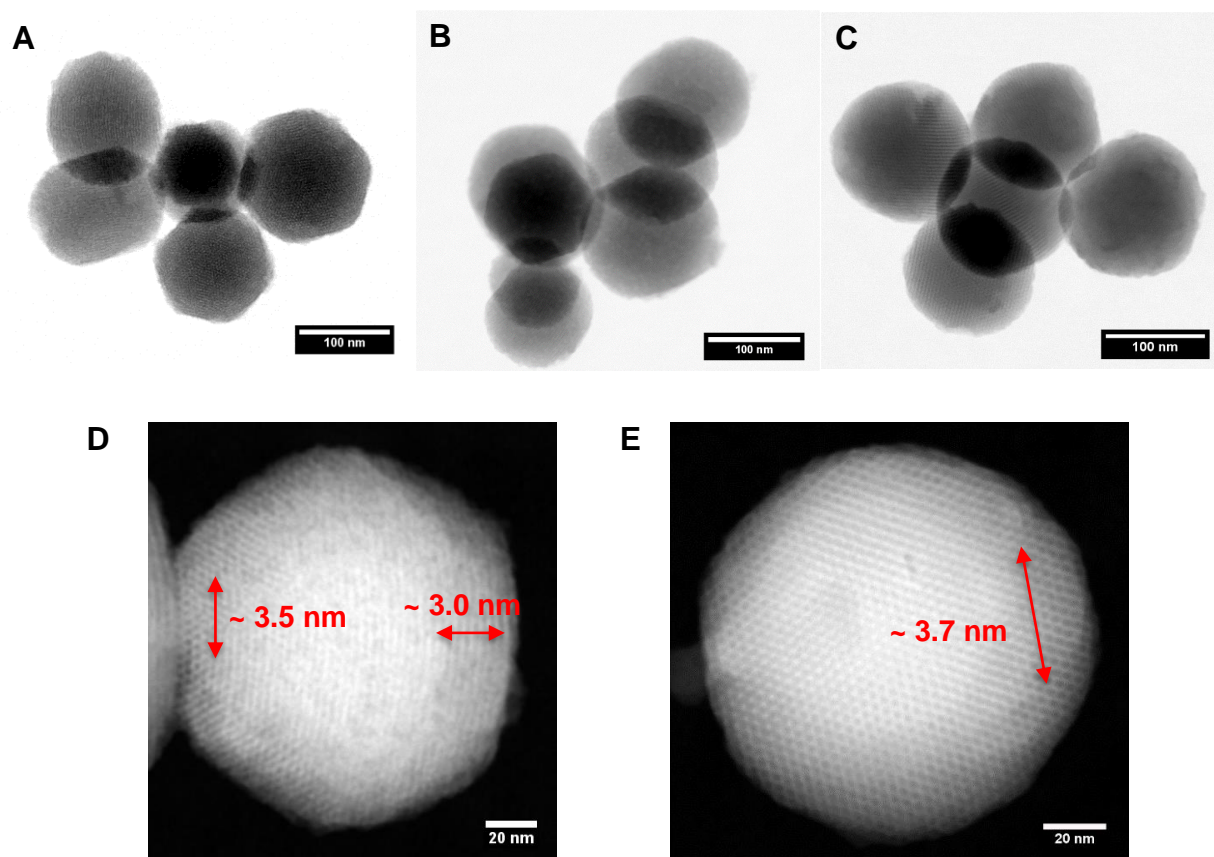


Figure S3. 35: Bright-field HR-TEM micrographs of **A) plain MSN**, **B) adsorbed CPC@MSN** and **C) templated CPC<MSN**. HAADF STEM to show the porous network and sizes of **D) CPC@MSN** and **E) CPC<MSN**. Using a 300 kV electron beam and analysed using ImageJ.

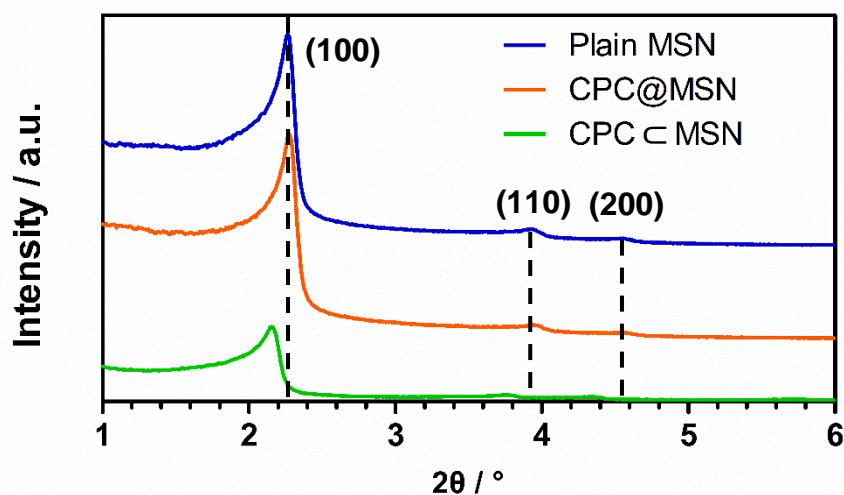
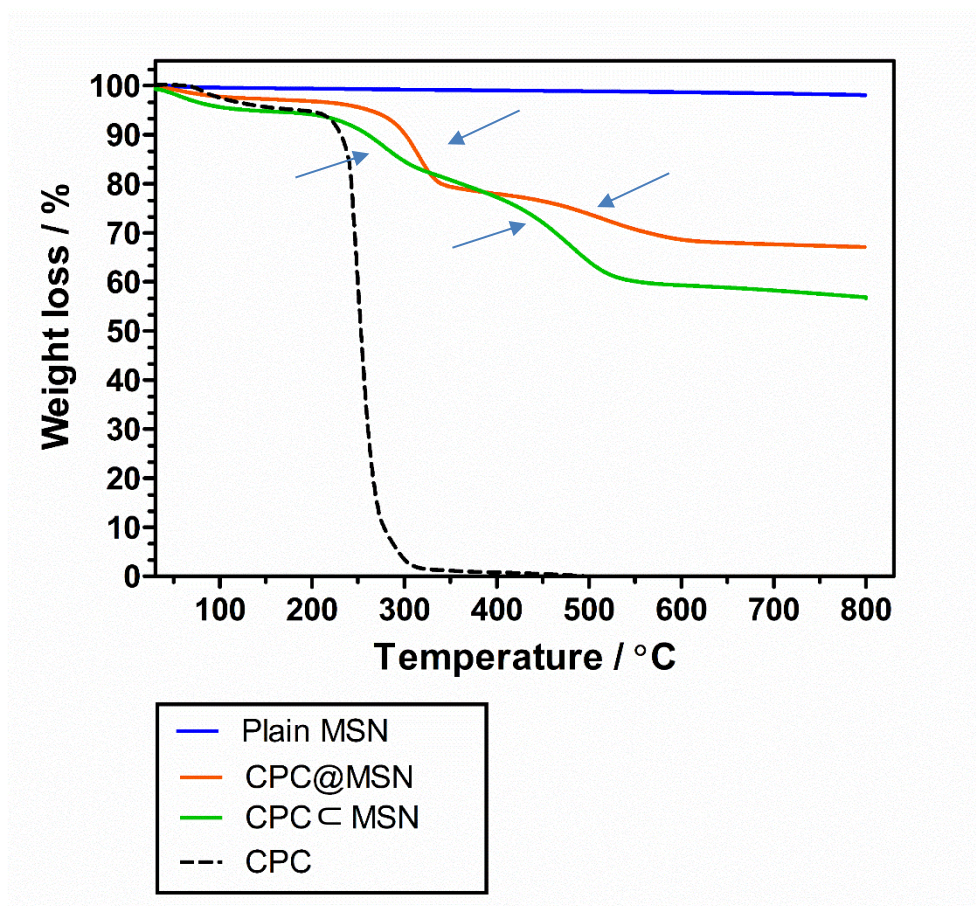


Figure S3. 36: Small angle powder X-ray diffraction (SAXRD) patterns of synthesised **plain MSN**, **CPC@MSN** and **CPC<MSN**. $2\theta \approx 2.26^\circ$ and two smaller peaks at 3.92° and 4.53° , indexed to (100), (110) and (200) respectively, typical of MCM-41 type MSNs, of a 2D hexagonal mesoporous structure.



Step assignment	Adsorbed CPC@MSN		Templated CPC⊂MSN	
	Region °C	Weight loss %	Region °C	Weight loss %
The loss of H ₂ O	<180	3	<180	5
1 st step of CPC	267 – 300	22	226 – 300	14
2 nd step of CPC	430-600	5	400-530	23

Figure S3. 37: TGA curves of **plain MSN**, **CPC@MSN**, **CPC⊂MSN** and **CPC**, showing the weight loss profiles with heating rate of 10 °C min⁻¹ from 30 to 800°C under nitrogen atmosphere. Step changes are reported in the summarised table to highlight temperature ranges and weight loss percentages due to CPC.

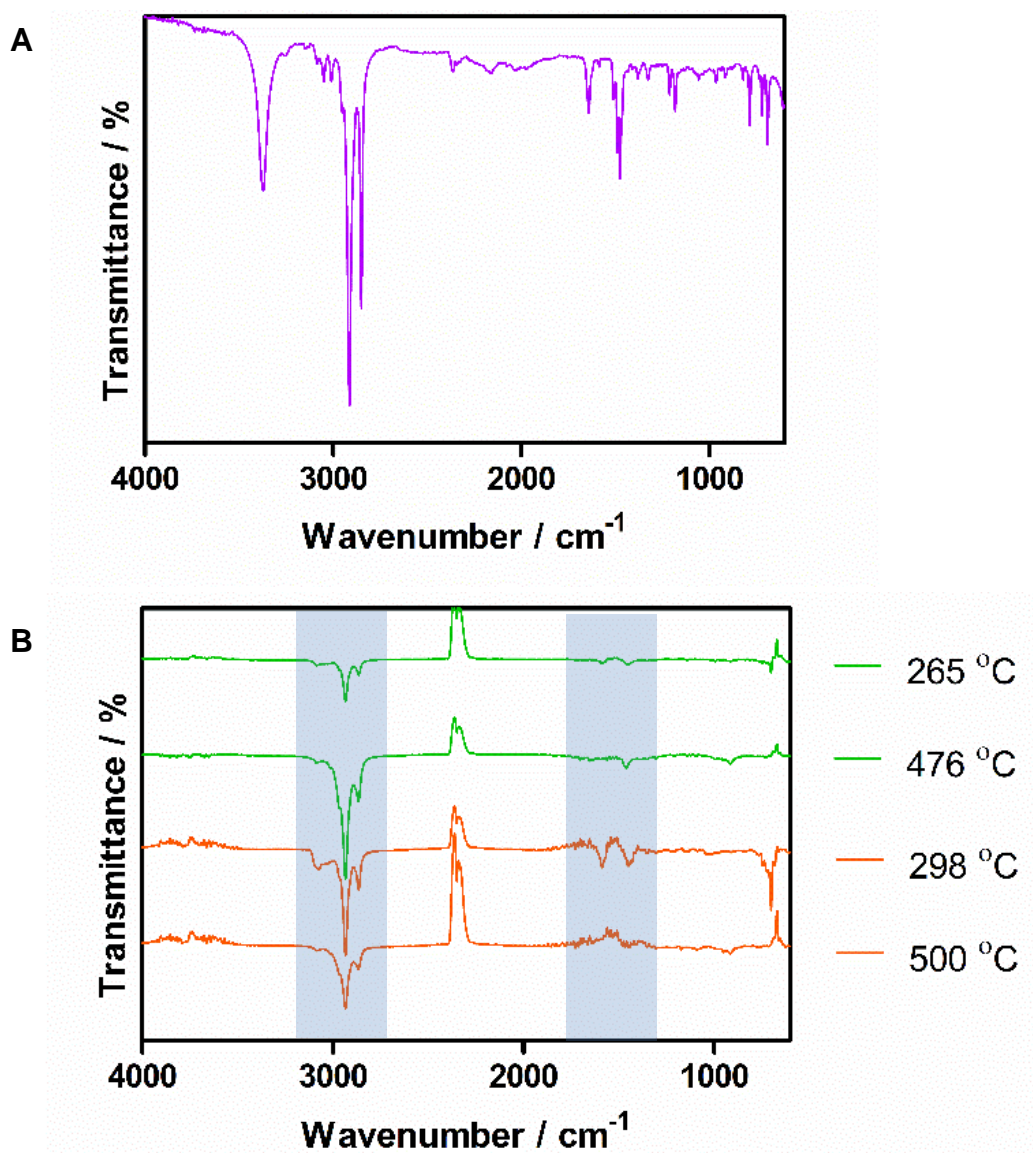
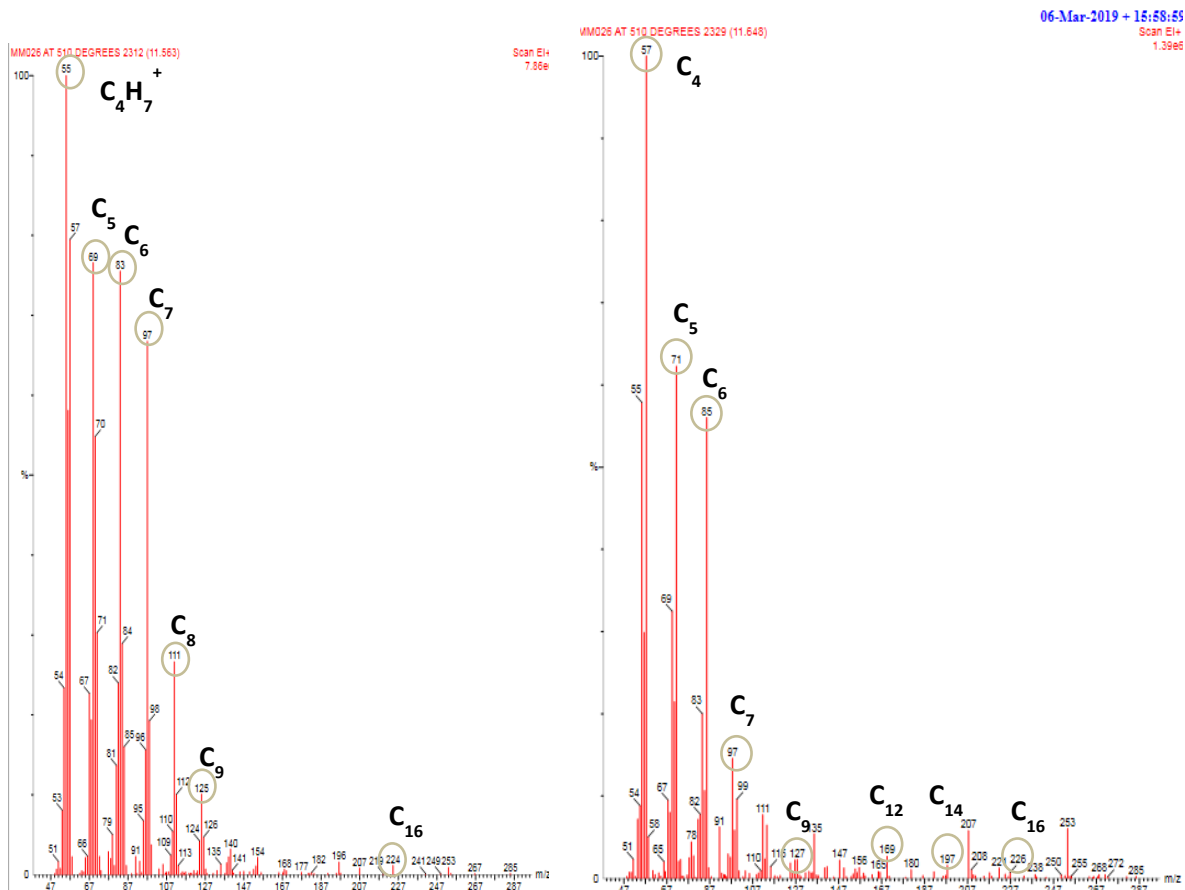
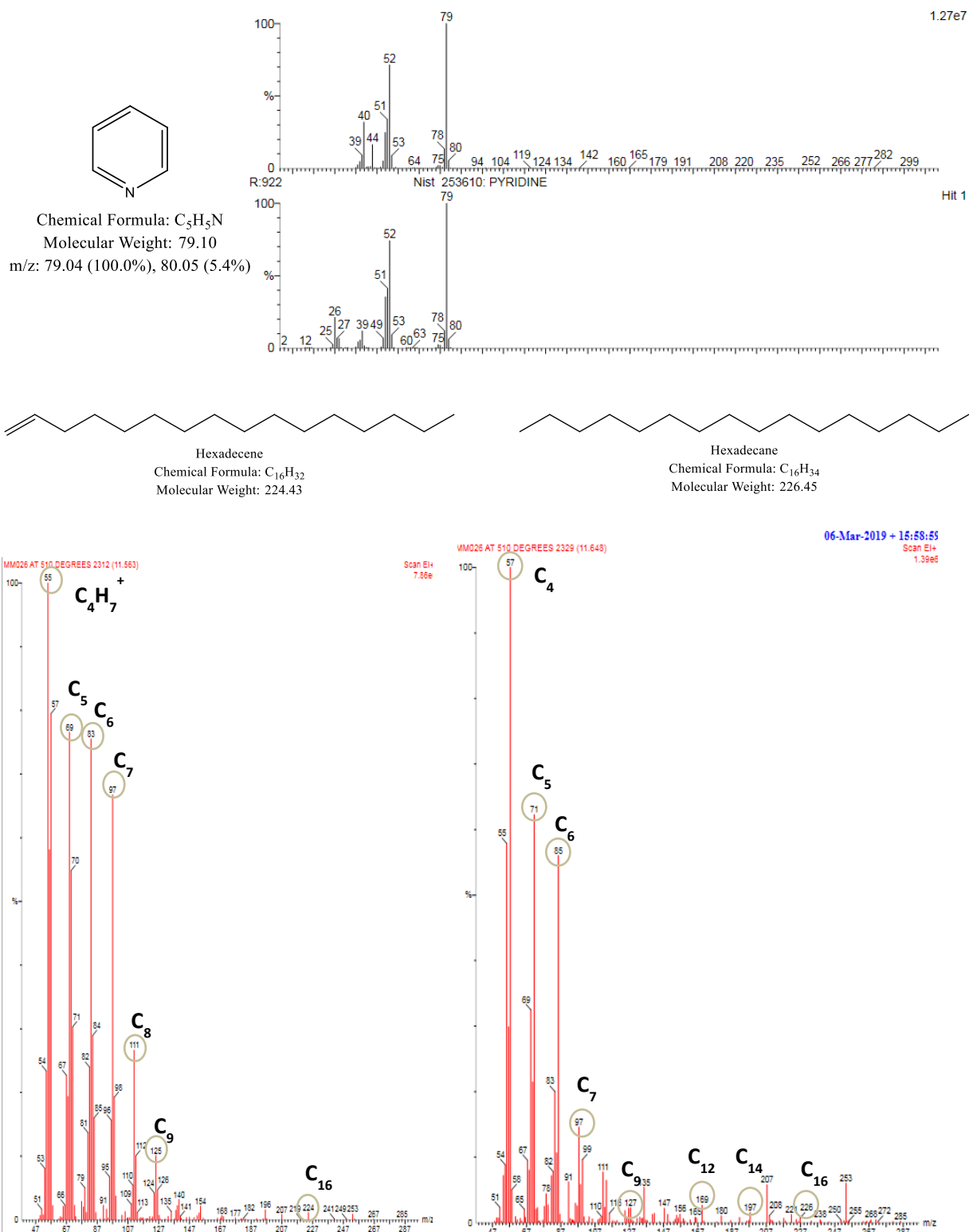


Figure S3. 38: FT-IR of **A)** pure CPC monohydrate and **B)** CPC from **CPC@MSN** (orange) and **CPC<MSN** (green) at derivative points from the TGA curve.

Chapter 3: The Synthesis, Optimisation & Characterisation of Cetylpyridinium Chloride Loaded Silica Nanoparticles



2.5.3. *In vitro* drug release studies

2.5.3.1 CPC loaded SNPs release

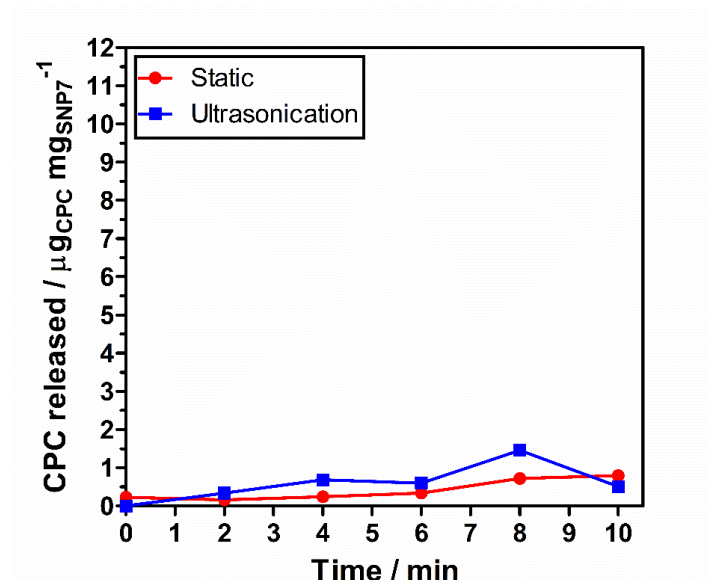


Figure S3. 40: Drug release profile of **SNP7** (2 mg mL^{-1} , H_2O , 37°C , pH 7.4) under static conditions (red line) and stimuli responsiveness from ultrasonic scaler (blue line) at P20, total 10 min (5 cycles). Release of CPC monitored by UV-Vis absorbance at λ_{max} 260 nm and CPC released (μg) per drug loaded NP (mg) calculated using TGA drug loading amount.

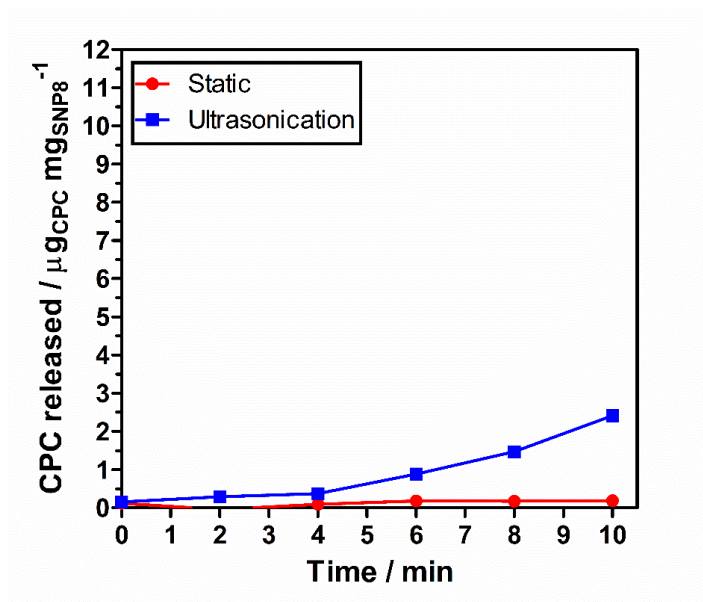


Figure S3. 41: Drug release profile of **SNP8** (2 mg mL^{-1} , H_2O , 37°C , pH 7.4) under static conditions (red line) and stimuli responsiveness from ultrasonic scaler (blue line) at P20, total 10 min (5 cycles). Release of CPC monitored by UV-Vis absorbance at λ_{max} 260 nm and CPC released (μg) per drug loaded NP (mg) calculated using TGA drug loading amount.

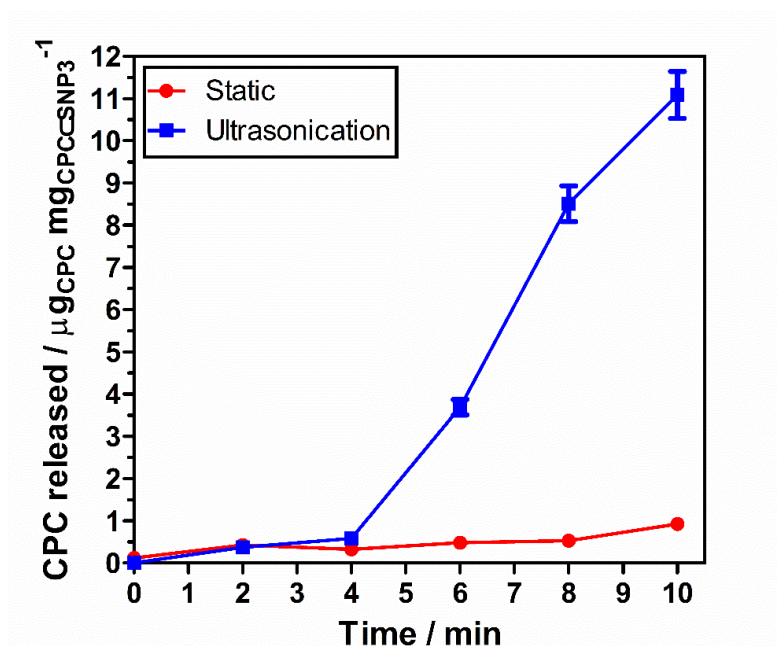


Figure S3. 42: Drug release profile of **SNP6 (CPC=SNP3)** (2 mg mL^{-1} , H_2O , 37°C , pH 7.4) under static conditions (red line) and stimuli responsiveness from ultrasonic scaler (blue line) at P20, total 10 min (5 cycles). Release of CPC monitored by UV-Vis absorbance at λ_{max} 260 nm and CPC released (μg) per drug loaded NP (mg) calculated using TGA drug loading amount.

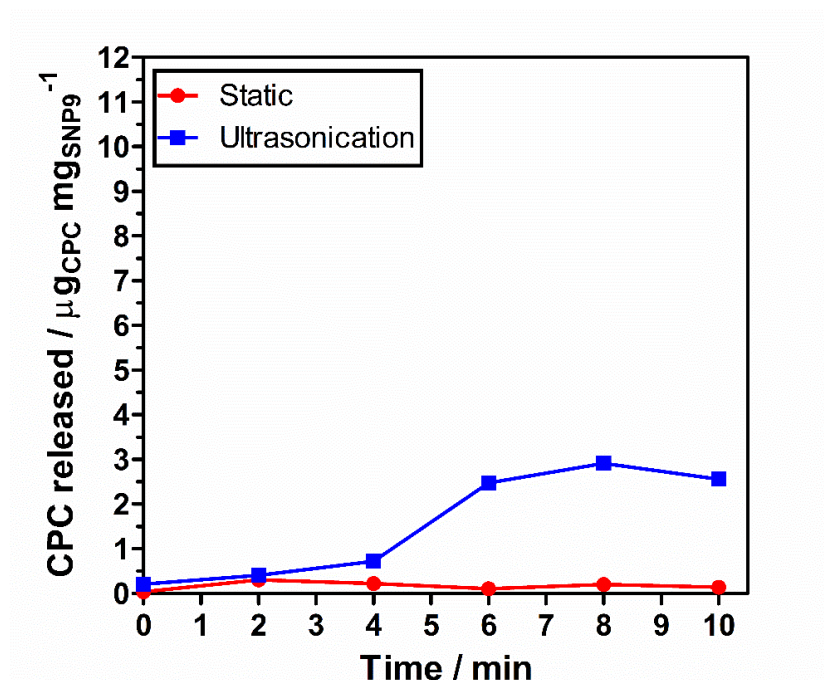


Figure S3. 43: Drug release profile of **SNP9** (2 mg mL^{-1} , H_2O , 37°C , pH 7.4) under static conditions (red line) and stimuli responsiveness from ultrasonic scaler (blue line) at P20, total 10 min (5 cycles). Release of CPC monitored by UV-Vis absorbance at λ_{max} 260 nm and CPC released (μg) per drug loaded NP (mg) calculated using TGA drug loading amount.

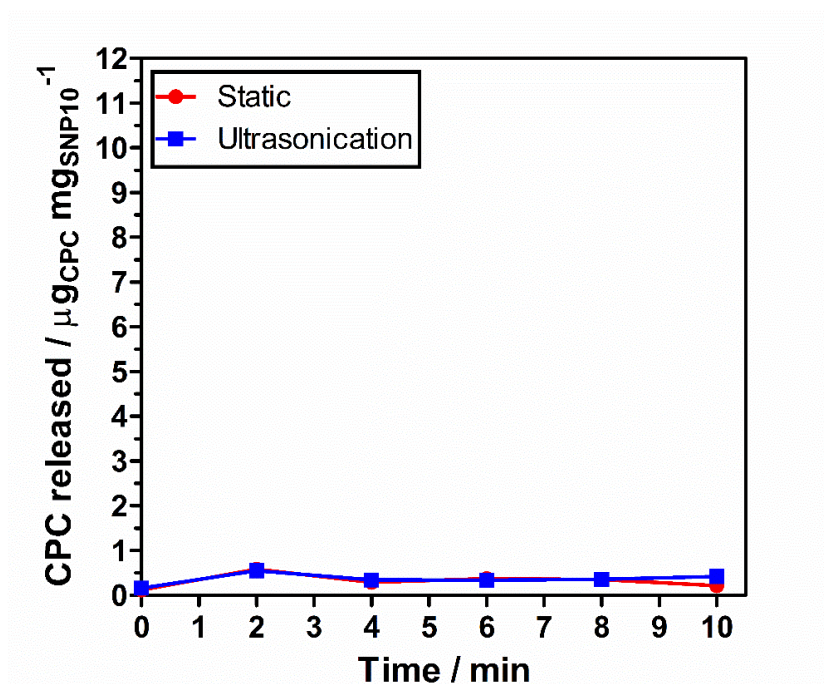


Figure S3. 44: Drug release profile of **SNP10** (2 mg mL⁻¹, H₂O, 37 °C, pH 7.4) under static conditions (red line) and stimuli responsiveness from ultrasonic scaler (blue line) at P20, total 10 min (5 cycles). Release of CPC monitored by UV-Vis absorbance at λ_{max} 260 nm and CPC released (μg) per drug loaded NP (mg) calculated using TGA drug loading amount.

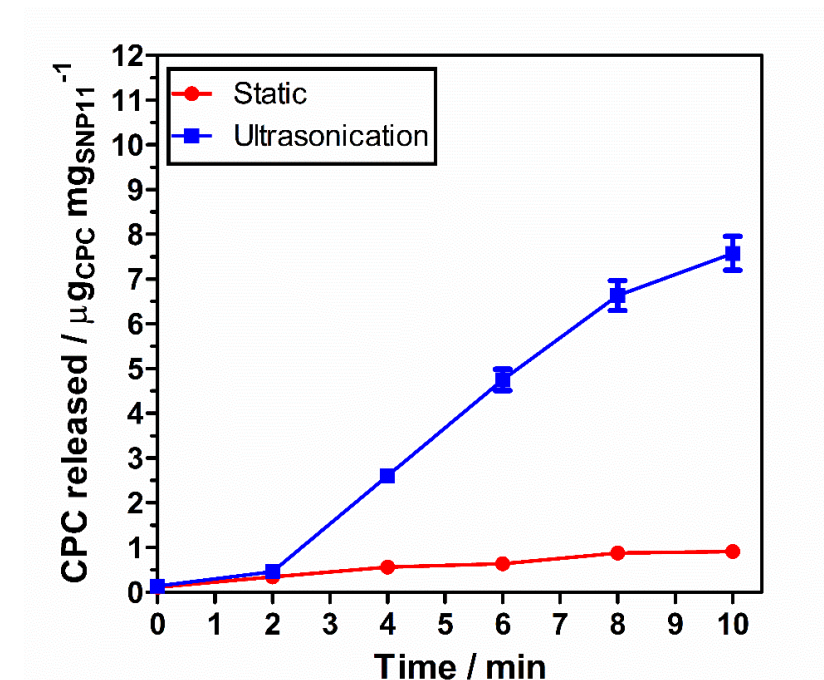


Figure S3. 45: Drug release profile of **SNP11** (2 mg mL⁻¹, H₂O, 37 °C, pH 7.4) under static conditions (red line) and stimuli responsiveness from ultrasonic scaler (blue line) at P20, total 10 min (5 cycles). Release of CPC monitored by UV-Vis absorbance at λ_{max} 260 nm and CPC released (μg) per drug loaded NP (mg) calculated using TGA drug loading amount.

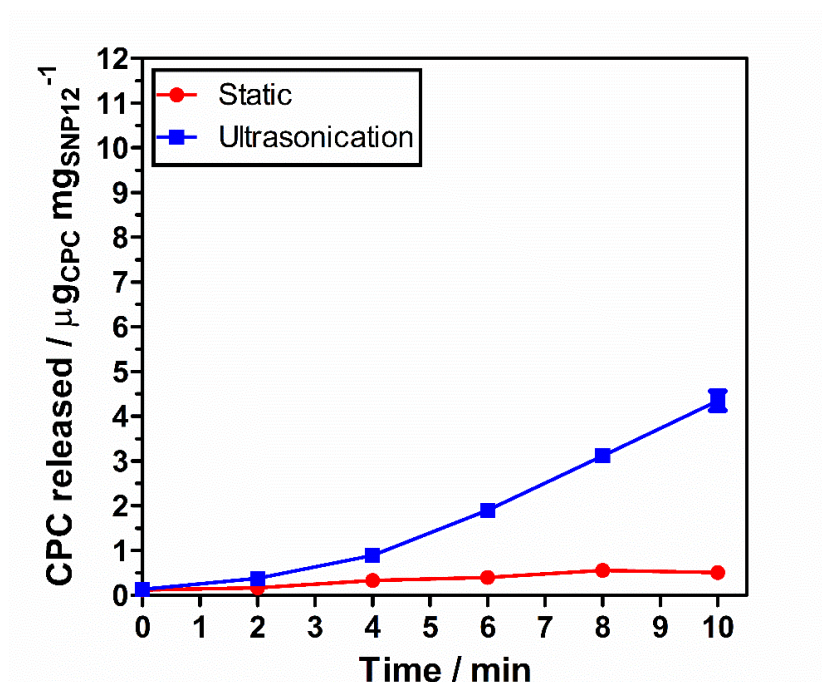


Figure S3. 46: Drug release profile of **SNP12** (2 mg mL^{-1} , H_2O , 37°C , pH 7.4) under static conditions (red line) and stimuli responsiveness from ultrasonic scaler (blue line) at P20, total 10 min (5 cycles). Release of CPC monitored by UV-Vis absorbance at λ_{max} 260 nm and CPC released (μg) per drug loaded NP (mg) calculated using TGA drug loading amount.

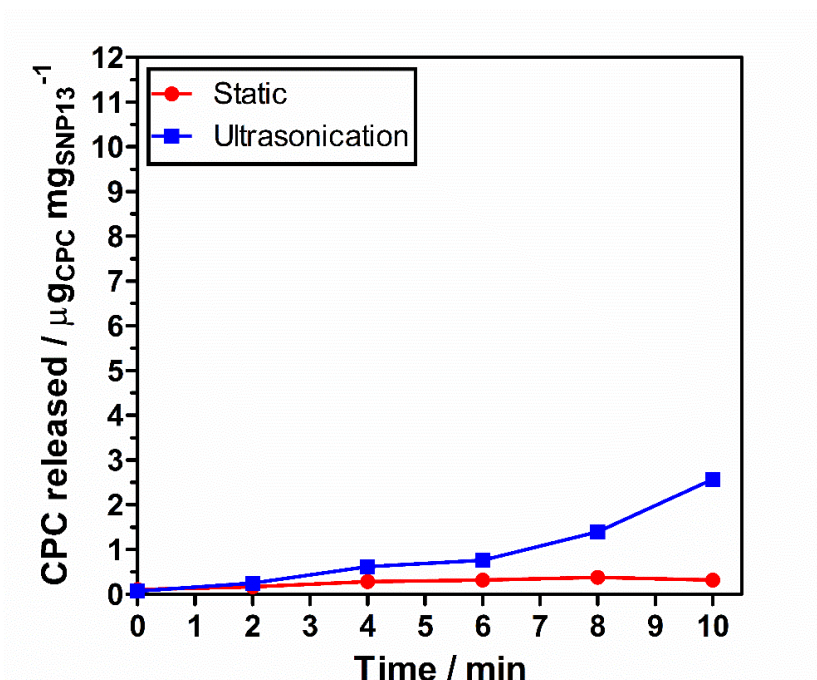


Figure S3. 47: Drug release profile of **SNP13** (2 mg mL^{-1} , H_2O , 37°C , pH 7.4) under static conditions (red line) and stimuli responsiveness from ultrasonic scaler (blue line) at P20, total 10 min (5 cycles). Release of CPC monitored by UV-Vis absorbance at λ_{max} 260 nm and CPC released (μg) per drug loaded NP (mg) calculated using TGA drug loading amount.

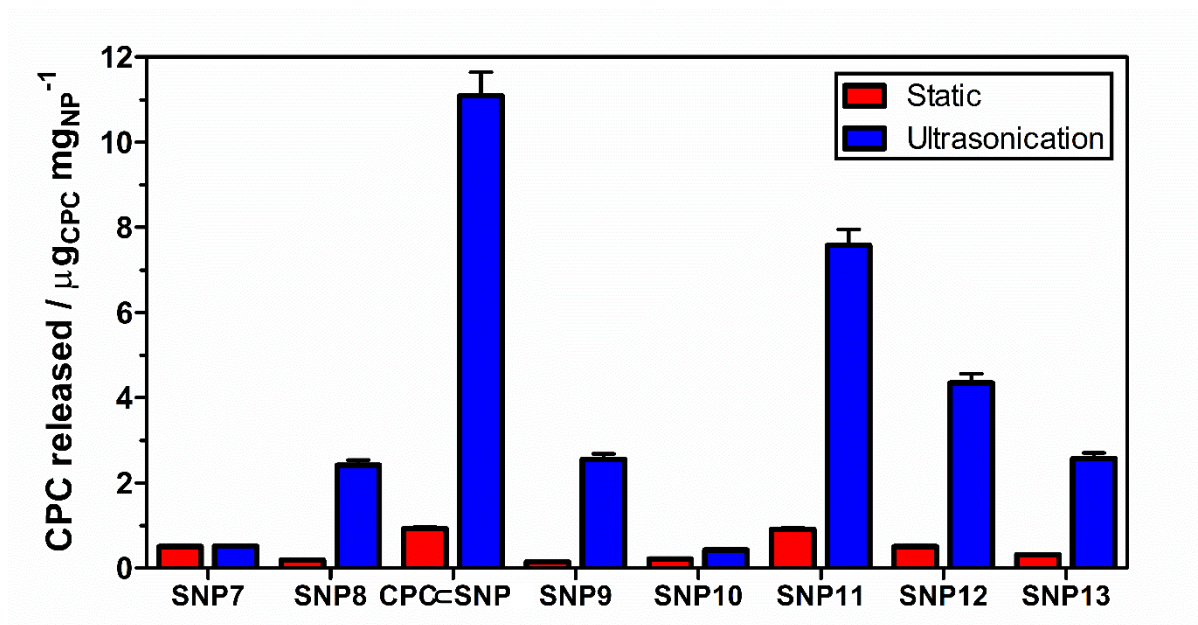


Figure S3. 48: Comparison of **SNPs** drug release after 10 mins (2 mg mL^{-1} , H_2O , 37°C , pH 7.4) under static conditions (red line) and stimuli responsiveness from ultrasonic scaler (blue line) at P20. Release of CPC monitored by UV-Vis absorbance at λ_{max} 260 nm and CPC released (μg) per drug loaded NP (mg) calculated using TGA drug loading amount.

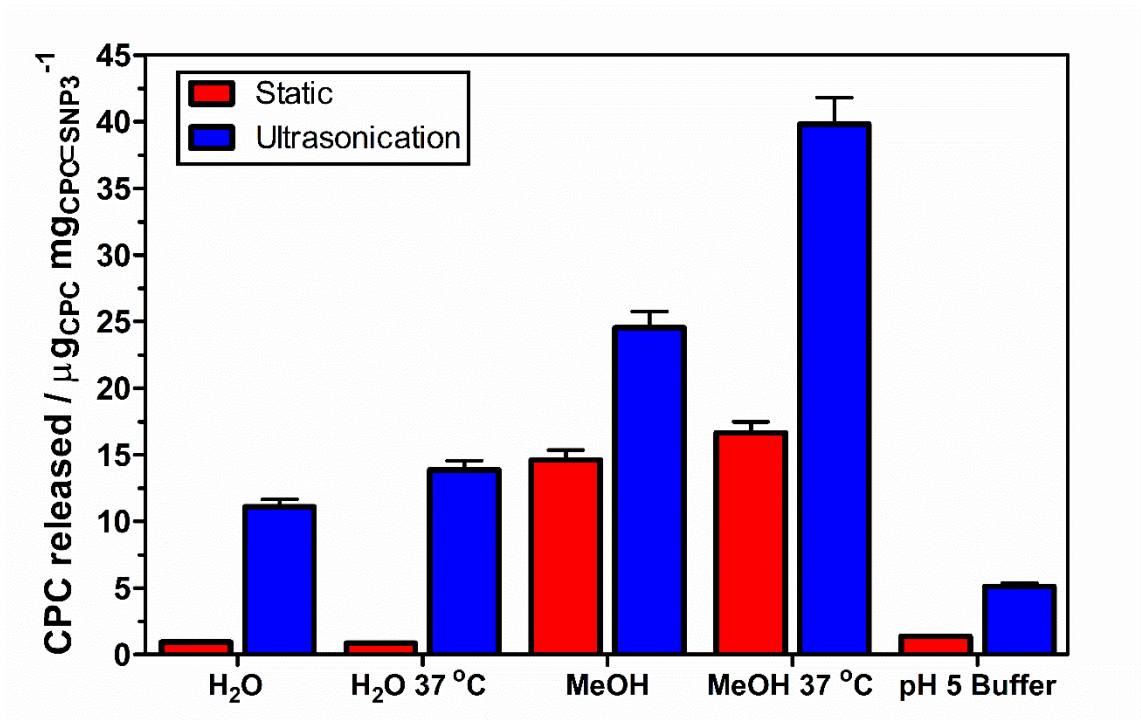


Figure S3. 49: Release media comparison under static conditions (red line) and stimuli responsiveness from ultrasonic scaler (blue line) at P20 of **CPC-SNP**. Release of CPC monitored by UV-Vis absorbance at λ_{max} 260 nm and CPC released (μg) per drug loaded NP (mg) calculated using TGA drug loading amount.

2.5.3.2. Other CPC loaded SNPs drug release

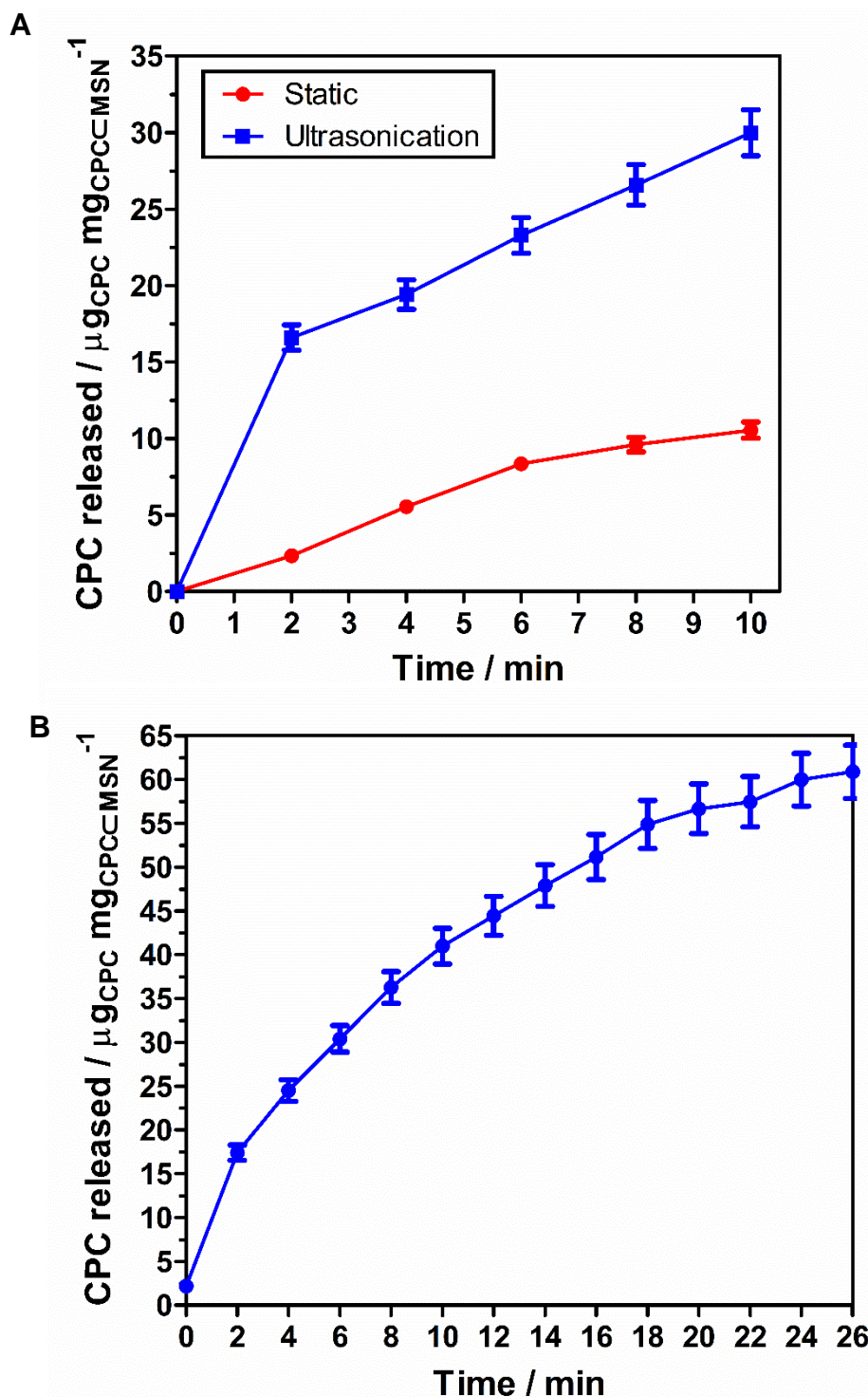


Figure S3. 50: Drug release profile of **templated CPC \subset MSN** (2 mg mL⁻¹, H₂O, 37 °C, pH 7.4): **A)** under static conditions (red line) and stimuli responsiveness from ultrasonic scaler (blue line) at P20, total 10 min (5 cycles). **B)** ultrasonic scaler at P20, total 26 min (13 cycles) to observe longer duration of release. Release of CPC monitored by UV-Vis absorbance at λ_{max} 260 nm and CPC released (μg) per drug loaded NP (mg) calculated using TGA drug loading amount.

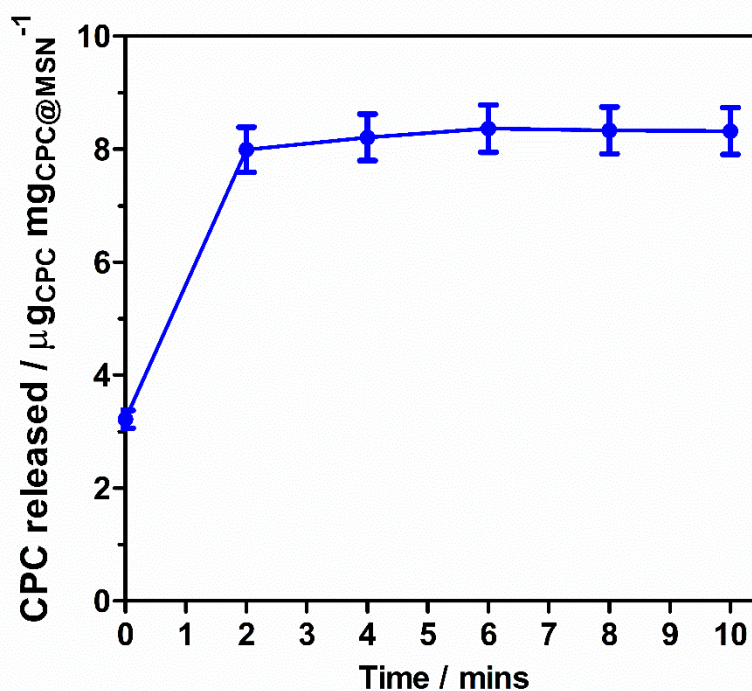
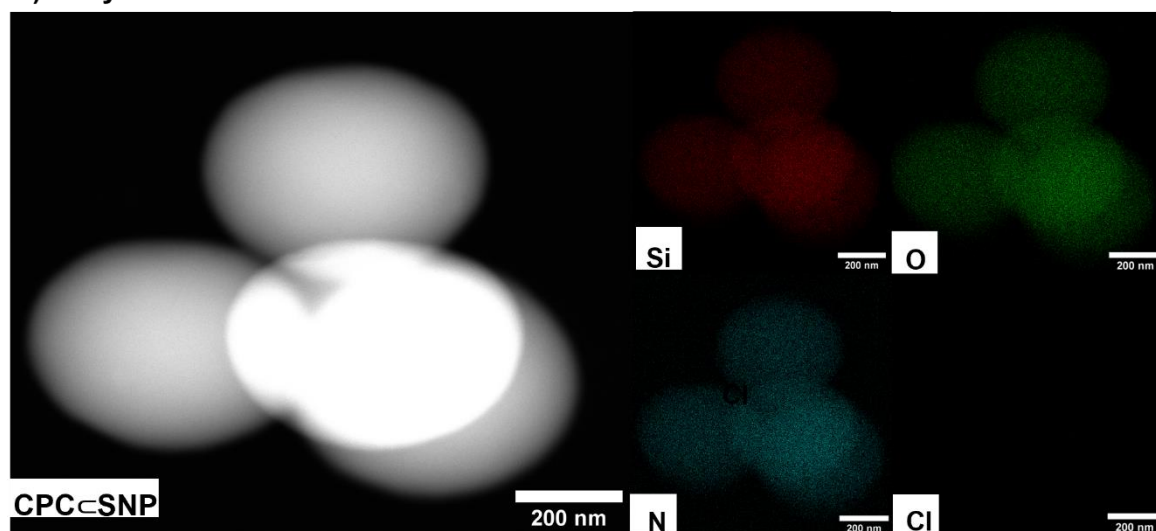


Figure S3. 51: Drug release profile of **adsorbed CPC@MSN** (2 mg mL^{-1} , H_2O , 37°C , pH 7.4) under stimuli responsiveness from ultrasonic scaler (blue line) at P20, total 10 min (5 cycles), showing burst release ad plateau. Release of CPC monitored by UV-Vis absorbance at λ_{max} 260 nm and CPC released (μg) per drug loaded NP (mg) calculated using TGA drug loading amount.

A) Fully loaded CPC=SNP



B) unloaded CPC=SNP with methanol

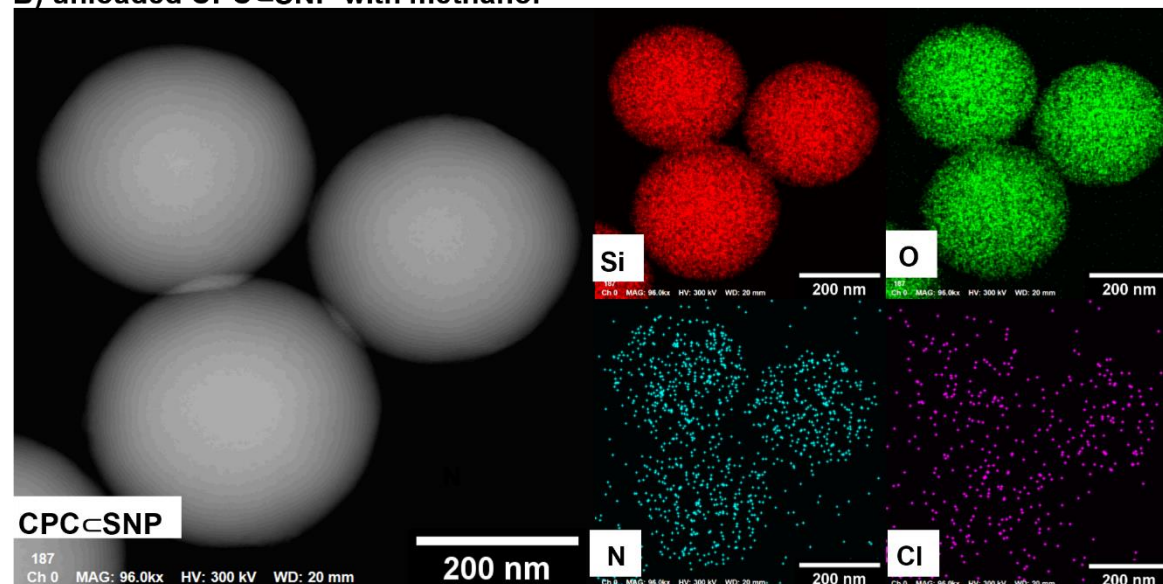


Figure S3. 52: HAADF STEM micrograph of **CPC=SNP** of **A)** loaded and **B)** unloaded post treatment with MeOH (1.5 mg mL^{-1} , stirred at 400 RPM, 72h) with corresponding EDS elemental mapping images. Magnification 96 kx, 300 kV electron beam.

3.6. References

- 1 S. Priyadarsini, S. Mukherjee and M. Mishra, *J. Oral Biol. Craniofacial Res.*, 2018, **8**, 58–67.
- 2 N. Y. Lee, W. C. Ko and P. R. Hsueh, *Front. Pharmacol.*, 2019, **10**, 1–10.
- 3 V. Mamaeva, C. Sahlgren and M. Lindén, *Adv. Drug Deliv. Rev.*, 2013, **65**, 689–702.
- 4 M. Varache, I. Bezverkhy, L. Saviot, F. Bouyer, F. Baras and F. Bouyer, *J. Non. Cryst. Solids*, 2015, **408**, 87–97.
- 5 M. Frasconi, Z. Liu, J. Lei, Y. Wu, E. Strekalova, D. Malin, M. W. Ambrogio, X. Chen, Y. Y. Botros, V. L. Cryns, J. P. Sauvage and J. Fraser Stoddart, *J. Am. Chem. Soc.*, 2013, **135**, 11603–11613.
- 6 X. Wu, Z. Wang, D. Zhu, S. Zong, L. Yang, Y. Zhong and Y. Cui, *ACS Appl. Mater. Interfaces*, 2013, **5**, 10895–10903.
- 7 X. Li, T. Tang, Y. Zhou, Y. Zhang and Y. Sun, *Microporous Mesoporous Mater.*, 2014, **184**, 83–89.
- 8 M. Colilla and M. Vallet-Regí, *Int. J. Mol. Sci.*, 2020, **21**, 1–32.
- 9 N. Mas, I. Galiana, L. Mondragón, E. Aznar, E. Climent, N. Cabedo, F. Sancenón, J. R. Murguía, R. Martínez-Máñez, M. D. Marcos and P. Amorós, *Chem. - A Eur. J.*, 2013, **19**, 11167–11171.
- 10 B. González, M. Colilla, J. Díez, D. Pedraza, M. Guembe, I. Izquierdo-Barba and M. Vallet-Regí, *Acta Biomater.*, 2018, **68**, 261–271.
- 11 J. Lin, Z. He, F. Liu, J. Feng, C. Huang, X. Sun and H. Deng, *Int. J. Nanomedicine*, 2020, **15**, 5377–5387.
- 12 T. Moodley and M. Singh, *Pharmaceutics*, 2021, **13**, 71.
- 13 A. Rahikkala, S. A. P. Pereira, P. Figueiredo, M. L. C. Passos, A. R. T. S. Araújo, M. L. M. F. S. Saraiva and H. A. Santos, *Adv. Biosyst.*, 2018, **2**, 1–33.
- 14 Y. Song, Y. Li, Q. Xu and Z. Liu, *Int. J. Nanomedicine*, 2016, **12**, 87–110.
- 15 J. L. Paris, P. de la Torre, M. V. Cabañas, M. Manzano, A. I. Flores and M. Vallet-Regí, *Acta Biomater.*, 2019, **83**, 372–378.
- 16 H. J. Kim, H. Matsuda, H. Zhou and I. Honma, *Adv. Mater.*, 2006, **18**, 3083–3088.
- 17 T. S. Anirudhan and A. S. Nair, *J. Mater. Chem. B*, 2018, **6**, 428–439.
- 18 J. L. Paris, M. V. Cabanas, M. Manzano and M. Vallet-Regí, *ACS Nano*, 2015, **9**, 11023–11033.

- 19 J. Wang, Y. Jiao and Y. Shao, *Materials (Basel)*., 2018, **11**, 2041.
- 20 X. Li, Z. Wang and H. Xia, *Front. Chem.*, 2019, **7**, 1–11.
- 21 Z. Jin, Y. Wen, Y. Hu, W. Chen, X. Zheng, W. Guo, T. Wang, Z. Qian, B. L. Su and Q. He, *Nanoscale*, 2017, **9**, 3637–3645.
- 22 Y. Chen, Y. Gao, H. Chen, D. Zeng, Y. Li, Y. Zheng, F. Li, X. Ji, X. Wang, F. Chen, Q. He, L. Zhang and J. Shi, *Adv. Funct. Mater.*, 2012, **22**, 1586–1597.
- 23 M. Ma, H. X. Xu, H. R. Chen, X. Q. Jia, K. Zhang, Q. Wang, S. G. Zheng, R. Wu, M. H. Yao, X. J. Cai, F. Q. Li and J. L. Shi, *Adv. Mater.*, 2014, **26**, 7378–7385.
- 24 X. Qian, W. Wang, W. Kong and Y. Chen, *J. Nanomater.*, 2014, **2014**, 1–8.
- 25 J. Liu, X. Jiang, C. Ashley and C. J. Brinker, *J. Am. Chem. Soc.*, 2009, **131**, 7567–7569.
- 26 Q. Cai, W. Y. Lin, F. S. Xiao, W. Q. Pang, X. H. Chen and B. S. Zou, *Microporous Mesoporous Mater.*, 1999, **32**, 1–15.
- 27 M. Grün, K. K. Unger, A. Matsumoto and K. Tsutsumi, *Microporous Mesoporous Mater.*, 1999, **27**, 207–216.
- 28 M. Grün, I. Lauer and K. K. Unger, *Adv. Mater.*, 1997, **9**, 254–257.
- 29 F. Lu, S. H. Wu, Y. Hung and C. Y. Mou, *Small*, 2009, **5**, 1408–1413.
- 30 J. young Kim, K. W. Park and O. Y. Kwon, *Microporous Mesoporous Mater.*, 2019, **285**, 137–141.
- 31 Q. Huo, R. Leon, P. M. Petroff and G. D. Stucky, *Science (80-.)*., 1995, **268**, 1324–1327.
- 32 D. Sun, L. Sun, M. Luo and Z. Gou, *Asian J. Chem.*, 2011, **23**, 5169–5170.
- 33 A. Yildirim, M. Turkydin, B. Garipcan and M. Bayindir, *RSC Adv.*, 2016, **6**, 32060–32069.
- 34 Q. He, Z. Zhang, Y. Gao, J. Shi and Y. Li, *Small*, 2009, **5**, 2722–2729.
- 35 S. P. Hudson, R. F. Padera, R. Langer and D. S. Kohane, *Biomaterials*, 2008, **29**, 4045–4055.
- 36 C. A. Stewart, Y. Finer and B. D. Hatton, *Sci. Rep.*, 2018, **8**, 1–12.
- 37 V. Dubovoy, A. Ganti, T. Zhang, H. Al-Tameemi, J. D. Cerezo, J. M. Boyd and T. Asefa, *J. Am. Chem. Soc.*, 2018, **140**, 13534–13537.
- 38 L. Tang and J. Cheng, *Nano Today*, 2013, **8**, 290–312.
- 39 L. M. Rossi, L. Shi, F. H. Quina and Z. Rosenzweig, *Langmuir*, 2005, **21**, 4277–4280.

- 40 D. J. Lewis, V. Dore, M. J. Goodwin, A. C. Savage, G. B. Nash, P. Angeli and Z. Pikramenou, *Meas. Sci. Technol.*, 2012, **23**, 084004.
- 41 D. Zhang, Z. Wu, J. Xu, J. Liang, J. Li and W. Yang, *Langmuir*, 2010, **26**, 6657–6662.
- 42 S. Claire, A. Damien, S. Ginton, H. Floyd, R. Sammons and Z. Pikramenou, *J. Dent.*, 2015, **43**, 1242–1248.
- 43 N. Vyas, R. L. Sammons, Z. Pikramenou, W. M. Palin, H. Dehghani and A. D. Walmsley, *J. Dent.*, 2017, **56**, 112–120.
- 44 V. García, M. Rioboo, J. Serrano, A. O'Connor, D. Herrera and M. Sanz, *Int. J. Dent. Hyg.*, 2011, **9**, 266–273.
- 45 A. Evans, S. J. Leishman, L. U. Walsh and W. K. Seow, *Aust. Dent. J.*, 2015, **60**, 247–254.
- 46 P. K. Sreenivasan, V. I. Haraszthy and J. J. Zambon, *Lett. Appl. Microbiol.*, 2013, **56**, 14–20.
- 47 S. Haps, D. E. Slot, C. E. Berchier and G. A. Van der Weijden, *Int. J. Dent. Hyg.*, 2008, **6**, 290–303.
- 48 X. Mao, D. L. Auer, W. Buchalla, K.-A. Hiller, T. Maisch, E. Hellwig, A. Al-Ahmad and F. Cieplik, *Antimicrob. Agents Chemother.*, 2020, **64**, 1–14.
- 49 S. Y. Lee and S. Y. Lee, *Biocontrol Sci.*, 2019, **24**, 13–21.
- 50 S. L. F. de Miranda, J. T. Damaceno, M. Faveri, L. C. Figueiredo, G. M. S. Soares and B. Bueno-Silva, *Braz. Dent. J.*, 2020, **31**, 103–108.
- 51 J. Latimer, J. L. Munday, K. M. Buzza, S. Forbes, P. K. Sreenivasan and A. J. McBain, *BMC Microbiol.*, 2015, **15**, 1–8.
- 52 A. A. Rafati, H. Gharibi and H. Iloukhani, *Phys. Chem. Liq.*, 2001, **39**, 521–532.
- 53 D. Varade, T. Joshi, V. K. Aswal, P. S. Goyal, P. A. Hassan and P. Bahadur, *Colloids Surfaces A Physicochem. Eng. Asp.*, 2005, **259**, 95–101.
- 54 A. Bhattarai, S. K. Shah and A. K. Yadav, *Nepal J. Sci. Technol.*, 2013, **13**, 89–93.
- 55 C. L. Huyck, *J. Am. Pharm. Assoc. (Scientific ed.)*, 1945, **34**, 5–11.
- 56 J. Stetefeld, S. A. McKenna and T. R. Patel, *Biophys. Rev.*, 2016, **8**, 409–427.
- 57 R. Garberoglio and M. Brannstrom, *Arch. Oral Biol.*, 1976, **21**, 355–362.
- 58 A. P. Morrow, O. O. Kassim and F. O. Ayorinde, *Rapid Commun. Mass Spectrom.*, 2001, **15**, 767–770.
- 59 F. Kunc, V. Balhara, Y. Sun, M. Daroszewska, Z. J. Jakubek, M. Hill, A.

- Brinkmann and L. J. Johnston, *Analyst*, 2019, **144**, 5589–5599.
- 60 F. Yarza, C. F. Morantes, M. L. Montes, N. Bellotti, J. Salduondo, S. Yapar, F. Cravero and R. M. Torres Sánchez, *Mater. Chem. Phys.*, 2020, **253**, 123390.
- 61 U. Bernauer, Q. Chaudhry, P. Coenraads, G. Degen, M. Dusinska, W. Lilienblum, E. Nielsen, T. Platzek, C. Suresh, C. Rastogi, J. Rousselle and B. Van, *Opinion of the scientific committee on consumer safety on 2,6-diaminopyridine*, 2015.
- 62 X. He, L. Hai, J. Su, K. Wang and X. Wu, *Nanoscale*, 2011, **3**, 2936–2942.
- 63 P. Kortesus, M. Ahola, M. Kangas, M. Jokinen, T. Leino, L. Vuorilehto, S. Laakso, J. Kiesvaara, A. Yli-Urpo and M. Marvola, *Biomaterials*, 2002, **23**, 2795–2801.
- 64 D. Ma, M. Li, A. J. Patil and S. Mann, *Adv. Mater.*, 2004, **16**, 1838–1841.
- 65 X. Wang, H. Chen, Y. Zheng, M. Ma, Y. Chen, K. Zhang, D. Zeng and J. Shi, *Biomaterials*, 2013, **34**, 2057–2068.
- 66 J. L. Paris, C. Mannaris, M. V. Cabañas, R. Carlisle, M. Manzano, M. Vallet-Regí and C. C. Coussios, *Chem. Eng. J.*, 2018, **340**, 2–8.
- 67 Y. Lv, Y. Cao, P. Li, J. Liu, H. Chen, W. Hu and L. Zhang, *Adv. Healthc. Mater.*, 2017, **6**, 1–10.
- 68 W. R. E. Laird and A. D. Walmsley, *J. Dent.*, 1991, **19**, 14–17.
- 69 B. Song, C. Wu and J. Chang, *Regen. Biomater.*, 2015, **2**, 229–237.
- 70 M. Manzano and M. Vallet-Regí, *Chem. Commun.*, 2019, **55**, 2731–2740.
- 71 A. D. Walmsley, S. C. Lea, B. Felver, D. C. King and G. J. Price, *Clin Oral Investig.*, 2013, **17**, 1227–1234.
- 72 W. Shi, F. Li, Q. Lin, G. Fang, L. Chen and L. Zhang, *IOP Conf. Ser. Earth Environ. Sci.*, 2020, **512**, 012141.
- 73 Z. Liu, C. Ji, B. Wang and S. Sun, *Micro Nano Lett.*, 2019, **14**, 1041–1045.
- 74 C. Kübel, A. Voigt, R. Schoenmakers, M. Otten, D. Su, T. C. Lee, A. Carlsson and J. Bradley, *Microsc. Microanal.*, 2005, **11**, 378–400.
- 75 O. L. Krivanek, M. F. Chisholm, V. Nicolosi, T. J. Pennycook, G. J. Corbin, N. Dellby, M. F. Murfitt, C. S. Own, Z. S. Szilagyi, M. P. Oxley, S. T. Pantelides and S. J. Pennycook, *Nature*, 2010, **464**, 571–574.
- 76 S. Rades, V. D. Hodoroba, T. Salge, T. Wirth, M. P. Lobera, R. H. Labrador, K. Natte, T. Behnke, T. Gross and W. E. S. Unger, *RSC Adv.*, 2014, **4**, 49577–49587.
- 77 J. Y. Zhang, J. Hwang, B. J. Isaac and S. Stemmer, *Sci. Rep.*, 2015, **5**, 1–10.

- 78 F. C. Lin, Y. Xie, T. Deng and J. I. Zink, *J. Am. Chem. Soc.*, 2021, **143**, 6025–6036.

Chapter 4: Biofilm Disruption through Controlled Antimicrobial Release from Ultrasound-Responsive Silica Nanoparticles

4.1. Introduction

Nanoparticle-based therapies have attracted much attention for their capabilities to help overcome limitations with current treatments. They can provide a more effective, safer, and affordable method to aid the delivery of approved drugs.^{1–5} Despite the extensive research of various nanomaterials for drug delivery systems, there are only approximately 30 nanoformulations clinically approved with the majority not reaching the clinical trials stage.^{6,7} SNPs, have many desirable properties, such as: ease of synthesis for further surface functionalisation, the size, shape and charge can be easily tuned, their ability to be loaded with drugs and improve their bioavailability for increased drug concentration at the site of action.⁸ Despite SNPs' numerous advantages for diagnosis and therapeutical applications, the clinical translation remains slow.⁹ Furthermore, SNP drug delivery systems have only recently gained traction for potential use for antimicrobial delivery, especially for oral dental diseases compared to anticancer agents.^{10–12}

Generally, drug loaded porous SNPs are hindered by uncontrolled drug leakage and require further functionalisation to block the release of the drug. As described in **Chapter 3**, a newly designed SNP loaded with cetylpyridinium chloride (CPC), **CPC-SNP** was synthesised in a one-pot reaction. Following successful

characterisation and investigation of the drug release profile, CPC was found to only release when triggered with ultrasonication. It was thought the mechanical and thermal effects, produced from the tip of the ultrasonic scaler (dental tool), commonly used to clean dental plaque from the surface of teeth, was responsible for the release of CPC.^{13–15} Therefore, the development of **CPC@SNP** has provided potential a drug delivery formulation that could be used to treat dental infections.

Biofilms are naturally formed on the oral surfaces and insufficient removal can lead to dental diseases, such as dental caries (tooth decay) and periodontal diseases.¹⁶ Although biofilm formation and structure have been extensively researched it still poses many challenges in dentistry. An important feature is the extracellular polymeric substances (EPS) matrix in biofilms, which can act as a barrier for diffusion and penetration of antimicrobial agents, considerably reducing their efficacy.¹⁷ The aim of the work described in this chapter was to use the ultrasonic scaler to not only disrupt the biofilm, but to release CPC from the drug delivery system to penetrate and kill bacteria.

4.2. Chapter Outline

The **CPC-SNP** drug delivery system with a triggered release was investigated for enhanced, controlled killing of oral bacteria, *Streptococcus sanguinis* biofilms. The particles and US scaler were applied to examine the changes to the biofilm viability and structure, as shown in **Figure 4. 1**.

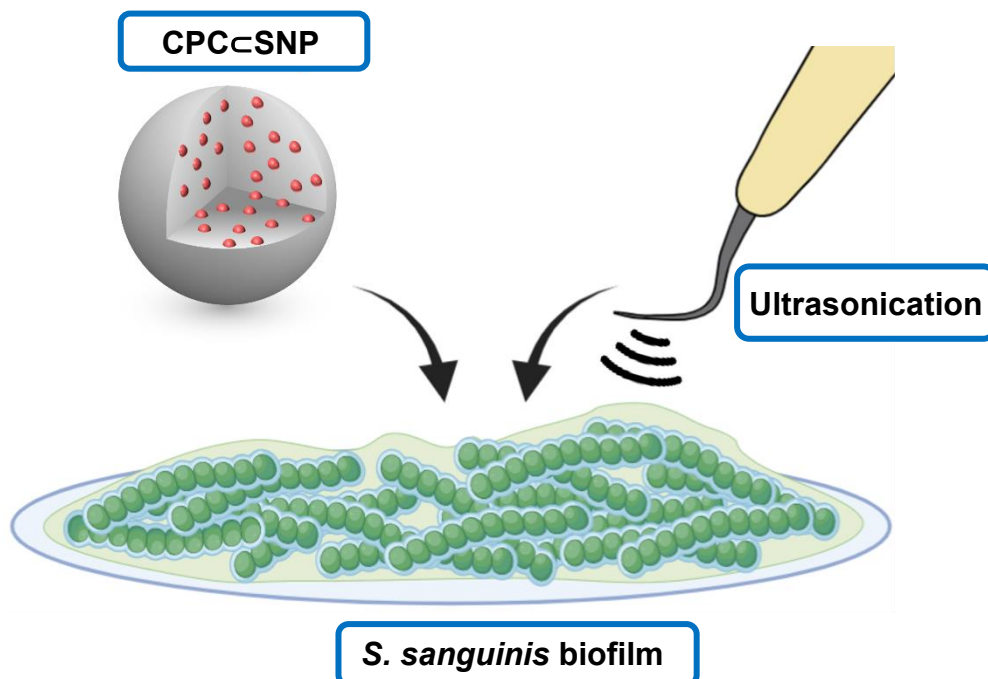


Figure 4. 1: Illustration of *S. sanguinis* biofilm treated with **CPC-SNP** combined with cavitation produced from an ultrasonic scaler. Diagram not to scale and created using BioRender.

Here in, it is reported the minimum amount of CPC and **Plain SNPs** required to kill *S. sanguinis*. The effect of uncontrolled release of CPC from different loaded SNPs using a simple agar diffusion assay is shown. Finally, the development of a biofilm model will be used to quantify the effect of **CPC-SNP** bacterial viability of *S. sanguinis* biofilms via two methods. The first by fluorescent live/dead staining for bacterial viability, based on membrane integrity. Confocal laser scanning microscopy (CLSM) facilitated visual findings and quantitative image analysis via a newly developed automated image

analysis tool by Mountcastle and co-workers¹⁸ was used. In parallel a more traditional method of colony counting (CFUs) was employed to determine live bacteria.¹⁹ The workflow plan followed can be seen in **Figure 4. 2**.

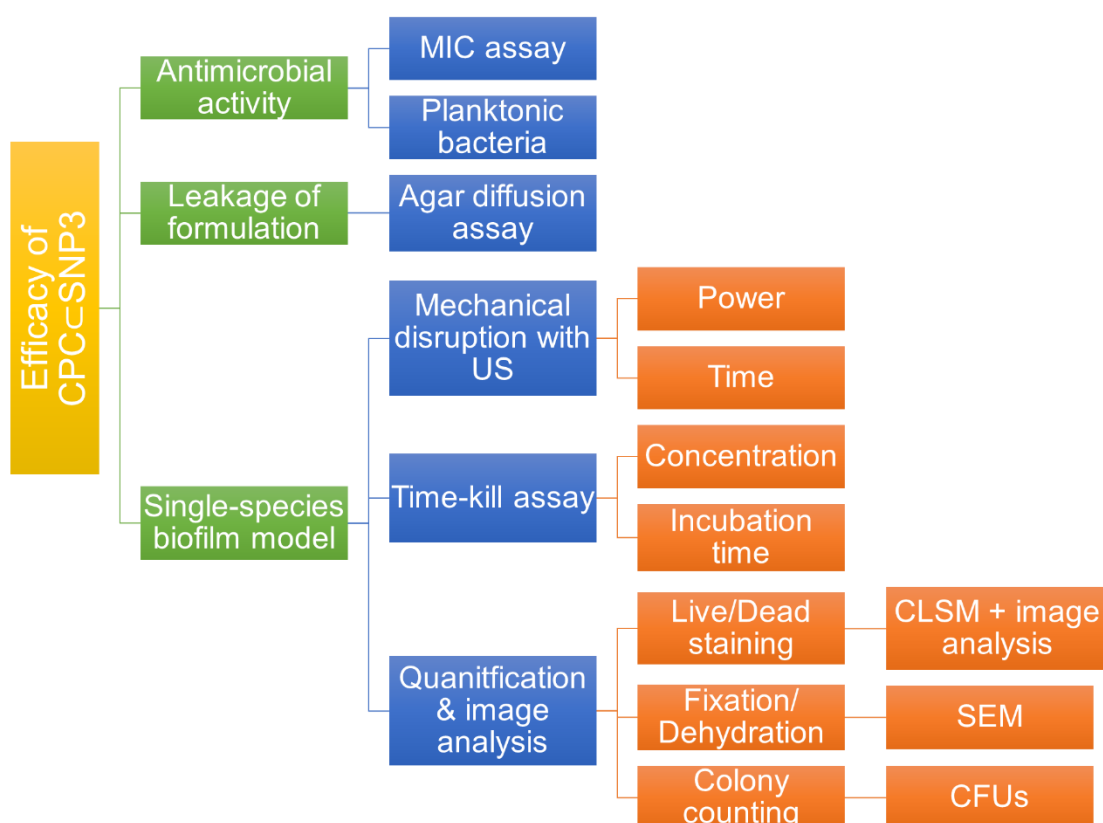


Figure 4. 2: Work-flow outline of key stages in the methodology of this chapter, highlighting the key experiments required to assess of the antimicrobial efficacy of **CPC_CSNP** formulation triggered with ultrasonic cavitation.

4.3. Results & Discussion

4.3.1. Antimicrobial susceptibility testing of CPC and CPC loaded

SNPs

Dental biofilms consist of complex communities of bacteria and interactions which are key for the etiology of dental caries and other oral diseases.²⁰ Certain bacteria, such as Streptococci and Lactobacilli are closely associated with caries.²¹ The antimicrobial agent cetylpyridinium chloride has been predominately incorporated into mouthwashes, in combination with other active agents to assist with the prevention of dental caries.^{22–24} To investigate the efficacy of the drug delivery system **CPC-SNP**, the susceptibility of bacteria to *S. sanguinis*, *S. mutans* and *E. faecalis* against the antimicrobial agent alone, pure CPC monohydrate, was first tested.

A minimum inhibitory concentration (MIC) assay was performed against *S. sanguinis* and *S. mutans*, as they are considered major pioneering organisms in plaque formation and *E. faecalis*, another prevalent bacterium associated with periodontal disease.^{25,26} The three species are Gram-positive bacteria and were representative microorganisms to test the drug antimicrobial activity. The MIC is the lowest concentration of an antimicrobial agent required to prevent visible growth of microorganisms over a 20 h period. This can be established visually by comparing the turbidity of bacteria in a well plate relative to the control, a standardised methodology followed from the British Society for Antimicrobial Chemotherapy Guidelines.^{27,28} The optical density at 600 nm (OD_{600nm}) was also recorded to support the visual MIC values obtained. The MIC of CPC in **Table 4.1** shows inhibitory values between 5-6 $\mu\text{g mL}^{-1}$ for all three tested bacterial species, which indicated the concentration of CPC required to inhibit growth of planktonic bacteria (free-floating).

Table 4. 1: Minimum inhibitory concentration (MIC) of CPC with bacterial strains *S. sanguinis*, *S. mutans* and *E. faecalis*. **Plain SNP** and **MSN** with bacterial strain *S. sanguinis* was determined visually and measured by the OD_{600nm} after 24 h incubation at 37 °C at 100 rpm. For all species the MIC was repeated in triplicates (n = 3).

	<i>S. sanguinis</i>	<i>S. mutans</i>	<i>E. faecalis</i>
CPC	< 6 µg mL ⁻¹	< 6 µg mL ⁻¹	< 5 µg mL ⁻¹
Plain SNP	> 16 mg mL ⁻¹	-	-
Plain MSN	> 16 mg mL ⁻¹	-	-

Although in the literature, MIC values of CPC against *S. mutans* and *S. sanguinis* have ranged from 0.12 – 5 µg mL⁻¹.^{29–31} This large range could vary for a number of reasons, for example different methods have uses other bacterial strains, grow medium to culture the bacteria and different initial concentration of bacteria and the time of determining the MIC. These changes can all influence the MIC values and induce the degree of susceptibility of bacterial species.³² To allow for a relevant comparison in this work, the same batch of CPC used in the synthesis of the drug delivery system, **CPC-SNP**, was used throughout the biological studies.

The MIC assay was also used to assess the antimicrobial activity of silica using concentrations between 0.125 – 16 mg mL⁻¹ of 300 nm **Plain SNP** and 200 nm **MSNs** against *S. sanguinis*. There was no visible change in bacteria viability and even when the OD_{600nm} measurements were taken after 24 h (see appendix section). Therefore, indicating silica particles did not have any antimicrobial activity against planktonic *S. sanguinis*, **Table 4. 1**.³³ From this point forward *S. sanguinis* strain was used for the

remaining experiments in this chapter. *S. sanguinis* was chosen because it is abundant in oral biofilms and is a commensal bacterial, that not only promotes oral health but can lead to pathogenicity given the opportunity. It is a primary coloniser in the oral cavity, aiding the attachment of succeeding organisms and plays a key role in oral biofilm development.²⁵ Also due to the complexity of biofilms, for ease it was better to understand the antimicrobial effect of **CPC-MSN** on a single species before introducing more bacterial strains into the experiments.

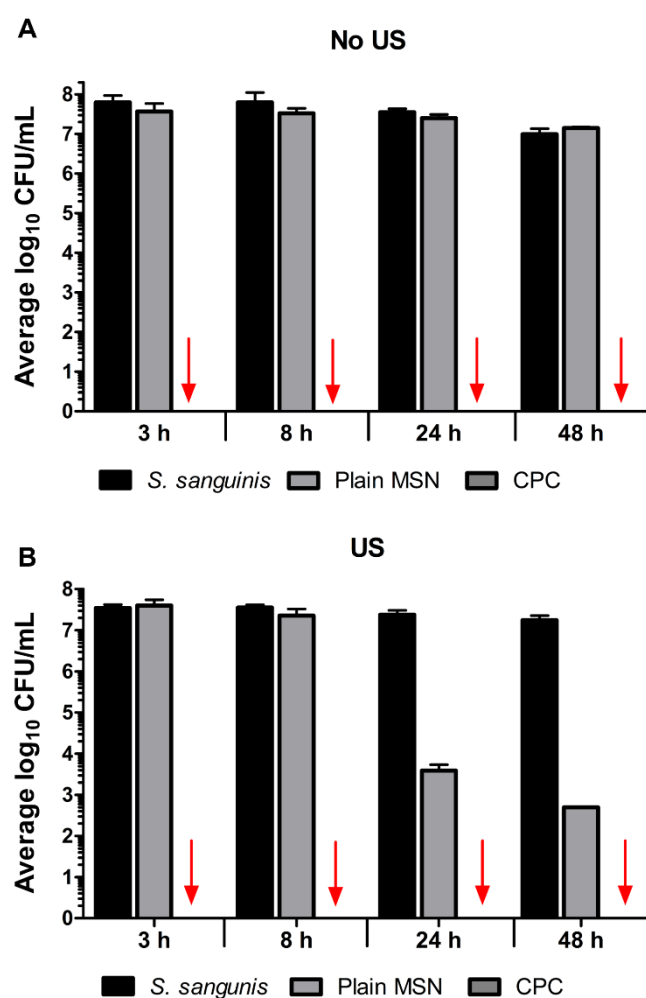


Figure 4. 3: The Bactericidal activity over 48 h of **Plain MSN** (6 mg mL⁻¹) and CPC (0.5 mg mL⁻¹) with and without US. The graph shows the surviving *S. sanguinis* bacteria after 3, 8, 24 and 48 h time points, reported as the average number of colony forming units (CFUs) with standard deviation (SD). **A)** No US and **B)** with US applied for 2 mins (P10) before samples were incubated. The red arrows show no bacterial colonies counted. Paired t-test showed the significant decrease in bacteria colonies of **Plain MSN** with time at 24 and 48h after initial US, with $p < 0.05$. The experiment was repeated in triplicate (n=3).

As well as, the MIC assays, the bactericidal activity of CPC and **Plain MSN** was examined by performing a time-kill assay.³¹ A *S. sanguinis* bacterial suspension was inoculated with 0.5 mg mL⁻¹ of CPC (the concentration commonly found in mouthrinses) and 6 mg mL⁻¹ of **Plain MSN** for 48 h. The bactericidal activity was monitored and determined by the standard Miles and Misra colony counting method.¹⁹ The cell viability was reported by the colony forming units per mL (CFU/mL) at time points taken at 3, 8, 24 and 48 h. The results in **Figure 4. 3A** showed that without applying US to the bacteria the viability remained between 7 to 8 log₁₀ over a 48 h period. This was also observed with **Plain MSNs**. However, a rapid bactericidal effect was exhibited by CPC after 3 h. In comparison, **Figure 4. 3B**, applying 2 min US to the samples before incubation, showed to decrease the bacterial viability after 24h with **Plain MSNs**. More than a 4log₁₀ difference was determined compared to bacteria only with US after 24 h. Therefore, particles could cause cell death in combination with US, rather than US alone. US for 2 min could cause disruption to the bacterial membrane enabling **Plain MSNs** to enter the bacteria , reducing the viability. Note that **Plain SNPs** were not used in this experiment, but was thought to have a similar effect on *S. sanguinis*.

Furthermore, the antibacterial efficacy in planktonic suspensions tests can differ significantly from the efficacy against bacteria in biofilms.³⁴ In particular, CPC's minimum biofilm inhibitory concentration (MBICs) has been reported to range from 7.81 to 15.63 µg mL⁻¹,²⁹ dependant on the species in the biofilm. Therefore, it would be more relevant for efficacy studies of **CPC-SNP** against bacteria in biofilms.

Before biofilm studies could be conducted it was necessary to test for the antimicrobial susceptibility to silica-drug formulations without any US applied for triggered release.

Agar diffusion methods have been used since the 1940's and approved by the Clinical and Laboratories Standards Institute. This method is used routinely for antimicrobial susceptibility testing.^{35,36} Therefore, an agar diffusion assay was an appropriate primary method to measure and compare the zones of inhibition of drug loaded SNPs applied to the wells created in the agar plates. The advantages of this technique included simplicity, low cost, and screening of several samples at once.³⁷

In **Figure 4. 4**, the agar diffusion assays show the results of the antimicrobial activity of CPC alone, unloaded and drug loaded silica samples against *S. sanguinis*. Circles were used to demonstrate the zones of inhibition, and these were then measured to determine the effect. Plate 1 showed the measured sizes of inhibitory zones from CPC, **CPC \subset MSN** and **CPC@MSN** were 12- 16 mm after 24 h. This confirmed CPC antimicrobial activity in the absence of silica, killing the bacteria uncontrollably. However, the assay also validated uncontrolled drug release from conventional drug loaded silica particles. These were **templated CPC \subset MSN** and **adsorbed CPC@MSN** samples that had be synthesised alongside **CPC \subset SNP**. They experienced rapid leakage of the drug. In comparison, **CPC \subset SNP** showed no zones of inhibition. Therefore, no visible changes to the bacteria supports that **CPC \subset SNP** synthetic procedure have created a system to delay the release of the CPC up until 24 h. These results were promising, by showing the system has the potential for controlled antimicrobial activity.

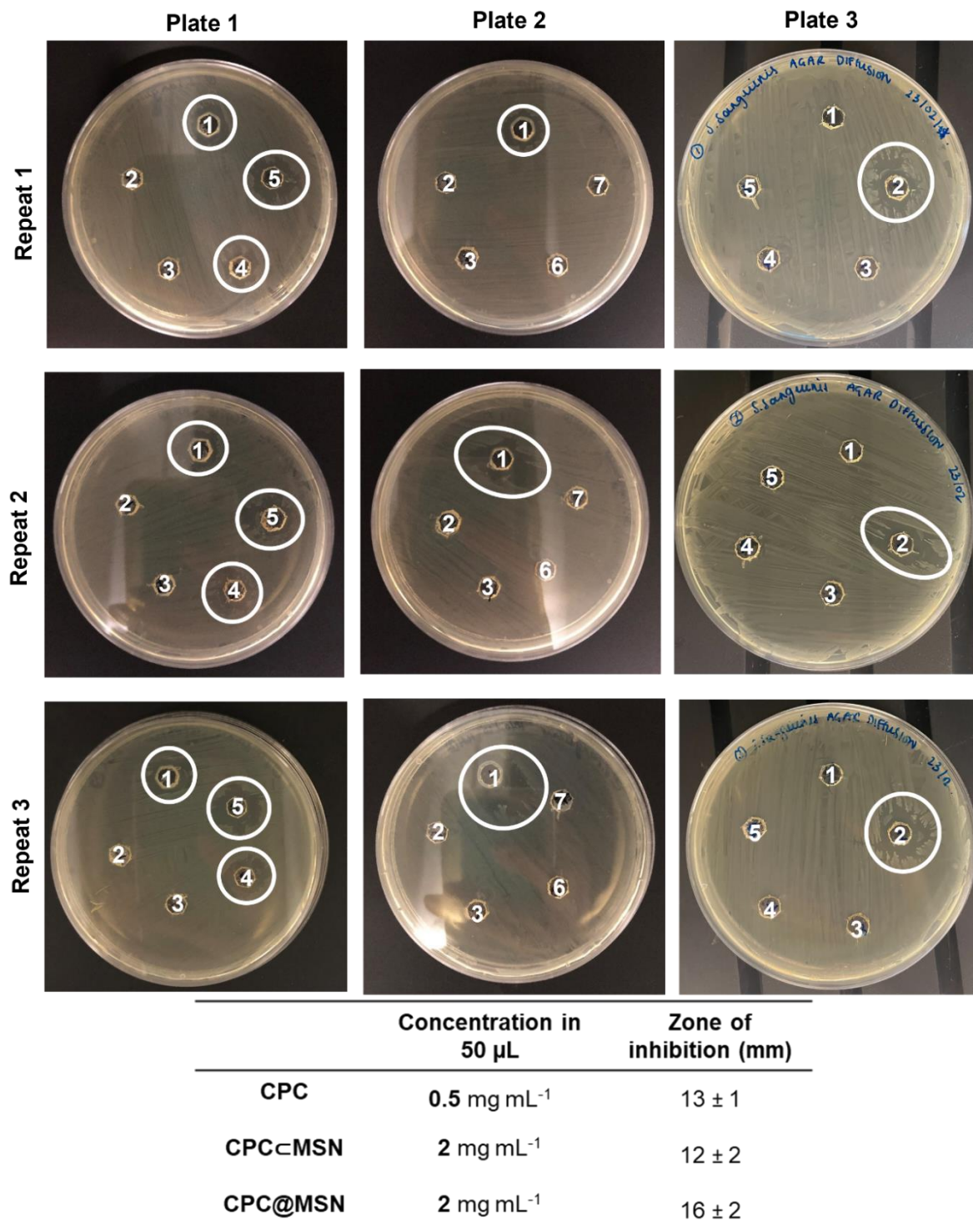


Figure 4. 4: Agar diffusion assay showing zones of growth inhibition around wells with 50 μ L of sample. Plate 1 shows: 1: **Pure CPC** (0.5 mg mL⁻¹), 2: **Plain MSN** (2 mg mL⁻¹), 3: **ultrapure H₂O**, 4: **CPC@MSN** (2 mg mL⁻¹), 5: **CPC@MSN** (2 mg mL⁻¹). Plate 2 shows: 1: **Pure CPC** (0.5 mg mL⁻¹), 2: **Plain SNP** (2 mg mL⁻¹), 3: **ultrapure H₂O**, 6: **CPC@MSN** (2 mg mL⁻¹), and 7: **CPC@MSN** (5 mg mL⁻¹). Plate 3: 1: **H₂O**, 2: **Pure CPC** (0.036 mM, 13 μ g mL⁻¹), 3: **CPC@MSN** (2 mg mL⁻¹), 4: **CPC@MSN** (10 mg mL⁻¹) and 5: **Plain SNP** (10 mg mL⁻¹). The diameters of the zones of inhibition were measured and averages and SD calculated (n=3). Plates inoculated with *S. sanguinis*.

4.3.2. US-responsive CPC-SNP tested on single-species biofilm model

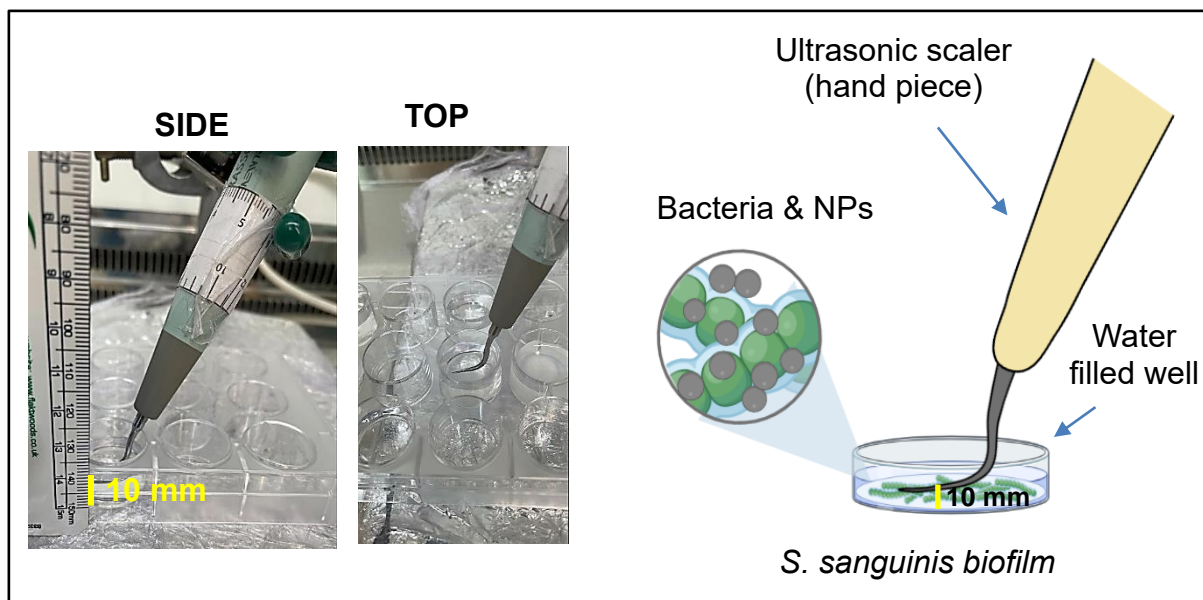


Figure 4. 5: Images and schematical representation of experimental set-up of the ultrasonic scaler for biofilm viability assay. A well plate with 72 h grown *S. sanguinis* biofilm covered Thermanox coverslip (13 mm diameter) was placed inside a well and the coverslip secured with double sided tape to ensure it remained in position during US. A solution (3 mL) containing the treatment was pipetted into the well. The ultrasonic scaler (Satelec P5 Newtron XS scaler, Acteon Group, USA) with tip 10P was fixed parallel and 10 mm away from the biofilm using a clamp stand to aid the positioning. The scaler was operated at a power setting of 10 (medium power) for 10s.

The initial antimicrobial susceptibility testing performed as described in **Section 4.3.1** enabled the development and aided the design of a biofilm model for further bactericidal activity evaluation. Biofilm communities are already complicated because their microorganisms are protected within an extracellular matrix of sugars, proteins, and DNA.^{38,39} These characteristics combined with the tolerance to antibiotics significantly increases the difficulty to prevent or eradicate existing bacteria present within the biofilm structure.^{40–43} Therefore, this study focused on a single-species *S. sanguinis* biofilm model that was grown for 72 h in a brain and heart infusion (BHI)

broth. *S. sanguinis* was grown over this period to ensure sufficient thickness and density of the biofilm for quantification, as shown in **Figure 4. 5**.

In the following studies, CLSM was used to image stained bacteria and quantify the amount of dead and live bacteria. SYTO 9 is a green, fluorescent stain, which stains all intact and membrane disrupted cells. Whilst PI stains only those with a compromised cell membrane by binding to nucleic acids. This results in enhanced red fluorescence. The fluorescence can be quantified by image analysis software, which had previously been validated for determination of viability of bacteria with varying morphologies.¹⁸ Plate counts (CFU/mL) were conducted in parallel to verify viability and ultimately determine the efficacy of **CPC-SNP** with ultrasonication.¹⁹

4.3.3. Mechanical disruption of *in vitro* *S. sanguinis* biofilms

The mechanical disruption of biofilms with US has been previously investigated for bacterial removal from surfaces. Especially for root canal treatments and from dental implants.^{44–48} Cavitation produced from ultrasonic devices has been found to weaken and physically remove biofilms, which reduces the antimicrobial resistance, as less antimicrobial action would be required and could enhance the removal when combined with antibiotics or nanoparticles.^{49,50} The removal process is dependent on time, frequency and intensity of cavitation applied. In this study the effect of applying cavitation on *S. sanguinis* biofilms was evaluated as described below.^{15,51}

Previously, in **chapter 3 (Section 3.3.3)**, the *in vitro* drug release studies were conducted with a maximum power setting (P20) at 2-minute intervals. However, these conditions removed majority of the biofilm from the coverslips due to the forces induced by the US tip.^{50,52} Therefore any potential antimicrobial effect of **CPC-SNP**

would be challenging to visualise with CLSM imaging.⁵¹ In this case, US was being used for drug release, rather than testing removal of biofilms from a surface. In a study published by Vyas *et al.*⁵¹, it was reported significant removal of the bacterial biofilms from titanium dental implant surfaces by using the same ultrasonic scaler (low power P10, 1 mm, 60s) used in this work. Also in the drug release studies 2 minutes US at maximum power (P20) would be too long for patient treatment, especially at maximum power setting (P20), which could cause damage to the tooth and gingiva. As a result, to ensure the biofilm remained attached to the surface of the coverslips a low power setting on the ultrasonic scaler was used. Also, to prevent the coverslip sample moving around inside the well, the scaler tip had to be positioned at distance of 10 mm parallel to the biofilm.

In **Figure 4. 6**, CLSM images showed the condition of the biofilm after exposure to US, with low power (P10) for either 5 or 10 seconds. The 2-dimensional (2D) images obtained after US were compared to bacteria with no US (negative control). The area of alive (green) bacteria was far more evident than the area of dead (red) bacteria present. To further observe the affect, several slices of images were obtained and examined throughout the depth of the biofilm sample, called z-stacks and combined to form 3-dimensional (3D) images. It was notable that *S. sanguinis* viability remained consistent throughout the sample and US did not cause complete removal of the biofilms. There are areas, with 10 seconds of US, where the biofilm appears thinner, indicating that US could cause some disruption. In the literature, the production of cavitation bubbles has been investigated with high-speed imaging using the same ultrasonic scaler device in this work. Images were captured and showed power settings

less than P10 produced little to no cavitation.⁵³ Therefore, the US tip could produce cavitation bubbles using a power setting of P10 that could have an effect on the biofilm.

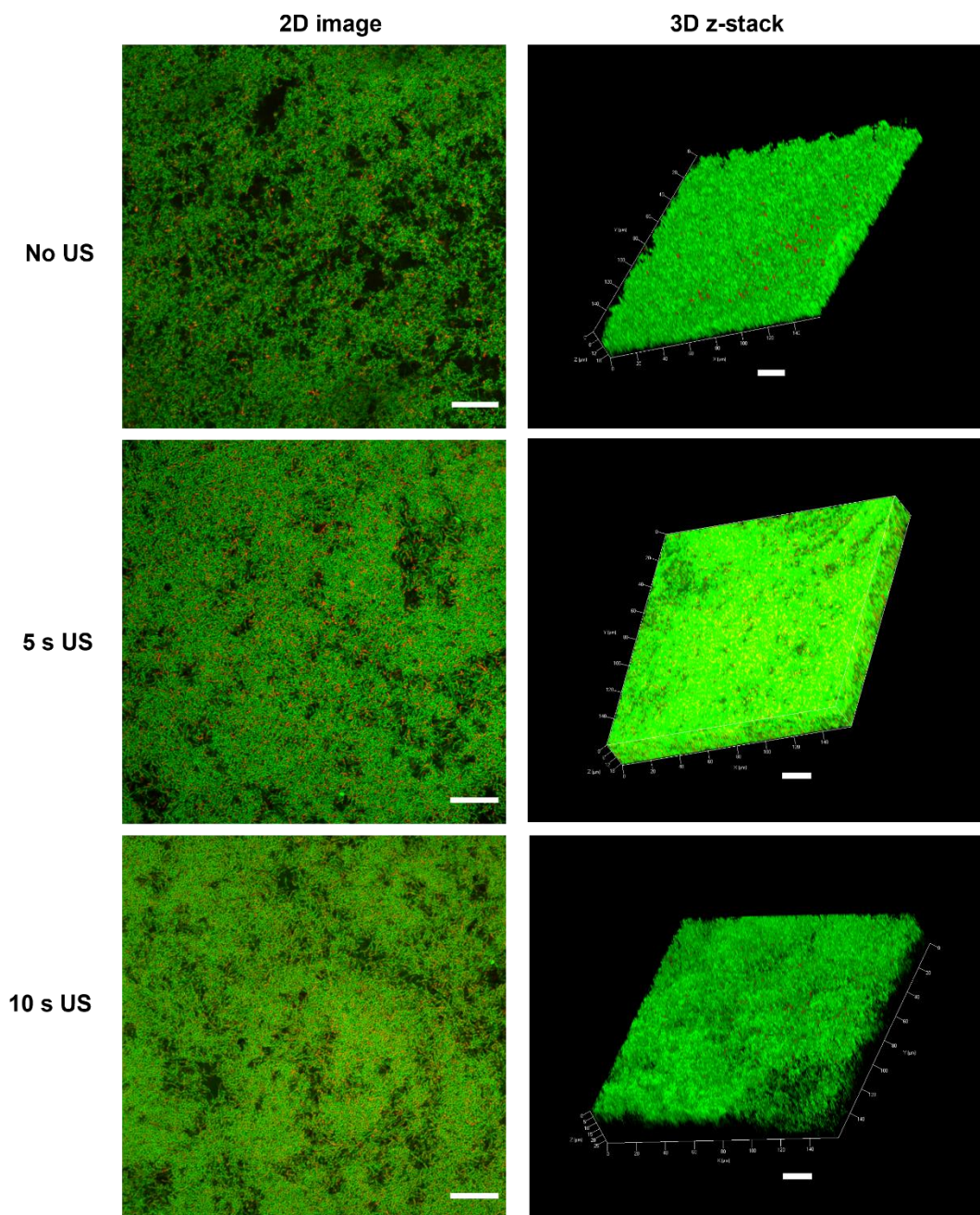


Figure 4. 6: 2D and 3D (z-stacks) CLSM images show visual representation of biofilms without and with US (P10). Scale bar represents 20 μm in 2D and 3D images.

The CLSM images were processed to quantify the average cell viability as a percentage. This was based on the total area of bacteria and area of dead bacteria, to calculate the live bacteria. According to the results in **Figure 4. 7A**, there was no significant difference in the mean percentage viability values by applying US on the biofilm surface for 5 s ($p = 0.2529$) or 10 s ($p = 0.0567$) compared to the negative control. To investigate the biofilm condition from the surface to deeper within the biofilm, the analysis protocol was applied to each image of the Z-stack images shown

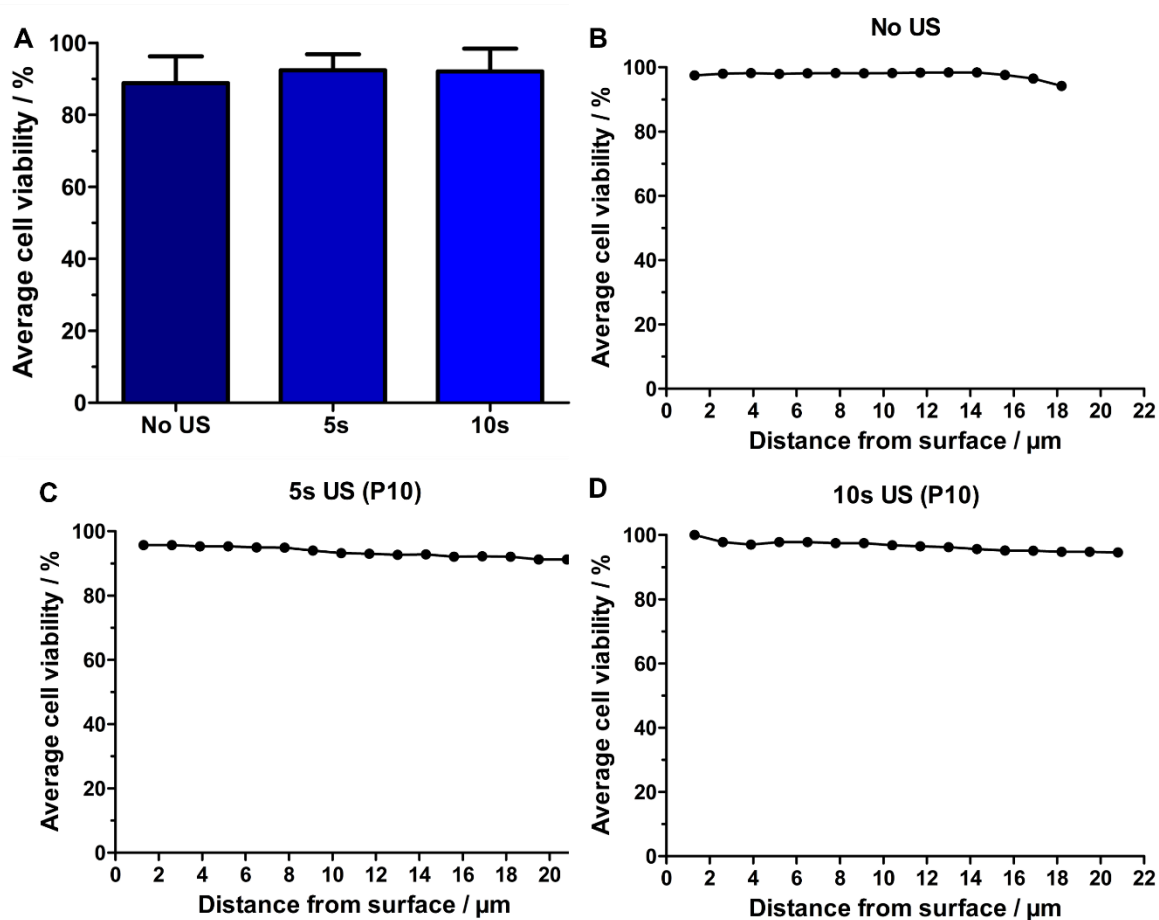


Figure 4. 7: Mechanical disruption of *S. sanguinis* biofilms, US was applied for 5s or 10 s at medium power (P10). **A)** Mean cell viability with standard deviation of *S. sanguinis* with no US (negative control) 90.27 ± 5.37 %, 5 s US 92.37 ± 4.44 % ($p = 0.2529$) and 10 s US 93.65 ± 4.11 % ($p = 0.0567$). No statistical significance on cell viability with US was shown, with $p < 0.05$ considered to indicate statistical significance. Image analysis was performed on at least five confocal images of each of three biological replicates ($n = 3$) and Mann Whitney U, unpaired t-test was used for the statistical analysis. **B-D)** Shows the cell viability though the depth of one biofilm.

in **Figure 4. 7B-D**. This showed that the viability remained consistent throughout the biofilm, up to 22 μm and US had little to no effect on viability. Therefore, for further studies with the ultrasonic scaler the parameters established were for 10 seconds at a power setting of P10 at 10 mm from the biofilm surface.

4.3.4. SEM imaging of biofilms

In parallel to the live/dead staining assays and colony counting methods, samples were imaged using SEM. From the images in **Figure 4. 8**, the structure of *S. sanguinis* biofilms with and without US were compared, as well as when treated with **CPC-SNP** and CPC. The characteristic appearance of *S. sanguinis* bacteria displayed chains or pairs of oval shaped cocci, as a result of cell division. After US was applied, the overall architecture of the biofilm changed. The long chains of cocci appeared to have separated and a string-like network was observed. This indicated that the ultrasonic device had possibly mechanically disrupted the biofilm due to the acoustic cavitation produced from the US, exposing more of the EPS matrix, appearing as thread like strands. The morphology of the bacterial cells had not changed and appeared to be structurally undamaged in accordance with results obtained with the previous viability assessments.

The SEM imaging clearly showed the difference with **CPC-SNP** before and after US. Large clusters of particles can be seen to lay on top of the bacterial colonies without using US. However, with US, the entanglement of the small, spherical **CPC-SNP** particles, indicated by the red arrows, is more visible with *S. sanguinis*. Also, the exposure of threads are possibly from the EPS structure. Treatment of the oral biofilms

with CPC in both instances showed no change in the bacteria's structure, but with the US the same string-like structure was displayed.

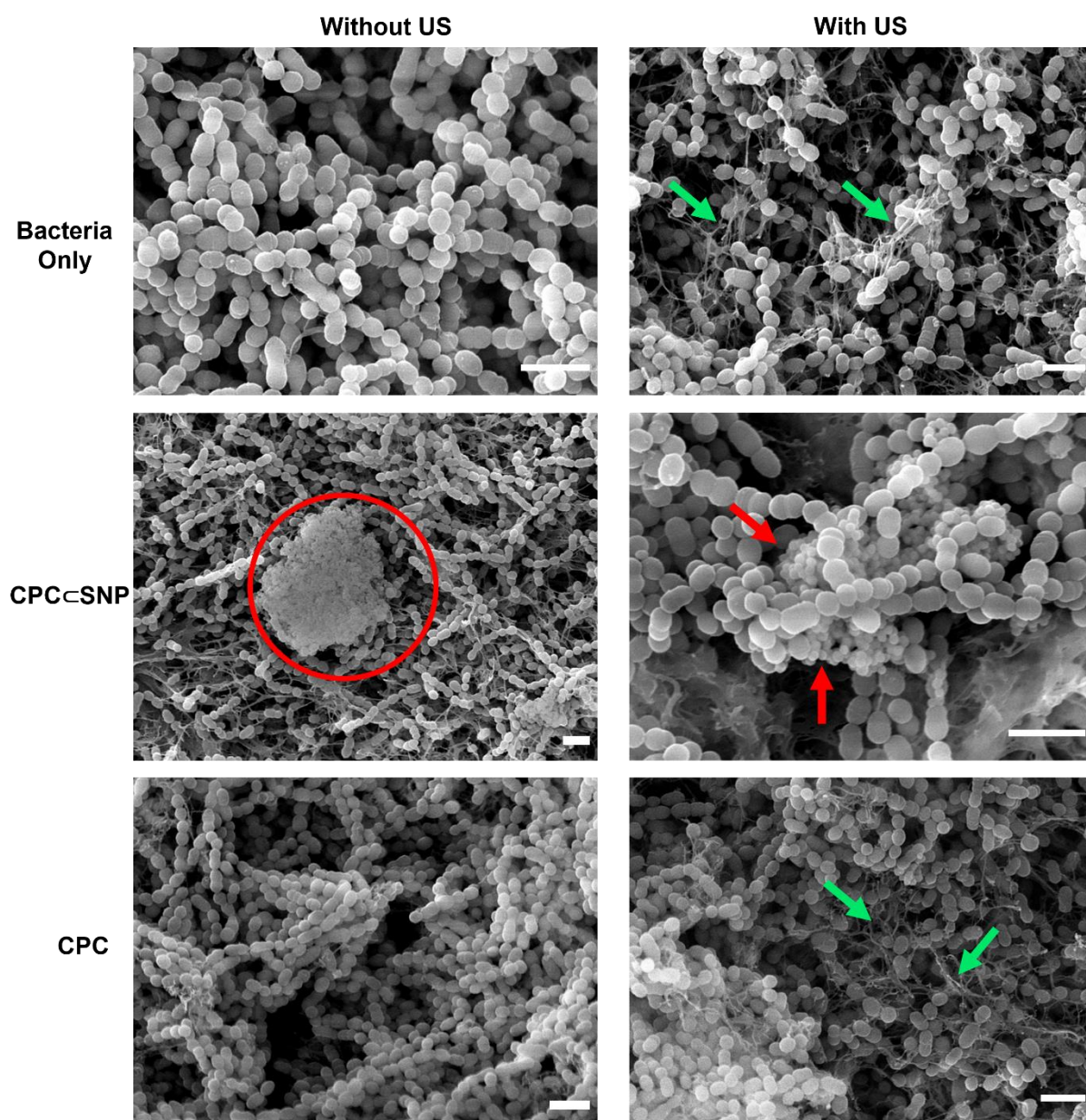


Figure 4. 8: Comparison of *S. sanguinis* biofilms with and without US and treated with **CPC-SNP** (2 mg mL⁻¹) and CPC (0.5 mg mL⁻¹). Arrows indicate changes to biofilm (green) and presence of drug loaded particles (red). Scale bar represents 2 μ m and magnification between 9-12 K x.

Employing the ultrasonic scaler could better dispersion of the particles so they can travel deeper into the biofilm. It is believed the EPS composition and charge can influence the interactions that can occur with NPs and free drug. From a study conducted by Fulaz *et al.*,⁵⁴ they tailored the surface charge of mesoporous silica nanoparticles (MSNs). They found positively charged MSNs were more inclined to cluster around the bacterial cells, due to strong electrostatic attraction with the negative peptidoglycan cell wall of *Staphylococcus aureus*, whereas negatively charged MSNs interacted greatly with its EPS matrix surrounding the cell. In this case, it is not clear if bacteria are dead from the SEM images because of the time frame. Therefore, the antimicrobial effect of **CPC@SNP** compared to **Plain SNP** and free CPC will need examination by determining the live and dead bacteria.

4.3.5. Time-kill assay with **CPC@SNP**

To evaluate the antimicrobial effect of the developed **CPC@SNP** sample, a particle solution was first added to the biofilm and US applied (P10, 10s). After, the biofilms were treated they were incubated for 5, 15 or 30 min. The bacterial viability was assessed to examine if the incubation time made a difference to the *S. sanguinis* biofilm after US treatment. In **Figure 4. 9**, **CPC@SNP** treated biofilms were compared to control samples of US only and CPC (0.5 mg mL⁻¹) with US, both incubated for 30 min. Biofilms treated with free CPC, showed a 55% decrease in cell death. Note that the uncertainty in the bacterial viability was due to only 5 random area were selected to image for each biological and technical replicate. Furthermore, biofilms treated with **CPC@SNP** with US and followed by 5, 15 and 30 min incubation, showed an average cell viability of $52 \pm 23 \%$, $48 \pm 25 \%$ and $4 \pm 2 \%$, respectively. The data showed a significant reduction in cell viability with longer incubation time after **CPC@SNP** with

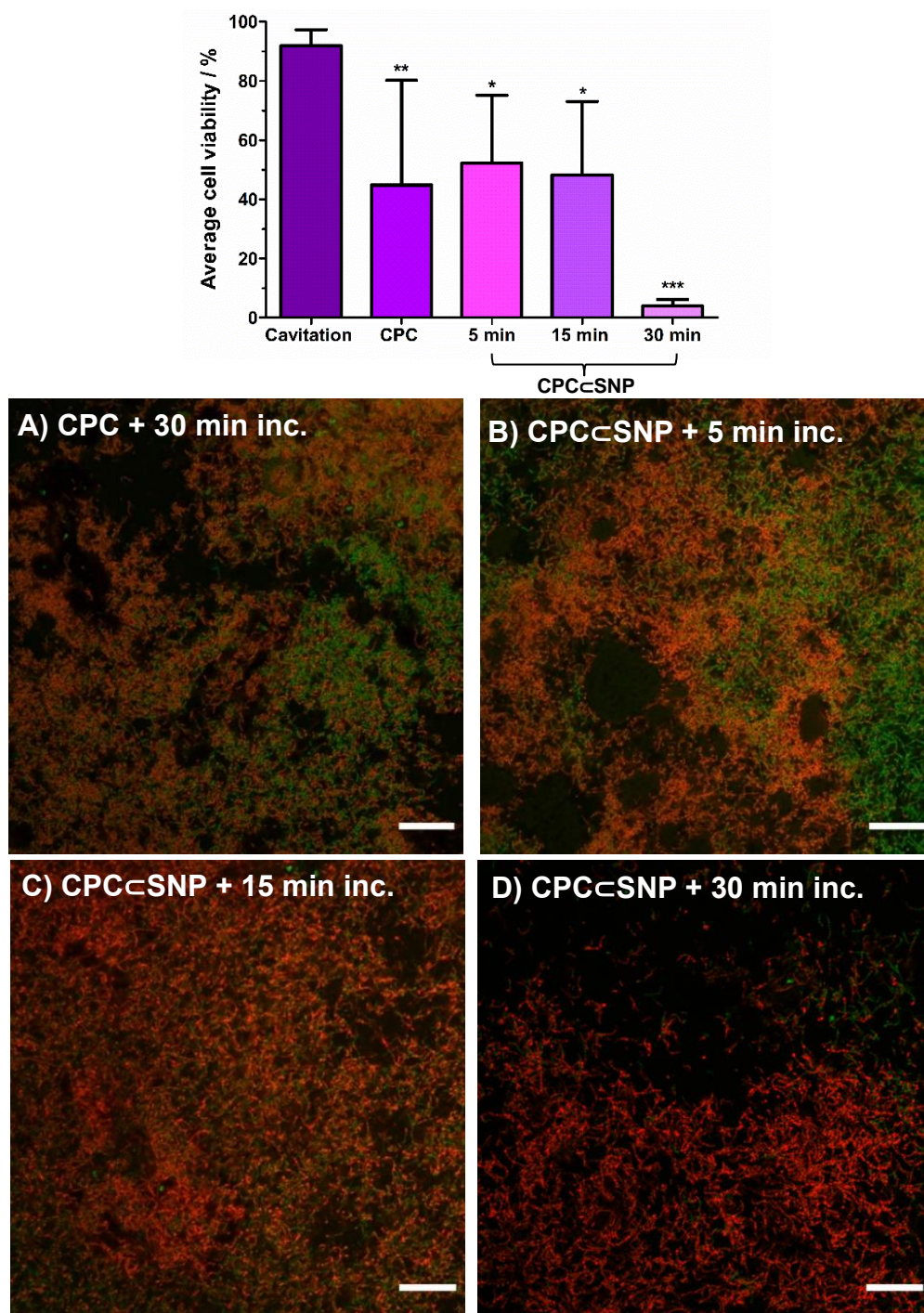


Figure 4. 9: Time-kill assay: the bactericidal effect of CPC in a drug delivery system with longer incubation times after using US on 72 h grown *S. sanguinis* biofilms. The results are represented by the mean cell viability percentage \pm standard deviation, (n=5) of three independent experiments. The statistical difference of the reduction in cell viability was compared to US only, was performed using a non-parametric Kruskal Wallis test and Dunn's multiple comparison post-test (*p < 0.05, **p < 0.01, ***p < 0.001). A randomly selected CLSM image is shown in **A)** CPC + 30 min incubation (positive) and **B-D) CPC@SNP** (10mg mL⁻¹) after 5-, 15- or 30-min incubation. Scale bar 20 μm

US than only using US or drug alone with US. This was visually supported by the images in **Figure 4. 9A-D**, where areas of red show a killing action of the biofilm.

Additional information was obtained to support the results displayed in **Figure 4. 9**. The 3D images were complimented by the depth profile analysis of the cell viability, shown in **Figure 4. 10**. Treatment with only CPC, showed to have greater influence on surface of the biofilm. Similar effects were observed with **CPC-SNP** using 5 and 15 min incubation periods. However, increasing the incubation time to 30 min exhibited significant cell death throughout the biofilm.

From **Figure 4. 9** and **Figure 4. 10**, the findings could suggest that CPC lacked diffusion through the biofilm network. Even though a concentration a hundred times greater than the MIC value of bacteria measured in a suspension culture was used. The positive charge of CPC facilitates the interaction with the negatively charged bacterial membrane causing disruption.^{31,55} Hence, the dramatic cell death observed closer to the biofilm surface. The bacterial susceptibility with free drug fluctuated and simultaneous use of US did not enhance the cell death. In comparison, treatment of **CPC-SNP** with US showed stronger red fluorescence with increasing incubation. This indicated that *S. sanguinis* cell membranes were disrupted and permeable. Therefore, the combination of drug released from silica structure and the US-trigger could induce a synergistic antimicrobial effect.

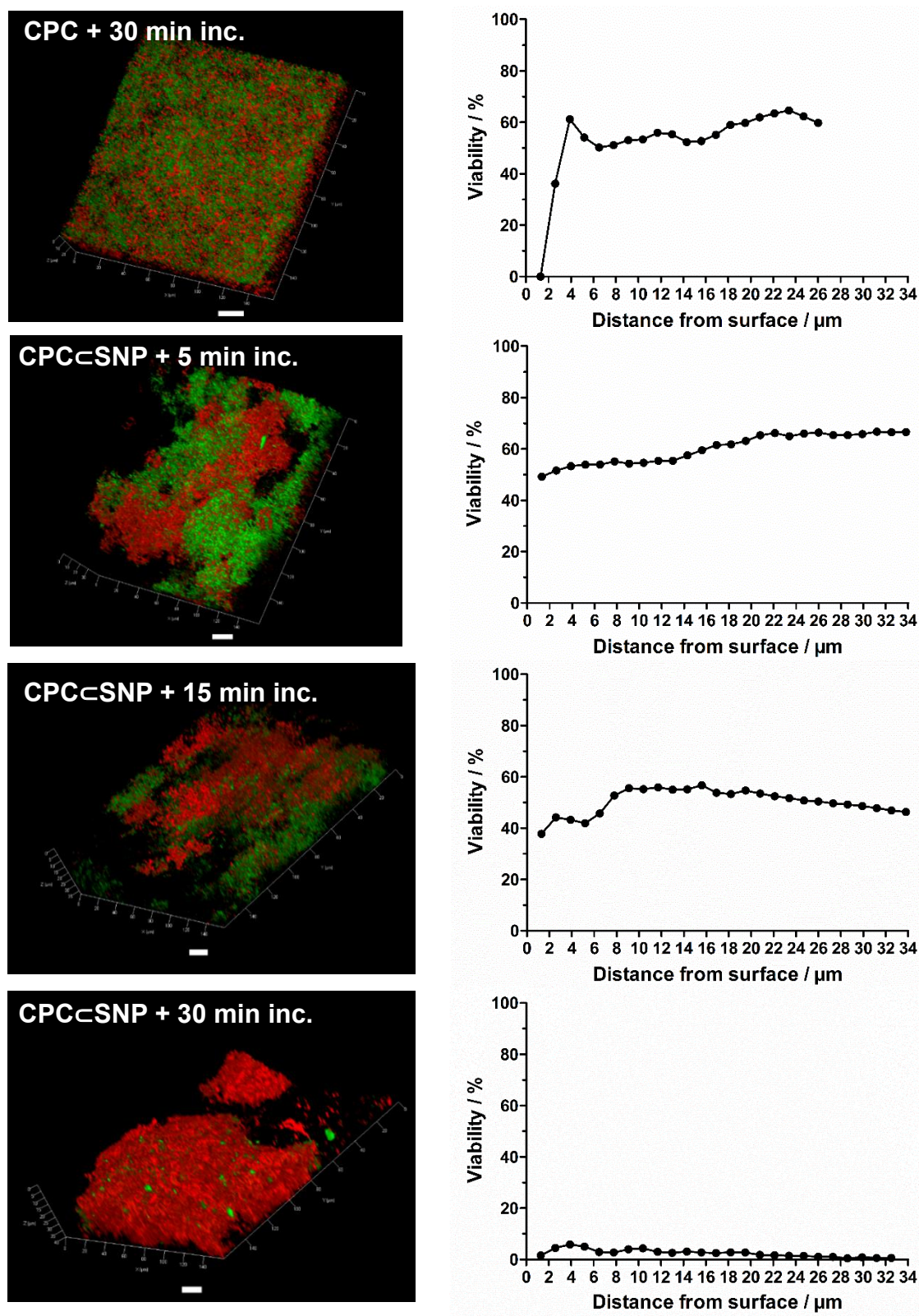


Figure 4. 10: A 3D representation of CLSM images obtained by z-stacks and analysed with ImageJ to quantify the mean percentage of live bacteria \pm SD (n=3). Confocal images show image scale bar of 20 μm .

After the initial biofilm studies, the amount of drug released with 10 s cavitation and 30 minutes of incubation was determined. This was done by measuring the released CPC absorbance ($\lambda_{260 \text{ nm}}$, $\epsilon_{4190 \text{ M}^{-1} \text{ cm}^{-1}}$) using UV-Visible spectroscopy, as shown in **Figure 4. 11**. The concentration of CPC released was $14 \mu\text{g mL}^{-1}$, which was over twice the amount of the MIC value for planktonic *S. sanguinis*. Therefore, adequate drug release could kill bacteria and could be compared to CPC alone under the same conditions.

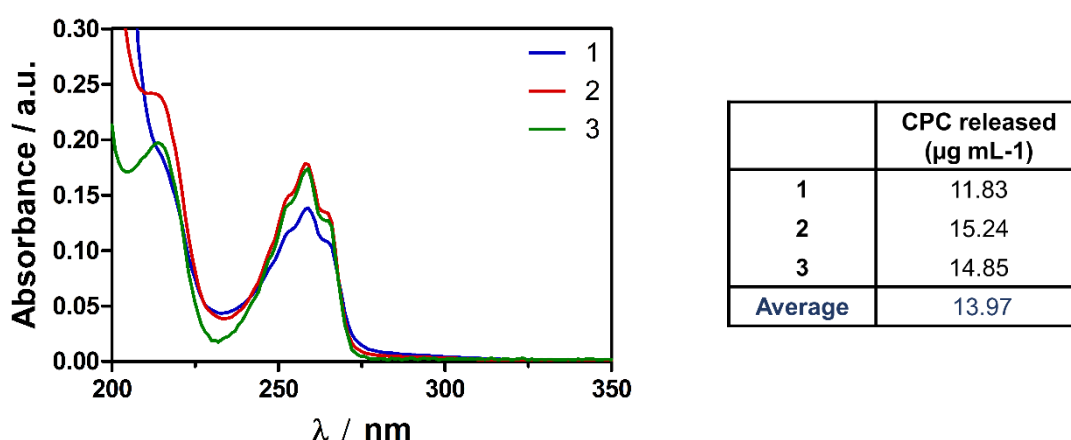


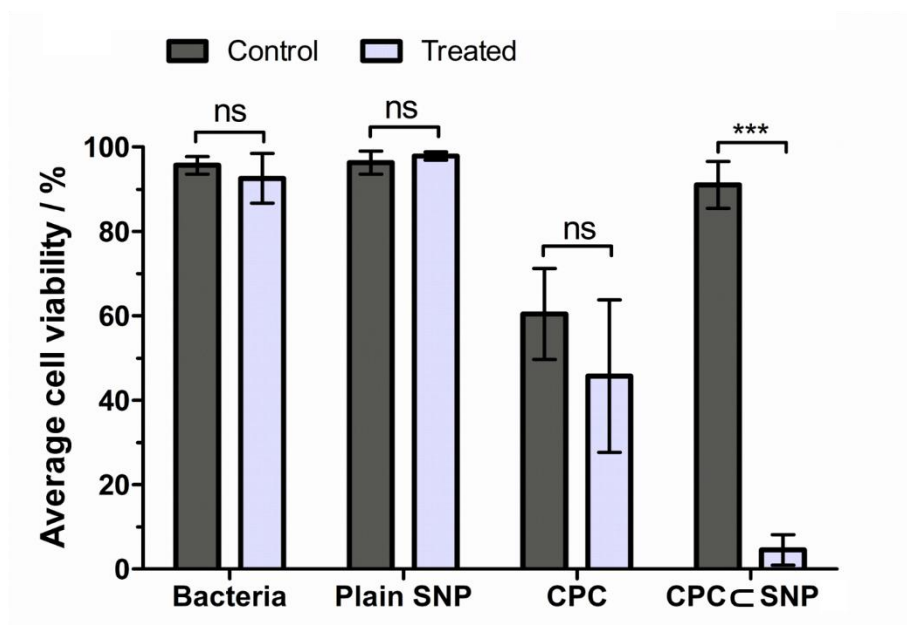
Figure 4. 11: Absorbance of CPC ($\lambda_{260 \text{ nm}}$, $\epsilon = 4190 \pm 0.12 \text{ M}^{-1} \text{ cm}^{-1}$) measured by UV-Visible spectroscopy to determine the amount drug released from **CPC@SNP** (10 mg mL^{-1}) triggered by US (P10, 10s) with 30 min incubation at 37°C . The table show the average CPC calculated from each replicate ($n=3$) for biofilm treatments.

4.5.6. The synergistic effect of ultrasonication and **CPC-SNP** on *S. sanguinis* biofilms

To further evaluate the synergistic effect of **CPC-SNP** triggered with US, the sample was compared to other drug loaded silica particles and control samples. The single-species *S. sanguinis* biofilms were exposed to drug loaded particles formulated with CPC, CPC alone and **Plain SNP** with and without US. This was to determine the cell viability with live/dead staining using CLSM imaging (**Figure 4. 12A**) and complimented by CFU-plating (**Figure 4. 12B**).

Both methods showed live bacteria with negligible change in biofilm viability with the control, no US ($95.7 \pm 2.1 \%$, 7.6 CFU/mL) and when treated with US ($92.6 \pm 5.9 \%$, 7.7 CFU/mL). **Plain SNP** (10 mg mL^{-1}) also exhibited the same behaviour and no change in viability was observed. In accordance with previous results from MIC and agar diffusion studies, where both approaches highlighted no antimicrobial activity of silica materials at high concentrations. In this study, image analysis and colony counting confirmed $\sim 95 \%$ viability of the biofilm. In contrast, a higher killing efficacy towards *S. sanguinis* biofilms was observed by a decrease in the proportion of live bacteria upon addition of CPC concentration of $14 \mu\text{g mL}^{-1}$. Using imaging analysis, the average percentage of alive bacteria was $60.4 \pm 10.8 \%$ and reduced slightly to $45.7 \pm 18.1 \%$ with US. However, the difference was not statistically significant.

A Bacterial viability from live/dead imaging analysis



B Bacterial viability from colony counting of live bacteria

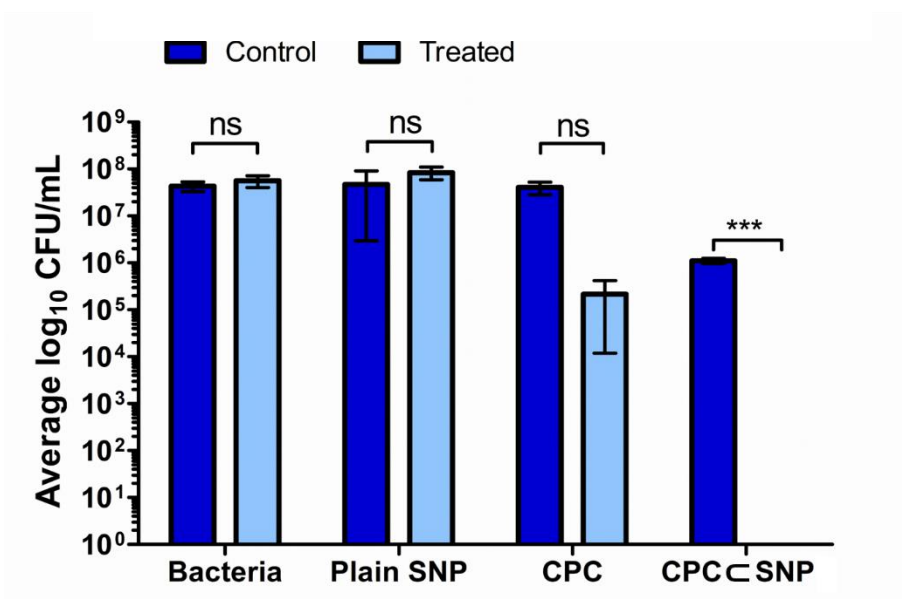


Figure 4. 12: Mean and standard deviation of bacterial viability using **A)** live/dead staining **B)** CFU counts (log₁₀ CFU/mL). *S. sanguinis* biofilms exposed to the following treatments: **Plain SNP** (10 mg mL⁻¹), **CPC** (14 µg mL⁻¹) and **CPC-SNP3** (10 mg mL⁻¹), without (control) and with (treated) US (P10, 10s) followed by 30 min incubation. Analysis of statistical significance, non-parametric Mann Whitney U test was used (**p*<0.05, ***p*<0.01 and ****p*<0.001).

CFU data showed a similar trend when CPC was applied with US, which led to a slight reduction of CFU by $<2 \log_{10}$ and again statistical tests showed no significance. The combination of ultrasonic cavitation and drug release from **CPC-SNP** particles led to stronger red fluorescence from the biofilms, showing the bacterial viability was reduced to $<4 \%$. The cell viability was reduced by $>6 \log_{10}$ compared to the control **CPC-SNP** without cavitation, when quantified using the CFU method. Both approaches showed a significant reduction in eradicating a single species cultured biofilm.

Moreover, the bacterial viability determined in **Figure 4. 12**, was validated with 3D images of the biofilm and analysis of the depth profile was based on live/dead bacteria, shown in **Figure 4. 13**. The untreated control of *S. sanguinis* and treated with US mostly showed green and no red fluorescence. The same with **Plain SNP**, having no influence on the bacterial viability throughout the depth of the biofilm. Treatment of CPC with US improved the antimicrobial activity, as seen by effecting bacteria deeper in the biofilm. Ultimately, **CPC-SNP** exhibited the two contrasting results in viability from the depth profiles.

Different antimicrobial efficacies have been found by treatment of CPC alone and **CPC-SNP**. Even though the drug concentration used to treat the biofilm was the same. In the literature, it is reported that the diffusion of CPC in *S. mutans* biofilms is slowed by an increase in the EPS density, which is usually triggered by the increase in sucrose concentration included in the culture medium.⁵⁶ Additionally, reports have suggested the micelle structure of CPC could experience steric exclusion from the biofilm matrix, causing bioaccumulation of the antimicrobial agent in certain regions.⁵⁷ This would explain the variability in percentage viability exhibited by CPC treatment,

which showed CPC did kill some areas of biofilm due to attractive interactions between CPC and bacteria.^{56–58}

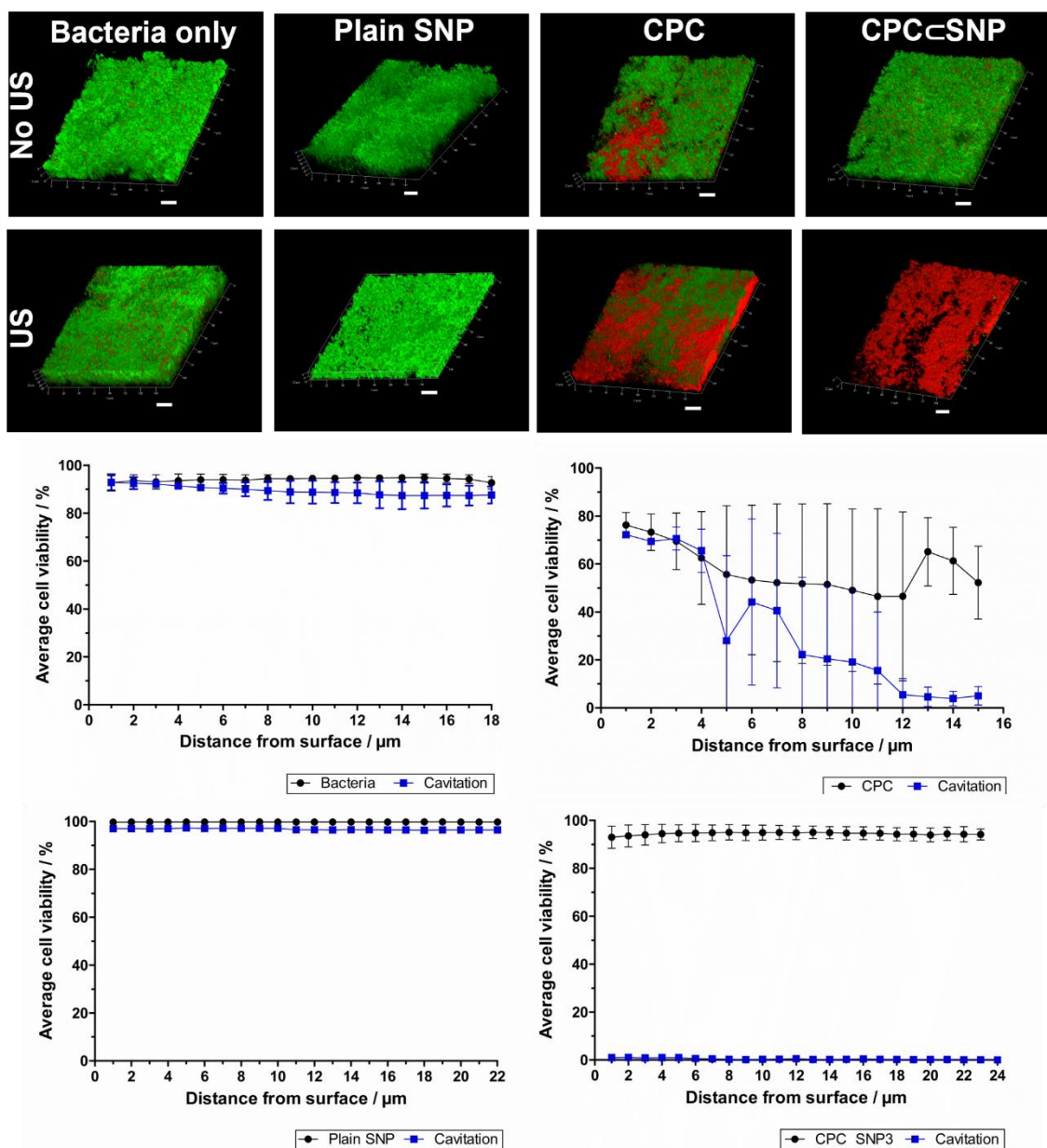


Figure 4. 13: CLSM 3D visualisation of *in vitro* *S. sanguinis* biofilms exposed to the following treatments: **Plain SNP** (10 mg mL⁻¹), **CPC** (14 μg mL⁻¹) and **CPC+SNP** (10 mg mL⁻¹), without and with US (P10, 10s) followed by 30 min incubation. Scale bar represents 20 μm. 2D images to form z-stacks were processed with automated image analysis and depth profile plotted to show average cell viability with SD throughout the biofilm (n=3).

However, the deviation in viability with free CPC supported that the EPS had possible influence on the penetration and diffusion of CPC throughout the biofilm. Furthermore, some CPC mouthrinse formulations have shown to only affect the layers closer to the surface of the biofilms grown for 48 h.⁵⁹ This was in accordance with the results observed in the biofilms studies in this work. Others have shown commercial mouthrinses with CPC work more effectively in combination with sodium fluoride or alcohol but require twice daily dosing over a period of time. In this study, the focus was on a maximum exposure time of 30 min. A treatment regime would require further investigation to determine the long-term impact on biofilm formation inhibition.

Furthermore, it was thought that the addition of US combined with CPC would lead to a stronger bactericidal effect. Using an ultrasonic scaler was shown by Vyas *et al.*⁵¹ to disrupt biofilms, exposing the EPS matrix and bacteria, which would have allowed not only penetration of CPC deeper into the biofilm but increased the interaction with the negative structure of the EPS matrix. Visualisation of the biofilm in 3D and assessment of corresponding viability, did show that CPC did have an effect deeper in the biofilm, In general CPC combined with US did not make a significant change to *S. sanguinis* viability. The CPC concentration found in commercial formulations is much higher, ranging from 0.05 to 0.1%.^{22,24,60,61} However, increasing the drug concentration and dosage time defeats the purpose of overcoming problems with antimicrobial resistance and delivery.

As expected, **Plain SNP** showed no inhibition on the biofilm and US made no difference to the percentage viability or CFU count. The reason for this could be due to the lack of ability to pass through cell membranes because of **Plain SNP's** large

size, hydrophobicity, and structure, which are key to preventing the growth of bacteria (bacteriostasis).³³ More importantly SNPs do not have antimicrobial activity.

Interestingly, combination of the active molecule with silica particles remarkably improved the antimicrobial performance of CPC. This improvement was only substantial once triggered by US, showing a synergistic effect. It has been thought, the US-trigger causes disruption of the phospholipid bilayer present in the cytoplasmic membrane inducing permeability, combined with release of CPC from the silica structure, thus increasing the drug interaction and penetration into the bacterial cells. Similar enhanced antibacterial effects have been described by other researchers, whom have used drug loaded NPs, for example vesicles, micelles and polymeric nanocarriers.^{62–64} Therefore, **CPC-SNP** is a promising platform as a smart drug delivery system, in which drug containing silica particles combined with US to improve the antimicrobial efficacy.

4.4. Conclusion

The developed **CPC-SNP** sample combined with US could provide a promising strategy for tackling challenges with drug delivery to biofilms and drug resistance. A proof-of-concept biofilm model was developed using a *S. sanguinis*. This enabled studies to be conducted to investigate the antimicrobial activity of drug loaded SNPs.

The antimicrobial activity of **CPC-SNP** was investigated against bacteria in both planktonic and biofilm form, relevant to species present in the oral cavity. A single-species biofilm, consisting of *S. sanguinis* was used as an established model to evaluate the antimicrobial action. This study demonstrated enhanced antimicrobial activity from the mechanical disruption stimulated by US combined with exposure to **CPC-SNP**, especially compared to free CPC. Despite CPC being commonly used as an antimicrobial treatment, CPC on its own showed to have poor ability to penetrate biofilms. These experiments have shown the advantage of using US with nanoparticles, as controlled drug release from **CPC-SNP** was achieved. It was thought US could not only facilitate the release of CPC but disrupt the biofilm network and increase the permeability of the bacterial cell walls. Therefore, increasing the bacteria to **CPC-SNP** exposure and causing significant bactericidal death.

Although these experiments in this chapter have shown significant findings, there are some limitations. Here, only one strain of bacteria has been tested, but was necessary to begin to understand the effects of US and nanoparticles with oral biofilms. Biofilms formed in the oral cavity are far more diverse and complex. Therefore, before **CPC-SNP** could be used as a treatment for dental diseases, further experiments would need to be conducted. For the next stages, this would include expanding the

screening of the developed drug loaded silica NPs against pathogenic bacteria in planktonic and biofilm form. Not only those related to dental infections and diseases, but to numerous healthcare-associated biofilm infections. In addition, to studying the particle and biofilm interaction would be valuable understanding the mechanism of action. For example, tracking the movement of the silica drug delivery system through the biofilm and into bacterial cells using reflectance microscopy. As these particles are not fluorescent, reflectance microscopy could differentiate between the particles and bacteria by their contrast. Alternatively, encapsulation of fluorescent dye would be useful for imaging. To gain a greater understanding of the behaviour **CPC-SNP** with **US**, multispecies biofilms would be step towards a more representative oral microenvironment.

Therefore, **CPC-SNP** could serve as model for other antimicrobial agents for dental disease.

4.5. Appendix

4.5.1. Minimum inhibitory concentration assay

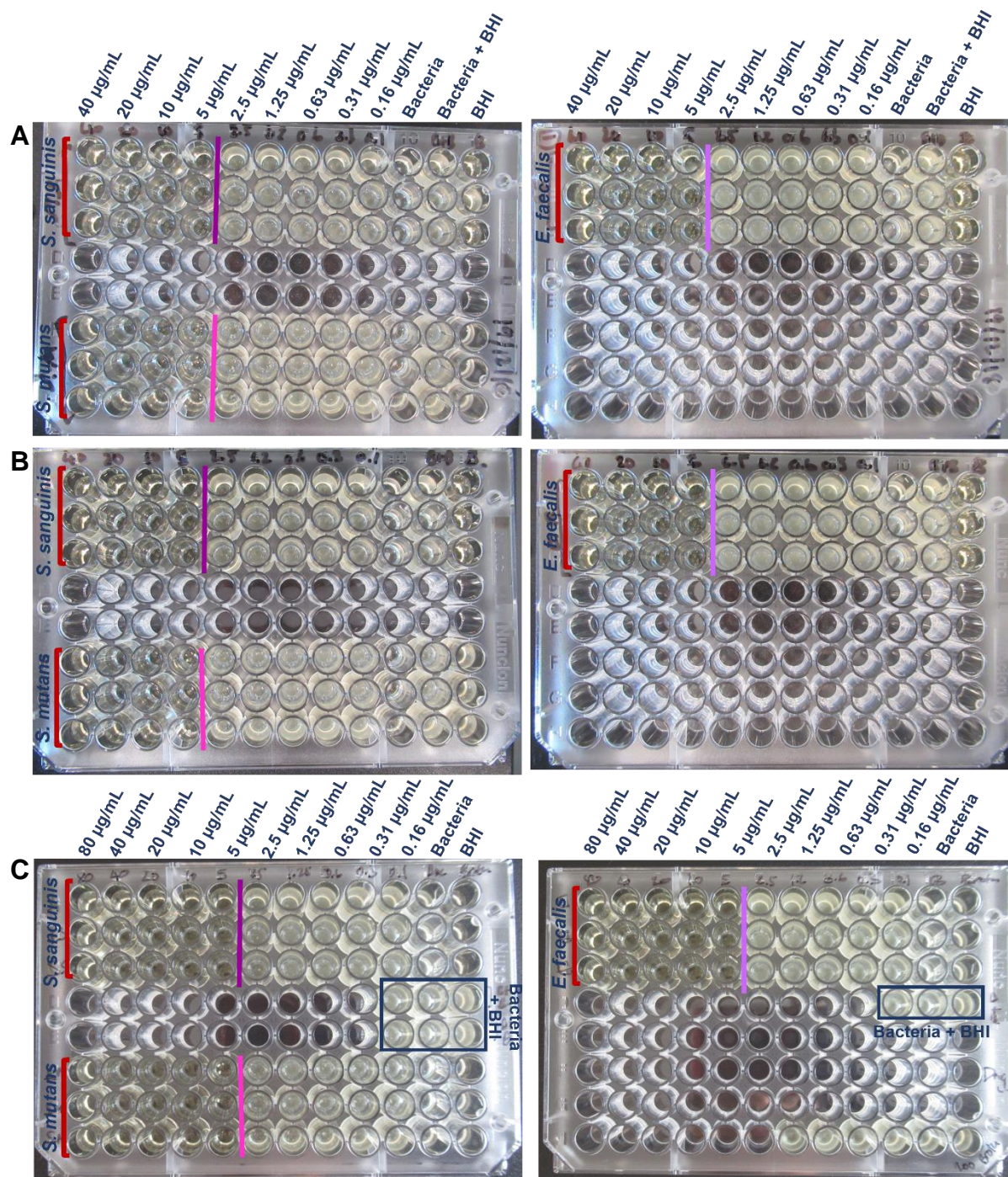


Figure S4. 1: Minimum inhibitory concentration (MIC) of CPC with bacterial strains *S. sanguinis*, *S. mutans* and *E. Faecalis*. The MIC value was observed visually and indicated by the purple lines, after 20 h incubation at 37 °C at 100 rpm. For all species the MIC was repeated in triplicates (n = 3).

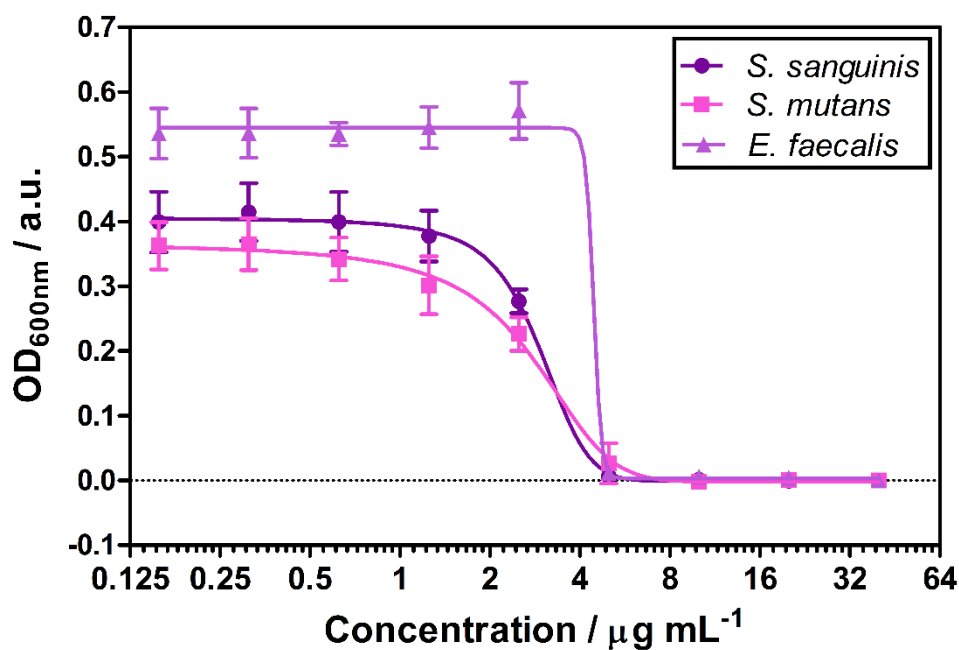


Figure S4. 2: Minimum inhibitory concentration (MIC) of CPC with bacterial strains *S. sanguinis*, *S. mutans* and *E. faecalis* measured by the OD_{600nm} after 24 h incubation at 37 °C at 100 rpm. For all species the average MIC with standard deviation was shown in the graph, repeated in triplicates (n = 3).

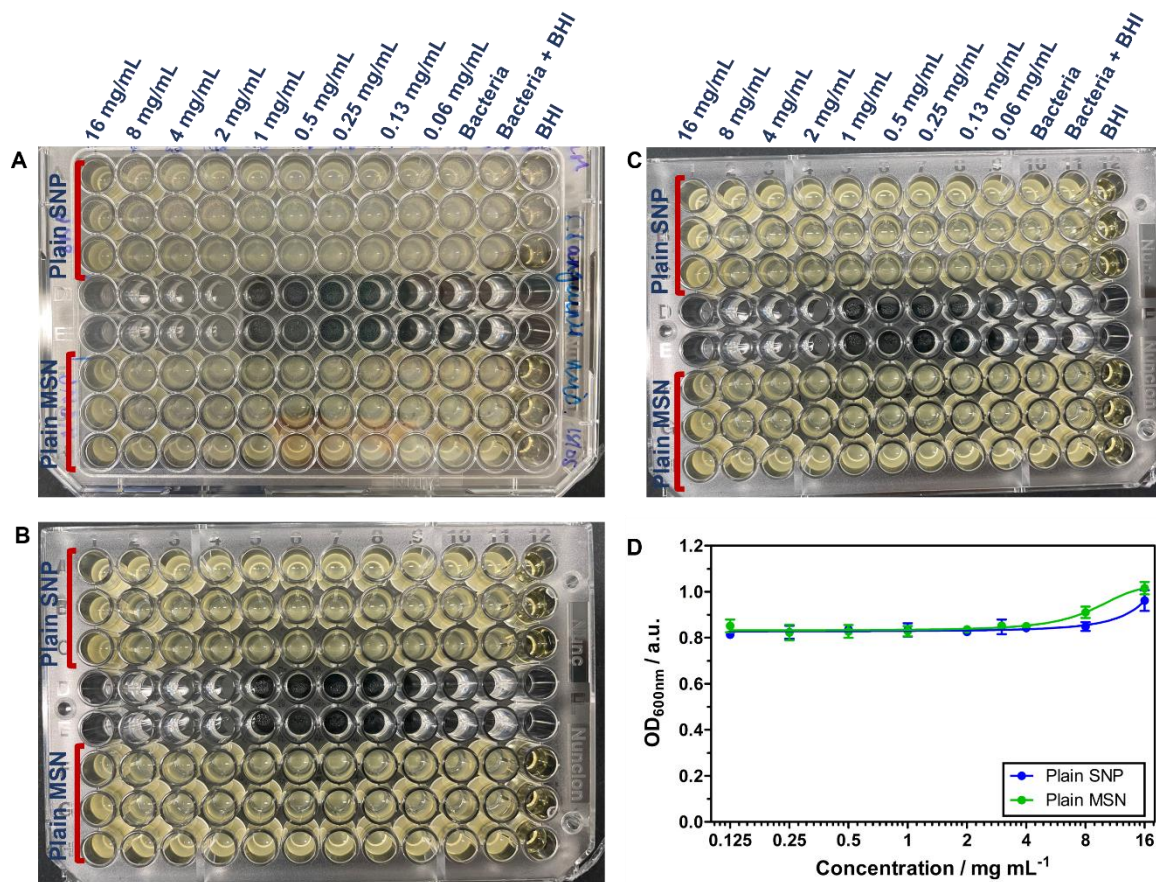


Figure S4. 3: Minimum inhibitory concentration (MIC) of **Plain SNP** and MSN against bacterial strain *S. sanguinis*. MIC values determined visually no killing occurred (**A-C**) and measured by the OD_{600nm} (**D**) after 24 h incubation at 37 °C at 100 rpm. The MIC was repeated in triplicates (n = 3).

4.5.2. Minimum biofilm inhibition concentration assay

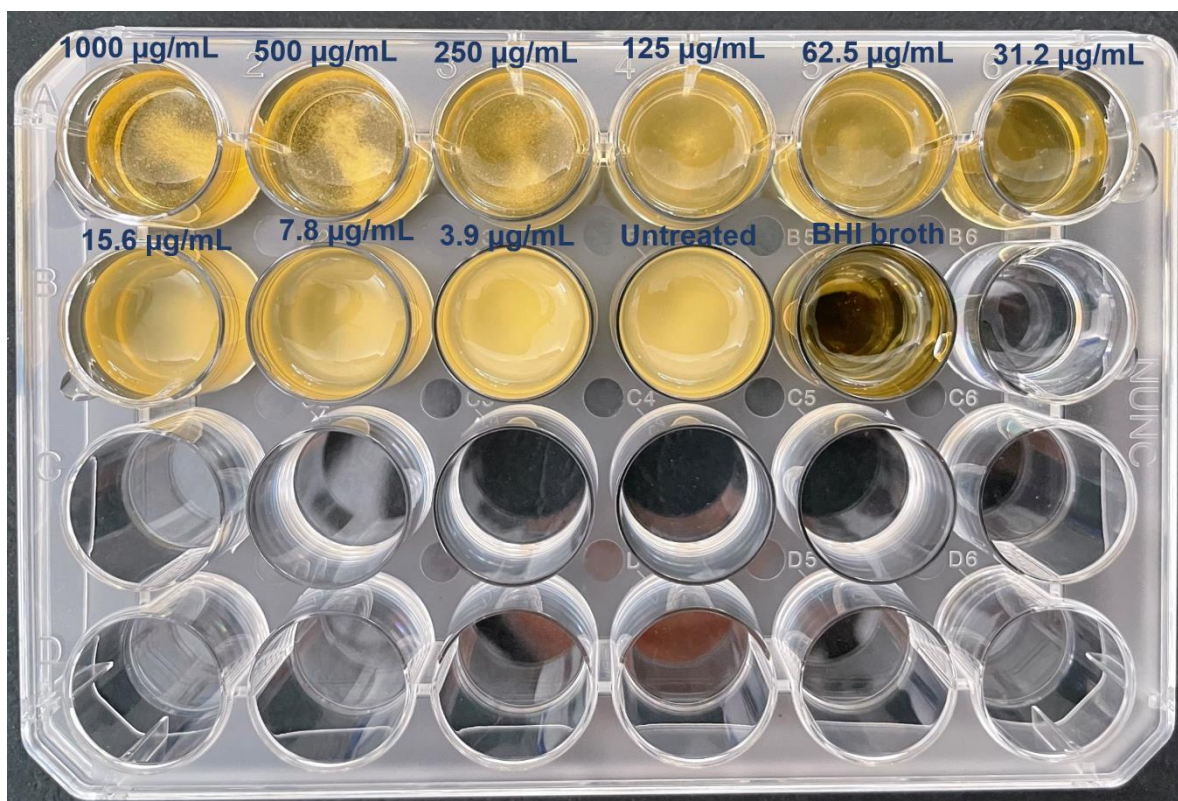


Figure S4. 4: Minimum biofilm inhibitory concentration (MBIC) of CPC against bacterial strain *S. sanguinis*. The MBIC value was observed visually, after 24 h incubation at 37 °C at 100 rpm

4.5.3. Confocal images

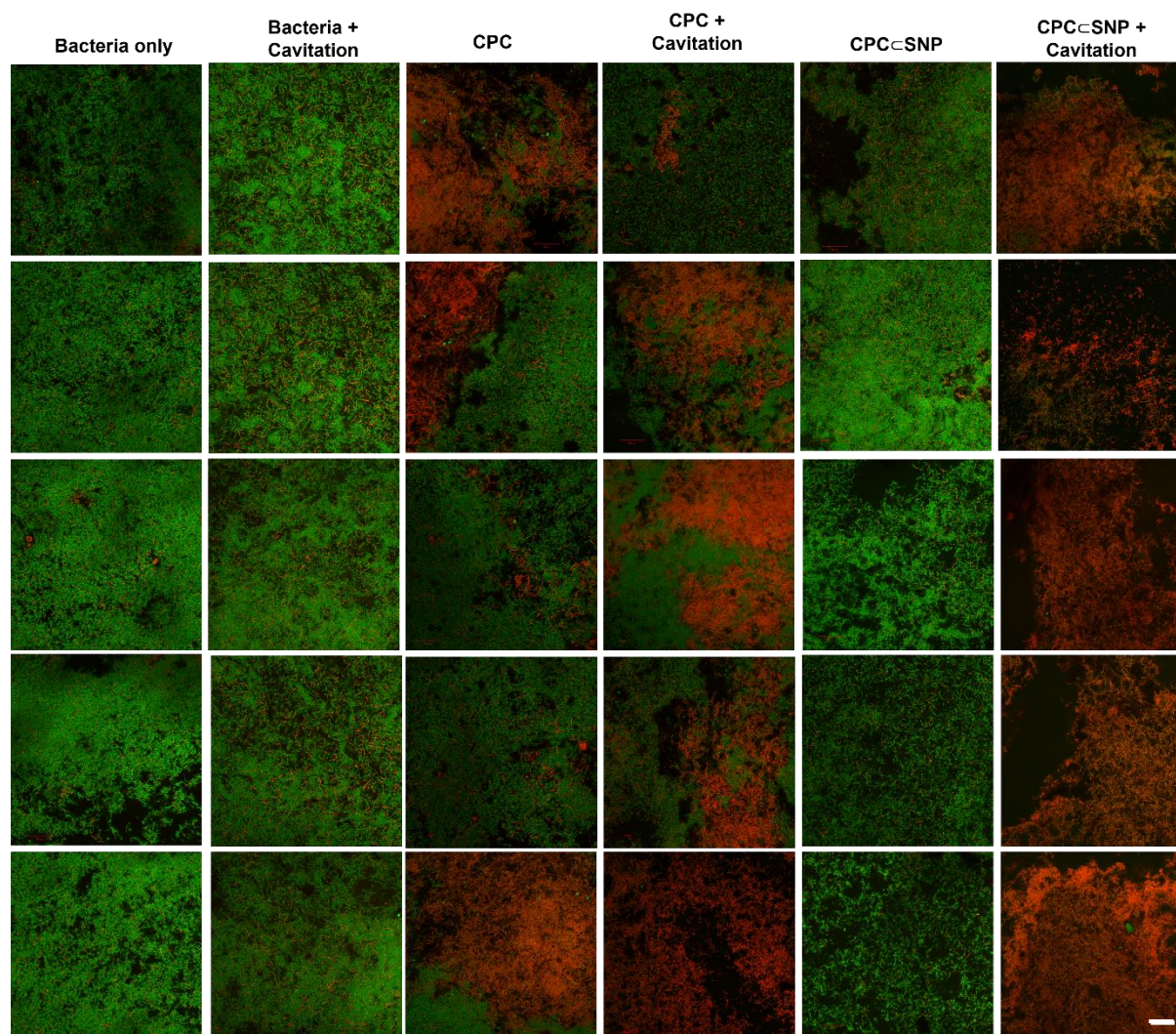


Figure S4. 5: CLSM images of five random areas of 72 h grown *S. sanguinis* biofilm after treatment of the following samples: **bacteria only**, **CPC** ($14 \mu\text{g mL}^{-1}$) and **CPC \subset SNP** (10 mg mL^{-1}). Treatments were repeated with US (P10, 10s). All samples were incubated for 30 min at 37°C in 5 % CO_2 before live/dead stained for imaging. Scale bar represents $20 \mu\text{m}$.

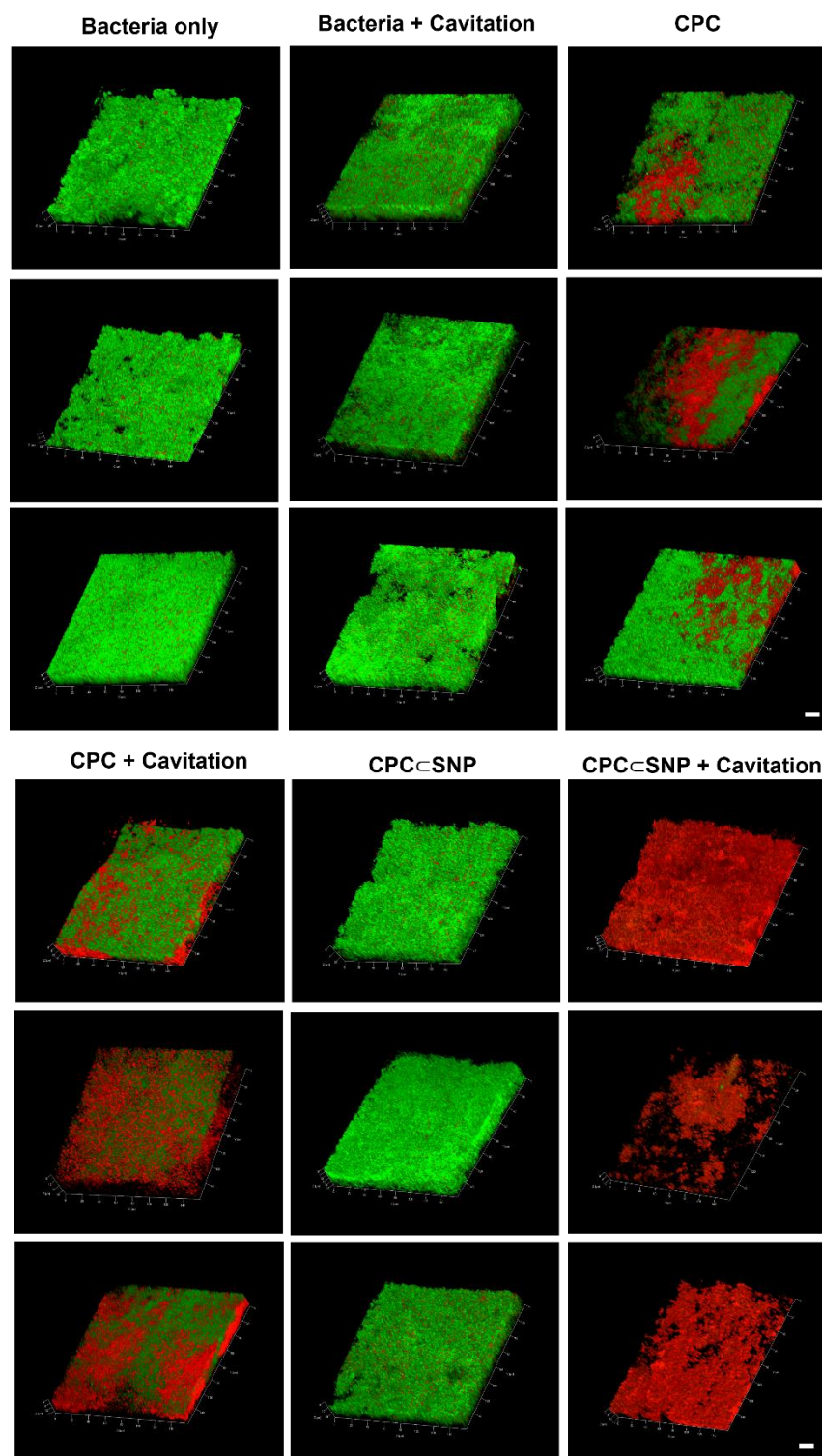


Figure S4. 6: CLSM images of Z-stack five random areas of 72 h grown *S. sanguinis* biofilm after treatment of the following samples: **bacteria only**, **CPC** ($14 \mu\text{g mL}^{-1}$) and **CPC+SNP** (10 mg mL^{-1}). Treatments were repeated with US (P10, 10s). All samples were incubated for 30 min at 37°C in 5 % CO_2 before live/dead stained for imaging. Scale bar represents $20 \mu\text{m}$.

4.5.4. CFU images

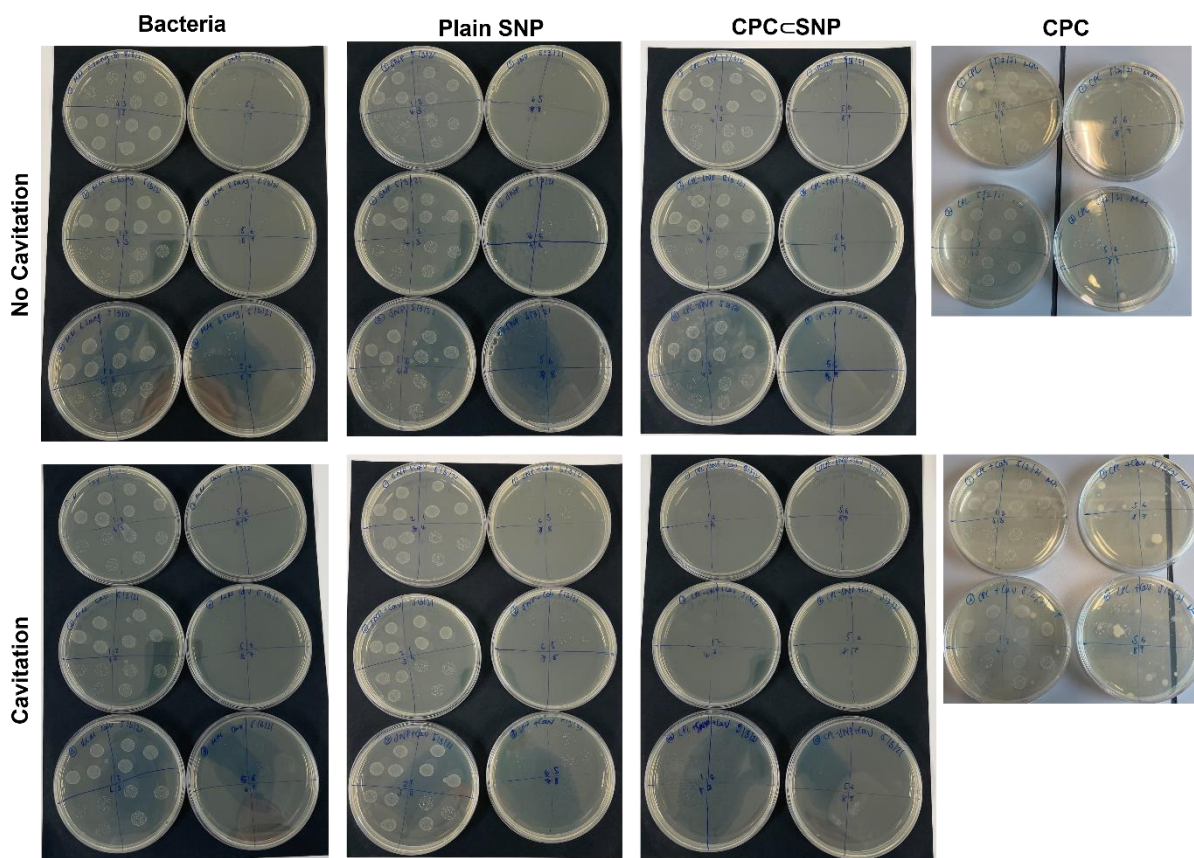


Figure S4. 7: Images taken of colonies grown on BHI agar after treatment of *S. sanguinis* biofilms: no treatment, **Plain SNP**, **CPC-SNP** and **CPC**. Each were compared to no US and US triggered by ultrasonic scaler at P10, 10s. The biofilms were removed from coverslips and resuspended in BHI broth. Bacterial suspensions were plated on BHI agar after serial dilution series. Plates were incubated for 24 h at 37 °C in 5 % CO₂ conditions. Colony count was determined as colony forming units of *S. sanguinis*. Repeated in triple triplicates, note not all images were taken for each sample. Biofilm treated with CPC and CPC + US images were obtained on a different experiment day.

4.5.5. SEM images

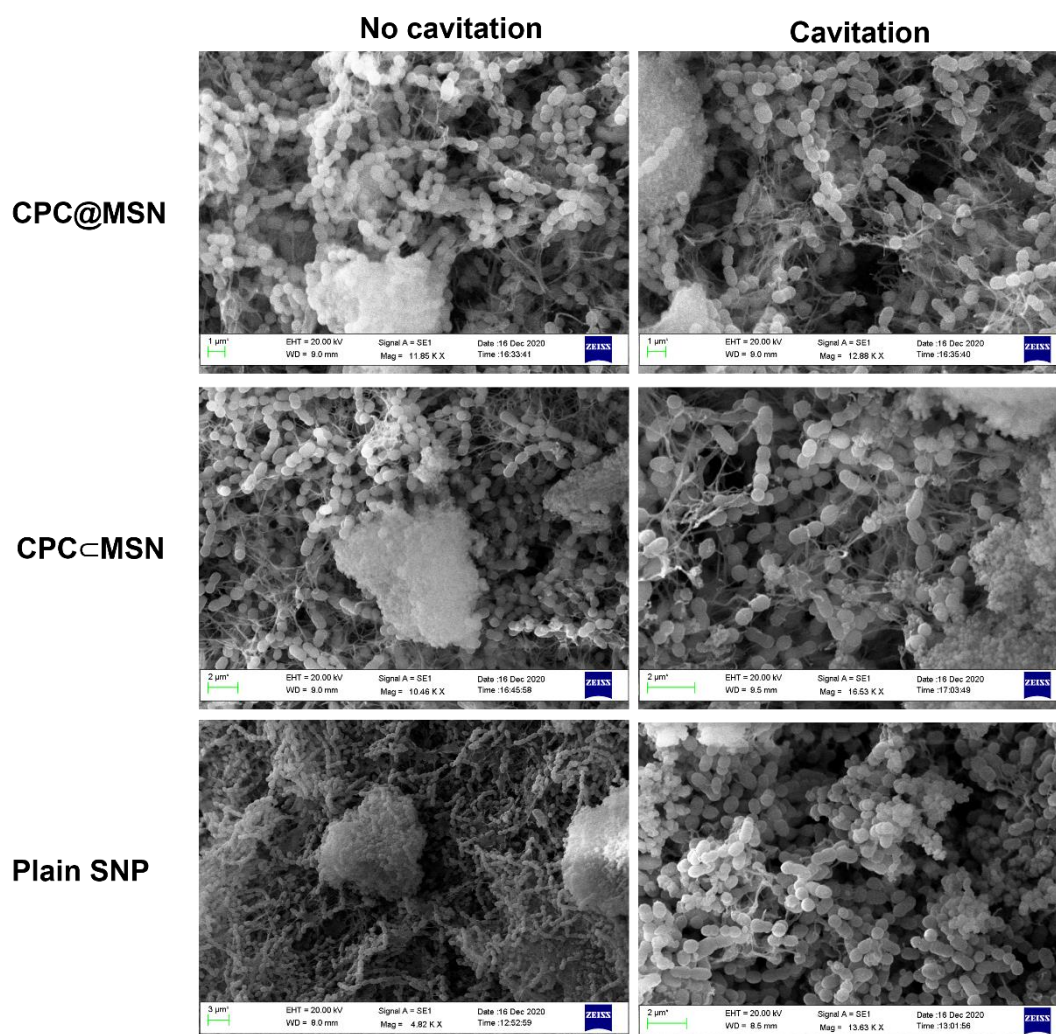


Figure S4. 8: SEM images to show comparisons of other treatments with and without US.

4.6. References

- 1 N. Y. Lee, W. C. Ko and P. R. Hsueh, *Front. Pharmacol.*, 2019, **10**, 1–10.
- 2 M. J. Mitchell, M. M. Billingsley, R. M. Haley, M. E. Wechsler, N. A. Peppas and R. Langer, *Nat. Rev. Drug Discov.*, 2021, **20**, 101–124.
- 3 Y. Yao, Y. Zhou, L. Liu, Y. Xu, Q. Chen, Y. Wang, S. Wu, Y. Deng, J. Zhang and A. Shao, *Front. Mol. Biosci.*, 2020, **7**, 1–14.
- 4 Y. Dang and J. Guan, *Smart Mater. Med.*, 2020, **1**, 10–19.
- 5 Y. C. Yeh, T. H. Huang, S. C. Yang, C. C. Chen and J. Y. Fang, *Front. Chem.*, 2020, **8**, 1–22.
- 6 A. C. Anselmo and S. Mitragotri, *Bioeng. Transl. Med.*, 2016, **1**, 10–29.
- 7 A. C. Anselmo and S. Mitragotri, *Bioeng. Transl. Med.*, 2021, **6**, 1–20.
- 8 L. Tang and J. Cheng, *Nano Today*, 2013, **8**, 290–312.
- 9 T. I. Janjua, Y. Cao, C. Yu and A. Popat, *Nat. Rev. Mater.*, 2021, **6**, 1072–1074.
- 10 M. A. S. Melo, S. F. F. Guedes, H. H. K. Xu and L. K. A. Rodrigues, *Trends Biotechnol.*, 2013, **31**, 459–467.
- 11 A. Shrestha and A. Kishen, *J. Endod.*, 2016, **42**, 1417–1426.
- 12 S. Priyadarsini, S. Mukherjee and M. Mishra, *J. Oral Biol. Craniofacial Res.*, 2018, **8**, 58–67.
- 13 Y. L. Chen, H. H. Chang, Y. C. Chiang and C. P. Lin, *J. Formos. Med. Assoc.*, 2013, **112**, 659–665.
- 14 A. D. Walmsley, *Phys. Procedia*, 2015, **63**, 201–207.
- 15 N. Vyas, K. Manmi, Q. Wang, A. J. Jadhav, M. Barigou, R. L. Sammons, S. A. Kuehne and A. D. Walmsley, *Ultrasound Med. Biol.*, 2019, **45**, 1044–1055.
- 16 V. Zijng, M. B. M. van Leeuwen, J. E. Degener, F. Abbas, T. Thurnheer, R. Gmür and H. J. M. Harmsen, *PLoS One*, 2010, **5**, e9321.
- 17 Y. Liu, Z. Ren, G. Hwang and H. Koo, *Adv. Dent. Res.*, 2018, **29**, 86–92.
- 18 S. E. Mountcastle, N. Vyas, V. M. Villapun, S. C. Cox, S. Jabbari, R. L. Sammons, R. M. Shelton, A. D. Walmsley and S. A. Kuehne, *npj Biofilms Microbiomes*, 2021, **7**, 1–12.
- 19 A. A. Miles, S. S. Misra and J. O. Irwin, *J. Hyg. (Lond.)*, 1938, **38**, 732–749.
- 20 P. D. Marsh, *Dent. Clin. North Am.*, 2010, **54**, 441–454.
- 21 D. Kim, J. P. Barraza, R. A. Arthur, A. Hara, K. Lewis, Y. Liu, E. L. Scisci, E. Hajishengallis, M. Whiteley and H. Koo, *Proc. Natl. Acad. Sci.*, 2020, **117**,

- 12375–12386.
- 22 J. Latimer, J. L. Munday, K. M. Buzza, S. Forbes, P. K. Sreenivasan and A. J. McBain, *BMC Microbiol.*, 2015, **15**, 1–8.
 - 23 S. Jenkins, M. Addy and R. G. Newcombe, *J. Clin. Periodontol.*, 1994, **21**, 441–444.
 - 24 P. K. Sreenivasan, V. I. Haraszthy and J. J. Zambon, *Lett. Appl. Microbiol.*, 2013, **56**, 14–20.
 - 25 M. R. Becker, B. J. Paster, E. J. Leys, M. L. Moeschberger, S. G. Kenyon, J. L. Galvin, S. K. Boches, F. E. Dewhirst and A. L. Griffen, *J. Clin. Microbiol.*, 2002, **40**, 1001–1009.
 - 26 J. A. Aas, A. L. Griffen, S. R. Dardis, A. M. Lee, I. Olsen, F. E. Dewhirst, E. J. Leys and B. J. Paster, *J. Clin. Microbiol.*, 2008, **46**, 1407–1417.
 - 27 J. M. Andrews, *J. Antimicrob. Chemother.*, 2001, **48**, 5–16.
 - 28 I. Wiegand, K. Hilpert and R. E. W. Hancock, *Nat. Protoc.*, 2008, **3**, 163–175.
 - 29 S. Y. Lee and S. Y. Lee, *Biocontrol Sci.*, 2019, **24**, 13–21.
 - 30 F.-A. Pitten and A. Kramer, *Arzneimittelforschung*, 2011, **51**, 588–595.
 - 31 X. Mao, D. L. Auer, W. Buchalla, K.-A. Hiller, T. Maisch, E. Hellwig, A. Al-Ahmad and F. Cieplik, *Antimicrob. Agents Chemother.*, 2020, **64**, 1–14.
 - 32 J. M. Schuurmans, A. S. Nuri Hayali, B. B. Koenders and B. H. ter Kuile, *J. Microbiol. Methods*, 2009, **79**, 44–47.
 - 33 B. Tian and Y. Liu, *Int. J. Appl. Ceram. Technol.*, 2021, **18**, 289–301.
 - 34 M. Wilson, *J. Med. Microbiol.*, 1996, **44**, 79–87.
 - 35 P. C. Trussell, E. A. Baird, D. Beall and G. A. Grant, *Can. J. Res.*, 1947, **25e**, 5–8.
 - 36 CLSI, *CLSI M100-ED29: 2019 Performance Standards for Antimicrobial Susceptibility Testing, 29th Edition*, 2019.
 - 37 M. Balouiri, M. Sadiki and S. K. Ibnsouda, *J. Pharm. Anal.*, 2016, **6**, 71–79.
 - 38 F. E. Dewhirst, T. Chen, J. Izard, B. J. Paster, A. C. R. Tanner, W.-H. Yu, A. Lakshmanan and W. G. Wade, *J. Bacteriol.*, 2010, **192**, 5002–5017.
 - 39 N. Wake, Y. Asahi, Y. Noiri, M. Hayashi, D. Motooka, S. Nakamura, K. Gotoh, J. Miura, H. Machi, T. Iida and S. Ebisu, *npj Biofilms Microbiomes*, 2016, **2**, 16018.
 - 40 P. S. Stewart and J. W. Costerton, *Lancet*, 2001, **358**, 135–138.
 - 41 R. M. Donlan and J. W. Costerton, *Clin. Microbiol. Rev.*, 2002, **15**, 167–193.

- 42 D. Davies, *Nat. Rev. Drug Discov.*, 2003, **2**, 114–122.
- 43 H. Van Acker, P. Van Dijck and T. Coenye, *Trends Microbiol.*, 2014, **22**, 326–333.
- 44 I. Ioannou, N. Dimitriadis, K. Papadimitriou, D. Sakellari, I. Vouros and A. Konstantinidis, *J. Clin. Periodontol.*, 2009, **36**, 132–141.
- 45 S. Oda, H. Nitta, T. Setoguchi, Y. Izumi and I. Ishikawa, *Periodontol. 2000*, 2004, **36**, 45–58.
- 46 G. Greenstein, *J. Am. Dent. Assoc.*, 2000, **131**, 1580–1592.
- 47 M. Erriu, C. Blus, S. Szmukler-Moncler, S. Buogo, R. Levi, G. Barbato, D. Madonnaripa, G. Denotti, V. Piras and G. Orrù, *Ultrason. Sonochem.*, 2014, **21**, 15–22.
- 48 P. R. Birkin, D. G. Offin, C. J. B. Vian, R. P. Howlin, J. I. Dawson, T. J. Secker, R. C. Hervé, P. Stoodley, R. O. C. Oreffo, C. W. Keevil and T. G. Leighton, *Phys. Chem. Chem. Phys.*, 2015, **17**, 20574–20579.
- 49 H. Koo, R. N. Allan, R. P. Howlin, P. Stoodley and L. Hall-Stoodley, *Nat. Rev. Microbiol.*, 2017, **15**, 740–755.
- 50 R. P. Howlin, S. Fabbri, D. G. Offin, N. Symonds, K. S. Kiang, R. J. Knee, D. C. Yoganantham, J. S. Webb, P. R. Birkin, T. G. Leighton and P. Stoodley, *J. Dent. Res.*, 2015, **94**, 1303–1309.
- 51 N. Vyas, R. L. Sammons, O. Addison, H. Dehghani and A. D. Walmsley, *Sci. Rep.*, 2016, **6**, 2–11.
- 52 N. Vyas, E. Pecheva, H. Dehghani, R. L. Sammons, Q. X. Wang, D. M. Leppinen and A. D. Walmsley, *PLoS One*, 2016, **11**, 2–13.
- 53 N. Vyas, H. Dehghani, R. L. Sammons, Q. X. Wang, D. M. Leppinen and A. D. Walmsley, *Ultrasonics*, 2017, **81**, 66–72.
- 54 S. Fulaz, H. Devlin, S. Vitale, L. Quinn, J. P. O'gara and E. Casey, *Int. J. Nanomedicine*, 2020, **15**, 4779–4791.
- 55 S. P. Denyer and G. S. A. B. Stewart, *Int. Biodeterior. Biodegrad.*, 1998, **41**, 261–268.
- 56 C. Sandt, J. Barbeau, M. A. Gagnon and M. Lafleur, *J. Antimicrob. Chemother.*, 2007, **60**, 1281–1287.
- 57 L. Marcotte, H. Therien-Aubin, C. Sandt, J. Barbeau and M. Lafleur, *Biofouling*, 2004, **20**, 189–201.
- 58 K. Ahmed, P. Gribbon and M. N. Jonest, *J. Liposome Res.*, 2002, **12**, 285–300.
- 59 J. Xiang, H. Li, B. Pan, J. Chang, Y. He, T. He, R. Strand, Y. Shi and W. Dong, *Am. J. Dent.*, 2018, **31**, 53–60.

- 60 F. Cieplik, E. Kara, D. Muehler, J. Enax, K. A. Hiller, T. Maisch and W. Buchalla, *Microbiologyopen*, 2019, **8**, 1–10.
- 61 A. Evans, S. J. Leishman, L. U. Walsh and W. K. Seow, *Aust. Dent. J.*, 2015, **60**, 247–254.
- 62 Y. Wang, K. Bi, J. Shu, X. Liu, J. Xu and G. Deng, *Nanoscale*, 2019, **11**, 4210–4218.
- 63 N. Rapoport, *Int. J. Pharm.*, 2004, **277**, 155–162.
- 64 T. G. Chan, S. V. Morse, M. J. Copping, J. J. Choi and R. Vilar, *ChemMedChem*, 2018, **13**, 1311–1314.
- 65 M. J. Dykstra, P. C. Mann, M. R. Elwell and S. V. Ching, *Toxicol. Pathol.*, 2002, **30**, 735–743.

Chapter 5: Ultrasound-responsive Drug Release & Delivery of Ciprofloxacin Encapsulated Silica Nanoparticles

5.1. Introduction

Endodontic infections occur in the dental pulp when microorganisms enter the root canal system.^{1,2} Sufficient elimination of microorganisms with current treatments is not always possible via chemo-mechanical preparations (removal of the pulp or necrotic debris from the canal) and drug delivery, as some pathogens can remain viable in the main canal and dentinal tubules.^{3,4} The persisting bacteria can become resistant to antimicrobial agents forming biofilms where there is no blood supply to hard tissues.^{3,5,6} Therefore, alternative interventions are required. These involve the use of antibiotics to increase the effective concentration in dentinal tubules and reach those areas that are not accessible to endodontic instruments.¹

Ciprofloxacin (CPX) is an antibiotic used for endodontic infections. It is the most potent fluoroquinolone in its class and has FDA approval to treat other severe bacterial infections, especially for respiratory and urinary tract infections.^{7,8} Fluoroquinolone's have the capacity to penetrate into tissues compared to other prescribed antibiotics. CPX has a broad range of antibacterial activity and has shown to be effective against oral Gram-positive bacteria (*S. aureus*, *S. epidermidis*, *Streptococcus species*), but especially Gram-negative microbes (*E. coli* and *P. aeruginosa*).^{2,4,9,10} CPX's potent activity is attributed to its chemical structure containing a fluorine atom (-F) and

piperazine ring (outlined in purple), as displayed in **Figure 5. 1**.^{8,11,12} Its mechanism of action works by inhibiting the activity of the bacteria enzyme DNA gyrase.¹³ DNA gyrase are a class of type II topoisomerase, responsible for inducing negative supercoils into DNA due to adenosine triphosphate hydrolysis. This can cause changes in the topology of DNA.¹⁴ Despite its high potency, CPX is at risk of antibiotic resistance against pathogenic bacteria.¹⁵ Some examples include reports of resistance to urinary *E. coli* ¹⁶ and treatment failure with CPX to eradicate *P. aeruginosa* biofilms.¹⁷ The cause of resistance is by mutational alterations in the DNA gyrase genes/topoisomerase IV genes, thus weakening the interaction between drug and bacterial enzyme.^{18,19} Therefore, with the rise of bacterial resistance, CPX benefit from a nanoparticle system, where delivery can be localised and transported to the infected site. This would protect CPX from causing any unwanted side effects and reduce the risk of antibiotic resistance. Especially as Gram-positive are harder to treat with CPX⁷

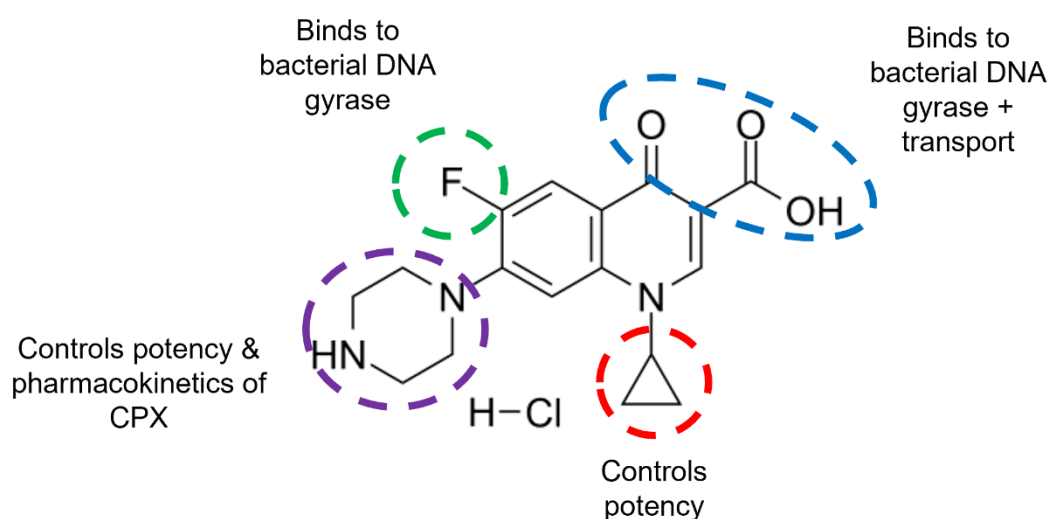


Figure 5. 1: The structure activity relationship of ciprofloxacin hydrochloride (CPX HCl) and the role of the different groups. Redrawn from Chu *et al.*¹¹

There have been reports of innovative strategies based on the use of nanotechnologies to incorporate CPX into nano-systems for drug delivery and controlled release.²⁰ The majority of CPX loaded NPs have been achieved with polymeric nanoparticles and their antimicrobial activity has been commonly examined against strains of Gram-positive *S. aureus* and Gram-negative *P. aeruginosa* in their planktonic or biofilm form.^{21–23} One study by Gheffar *et al.*,²³ entrapped CPX inside the micropores of poly(lactic-co-glycolic acid)- nanoparticles (PLGA-NPs) and investigated the influence of plain PLGA-NPs antibacterial activity against *S. aureus* planktonic culture. They found smaller particles were more biocidal compared to larger particles. This effect was attributed to their higher specific volume of 60 nm NPs. In addition, surface modification with poly(ethylene glycol) (PEG) chains created NPs with sizes of 81 nm, a negative surface charge of -45 mV and drug loading of 4%. PEGylation showed improved adhesion on the bacterial cell surface of CPX-PLGA-NPs compared to free CPX with 5 days old *S. aureus* biofilms. This was demonstrated by the minimum biofilm eradication concentration (MBEC) of CPX loaded PLGA-NPs and free CPX values of 37.5 $\mu\text{g mL}^{-1}$ and 512 $\mu\text{g mL}^{-1}$, respectively.

Other polymeric systems that used PLGA-NPs loaded with CPX loaded were reported by Günday *et al.*.²³ They included the NPs in a tissue engineered nanofiber scaffold to achieve a local antibiotic delivery. The CPX loaded PLGA-NPs were biodegradable and had a size of 108 nm, a charge of -30.5 mV and an encapsulation efficiency of 60-80%. The release was driven by slow diffusion from the polymer NPs over 2 weeks. They also showed a reduced drug dosage was needed to treat *S. aureus* and *P. aeruginosa* compared to free drug. Another NP system described by Page-Clisson *et al.*,²¹ used polymer materials for NP formulation to examine the CPX loading and

release properties. However, this release system was limited due to 30% of the CPX forming tight chemical bonds during the polymerization process, as monitored by NMR spectroscopy. Furthermore, chitosan is a polysaccharide commonly used in the preparation of NPs. It has a dual role of possessing high antimicrobial activity and being a mucoadhesive material by electrostatic interactions with the negatively charged bacterial cell wall.^{24,25} Sobhani *et al.*,²⁴ fabricated pH sensitive chitosan NPs via a gelation method and achieved a CPX encapsulation efficiency of 23%. The drug release was investigated by diffusion from the NP. The MIC determination showed 50% less of CPX loaded chitosan NP were required than free CPX against *E. coli* and *S. aureus*.

Silica systems, such as mesoporous and SBA-type NPs have been investigated to incorporate CPX as an alternative to polymer-based NPs. Optimised SBA-15 NPs were able to load 18% of CPX into the pores with sizes of 6.7 nm. The carrier also increased CPX's solubility by 10-fold.²⁶ Mechanical stirring released 60% of the loaded CPX, which equated to a rate of 0.98 $\mu\text{g h}^{-1}$. However, the CPX-SBA-15 NPs were not tested for their antimicrobial activity. Another silica system used silica coated silver NPs which were then embedded in chitosan entrapped CPX.²⁵ This hybrid system was developed to treat infections caused by *P. aeruginosa* in cystic fibrosis patients for delivery to the lungs via inhalation. The particles had a size range between 100-200 nm, surface charge of 25-30 mV and encapsulation efficiency of 73%. It was found that the hybrid NPs were 3-4-fold more effective against inhibiting growth and biofilm formation of *P. aeruginosa*. This was enhanced by using silver NPs and chitosan to provide a positive charge for increase mucoadhesive properties.

Despite increasing interest of CPX loaded NPs to treat various chronic infections, there is lack of research of SNPs to encapsulate CPX. Such an approach may prove useful for dental infections.^{27–30} One approach is to apply a mesoporous silica coating on implants, which is functionalised on the surface with sulfonic acid groups to aid the loading of CPX.³¹ This method of using disk diffusion method from mesoporous films, showed a slow drug release and suppression of bacterial proliferation for up to 10 days against *P. aeruginosa*.

The majority of CPX drug release mechanisms from NPs, focus on slow passive diffusion, pH sensitive conditions or enzyme responsiveness.^{20,32,33} There are very few accounts of polymeric NP systems stimulated by ultrasonication. For example, Khorshidi *et al.* describe the responsiveness of CPX release from alginate fibres with ultrasonication stimulation.³⁴ The ultrasound external trigger promoted a $35 \mu\text{g mL}^{-1}$ release over a 48 h period, compared to $13.4 \mu\text{g mL}^{-1}$ without ultrasound. The use of CPX stimulated release via ultrasound is an interesting avenue for dental applications and is so far underexplored. Therefore, ultrasonication as a possible avenue for producing a quick, on-demand release of CPX is attractive. Ultrasound enhance the activity of CPX and localised delivery to oral microorganisms, important to combat dental infections.

5.2. Chapter outline

This aim of this chapter was to investigate if antibiotics can be encapsulated into the same one-pot synthesised drug delivery system developed in **Chapter 3**. Here, ciprofloxacin (CPX) will be used as the antibiotic drug of interest. The controlled drug release will be tested with US to understand if the mechanism can be applied to more than one drug delivery system. Finally, the antibacterial activity will be tested on more than one strain of bacteria. The purpose of this will be to evaluate the behaviour of other planktonic and biofilms against CPX loaded silica particles. Also, to understand if the size of NP makes a difference to antibacterial activity.

First, CPX loaded SNPs will be synthesised with the method used in **Chapter 3 (method A)** and an alternative synthesis to yield smaller NPs was developed, **method B**. Also, **method C** will be used as a control method for comparison to the other synthesised preparations. The synthesis pathways for these methods are displayed in **Figure 5. 2**.

The drug loaded particles will be characterised with previously used techniques to confirm the physical and chemical structure of various **CPX \subset SNPs**. Additionally, the ultrasonic scaler will be employed to aid a triggered drug release, which will be monitored by the absorbance of CPX and confirm if the ultrasonic scaler is viable a tool to achieve a controlled drug release.

Furthermore, the antimicrobial activity will be reported for pure CPX against five different strains of Gram-positive and Gram-negative bacteria: *S. sanguinis*, *S. mutans*, *E. faecalis* and *P. aeruginosa* (PA14 and PA01N). Biofilms of both

streptococcus species will be grown to evaluate the efficacy of CPX loaded NPs with and without US.

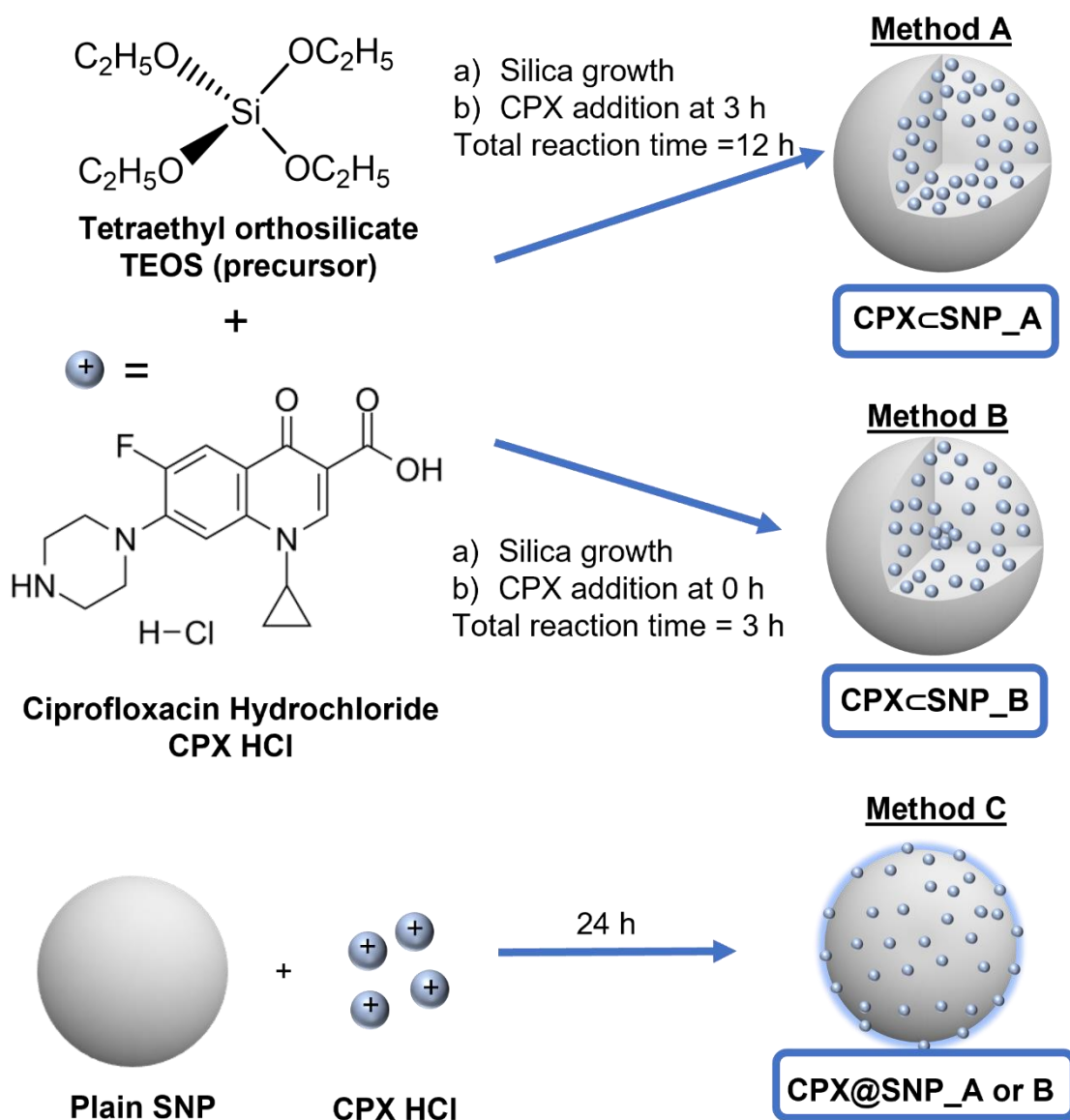


Figure 5. 2: Synthesis design to show the different pathways to achieve drug loaded silica nanoparticles. **Method A** and **B** are synthetic routes for encapsulation of CPX and **Method C** is the adsorption of CPX on the **Plain SNP** surface. Particles and drug molecules not to scale.

5.3. Results & Discussion

5.3.1. Development of CPX loaded SNPs

The one pot synthesis of CPX encapsulated SNPs was first attempted with the non-porous method described in **Chapter 3**. In brief, this method was based on the Stöber method³⁵, where all reagents were added at the beginning of the reaction using TEOS as the silica precursor and ammonia as the base catalyst. The addition of CPX was at 3 h and the reaction was continued for a total of 12 h. This synthesis enabled the inclusion of the drug during the growth of silica particles and this approach was to encapsulate CPX, termed **method A**.

In **Figure 5. 3**, the table shows two different drug concentrations added at 3 h, 60 mg and 90 mg in 3 mL solution, which yielded **CPX \subset SNP_A1** and **CPX \subset SNP_A2** particles, respectively. The use of a HCl salt form of CPX (ciprofloxacin hydrochloride) enabled 20 times higher solubility (30 mg mL⁻¹) than that of pure CPX in water and increased the possibility for higher drug loading in silica.^{36,37} Despite the high drug loading efficiency of 85 % (51 mg) obtained for **CPX \subset SNP_A1** there was no release observed when applying US from the ultrasonic scaler. On the other hand, increasing the concentration enabled observable of drug release with US, but a much lower drug loading efficiency of 7 % (6.3 mg) was achieved. Even though the procedure mainly differed by the concentration of CPX, there was a significant difference in the encapsulation efficiency. Therefore, to improve the drug loading abilities **method B** was examined.

A few adjustments were made to **method A** to synthesis **method B**. The first change was the time of reaction, which was shortened from 12 h to 3 h in total and the drug

was introduced into the reaction at time 0 h. For samples **CPX \subset SNP_B1** to **CPX \subset SNP_B3** a low drug concentration was used, and the calculated drug entrapment varied from 26 to 38 % (0.065 – 0.57 mg). As a result, addition of such low drug concentrations led to no release, as confirmed by absorbance for these samples. Note that **CPX \subset SNP_B3** used 4 mL more base catalyst in the reaction than **CPX \subset SNP_B2** and had no influence on the drug loading. Nevertheless, the higher loaded samples with 18 mg for **CPX \subset SNP_B4** and 62 mg for **CPX \subset SNP_B5**, yielded

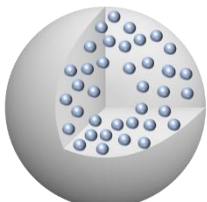
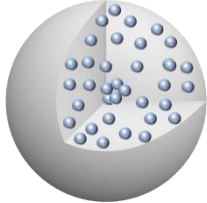
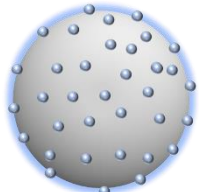
Method A 				
Sample	Initial drug added / mg	Drug loading entrapment / %	Release with cavitation	
CPX \subset SNP_A1	60	85	No	
CPX \subset SNP_A2	90	7	Yes	
Method B 				
Sample	Initial drug added / mg	Drug loading entrapment / %	Release with cavitation	
CPX \subset SNP_B1	0.25	26	No	
CPX \subset SNP_B2	1.5	32	No	
CPX \subset SNP_B3	1.5	38	No	
CPX \subset SNP_B4	18	28	Yes	
CPX \subset SNP_B5	62	19	Yes	
Method C 				
Sample	Initial drug added / mg	Drug loading entrapment / %	Release with cavitation	
CPX@SNP_A	400	12	Yes	
CPX@SNP_B	400	9	Yes	

Figure 5. 3: Method A: synthetic route involves addition of CPX after 3 h and total reaction time was 12 h. **Method B:** CPX was added at time 0 h and reaction time was 3 h. **Method C:** traditional drug adsorption synthesis of **Plain SNP** stirred with CPX for 24 h. The respective tables showed initial drug added, the efficiency percentage of drug loaded, and it was stated if any release was observed with US.

particles with 28 % (5 mg) and 19 % (10.8 mg) drug entrapped, respectively. Increasing the amount of CPX lead to observable absorbance of the drug when the release was monitored with UV-Visible spectroscopy.

Method C was used as a control synthesis for comparison when characterising the particles. This traditional method incorporates charged agents, commonly through a two or more-step procedure.^{38–40} The first step of synthesis requires the formation of **plain SNPs** with no drug. The subsequent addition of the drug in solution allows for interaction with the negatively charged silica surface through electrostatic forces. If this is not possible, the silica surface can be modified through various functionalisation's to coat the SNPs and enable attachment of the desired drug. In this case, the **Plain SNPs** had a negative charge of -45 mV and were used to attract the positively charged CPX molecule via the nitrogen of the piperazine moiety. A NP:drug ratio of 1:4 was used to ensure CPX was added in excess to maximise the drug-particle electrostatic interactions and loading. This was within the solubility limits in water. The newly formed particles **CPX@SNP_A** and **CPX@SNP_B** had a loading efficiency of 12 % (48 mg) and 9 % (36 mg), respectively. Even though a greater amount of the drug had been loaded, the issue with this method was the multi-step synthesis and uncontrolled drug release.

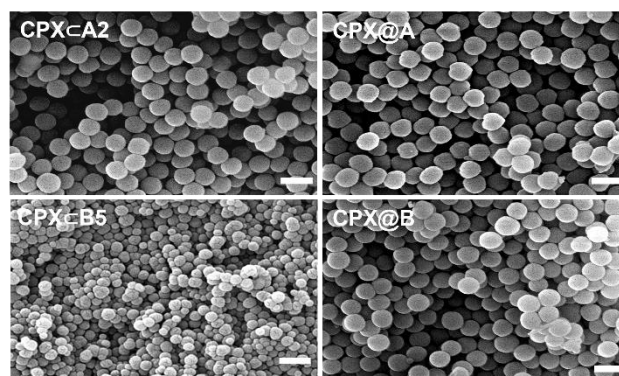
5.3.2. Characterisation of CPX loaded NP's

The particle samples that showed preliminary drug release, **CPX@SNP_A2**, **CPX@SNP_B4** and **CPX@SNP_B5** (**Figure 5. 3**) were further characterised using DLS, zeta potential, MALDI-TOFMS and FT-IR, as shown in **Figure 5. 4**. The adsorbed NPs were used for comparison.

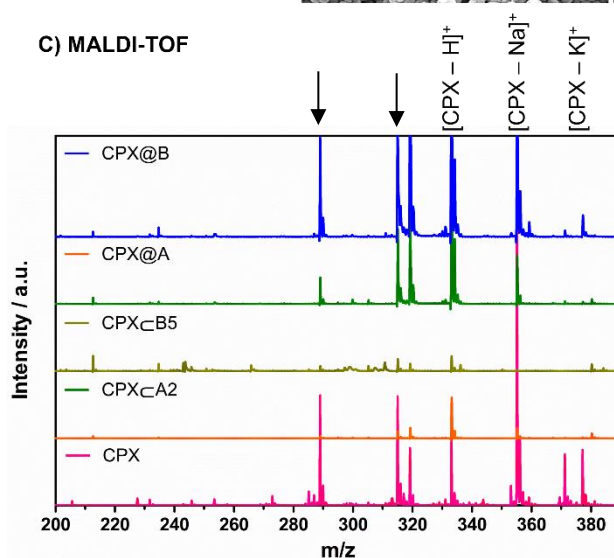
A) Size & Charge

Sample	D_H by Intensity / nm	D_H by Number / nm	PDI	ζ / mV
CPX \subset SNP_A2	295 \pm 83	260 \pm 79	0.099	-33 \pm 9
CPX \subset SNP_B4	180 \pm 35	163 \pm 37	0.125	-40 \pm 6
CPX \subset SNP_B5	103 \pm 32	90 \pm 26	0.686	-35 \pm 7
CPX@SNP_A	153 \pm 21	147 \pm 26	0.817	10 \pm 4
CPX@SNP_B	164 \pm 32	160 \pm 35	1.000	-20 \pm 6

B) Morphology



C) MALDI-TOF



D) FT-IR

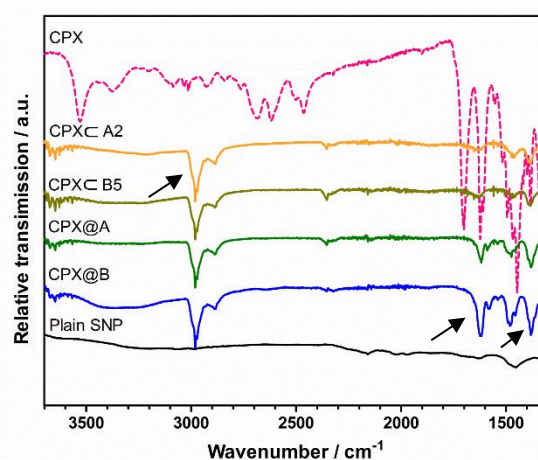


Figure 5. 4: Summarised characterisation of CPX loaded SNP samples. **A)** Table to show the sizes of NPs obtained by DLS and surface charge from the zeta potential. **B)** SEM imaging of NPs to confirm the morphology and size. Spectroscopy techniques were used to indicate the incorporation of CPX drug into the silica obtained with: **C)** MALDI-TOFMS and **D)** FT-IR.

The DLS measurement of the hydrodynamic diameter of **CPX \subset SNP_A2**, gave particle sizes of 295 nm with good PDI. This demonstrated the particles had a narrow size distribution. The size was further supported by visual representation with SEM imaging, which showed **CPX \subset SNP_A2**'s spherical and uniform morphology. These particles were larger than **Plain SNP**, which had a size of 238 nm. The change suggested that CPX had been included inside the NPs during synthesis. The surface charge of **CPX \subset SNP_A2** was measured by the zeta potential and compared against control particles **Plain SNP** with no drug and **CPX@SNP_A**. The negative charge of **CPX \subset SNP_A2** (-33 mV) indicated that CPX had been successfully encapsulated and that majority was inside rather than adsorbed on the surface. **CPX@SNP_A** had a charge of -20 mV, which showed a greater shift towards a positive value. Therefore, if any CPX had been adsorbed on the surface of **CPX \subset SNP_A2** it seems there was not enough to increase the positive charge of the particles.

The alternative **method B** revealed smaller sized particles and high negative surface charges of 180 nm, -40 mV and 103 nm, -35 mV for **CPX \subset SNP_B4** and **CPX \subset SNP_B5**, respectively. The size difference to **method A** could be attributed to the shorter reaction time, meaning less time for the silica network to grow. It should be noted that in both methods, the TEOS concentration was kept the same. Therefore, there would have been unreacted starting material in **method B**, producing particles with a smaller size and higher negative density.²³ Hence, the surface charge reached up to -40 mV using **method B**. Additionally, SEM (**Figure 5. 4B**) was employed to validate the size and shape of the particle samples. All three methods produced particles of uniform and spherical shape. The sizes when processed with the ImageJ software and the diameters matched that obtained with DLS.

To confirm the presence of CPX and the successful modification of SNPs, the prepared samples were characterised by MALDI-TOF mass spectrometry and FT-IR spectroscopy. In **Figure 5. 4C** the mass spectrum of pure CPX showed m/z peaks at 332, 335 and 371, which were attributed to $[\text{CPX-H}]^+$, $[\text{CPX-Na}]^+$ and $[\text{CPX-K}]^+$, respectively. The main characteristic peak of $[\text{CPX-H}]^+$ was observed for the drug loaded particles as well as other prominent reference peaks, such as 314 m/z and 288 m/z , that indicated loss of water and carboxyl group, respectively. The spectra confirmed that CPX was present in both **CPX \subset SNP_A2** and **CPX \subset SNP_B5**.

Plain SNPs had already been characterised by FT-IR, as reported in **Chapter 3**. There it was revealed the silica architecture was constructed of asymmetric and symmetrical stretching vibration bands of Si-O-Si and Si-OH. The peaks at 1055, 951, 794 and 667 cm^{-1} were identified as $\nu_{\text{as}}(\text{Si-O-Si})$, $\nu_{\text{as}}(\text{Si-OH})$, $\nu_{\text{s}}(\text{Si-O-Si})$ and $\delta(\text{Si-O-Si})$ respectively. These peaks were also exhibited for all the drug loaded NPs, confirming the formation of the silica network.

Furthermore, encapsulated **CPX \subset SNP's** and adsorbed **CPX@SNP's** showed the successful modification with CPX in **Figure 5. 4D**. New bands were displayed between 2980-2885 cm^{-1} , which were assigned to the aromatic stretching vibrations of C-H in the CPX molecule. The bands at 1652 and 1471 cm^{-1} were attributed to the vibrational stretching of carbonyl groups on the pyridone ring, $\nu(\text{C=O})$ and $\nu(\text{C-O})$, respectively. The peaks of the amine $\delta(\text{N-H})$ bend and the $\nu(\text{C-N})$ stretch were more weakly observed for **CPX \subset SNP_A2** and **CPX \subset SNP_B5** compared to when CPX was adsorbed onto the SNP for **CPX@SNP_A** and **CPX@SNP_B**. The stronger bands shown in both **adsorbed CPX@SNP's** spectra, could suggest a higher drug loading and/or the drug was on the surface of the particles. It was also anticipated that the

fluorine group $\nu(\text{C-F})$ would be evident between $1050\text{--}1000\text{ cm}^{-1}$. However, this overlapped and was hidden by the broad and strong intensity bands associated with silica. Although the observed C-F band would have been useful, there was enough evidence to confirm the SNPs synthesised using **method A** and **B** demonstrated the presence of the CPX drug.

To determine the amount of CPX loaded within the SNPs, the TGA was used to measure the percentage weight loss due to the organic drug. The drug entrapment had already been calculated, as described earlier in this section and was complemented by the TGA studies. From the summarised data presented in **Table 5. 1**, the TGA results showed the amount of CPX loaded into SNP, obtained from weight loss curves (**Appendix Figure S5.12-16**). In general, the initial weight loss step occurred at $<180^\circ\text{C}$, attributed to H_2O moisture in the sample and condensation of hydroxyl groups from the SNP. The second was due to the mass loss of CPX. Note that there was no quantifiable mass loss with **Plain SNPs** containing no drug.

Table 5. 1: TGA data to show the temperature range at which the assigned weight loss percentage occurred due to CPX from drug loaded NPs, post-synthesis of **method A** and **B** synthesis to determine the absolute drug content mass, μg of CPX per mg of CPX loaded SNP.

Sample	Step assignment				Absolute drug content / μg _{CPX} mg _{CPX-NP} ⁻¹	
	H ₂ O		CPX			
	Region / °C	Weight loss / %	Region / °C	Weight loss / %		
CPX⊂SNP_A2	<180	6.6	265 – 530	3.3		33
CPX@SNP_A	<180	5.9	435 – 482	10.5		105
CPX⊂SNP_B5	<180	7.8	282 – 475	2.4		24
CPX@SNP_B	<180	5.4	416 – 490	16.7		167

The data obtained from the TGA analysis were in good agreement with UV-Visible measurements, which indicated CPX had been successfully loaded in SNPs. Both **CPX \subset SNP_A2** and **CPX \subset SNP_B5** showed the greatest weight loss between 265 and 530 °C, which was in accordance with the profile shown for pure CPX. The drug loading per mg of CPX within SNPs was determined as 33 and 24 $\mu\text{g}_{\text{CPX}} \text{mg}_{\text{CPX}\subset\text{SNP}}^{-1}$ for **CPX \subset SNP_A2** and **CPX \subset SNP_B5**, respectively. The relatively low amount of CPX loading might be attributed to CPX's charge that is dependent on pH. CPX can have both negative and positive charges at the same time, and this could hinder the electrostatic interaction with silica's overall negative charge. Despite this, the broad temperature range possibly indicated that CPX was distributed throughout the SNP structure and deeper CPX contained within the core of silica may be harder to remove, as silica can withstand high temperatures.

Also, there is no standardised method for determining the amount of drug loaded in NPs. Majority of the CPX loaded particles have been reported as a loading efficiency percentage rather than the mass within the particles. As a result, this made it difficult to make direct comparisons with CPX NPs reported in the literature and these developed in this work. Generally, polymeric NP systems reported drug loading efficiencies as low as 23% to 80%^{21,22,24} and one example loaded 3.6% of CPX, achieving particle sizes with diameters of 81 nm and a surface charge of -45 mV,²³ similar to the **CPX \subset SNP_B5** particles. Silica-based NP systems, which achieved drug loading all had a highly porous structure, hence it would be expected to have greater drug loading entrapment. For example, one mesoporous silica SBA-16 sample, in which the drug was anchored to the surface, resulted in 22% drug loading, determined by TGA and 29% by UV-Visible spectroscopy.³⁰ Another achieved a 73% loading

efficiency. However, the silica porous systems required additional surface functionalisation to trap the drug in the NP.²⁵ More promisingly in this work, results demonstrated that **methods A** and **B** had successfully achieved encapsulated CPX in a one-pot synthesis without additional functionalisation of the silica and minimal uncontrolled drug leakage.

In contrast, adsorbed CPX type samples of **CPX@SNP_A** and **CPX@SNP_B**, had a CPX weight loss that occurred at temperatures >400°C and had a drug loading of 105 and 167 $\mu\text{g}_{\text{cpx}} \text{mg}_{\text{cpx@snp}}^{-1}$, respectively. The narrow decomposition temperature range suggested that it is unlikely that CPX infiltrated the SNP and remains predominantly on the surface due to the non-porous character. This was further indicated by the faster rate of CPX weight loss.

5.3.3. *In Vitro* drug release comparisons of CPX loaded NP's

After successfully characterisation of **CPX<SNP_A2** and **CPX<SNP_B5**, the next stage was to evaluate US responsiveness for drug release. Previously (**Chapter 3**), US produced from an ultrasonic scaler tip proved to be highly effective at providing a triggered and controlled drug release when immersed in solution with the particles.

In **Figure 5. 5**, the drug release profiles of **CPX<SNP_A2**, **CPX<SNP_B5** and **CPX@SNP** are shown with and without US. Without using US there was some initial release of CPX from the SNP samples. The overall leakage was 0.06 and 0.03 $\mu\text{g}_{\text{cpx}} \text{mg}_{\text{cpx<snp}}^{-1}$ from **CPX<SNP_A2** and **CPX<SNP_B5**, respectively. The release plateaued after 2 and 4 mins. The small amount of CPX release with no US trigger could strongly suggest that there was drug on the surface of the SNPs. Therefore, easily diffused into the water. Even though there was a small, uncontrolled amount of

CPX released, the concentration was below the minimum inhibitory concentration to have any antibacterial activity against various bacterial species.^{41–44}

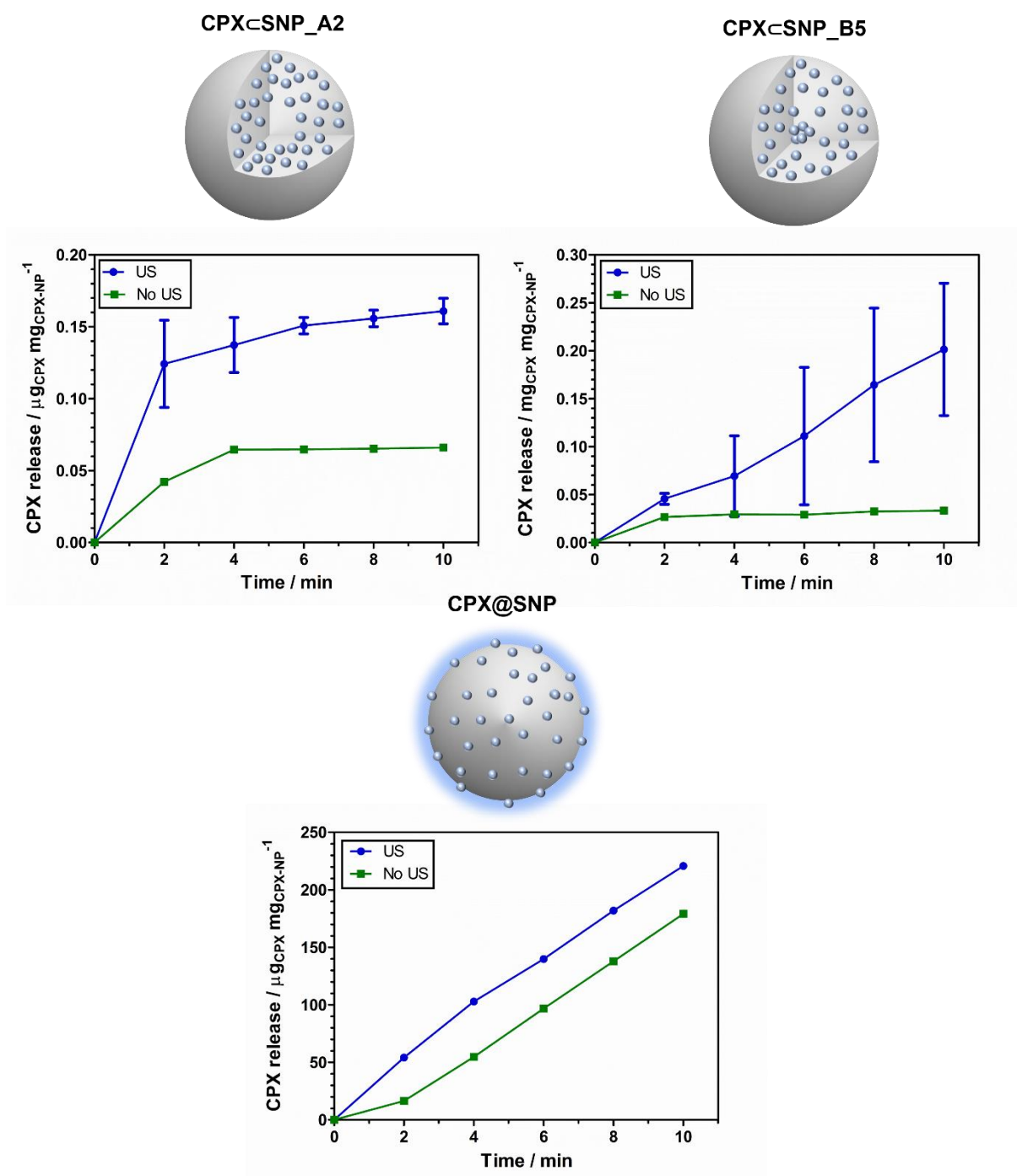


Figure 5. 5: Drug release profiles of CPX encapsulated NP's: **CPX \subset SNP_A2** (10 mg mL⁻¹) and **CPX \subset SNP_B5** (10 mg mL⁻¹) and CPX adsorbed NP: **CPX@SNP** (10 mg mL⁻¹) in H₂O at 37 °C. The average amount of CPX released with standard deviation, repeated in triplicate (n=3).

On the other hand, the drug release kinetics with US applied the particles generally faster and a greater amount was released. The parameters for release consisted of the US tip placed inside a solution containing the particles and US was applied in 2 min cycles over 10 min. The ultrasonic scaler was adjusted to the highest power setting (P20, frequency 36 kHz). The sample **CPX \subset SNP_A2**, which were 300 nm in diameter, showed an initial burst release that occurred with 2 min US. This was followed by a gradual release of up to $0.16 \mu\text{g}_{\text{cpx}} \text{mg}_{\text{cpxcnp}}^{-1}$ after 10 min. In comparison, a steady release kinetics was exhibited from **CPX \subset SNP_B5** and obtained a higher release after 10 mins of $0.25 \mu\text{g}_{\text{cpx}} \text{mg}_{\text{cpxcnp}}^{-1}$. Whereas the drug release kinetics from adsorbed **CPX@SNP** was very rapid, which released $220 \mu\text{g}_{\text{cpx}} \text{mg}_{\text{cpx@snp}}^{-1}$ with 10 min US.

To understand different release profiles from the three drug loaded particles, the effects of cavitation from US needed to be considered as they are a major contributing factor. Cavitation depends on several parameters, such as the frequency, pressure, surface tension and space available. It is likely at a high-power setting with a frequency of 36 kHz, cavitation was produced in water. At high energy, turbulence around the scaler tip could have resulted in rapid bubble formation and implosion in a few microseconds. It may be possible that the cavitation led to high amplitude shockwaves that have come into contact with the particle surfaces. The emission of energy from the imploded bubbles may have caused microcracks in the silica wall to promote the diffusion of CPX. In addition to this, as mentioned before cavitation can be influenced by the space available. Depending on the surrounding environment, such as the fluid, particles and material of the container used for the drug release study, can affect the frequency of bubble formation. The sizes of **CPX \subset SNP_A2** had a larger diameter than **CPX \subset SNP_B5**. Although the initial release from **CPX \subset SNP_A2** was rapid, overall

CPX \subset SNP_B5 had a higher drug release. This could suggest there a higher probability of frequent bubble bombardment with smaller particles. ^{.23} The effect of cavitation on adsorbed **CPX@SNP**'s, showed both rapid and greater drug release. This indicated CPX was on the surface of the SNP and the activity of US could easily stimulate the release of CPX.

Other modes of action produced from cavitation in the splitting of water particles into free radicals. The splitting and reforming of water molecules releases energy and in the form of heat. Thus, free radicals can be damaging to the silica to expel CPX. The phenomenon of cavitation in water is too fast to be observed by the naked eye. Hence, further experiments to detect cavitation occurring with chemiluminescence or high-speed imaging would be advantageous to confirm the effect of cavitation on the drug delivery system.

5.3.4. Determination of minimum inhibitory concentration and antimicrobial activity of CPX and formulations

To investigate the antibacterial activity of free CPX, five bacterial strains were chosen to determine the minimum inhibitory concentration (MIC). Exposure of bacteria to a CPX concentration range of 0.048 – 80 $\mu\text{g mL}^{-1}$ resulted in the determination of MIC values shown in **Table 5. 2**. The supporting images are shown in **Appendix, Figure S5.19-21**.

The Gram-negative strain of *P. aeruginosa* PA14 showed a greater susceptibility to CPX of $<0.08 \mu\text{g mL}^{-1}$ compared to PA01-N, which had an MIC value of $0.3 \mu\text{g mL}^{-1}$. The MIC recorded for *S. sanguinis* and *S. mutans* were 5 and $2.5 \mu\text{g mL}^{-1}$, respectively.

The other bacterial species tested was *E. faecalis*, as it plays a key role in dental root infections and showed an MIC value of 1.25 $\mu\text{g mL}^{-1}$.

Table 5. 2: MIC values of CPX against bacterial strains: *P. aeruginosa* species, *S. sanguinis*, *S. mutans* and *E. faecalis*, determined visually and measured by the OD_{600nm} after 24 h incubation at 37 °C, shaking at 100 rpm. For all species the MIC experiment was repeated in triplicates (n = 3).

Bacterial species	MIC / $\mu\text{g mL}^{-1}$
<i>P. aeruginosa</i> PA14	0.08
<i>P. aeruginosa</i> PAO1-N	0.3
<i>S. sanguinis</i> ATCC 10556	5
<i>S. mutans</i> 3209	2.5
<i>E. faecalis</i> E1071	1.25

The human oral cavity is a diverse bacterial microenvironment and there are many pathogenic species that contribute towards dental diseases and infections.^{45,46} Preventing and controlling dental caries and other dental related disease is still a great challenge due to increasing tolerance and resistance to antibiotics.^{17,47,48} CPX has been shown to inhibit both Gram-positive and Gram-negative bacteria, as confirmed by the MIC values shown in **Table 5. 2**. This confirmed that Gram-negative bacteria, *Pseudomonas* species were more sensitive to CPX. CPX is a fluoroquinolone antibiotic with its primary mechanism of action through the inhibition of bacterial DNA gyrase and topoisomerase IV,⁴¹ responsible for the drug's potent antibacterial activity. Despite CPX's antibacterial properties, therapeutic failure has been reported in previous studies when used to treat various bacterial infections.^{17,48} In one study with *P. aeruginosa* biofilms, Soares *et al.*¹⁷ reported that although CPX was responsible for

killing the majority of cells within the biofilm populations, there were remaining surviving cells, which was attributed to their resistance to CPX. However, increasing the dose strength of CPX can lead to toxic and adverse side effects. Therefore, incorporating into a silica shell can protect CPX from antimicrobial resistance and control its delivery to harmful bacteria.

The antimicrobial susceptibility of the five bacterial species to silica-drug formulations were evaluated by determining their zone of inhibition using the agar diffusion assay method. **Table 5. 3** showed the size of the zones created by CPX antibacterial activity. No zones were formed around **Plain SNP**. Concentrations of, 2 mg mL⁻¹ of CPX showed zones of inhibition against all five species of bacteria, as the concentration used was higher than the determined MIC values. Both *P. aeruginosa* strains, showed larger inhibitory zones approximately 45-48 mm, which indicated CPX was more effective against Gram-negative bacteria.

Table 5. 3: The antimicrobial susceptibility against *S. sanguinis*, *S. mutans*, *E. faecalis* and *P. aeruginosa* species to the following samples: 1) H₂O, 2) **CPX@SNP_A** (10 mg mL⁻¹), 3) **CPX<SNP_A2** (10 mg mL⁻¹), 4) **Plain SNP** (10 mg mL⁻¹) or 5) CPX (2 mg mL⁻¹) were measured by zones of inhibition (in mm) using an agar diffusion method with wells loaded with 50 µL of each samples and repeated in triplicates (n=3).

Sample	Concentration in 50 µL	<i>S. sanguinis</i>	<i>S. mutans</i>	<i>E. faecalis</i>	<i>P. aeruginosa</i> PAO1N	<i>P. aeruginosa</i> PA14
1. H ₂ O	50 µL	None	None	None	None	None
2. CPX@SNP_A	10 mg mL ⁻¹	21 ± 0.6	27 ± 1	23 ± 1	36 ± 1	38 ± 3
3. CPX<SNP_A2	10 mg mL ⁻¹	None	None	None	17 ± 2	15 ± 2
4. Plain SNP	10 mg mL ⁻¹	None	None	None	16 ± 0	None
5. CPX	2 mg mL ⁻¹	30 ± 3	40 ± 1	28 ± 2	48 ± 2	45 ± 2

Furthermore, with adsorbed type particles, **CPX@SNP_A**, at concentration of 10 mg mL⁻¹ produced zones of inhibition ranging from 21 to 38 mm. This agreed with previous studies in **Section 5.3.2.**, which suggest CPX was on the silica surface. The uncontrolled release was confirmed by the inhibitory zones in the agar diffusion assay.

One of the CPX encapsulated particles, **CPX \subset SNP_A2** was tested for its activity against the bacterial strains. More promisingly the formulation showed no zones of inhibition against the three Gram-positive strains. Small zones between 15-17 mm appeared for both *P. aeruginosa* strains with a 10 mg mL⁻¹ concentration. The previous drug release studies with **CPX \subset SNP_A2**, under static conditions (no US trigger) showed a small initial release. Therefore, it is possible CPX on or close to the surface of the silica may contribute toward the inhibition of *P. aeruginosa*, which is more susceptible to CPX.

5.3.5. The antibacterial effect of CPX \subset SNP nanosystems against *S. sanguinis* biofilms

To investigate the effectiveness of **CPX \subset SNP_A2** and **CPX \subset SNP_B5** on biofilms with US, the amount of drug released was determined prior to biofilm studies. The concentration of CPX was calculated from its absorbance using UV-Visible spectroscopy (**Figure 5. 6**). To promote drug release, the ultrasound tip was immersed into the drug-silica solution. It was stimulated for 10 seconds at a low power setting (P10). This was followed by a 30 min incubation period at 37 °C. The idea was to mimic the conditions that would be used in the biofilm experiments to calculate the expected CPX release. The amount of CPX released in solution for **CPX \subset SNP_A2** and **CPX \subset SNP_B5** was 1.5 and 0.68 $\mu\text{g mL}^{-1}$, respectively. In the following biofilm studies, the lowest CPX concentration of 0.68 $\mu\text{g mL}^{-1}$ was used as a positive control for comparison to the drug loaded silica particles.

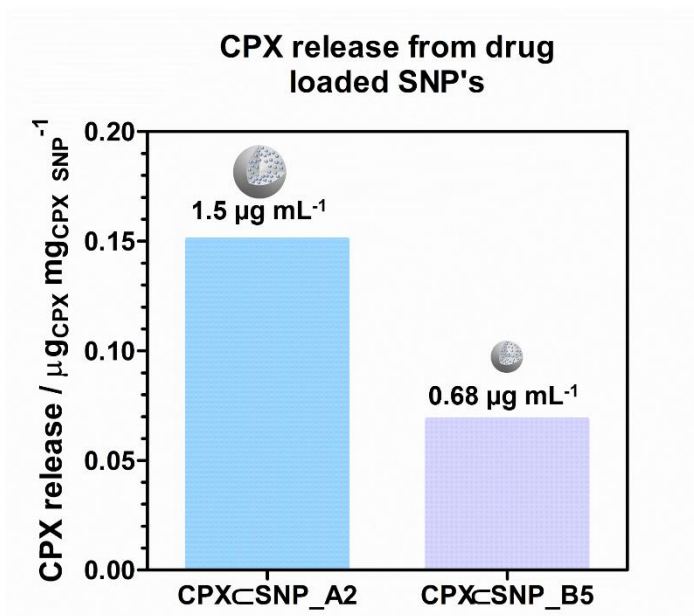


Figure 5. 6: Drug release determined for biofilm studies from **CPX \subset SNP_A2** (10 mg mL^{-1}) and **CPX \subset SNP_B5** (10 mg mL^{-1}) with 10 s cavitation at power setting P10 in H_2O at 37 °C, measured by the absorbance of CPX using UV-Visible spectroscopy.

A *S. sanguinis* biofilm model was used to test the antimicrobial efficacy of two different sized CPX loaded SNPs with US. First, CSLM images of the biofilm were obtained as shown in **Figure 5. 7A** and processed to quantify the percentage viability of live bacteria with and without applying US. This was displayed by the bar graph in **Figure 5. 7B** . The **Plain SNPs** (2 mg mL^{-1}) did not exhibit any antibacterial activity against *S. sanguinis*. This was consistent with the MIC results reported in **Chapter 4**, which showed high concentrations of **Plain SNPs** (MIC value $<16 \text{ mg mL}^{-1}$) had no effect.

Next the biofilms were treated with CPX ($0.68 \text{ } \mu\text{g mL}^{-1}$). CPX on its own showed $86 \pm 3\%$ ($p = 0.0278$) of the bacteria in the biofilm were live and $82 \pm 3\%$ with US. This indicated majority of the bacteria survived and not effected by CPX or US. This was possibly due to the low CPX concentration used, which was not enough to kill bacteria in a biofilm. More so CPX is known to have a lower susceptibility to Gram-positive bacteria.^{51,52} However, US did not enhance the activity of CPX on the biofilm. This indicated CPX alone was not enough to kill *S. sanguinis*.

The influence of drug loaded particle, **CPX<SNP_A2** and **CPX<SNP_B5** without US had no significant effect on the bacterial viability with $89 \pm 7\%$ ($p = 0.7551$) and $94 \pm 4\%$ ($p = 0.1490$) live bacteria remaining after treatment, respectively. It should be noted, the **CPX<SNP_A2** sample showed areas in the 3D biofilm image where there was no visible bacteria. This was possibly due to washing the biofilm surface, which could have dislodged some of the bacteria from the coverslip, but the overall viability remained high.

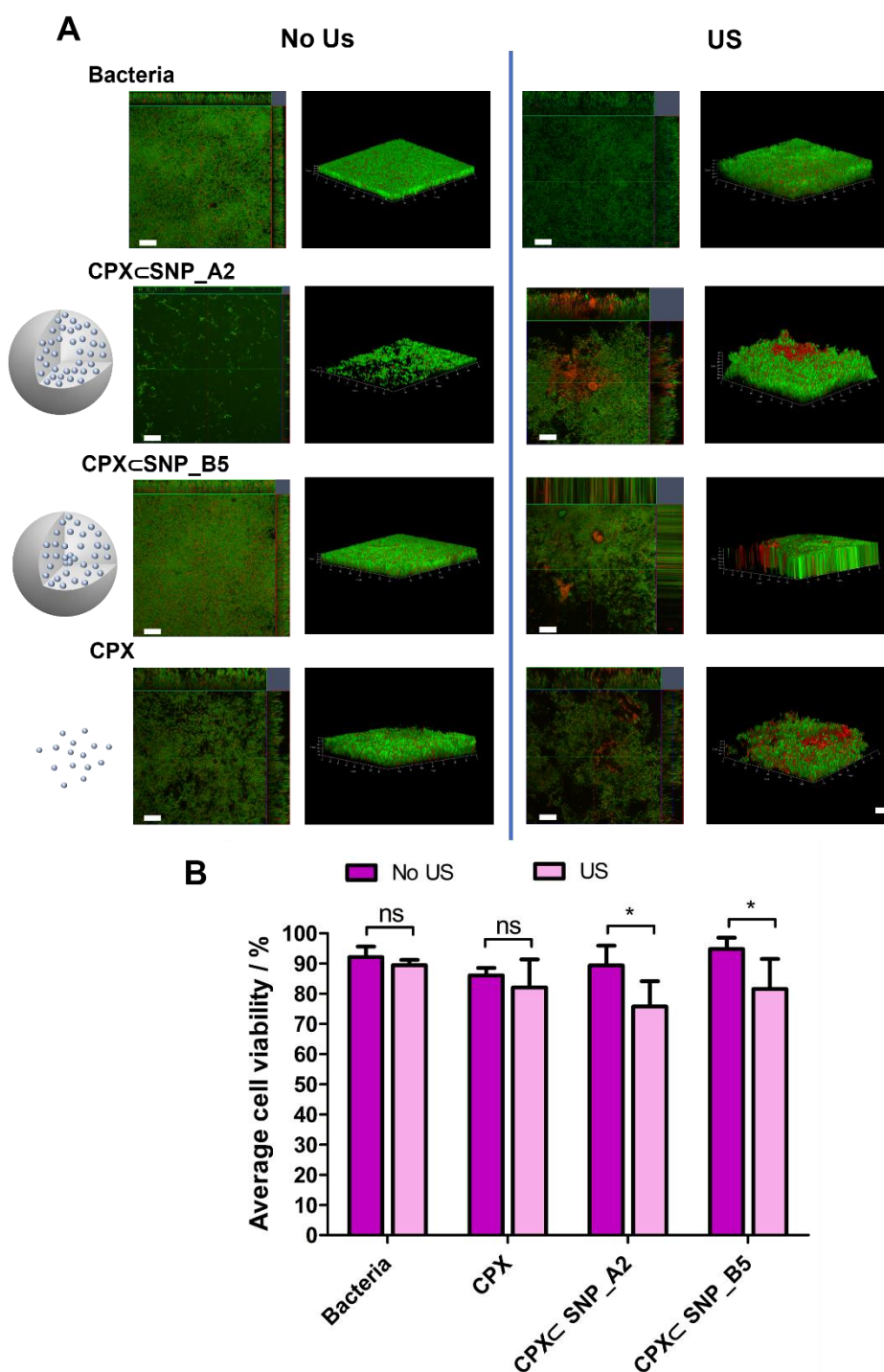


Figure 5. 7: The antibacterial activity of CPX loaded drug delivery systems that have are different in diameter sizes. **A)** CLSM images are shown in 2D and z-stacked to form 3D images of **CPX\subsetSNP_A2** (10 mg mL⁻¹), **CPX\subsetSNP_B5** (10 mg mL⁻¹) and **CPX** (0.68 μ g mL⁻¹) exposed to no US and with US (P10, 10s). Scale bar represents 20 μ m. **B)** Mean and standard deviation of percentage of viability of *S. sanguinis* biofilms. Five images per samples were analysed, conducted as independent triplicates (n=3). The statistical difference in the cell viability between no US and with US was compared. This was performed using a non-parametric Kruskal Wallis test and Dunn's multiple comparison post-test (**p*<0.05).

When the biofilm was treated with **CPX \subset SNP_A2** or **CPX \subset SNP_B5** particles with US, there was a <10% decrease in viability, which was calculated as $78 \pm 8\%$ ($p = 0.0183$) and $82 \pm 10\%$ ($p = 0.0140$) viable cells, respectively. Although the decrease in viability was not obvious, as large areas of the biofilms looked largely unaffected from the CLSM images, it was a significant change when compared to the control samples. This could suggest that CPX encapsulated into a silica drug delivery system can have some influence on enhancing the antimicrobial activity of CPX in a biofilm, but only in combination with US.

5.3.6. The antibacterial effect of CPX \subset SNP nanosystems against *S. mutans* biofilms

To further examine the effects of **CPX \subset SNP** and US, another Gram-positive bacteria was tested. *S. mutans* is an early coloniser on the tooth surface like *S. sanguinis*. However, *S. mutans* are able to survive in acidic conditions and interact with other colonising bacteria. In contrast to *S. sanguinis*, *S. mutans* is related to poor health, as it is an acid producing bacterium and a primary causative agent of dental caries.^{56,57} There are no studies of CPX encapsulated into a silica system responsive to US that have been shown to be effective against *S. mutans* biofilms. Therefore, this study uses a more relevant strain of bacteria related to dental infections and disease to examine antimicrobial efficacy of the synthesised CPX drug loaded SNPs.

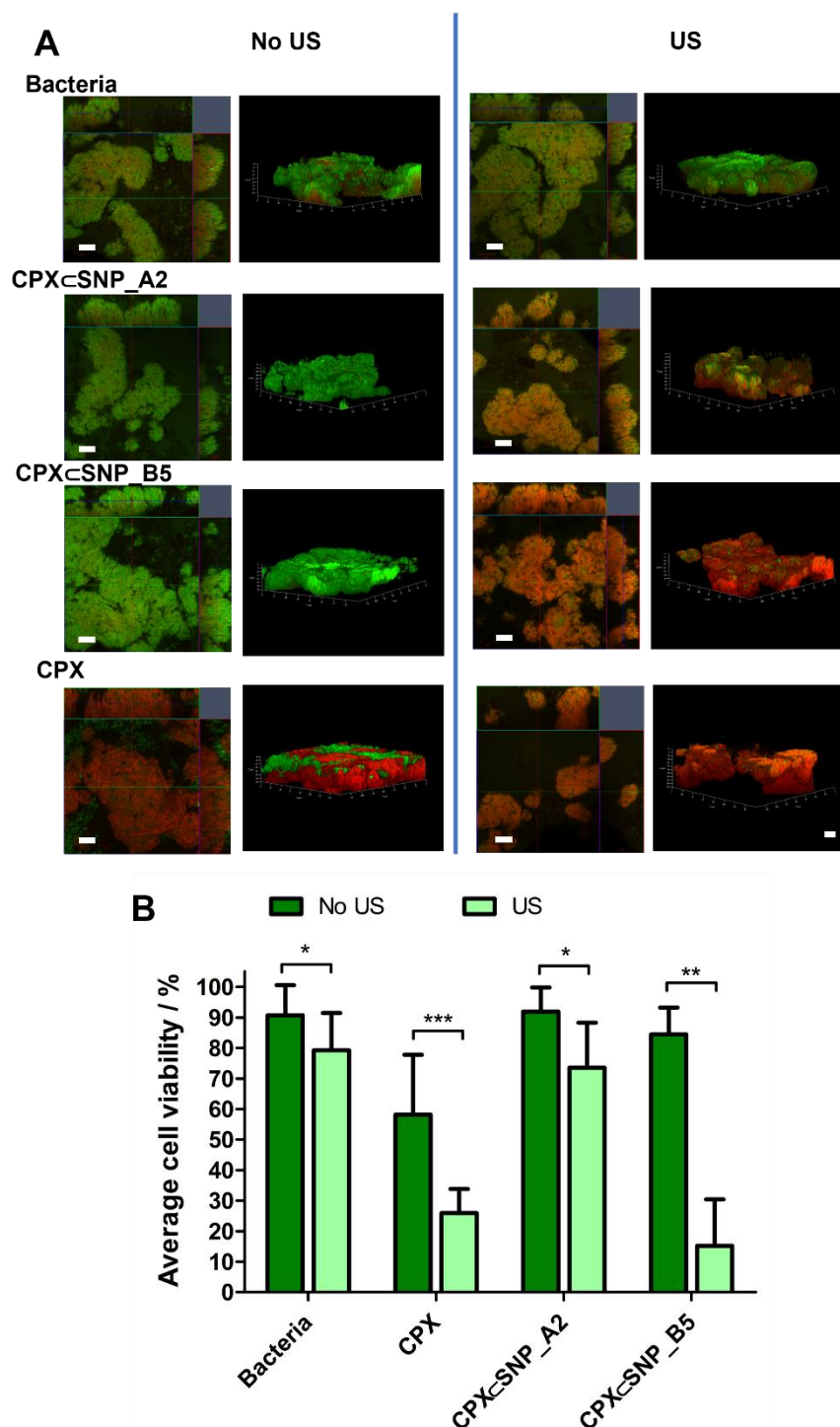


Figure 5. 8: The antibacterial activity of CPX loaded drug delivery systems that have are different in diameter sizes. **A)** CLSM images are shown in 2D and z-stacked to form 3D images of **CPX_CSNP_A2** (10 mg mL⁻¹), **CPX_CSNP_B5** (10 mg mL⁻¹) and **CPX** (0.68 µg mL⁻¹) exposed to no US and with US (P10, 10s). Scale bar represents 20 µm. **B)** Mean and standard deviation of percentage of viability of *S. mutans* biofilms. Five images per samples were analysed, conducted as independent triplicates (n=3). The statistical difference in the cell viability between no US and with US was compared. This was performed using a non-parametric Kruskal Wallis test and Dunn's multiple comparison post-test (**p*<0.05, ** *p*<0.01, *** *p*<0.001).

S. mutans biofilms were grown under the same conditions as for the single-species biofilms with *S. sanguinis* and treated in the same way. Before analysis, the established, 3-day-old biofilms were exposed to US and CPX particles. In **Figure 5.8A**, the CLSM images with the live/dead stain showed a healthy biofilm with no US applied. The untreated control had a viability of $91 \pm 10\%$ and with US only this decreased to $79 \pm 12\%$ ($p=0.0355$). It is possible that US, in this instance had some effect on the cell viability. The depth profiles were also examined in **Figure 5. 8A**. The bottom of the biofilm which was closer to the surface of the coverslip had higher regions of red. There are several reasons for this outcome. *S. mutans* could have been more susceptible to the effects of cavitation, causing cell disruption. However, not all repeats of the samples showed dead bacteria following US exposure. The more likely explanation was that biofilm may not have been receiving enough nutrients, a limitation to using a static method to grow biofilms.⁵⁸

Addition of free CPX ($0.68 \mu\text{g mL}^{-1}$) to the biofilm, confirmed that *S. mutans* bacteria were more susceptible to the antimicrobial agent than *S. sanguinis*, which was in agreement with MIC measurements. The MIC value of CPX against *S. mutans* was $2.5 \mu\text{g mL}^{-1}$ and this was consistent with other literature findings ($0.125\text{--}16 \mu\text{g mL}^{-1}$).^{52,59} CPX only, showed $58 \pm 20\%$ of the bacteria were still alive. This decreased significantly to $26 \pm 8\%$ ($p<0.0001$) when combined with US. Not only did these viability results show the sensitivity of *S. mutans* biofilms to CPX, but the bactericidal properties were enhanced with the addition of US. There is a strong assumption the effects of cavitation are responsible for the increased cell death. Using US could improve dispersion of CPX into the biofilm, allowing greater interaction with the bacterial cells. Another suggestion was the mechanism of sonoporation, as a result of cavitation. The

temporary opening in cell membrane and wall can allow for the exchange of substances in and out of the cell. Cavitation exposure may be a driving force to deliver and distribute antibiotics to these bacteria embedded within a biofilm. The other reason was *S. mutans* has a different biofilm structure to *S. sanguinis*, hence was more susceptible to CPX.⁵⁸

Treating the biofilms with only **CPX \subset SNP_A2** (10 mg mL⁻¹) or **CPX \subset SNP_B5** (10 mg mL⁻¹) particles, showed high bacterial viability of $92 \pm 8\%$ ($p=0.6498$) and $84 \pm 9\%$ ($p=0.0878$), respectively. The lack of antibacterial killing was promising because it indicated that the drug loaded silica particles managed to contain the drug within the silica, leading to having no influence on the viability. Furthermore, **CPX \subset SNP_A2** and **CPX \subset SNP_B5** particles triggered with US, showed a reduction in viability to $74 \pm 15\%$ ($p=0.0173$) and $22 \pm 27\%$ ($p=0.0013$), respectively. Both these formulations resulted in an increased bactericidal activity within the biofilm. This was shown by the greater dead areas of bacteria compared to no US. More interestingly, **CPX \subset SNP_B5** exhibited a significant effect ($p=0.0013$) with US compared to **CPX \subset SNP_A2**.

This difference in bactericidal efficacy may depend on different parameters, including size, shape, surface charge of the particles and the biofilm architecture.^{60–62} Biofilms have a highly porous network which offers a pathway for the diffusion of particles into their structure. They contain extracellular polymeric substances (EPS), known to provide structural stability and adhere bacteria cells together.^{63,64} The transport of small molecule drugs can be hindered by the porous matrix due to the interactions with the physicochemical matrix of EPS. Therefore, limiting the amount of antibiotic to the denser and deeper parts of the biofilm.⁶⁵ The CLSM images showed CPX alone failed

to kill all the bacteria in the biofilm and was hindered by *S. mutans* biofilm structure. On the other hand, treatment with US and the drug suggests the antibacterial differences observed are due to possible thermal and mechanical effects from using ultrasonic scaler. The US waves generated could allow better distribution of free CPX and disruption to the bacterial membrane, increasing the permeability to CPX.

When CPX was encapsulated within the SNPs, **CPX \subset SNP_A2** and **CPX \subset SNP_B5** this resulted in different amounts of bacterial viability. The size of **CPX \subset SNP_B5** particles was 100 nm, three times smaller than **CPX \subset SNP_A2** particles (diameters 300 nm). It seems that size of particles can also have a role to play at enhancing the antibacterial activity in biofilms. Recent studies have reported that smaller particles have a greater influence on the antibacterial activity.^{62,66,67} For example, a study with silver NPs of difference sizes and charges showed that large sizes slowed the self-diffusion. However, the movement of NPs was also dependant on the density of the biofilm and harder for larger NPs greater than 50 nm to penetrate the biofilm.⁶⁸

It is unclear if the charge may affect the fate and transport of the particles in this biofilm. In this case, **CPX \subset SNP_A2** and **CPX \subset SNP_B5** had an overall negative surface charge of -33 and -35 mV respectively. In particular, positively charged NPs have been found to be more effective against Gram-positive bacteria.^{62,68–71} However, other SNPs developed using nitric oxide do not rely on direct NP-cell contact. In contrast, they appeared to be highly effective at controlling the pathogenic biofilm growth.⁷² The highly negative charge of **CPX \subset SNP_A2** and **CPX \subset SNP_B5** was not considered to contribute towards the killing effect.

The shape of both particles was shown by the SEM images to be spherical with uniform morphology. Hence, the shape was not thought to be a reason for **CPX \subset SNP_B5** higher bactericidal activity. Therefore, this suggests that smaller sized particles were more important to obtain an enhanced antibacterial activity with US.

The fundamental mechanisms guiding interactions between the drug loaded NPs and *S. sanguinis* and *S. mutans* biofilms are still unclear from these experiments. Further analysis and tests would be needed to determine the killing mechanism. Promisingly, ultrasonic scaler was central to all the studies, providing various effects, such as from cavitation that could have contributed towards biophysical effects and to induce a synergistic effect. Cavitation is thought to be a dominant force to disrupt the biofilm, aiding penetration of the drug loaded particles, especially for **CPX \subset SNP_B5** with small sizes. This offers an opportunity for transportation and localised drug delivery, of small particles to impact the viability of bacteria in a biofilm.

5.4. Conclusions

In this work, CPX, an antibiotic drug was successfully incorporated into SNPs in a one-pot approach. The original proof-of-concept drug delivery model (**Chapter 3**) was improved, to yield **CPX \subset SNP_B5** NPs. The shorter reaction time and addition of CPX at the start of the reaction achieved **CPX \subset SNP_B5** with smaller NP sizes of ~100 nm diameters.

The SNP framework provided protection and a barrier to prevent uncontrolled release of CPX. Furthermore, **CPX \subset SNP_B5** showed promising on-demand release from applying the US. The release behaviour indicated the effects of US were responsible for forcing CPX from the SNP carrier. Thus, supporting **CPX \subset SNP**'s could be sensitive to the thermal and mechanical effects of cavitation produced from the ultrasonic scaler.

The **CPX \subset SNP**'s showed to enhance CPX's antimicrobial activity against Gram-positive bacteria, *S. mutans* by activation with US. *S. mutans* biofilms were more susceptible to **CPX \subset SNP**'s than *S. sanguinis* biofilms. However, more noticeably with the 100 nm sized **CPX \subset SNP** .

The fundamental mechanisms guiding the interactions between CPX release from the SNP and biofilms remains unknown. However, these studies have shown how the particle size could influence the antimicrobial activity. They provide a strong foundation for a one-pot synthesis with other antimicrobials and antibiotics to overcome drug-resistance and controlled deliver with triggered release. As CPX has a fluoroquinolone structure, it has fluorescent properties. This could aid tracking particle through a biofilm using imaging techniques to help understand the influence of **CPX \subset SNP** and US.

5.5. Appendix

Sample	TEOS / mL	NH ₄ OH / mL	ETOH / mL	H ₂ O / mL	CPX solution
CPX⊂SNP_A1	2.4	1.88	26.66	1.57	3 mL (20 mg mL ⁻¹)
CPX⊂SNP_A2	2.4	1.88	26.66	1.57	3 mL (30 mg mL ⁻¹)
CPX⊂SNP_B1	1.3	3	22.7	-	3 mL (0.5 mg mL ⁻¹)
CPX⊂SNP_B2	1.3	7	18.7	-	3 mL (0.5 mg mL ⁻¹)
CPX⊂SNP_B3	2	1.5	25	-	0.5 mL (0.5 mg mL ⁻¹)
CPX⊂SNP_B4	2	1.5	30	-	0.5 mL (36 mg mL ⁻¹)
CPX⊂SNP_B5	2	1.5	30	-	3 mL (20 mg mL ⁻¹)
Plain SNP A	2.4	1.88	26.66	1.57	-
CPX@SNP_A	-	-	-	35	200 mg + 100 mg Plain SNP A
Plain SNP B	2	1.5	30	-	-
CPX@SNP_B	-	-	-	35	200 mg + 100 mg Plain SNP B

Figure S5. 1: Synthesis of particles with CPX, reagent starting amounts.

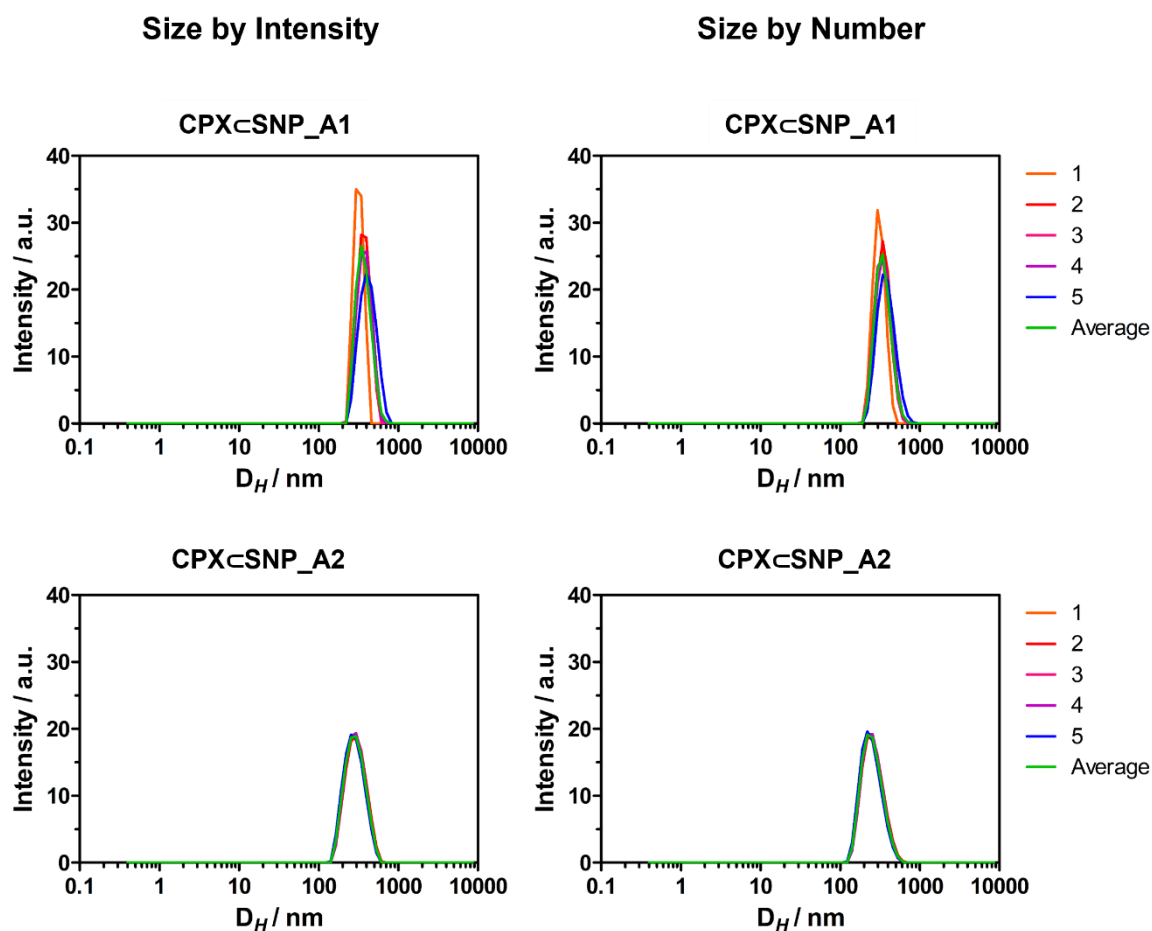


Figure S5. 2: DLS analysis of size distribution: **CPX ζ SNP_A1** and **CPX ζ SNP_A2** in H₂O. **CPX ζ SNP_A1**: 372 ± 81 nm (intensity), 332 ± 82 nm (number) and PDI: 0.287. **CPX ζ SNP_A2**: 295 ± 83 nm (intensity), 260 ± 78 nm (number) and PDI: 0.099.

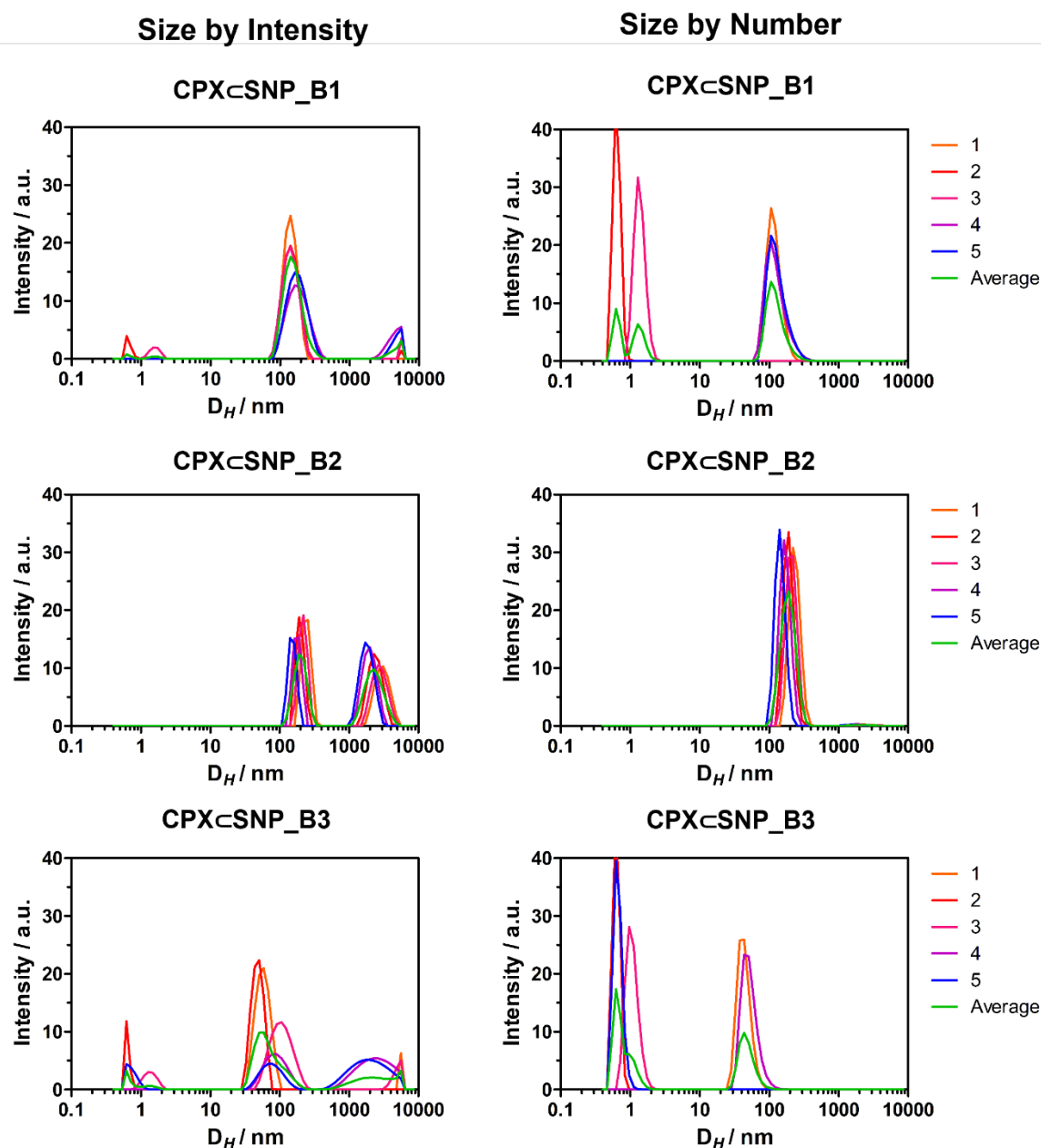


Figure S5. 3: DLS analysis of size distribution: **CPX ζ SNP_B1**, **CPX ζ SNP_B2** and **CPX ζ SNP_B3** in H₂O. **CPX ζ SNP_B1**: 159 ± 49 nm (intensity), 127 ± 41 nm (number) and PDI: 0.484. **CPX ζ SNP_B2**: 201 ± 41 nm (intensity), 190 ± 45 nm (number) and PDI: 0.719. **CPX ζ SNP_B3**: 100 ± 38 nm (intensity), 53 ± 15 nm (number) and PDI: 0.714.

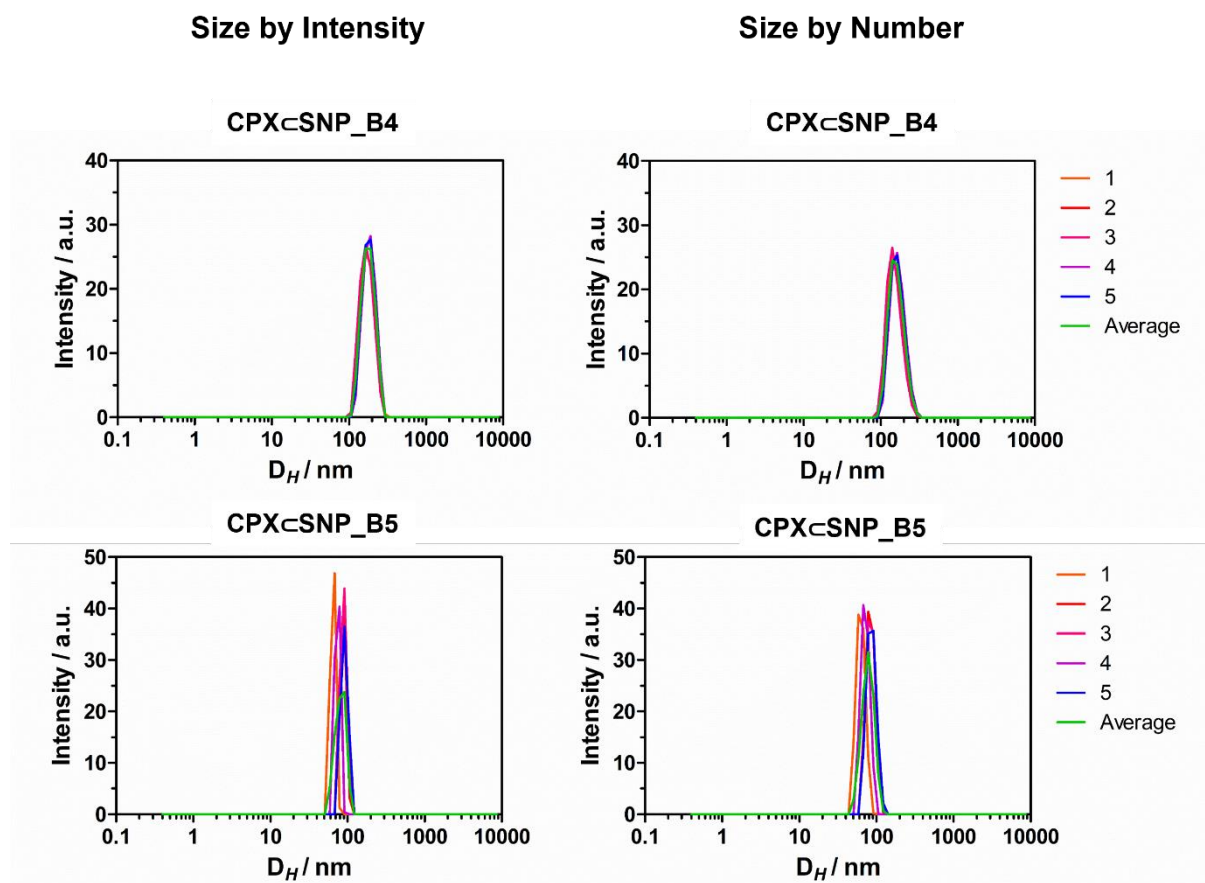


Figure S5. 4: DLS analysis of size distribution: **CPX ζ SNP_B4** and **CPX ζ SNP_B5** in H₂O. **CPX ζ SNP_B4:** 180 \pm 34 nm (intensity), 162 \pm 37 nm (number) and PDI: 0.125. **CPX ζ SNP_B5:** 103 \pm 32 nm (intensity), 90 \pm 26 nm (number) and PDI: 0.686.

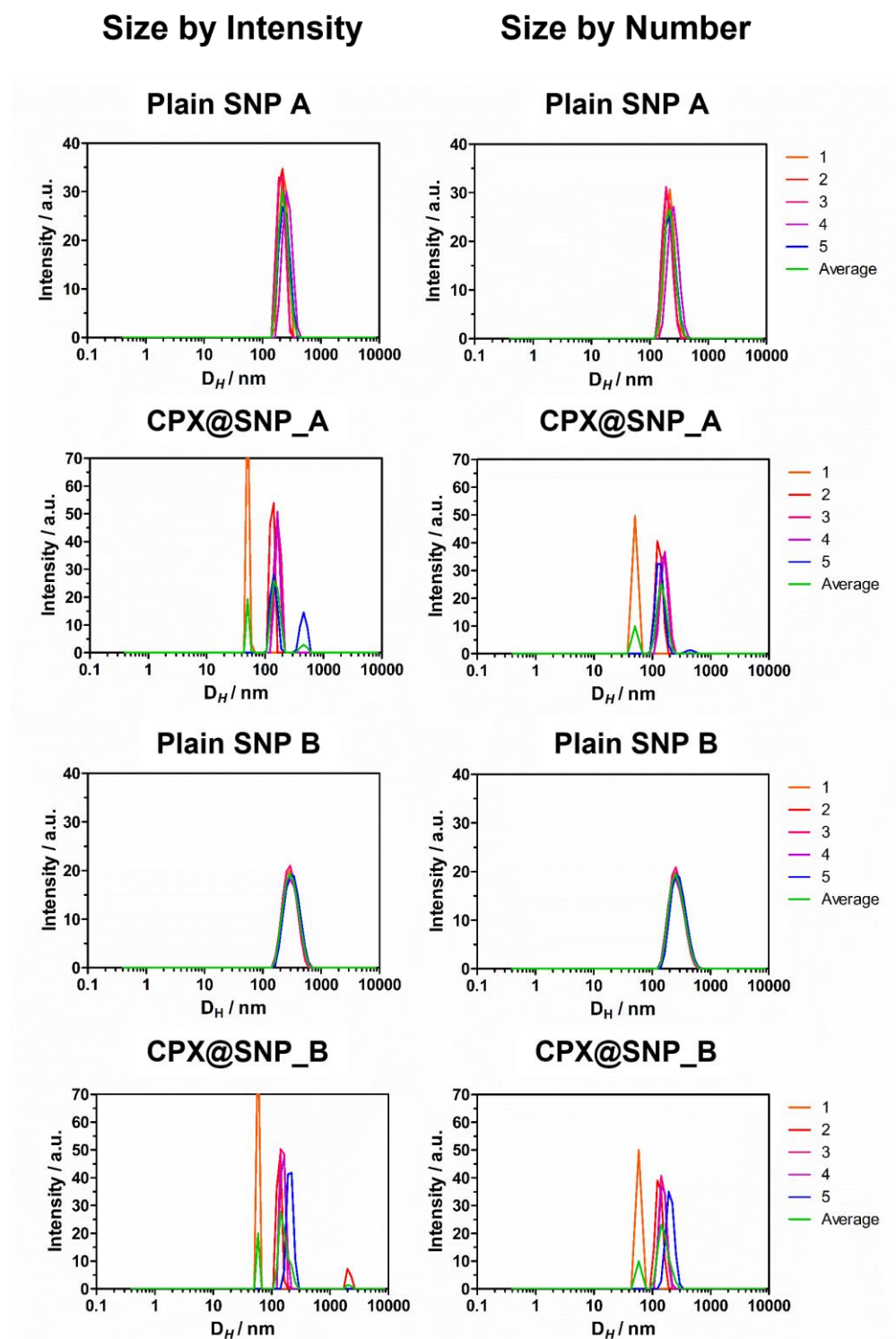


Figure S5. 5: DLS analysis of size distribution: **Plain SNP A**, **CPX@SNP_A**, **Plain SNP B** and **CPX@SNP_B** in H₂O. **Plain SNP A:** 180 ± 34 nm (intensity), 162 ± 37 nm (number) and PDI: 0.125. **CPX@SNP_A:** 152 ± 21 nm (intensity), 147 ± 26 nm (number) and PDI: 0.817. **Plain SNP B:** 250 ± 41 nm (intensity), 241 ± 45 nm (number) and PDI: 0.225. **CPX@SNP_B:** 164 ± 32 nm (intensity), 160 ± 35 nm (number) and PDI: 1.000.

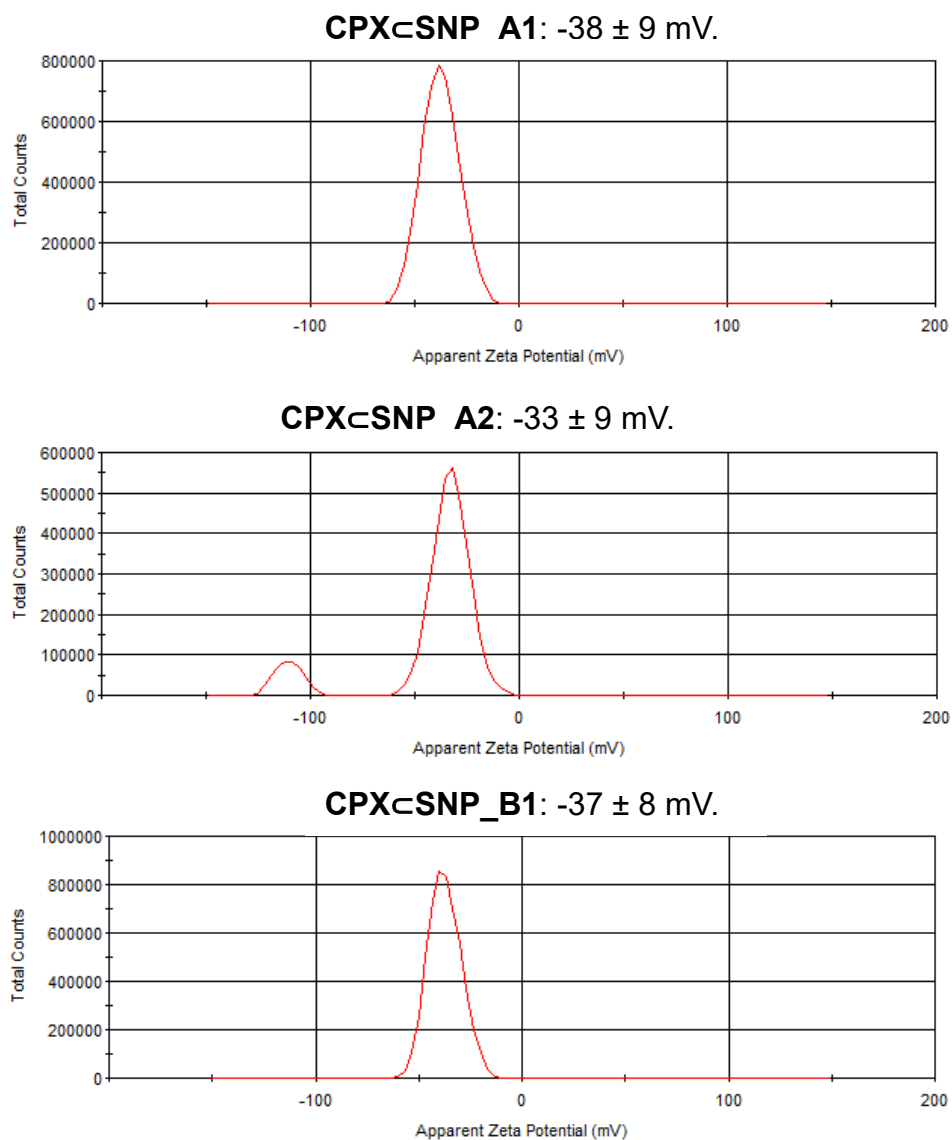
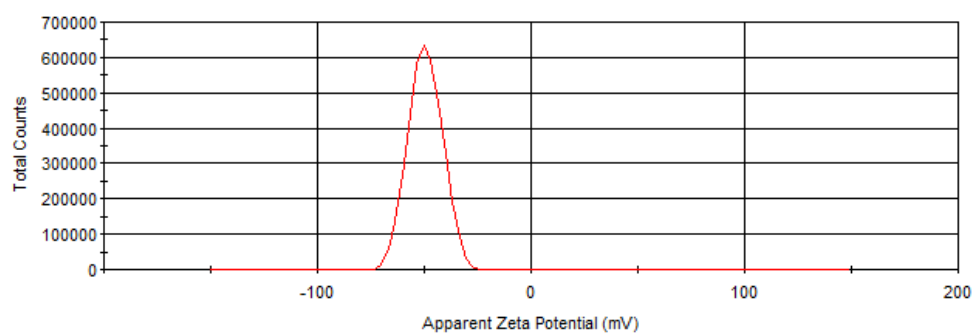
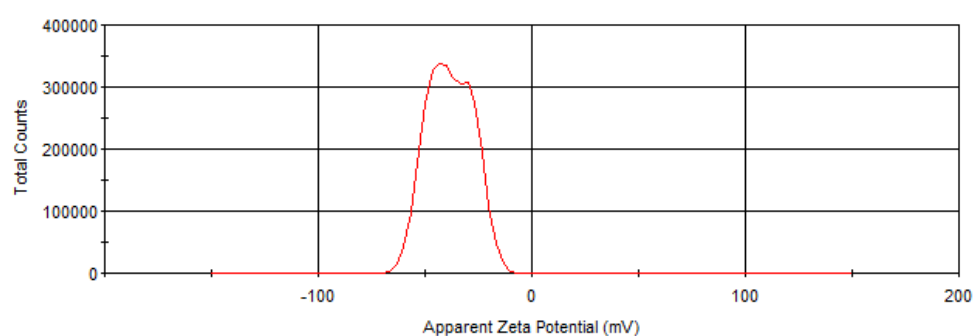


Figure S5. 6: DLS analysis in H₂O of zeta potential charge.

CPX \subset SNP_B2: -49 ± 8 mV.



CPX \subset SNP_B3: -38 ± 3 mV.



CPX \subset SNP_B4: -36 ± 5 mV.

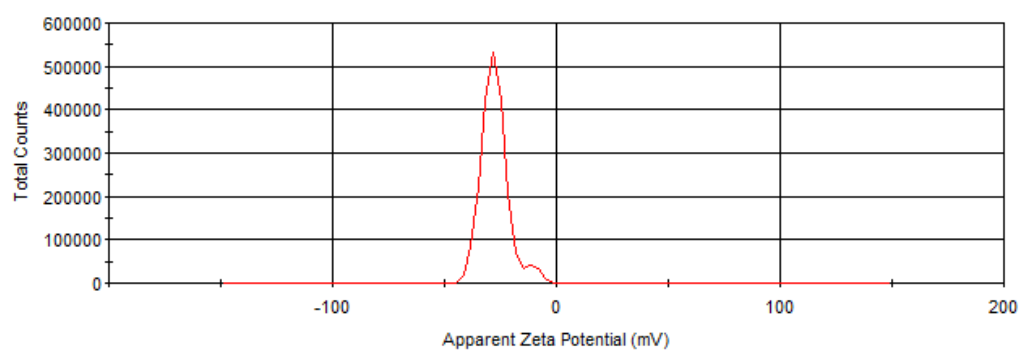
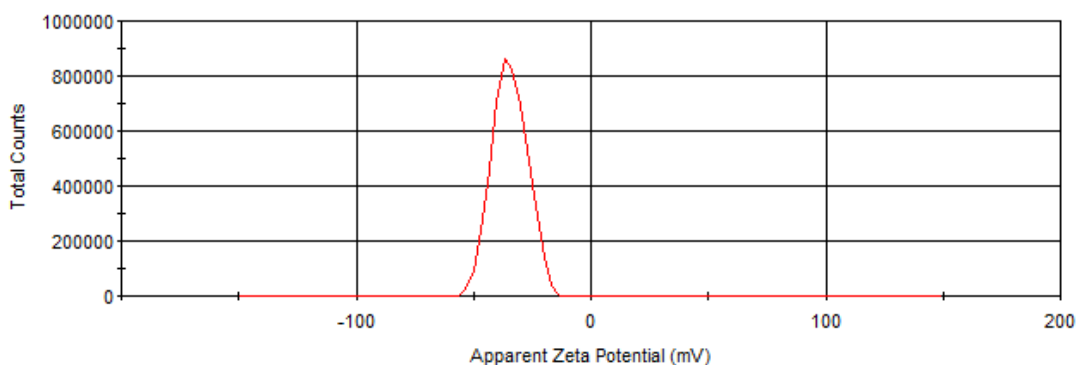
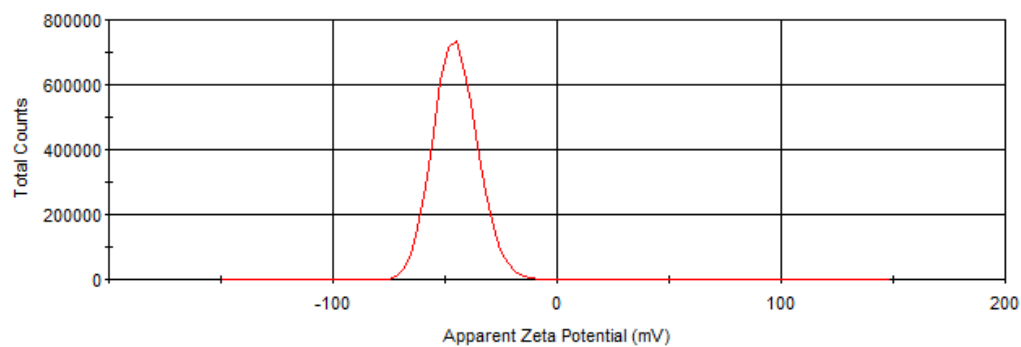


Figure S5. 7: DLS analysis in H₂O of zeta potential charge.

CPX_cSNP_B5: -35 ± 7 mV.



Plain SNP A: -45 ± 9 mV.



CPX@SNP_A: $+10 \pm 4$ mV and 30 ± 4 mV (2 populations).

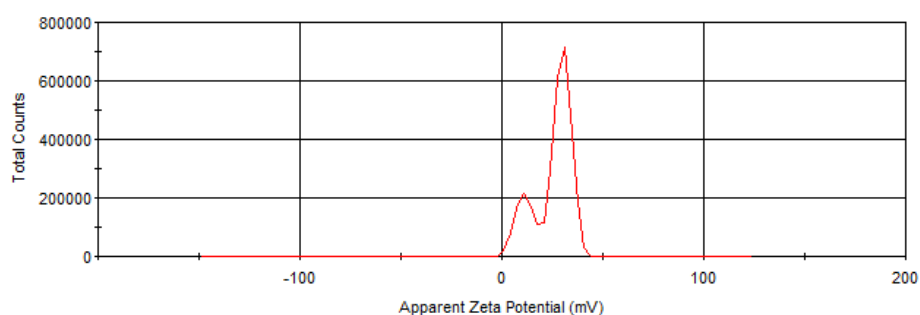
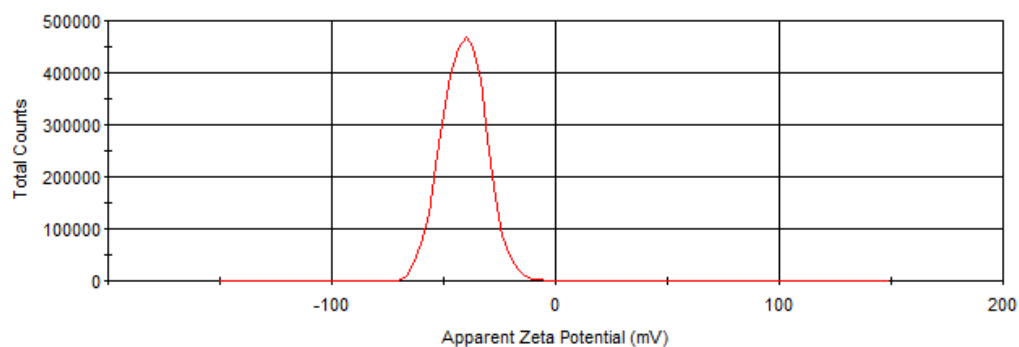


Figure S5. 8: DLS analysis in H₂O of zeta potential charge.

Plain SNP B: -40 ± 10 mV.



CPX@SNP_B: -19 ± 6 mV.

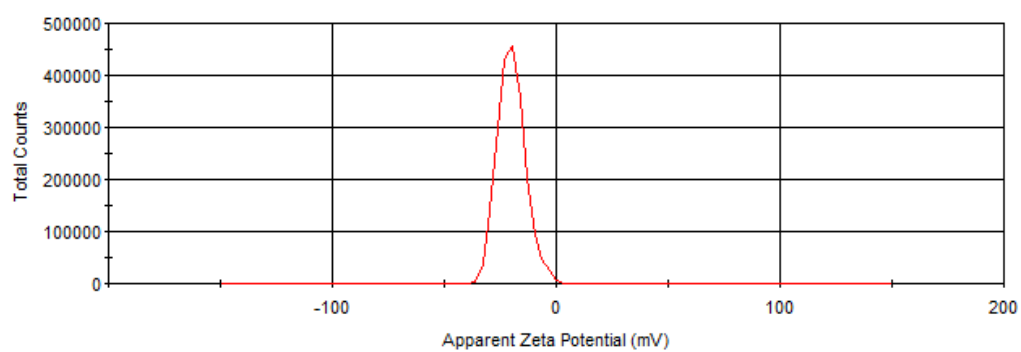


Figure S5. 10: DLS analysis in H₂O of zeta potential charge.

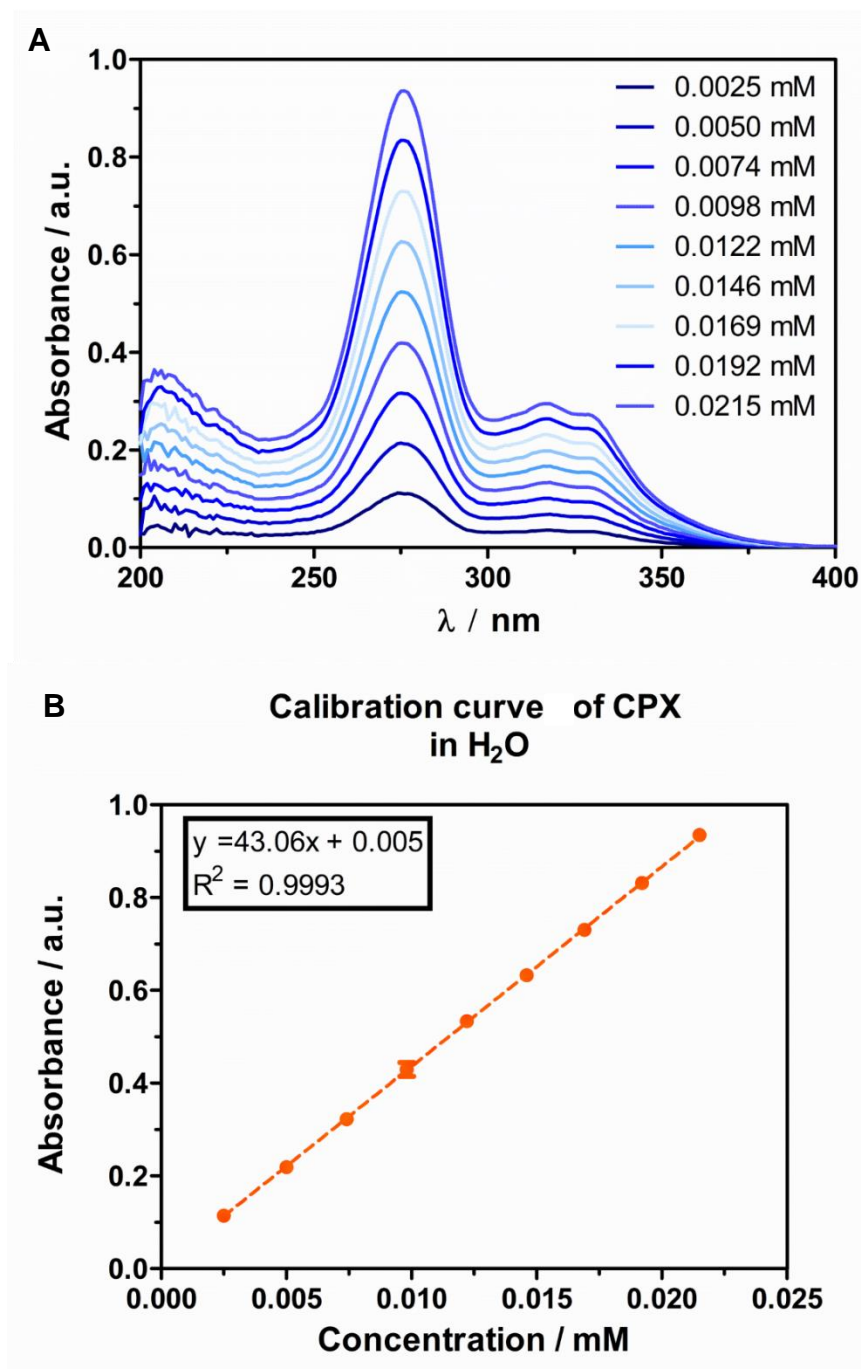


Figure S5. 11: A) UV-Visible absorbance of CPX in H₂O at different concentrations (0.0025 - 0.0215 mM). **B)** Calibration curve of CPX to calculate the absorption coefficient (ϵ) using the Beer Lamberts Law. Concentration plotted against absorbance at $\lambda_{\text{max}}=275$ nm to determine $\epsilon = 43060 \pm 56 \text{ M}^{-1}\text{cm}^{-1}$ (mean and standard deviation, $n=3$).

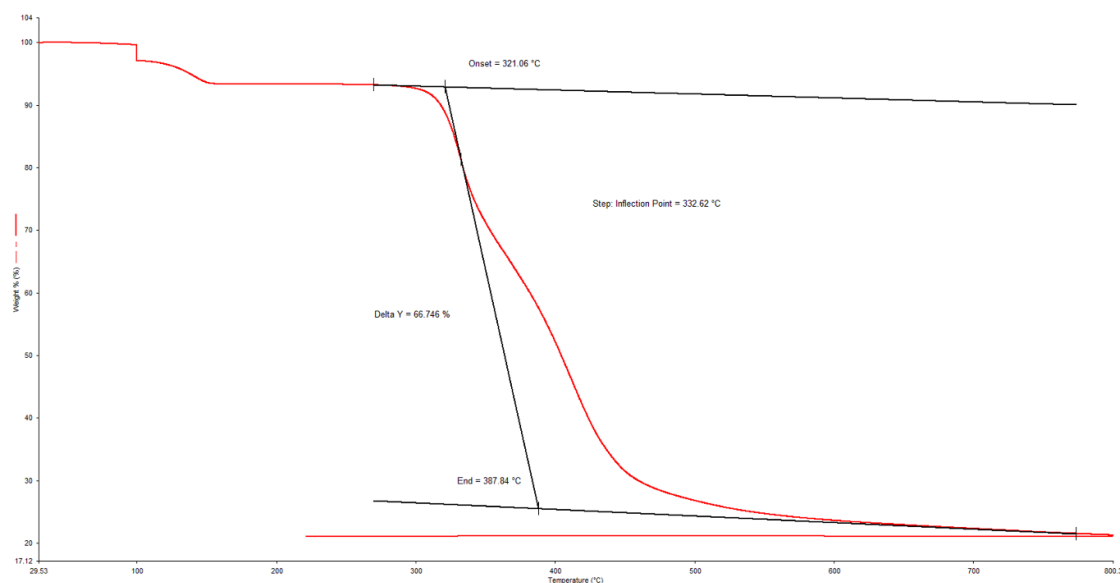


Figure S5. 13: TGA curve of **CPX**, Showing the overall weigh loss with increasing temperature.

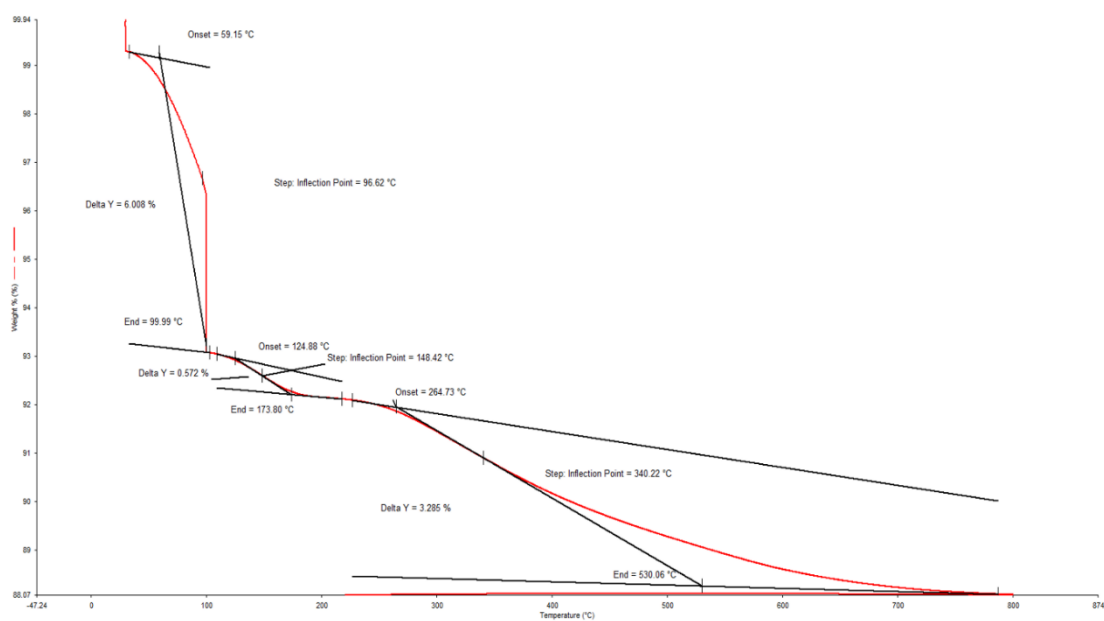


Figure S5. 14: TGA curve of **CPX_SNP_A2**, Showing the overall weigh loss with increasing temperature.

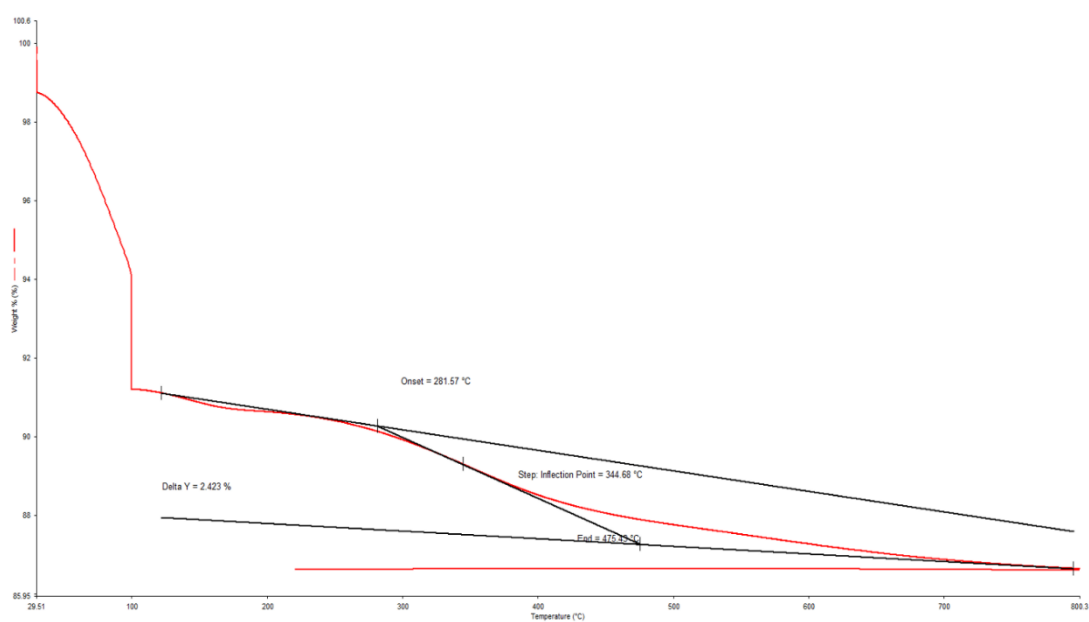


Figure S5. 15: TGA curve of **CPX-SNP_B5**, Showing the overall weigh loss with increasing temperature.

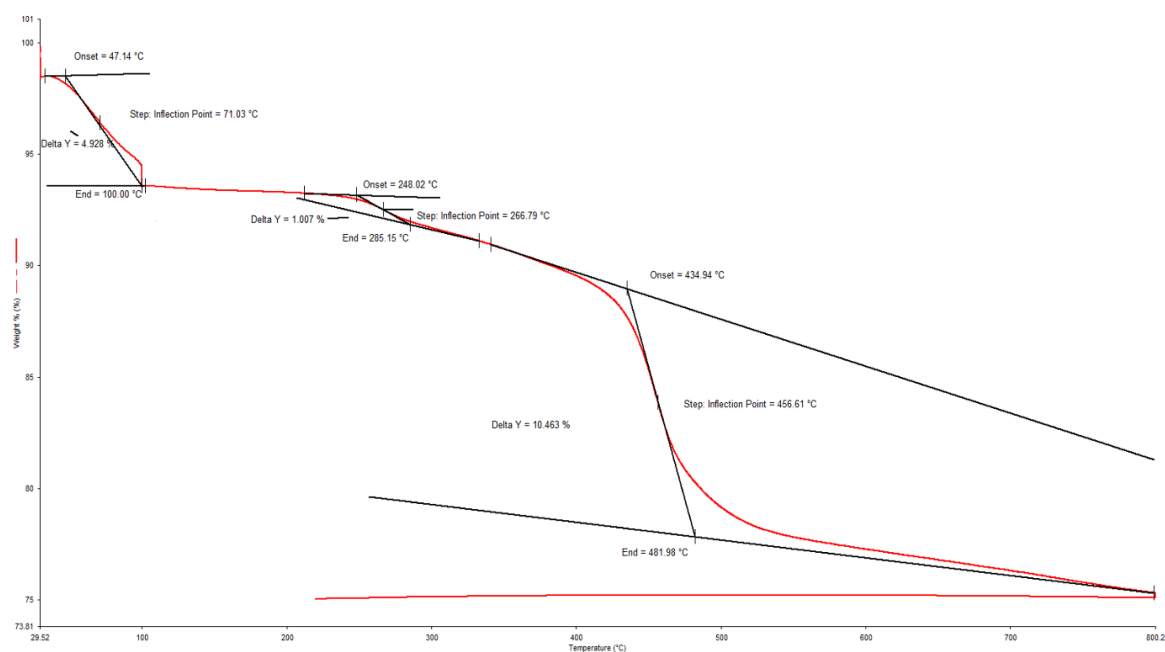


Figure S5. 16: TGA curve of **CPX@SNP_A**, Showing the overall weigh loss with increasing temperature.

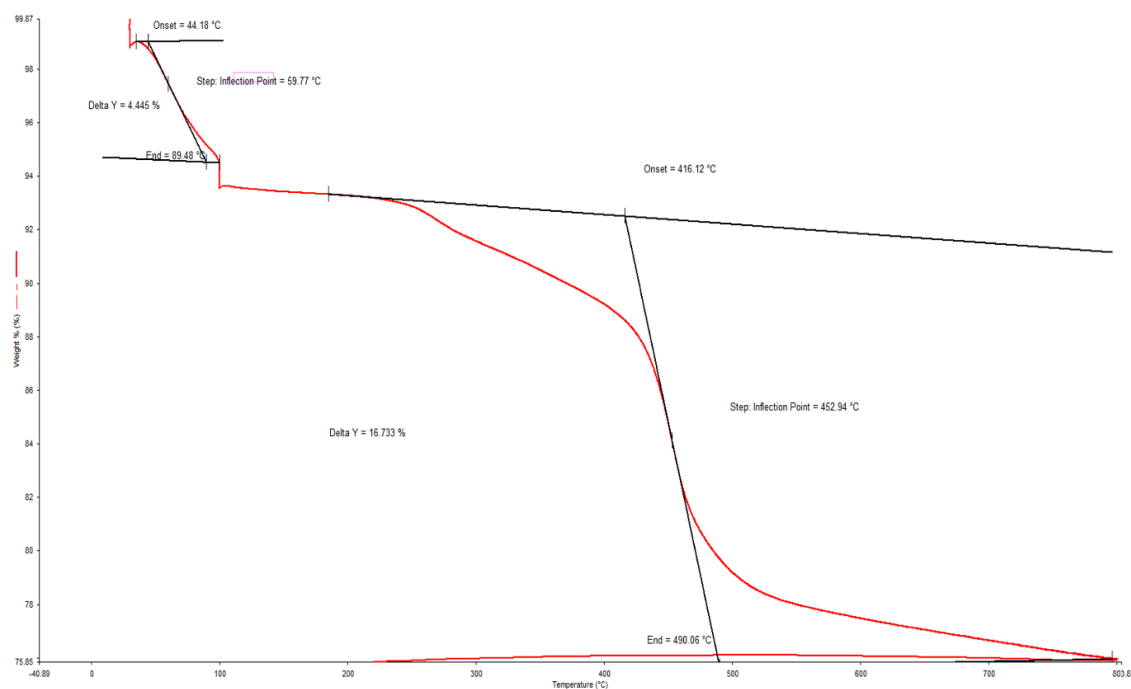


Figure S5. 17: TGA curve of **CPX@SNP_B**, Showing the overall weigh loss with increasing temperature.

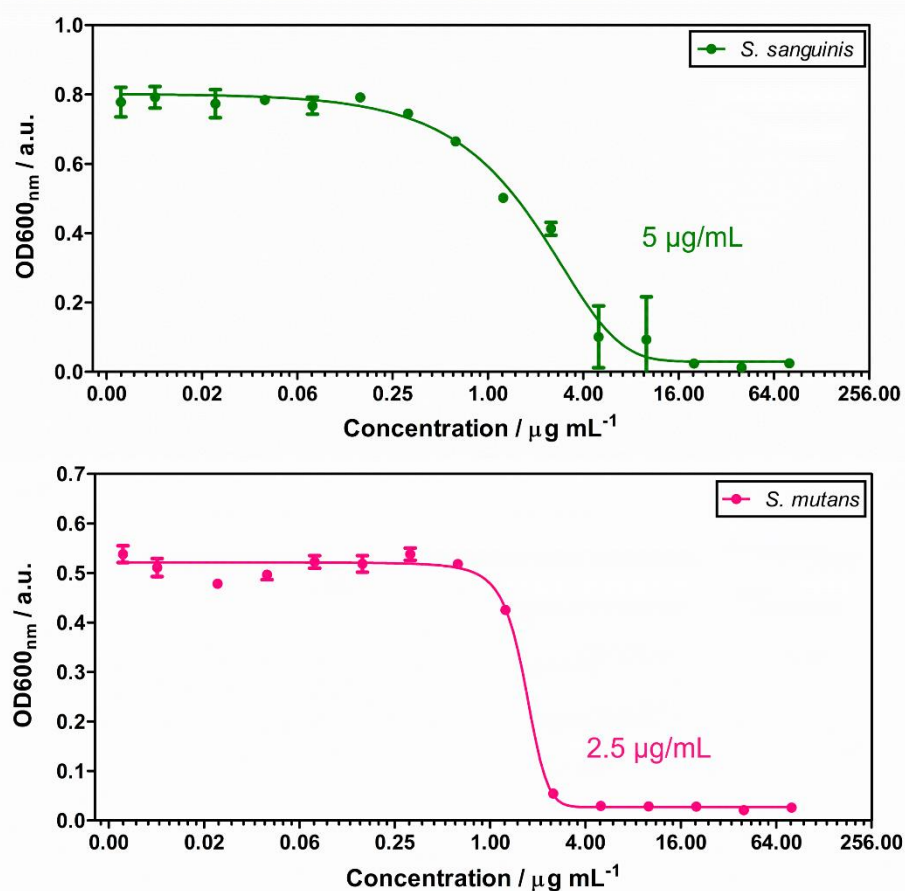
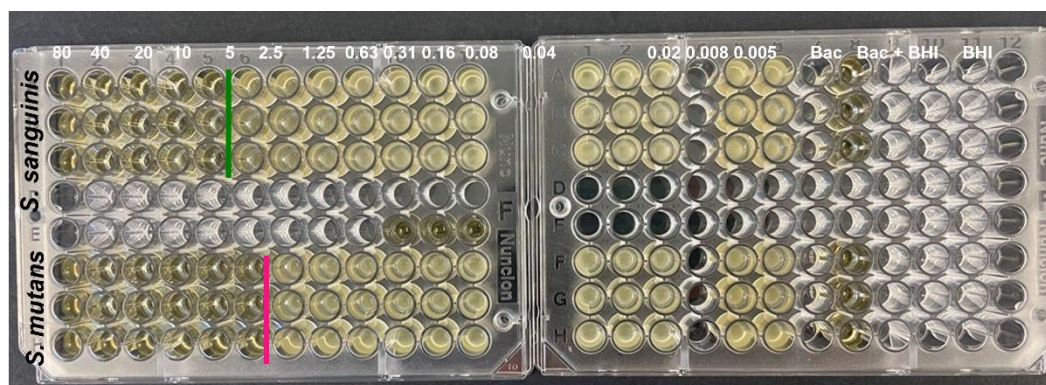


Figure S5. 18: Minimum inhibitory concentration (MIC) of CPX against bacterial strains *S. sanguinis* and *S. mutans*. The MIC value was observed visually and measured by the OD_{600nm}, after 20 h incubation at 37 °C at 100 rpm. For all species the MIC was repeated in triple triplicates (n = 3).

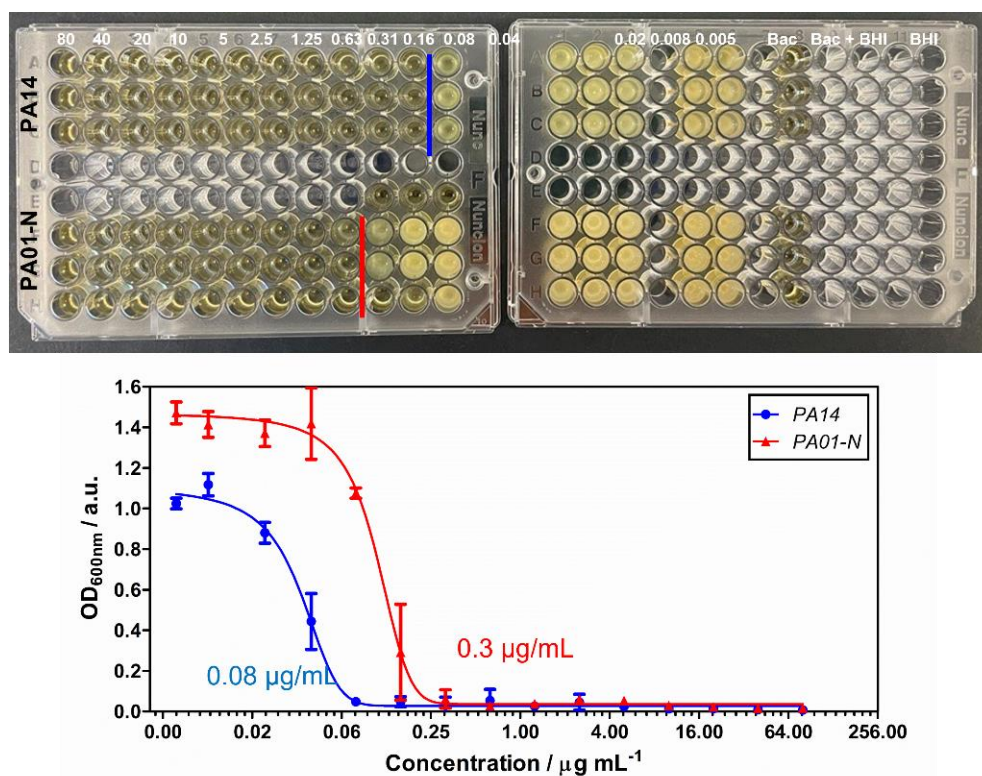


Figure S5. 19: Minimum inhibitory concentration (MIC) of CPX against bacterial strains of *P. aeruginosa*: PA14 and PA01-N. The MIC value was observed visually and measured by the OD_{600nm}, after 20 h incubation at 37 °C at 100 rpm. For all species the MIC was repeated in triple triplicates (n = 3).

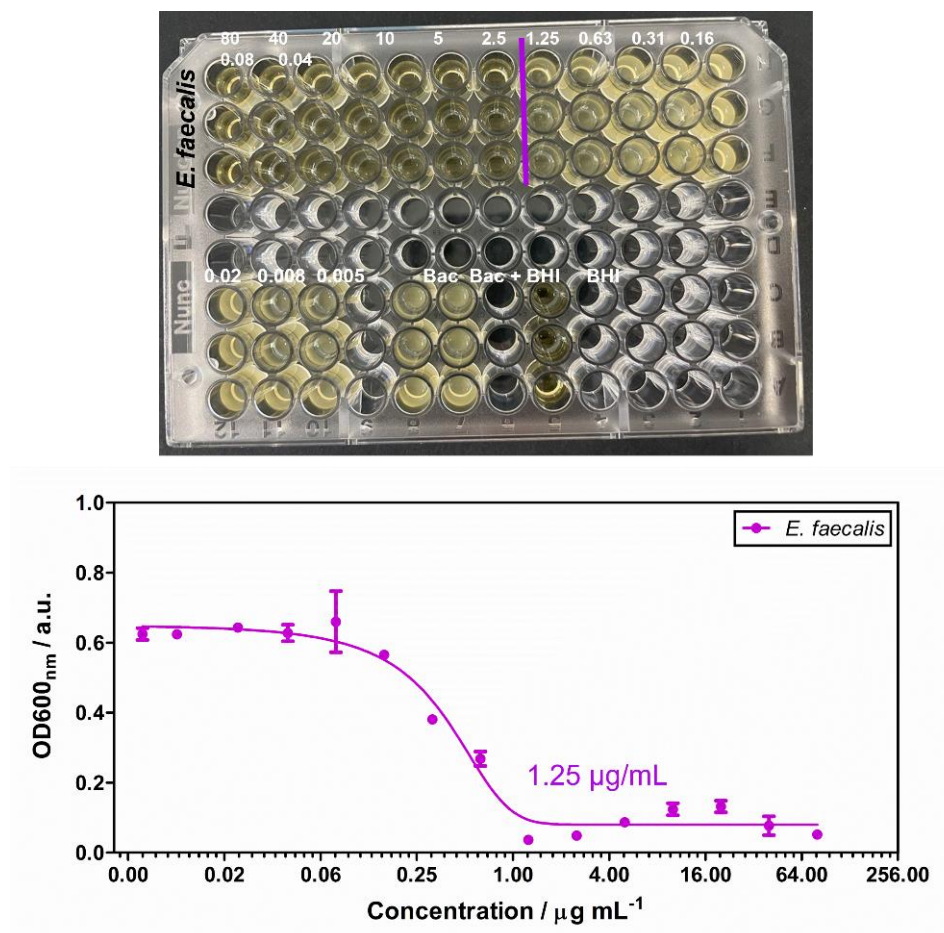


Figure S5. 20 Minimum inhibitory concentration (MIC) of CPX against bacterial strain of *E. faecalis*. The MIC value was observed visually and measured by the OD_{600nm}, after 20 h incubation at 37 °C at 100 rpm. For all species the MIC was repeated in triple triplicates (n = 3).

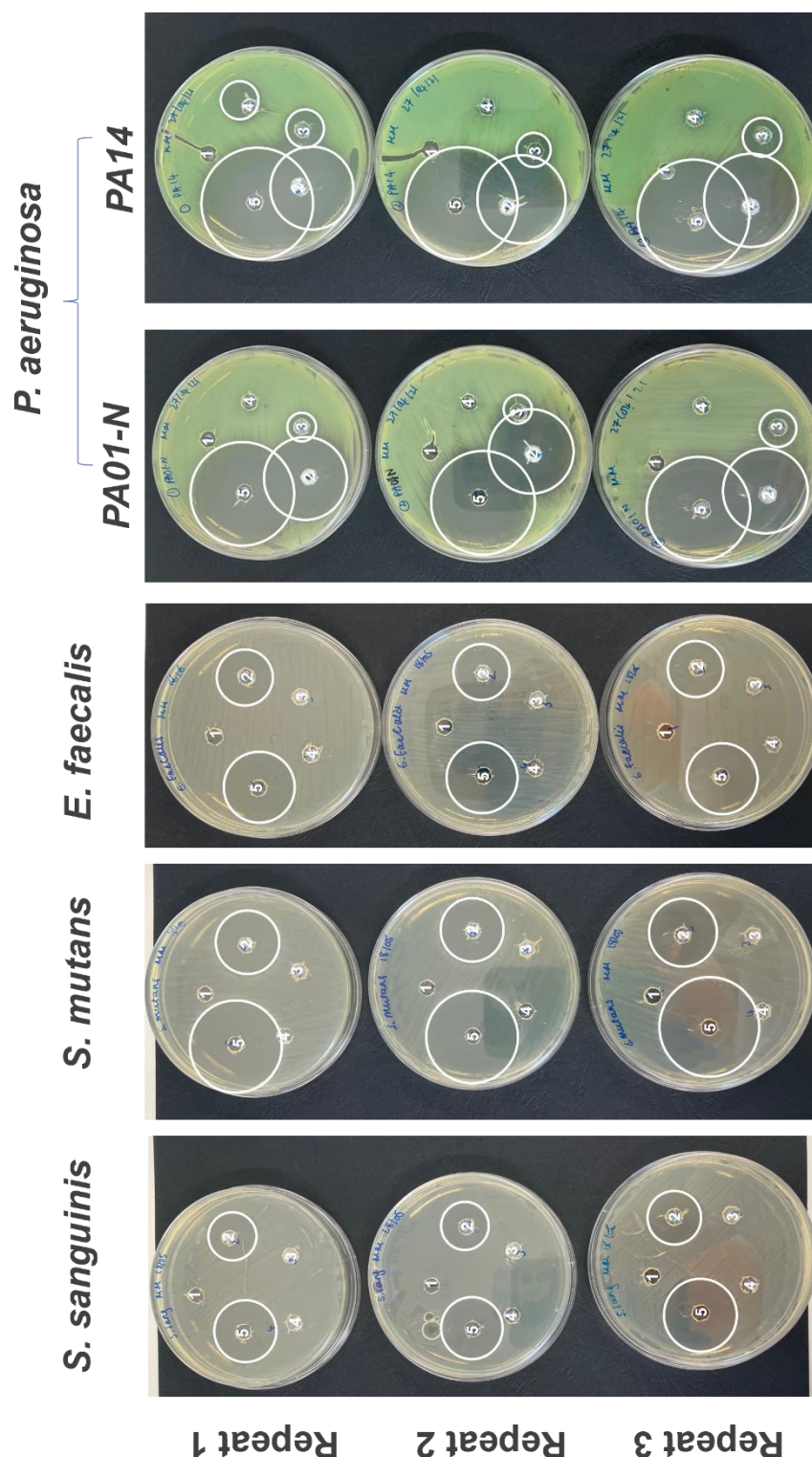


Figure S5. 21: Agar diffusion assay showing zones of growth inhibition around wells with 50 μL of sample. Plate 1 shows: 1: **ultrapure H_2O** (50 μL), 2: **CPX@SNP A** (10 mg mL^{-1}), 3: **CPX@SNP_A2** (10 mg mL^{-1}), 4: **Plain SNP** (10 mg mL^{-1}), 5: **CPX** (2 mg mL^{-1}). The diameters of the zones of inhibition were measured across and averages calculated ($n=3$). Plates inoculated with *S. sanguinis*, *S. mutans*, *E. faecalis* or *P. aeruginosa*; PA14 or PA01N.

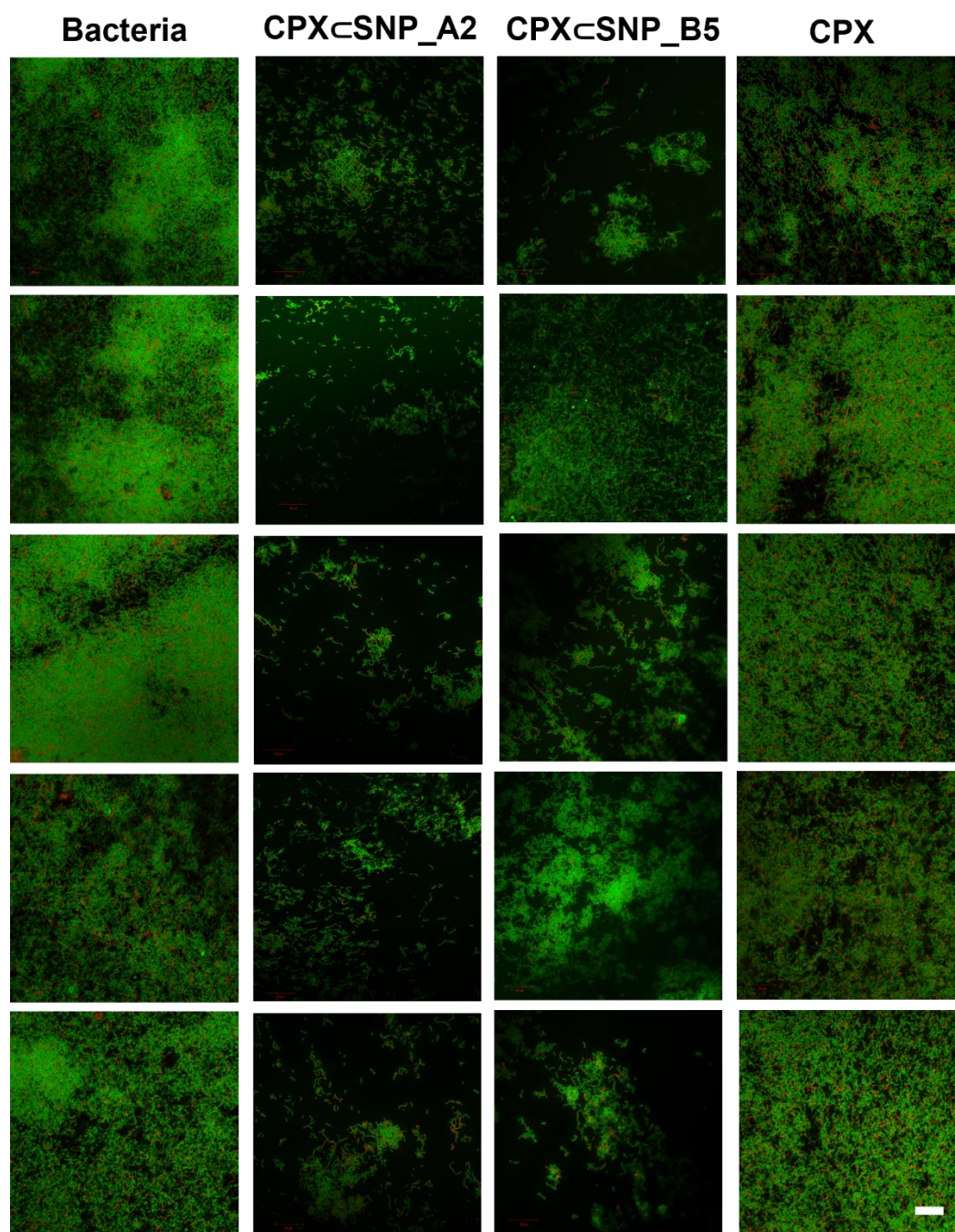


Figure S5. 23: CLSM images of five random areas of 72 h grown *S. sanguinis* biofilm after treatment without US and with the following samples: **bacteria only**, **CPX** ($0.68 \mu\text{g mL}^{-1}$), **CPX \subset SNP_A2** (10 mg mL^{-1}) and **CPX \subset SNP_B5** (10 mg mL^{-1}). All samples were incubated for 30 min at 37°C in 5 % CO_2 before washed and stained with live/dead dyes and fixed for imaging. Images were analysed with automatic image analysis protocol in ImageJ for quantification of the percentage of live (green) and dead (red) bacteria. Scale bar represents $20 \mu\text{m}$.

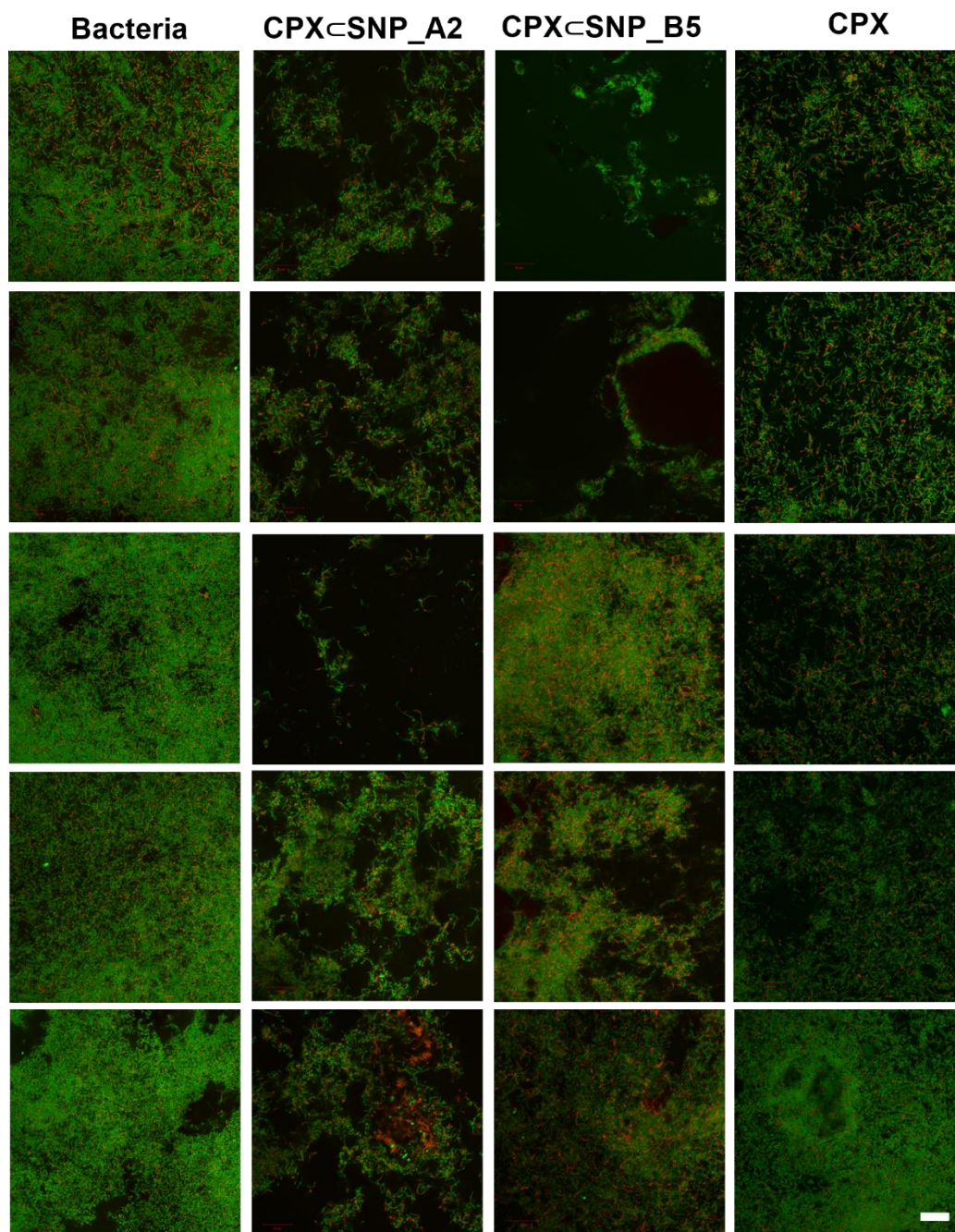


Figure S5. 24: CLSM images of five random areas of 72 h grown *S. sanguinis* biofilm after treatment with US and the following samples: **bacteria only**, **CPX** ($0.68 \mu\text{g mL}^{-1}$), **CPX \subset SNP_A2** (10 mg mL^{-1}) and **CPX \subset SNP_B5** (10 mg mL^{-1}) each with cavitation applied for 10s at power setting P10. All samples were incubated for 30 min at 37°C in 5 % CO_2 before washed and stained with live/dead dyes and fixed for imaging. Images were analysed with automatic image analysis protocol in ImageJ for quantification of the percentage of live (green) and dead (red) bacteria. Scale bar represents $20 \mu\text{m}$.

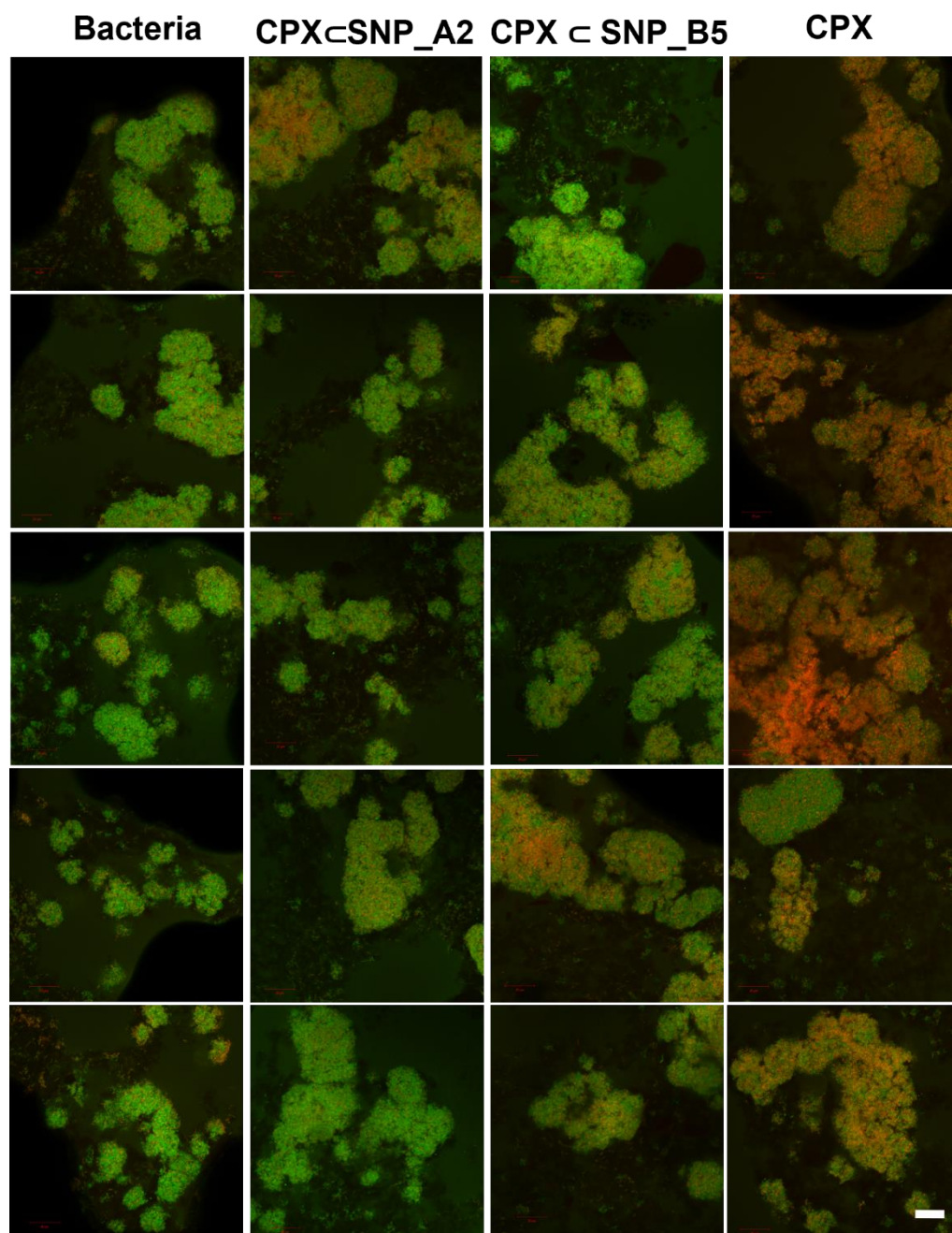


Figure S5. 25 CLSM images of five random areas of 72 h grown *S. mutans* biofilm after treatment without US and with the following samples: **bacteria only**, **CPX** ($0.68 \mu\text{g mL}^{-1}$), **CPX \subset SNP_A2** (10 mg mL^{-1}) and **CPX \subset SNP_B5** (10 mg mL^{-1}). All samples were incubated for 30 min at 37°C in 5 % CO_2 before washed and stained with live/dead dyes and fixed for imaging. Images were analysed with automatic image analysis protocol in ImageJ for quantification of the percentage of live (green) and dead (red) bacteria. Scale bar represents 20 μm .

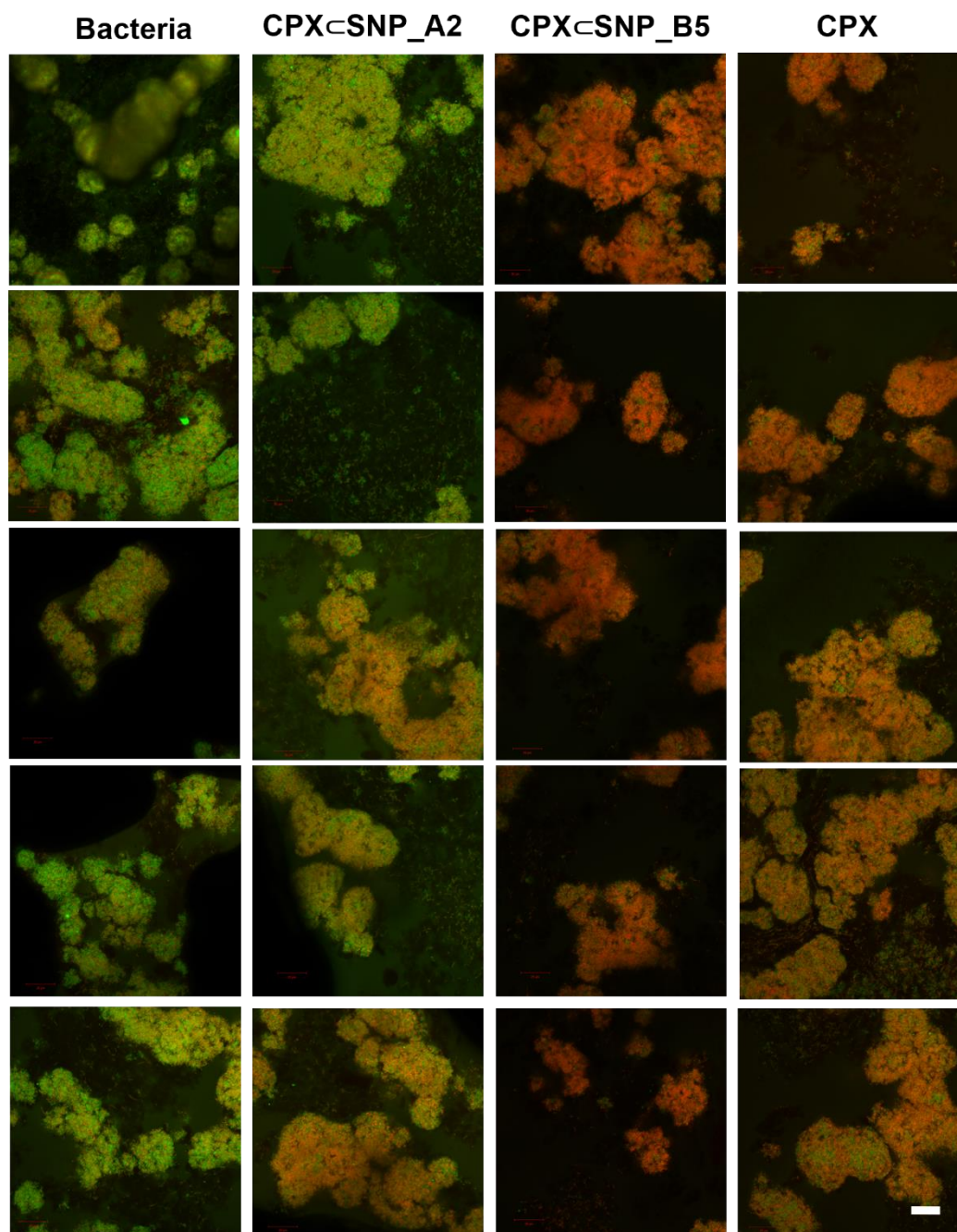


Figure S5. 26: CLSM images of five random areas of 72 h grown *S. mutans* biofilm after treatment with US and the following samples: **bacteria only**, **CPX** ($0.68 \mu\text{g mL}^{-1}$), **CPX \subset SNP_A2** (10 mg mL^{-1}) and **CPX \subset SNP_B5** (10 mg mL^{-1}) each with cavitation applied for 10s at power setting P10. All samples were incubated for 30 min at 37°C in 5 % CO_2 before washed and stained with live/dead dyes and fixed for imaging. Images were analysed with automatic image analysis protocol in ImageJ for quantification of the percentage of live (green) and dead (red) bacteria. Scale bar represents $20 \mu\text{m}$.

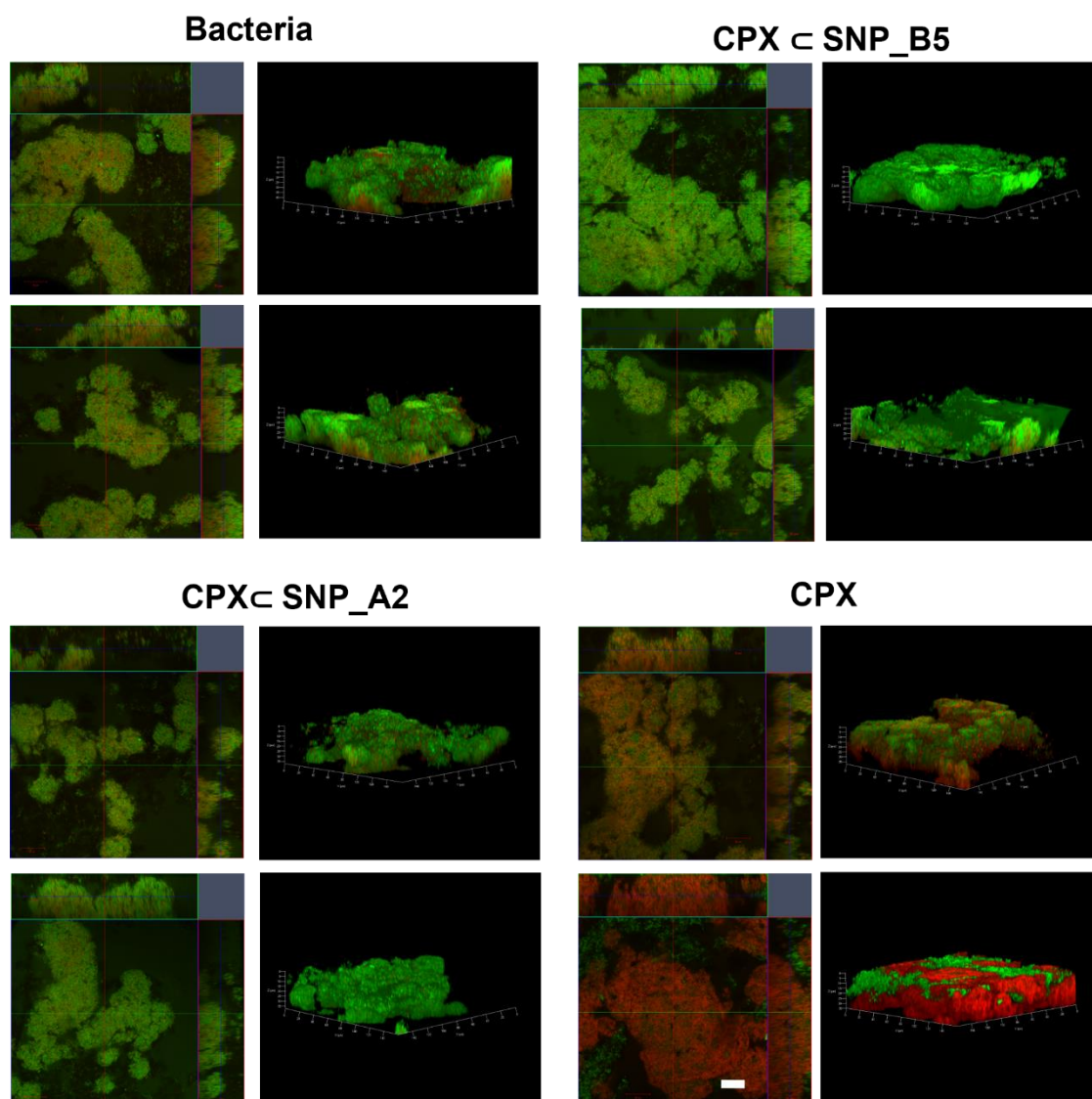


Figure S5. 27: CLSM images constructed of z-stacked images of random areas of 72 h grown *S. mutans* biofilm after treatment without US and with the following samples: **bacteria only**, **CPX** ($0.68 \mu\text{g mL}^{-1}$) and **CPX \subset SNP_A2** (10 mg mL^{-1}) and **CPX \subset SNP_B5** (10 mg mL^{-1}). All samples were incubated for 30 min at 37°C in 5 % CO_2 before washed and stained with live/dead dyes and fixed for imaging. Images were analysed with automatic image analysis protocol in ImageJ for quantification of the percentage of live (green) and dead (red) bacteria. Scale bar represents $20 \mu\text{m}$.

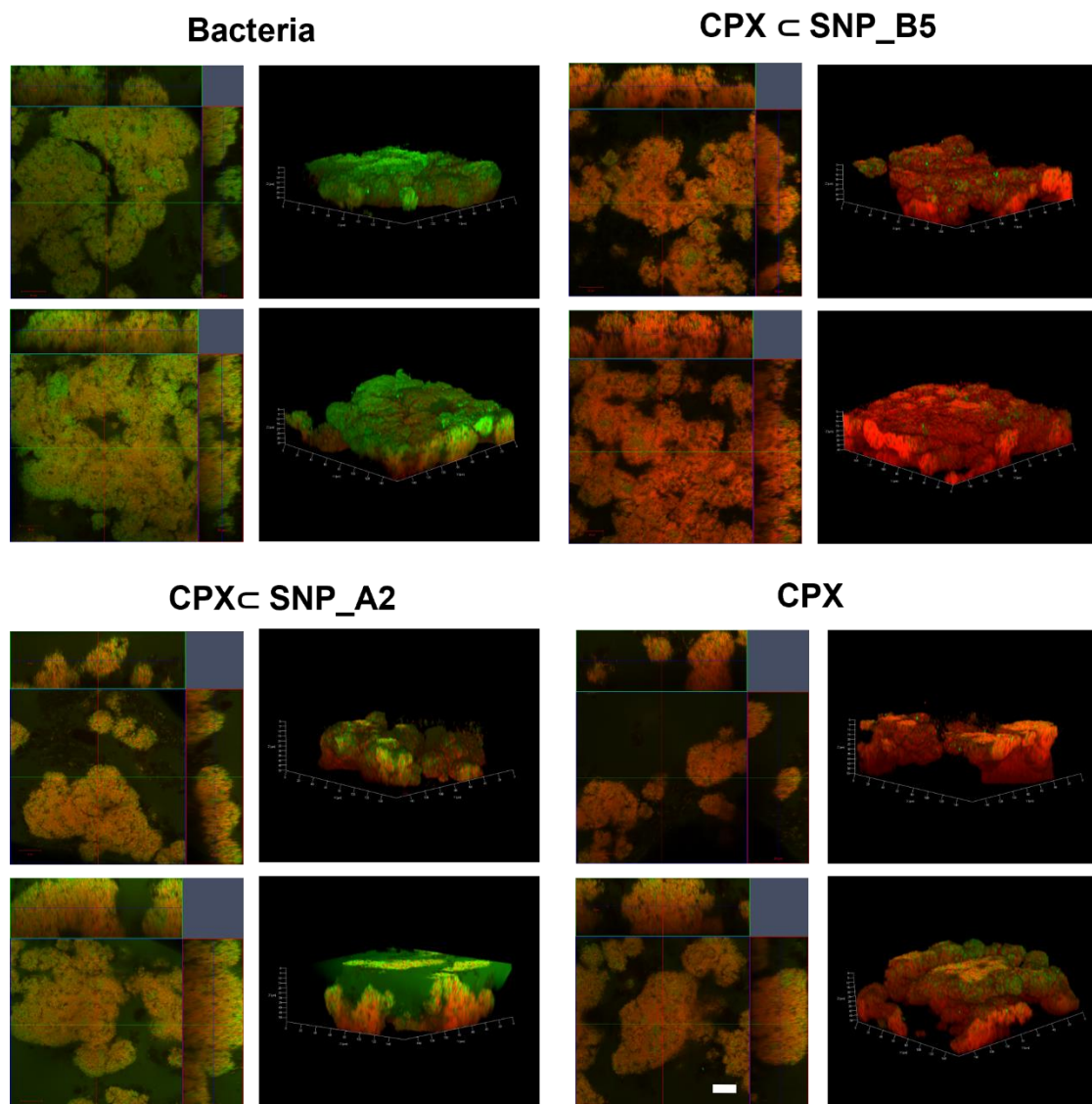


Figure S5. 28: CLSM images constructed of z-stacked images of random areas of 72 h grown *S. mutans* biofilm after treatment with US and the following samples: **bacteria only**, **CPX** ($0.68 \mu\text{g mL}^{-1}$) and **CPX \subset SNP_A2** (10 mg mL^{-1}) and **CPX \subset SNP_B5** (10 mg mL^{-1}) each with cavitation applied for 10s at power setting P10. All samples were incubated for 30 min at 37°C in 5 % CO_2 before washed and stained with live/dead dyes and fixed for imaging. Images were analysed with automatic image analysis protocol in ImageJ for quantification of the percentage of live (green) and dead (red) bacteria. Scale bar represents $20 \mu\text{m}$.

5.6. References

- 1 I. F. Persoon and A. R. Özok, *Curr. Oral Heal. Reports*, 2017, **4**, 278–285.
- 2 V. Peciuliene, R. Maneliene, E. Balcikonyte and S. Drukteinis, *Balt. Dent. Maxillofac. J.*, 2008, **10**, 4–9.
- 3 M. B. Ferreira, S. Myiagi, C. G. Nogales, M. S. Campos and J. L. Lage-Marques, *J. Appl. Oral Sci.*, 2010, **18**, 259–263.
- 4 S. N. Kaushik, J. Scofield, A. Andukuri, G. C. Alexander, T. Walker, S. Kim, S. C. Choi, B. C. Brott, P. D. Eleazer, J. Y. Lee, H. Wu, N. K. Childers, H. W. Jun, J. H. Park and K. Cheon, *Biomater. Res.*, 2015, **19**, 1–10.
- 5 J. F. Siqueira, *Oral Surgery, Oral Med. Oral Pathol. Oral Radiol. Endodontology*, 2002, **94**, 281–293.
- 6 G. Svensater and G. Bergenholtz, *Endod. Top.*, 2004, **9**, 27–36.
- 7 G. J. Khan, R. A. Khan, I. Majeed, F. A. Siddiqui and S. Khan, *Prof. Med. J.*, 2015, **22**, 001–005.
- 8 G. Anquetin, J. Greiner, N. Mahmoudi, M. Santillana-Hayat, R. Gozalbes, K. Farhati, F. Derouin, A. Aubry, E. Cambau and P. Vierling, *Eur. J. Med. Chem.*, 2006, **41**, 1478–1493.
- 9 W. E. Kantz and C. A. Henry, *Arch. Oral Biol.*, 1974, **19**, 91–96.
- 10 H. J. Rolph, A. Lennon, M. P. Riggio, W. P. Saunders, D. MacKenzie, L. Coldero and J. Bagg, *J. Clin. Microbiol.*, 2001, **39**, 3282–3289.
- 11 G. S. Tillotson, *J. Med. Microbiol.*, 1996, **44**, 320–324.
- 12 D. T. W. Chu and P. B. Fernandes, *Antimicrob. Agents Chemother.*, 1989, **33**, 131–135.
- 13 J. D. Walters, F. Zhang and R. J. Nakkula, *Antimicrob. Agents Chemother.*, 1999, **43**, 2710–2715.
- 14 F. Collin, S. Karkare and A. Maxwell, *Appl. Microbiol. Biotechnol.*, 2011, **92**, 479–497.
- 15 D. Sharma, R. P. Patel, S. T. R. Zaidi, M. M. R. Sarker, Q. Y. Lean and L. C. Ming, *Front. Pharmacol.*, 2017, **8**, 1–7.
- 16 O. Fasugba, A. Gardner, B. G. Mitchell and G. Mnatzaganian, *BMC Infect. Dis.*, 2015, **15**, 545.
- 17 A. Soares, V. Roussel, M. Pestel-Caron, M. Barreau, F. Caron, E. Bouffartigues, S. Chevalier and M. Etienne, *Front. Microbiol.*, 2019, **10**, 1–10.
- 18 S. M. Hamed, W. F. Elkhatab, H. A. El-Mahallawy, M. M. Helmy, M. S. Ashour and K. M. A. Aboshanab, *Sci. Rep.*, 2018, **8**, 1–10.

- 19 P. C. Sharma, A. Jain, S. Jain, R. Pahwa and M. S. Yar, *J. Enzyme Inhib. Med. Chem.*, 2010, **25**, 577–589.
- 20 Y. C. Yeh, T. H. Huang, S. C. Yang, C. C. Chen and J. Y. Fang, *Front. Chem.*, 2020, **8**, 1–22.
- 21 M. E. Page-Clisson, H. Pinto-Alphandary, M. Ourevitch, A. Andremonet and P. Couvreur, *J. Control. Release*, 1998, **56**, 23–32.
- 22 C. Günday, S. Anand, H. B. Gencer, S. Munafò, L. Moroni, A. Fusco, G. Donnarumma, C. Ricci, P. C. Hatir, N. G. Türeli, A. E. Türeli, C. Mota and S. Danti, *Drug Deliv. Transl. Res.*, 2020, **10**, 706–720.
- 23 C. Gheffar, H. Le, T. Jouenne, A. Schaumann, A. Corbière, D. Vaudry, D. LeCerf and C. Karakasyan, *Part. Part. Syst. Charact.*, 2021, **38**, 1–9.
- 24 Z. Sobhani, S. M. Samani, H. Montaseri and E. Khezri, *Adv. Pharm. Bull.*, 2017, **7**, 427–432.
- 25 H. Al-Obaidi, R. Kalgudi and M. G. Zariwala, *Eur. J. Pharm. Biopharm.*, 2018, **128**, 27–35.
- 26 B. de J. Mora, L. Filipe, A. Forte, M. M. Santos, C. Alves, F. Teodoro, R. Pedrosa, M. R. Carrott, L. C. Branco and S. Gago, *Pharmaceutics*, 2021, **13**, 1–16.
- 27 I. Gessner, E. Krakor, A. Jurewicz, V. Wulff, L. Kling, S. Christiansen, N. Brodusch, R. Gauvin, L. Wortmann, M. Wolke, G. Plum, A. Schauss, J. Krautwurst, U. Ruschewitz, S. Ilyas and S. Mathur, *RSC Adv.*, 2018, **8**, 24883–24892.
- 28 G. F. Andrade, V. S. Gomide, A. C. da Silva Júnior, A. M. Goes and E. M. B. de Sousa, *J. Mater. Sci. Mater. Med.*, 2014, **25**, 2527–2540.
- 29 M. J. Rosemary, I. MacLaren and T. Pradeep, *Langmuir*, 2006, **22**, 10125–10129.
- 30 G. F. Andrade, J. A. Q. A. Faria, D. A. Gomes, A. L. B. de Barros, R. S. Fernandes, A. C. S. Coelho, J. A. Takahashi, A. da Silva Cunha and E. M. B. de Sousa, *J. Sol-Gel Sci. Technol.*, 2018, **85**, 369–381.
- 31 N. Ehlert, M. Badar, A. Christel, S. J. Lohmeier, T. Luessenhop, M. Stieve, T. Lenarz, P. P. Mueller and P. Behrens, *J. Mater. Chem.*, 2011, **21**, 752–760.
- 32 M. G. Arafa, H. A. Mousa and N. N. Afifi, *Drug Deliv.*, 2020, **27**, 26–39.
- 33 Y. Bourgat, C. Mikolai, M. Stiesch, P. Klahn and H. Menzel, *Antibiotics*, 2021, **10**, 653.
- 34 S. Khorshidi and A. Karkhaneh, *J. Biosci.*, 2018, **43**, 959–967.
- 35 W. Stober, A. Fink and E. Bohn, *J. Colloid Interface Sci.*, 1968, **26**, 62–69.
- 36 M. E. Olivera, R. H. Manzo, H. E. Junginger, K. K. Midha, V. P. Shah, S.

- Stavchansky, J. B. Dressman and D. M. Barends, *J. Pharm. Sci.*, 2011, **100**, 22–23.
- 37 F. Varanda, M. J. Pratas De Melo, A. I. Caço, R. Dohrn, F. A. Makrydaki, E. Voutsas, D. Tassios and I. M. Marrucho, *Ind. Eng. Chem. Res.*, 2006, **45**, 6368–6374.
- 38 F. Tang, L. Li and D. Chen, *Adv. Mater.*, 2012, **24**, 1504–1534.
- 39 V. Selvarajan, S. Obuobi and P. L. R. Ee, *Front. Chem.*, 2020, **8**, 1–16.
- 40 B. G. Trewyn, I. I. Slowing, S. Giri, H. Chen and V. S.-Y. Lin, *Acc. Chem. Res.*, 2007, **40**, 846–853.
- 41 H. A. Friedel, D. M. Campoli-Richards and K. L. Goa, *Drugs*, 1989, **37**, 491–522.
- 42 CLSI, *CLSI M100-ED29: 2019 Performance Standards for Antimicrobial Susceptibility Testing, 29th Edition*, 2019.
- 43 G. T. Hansen, X. Zhao, K. Drlica and J. M. Blondeau, *Int. J. Antimicrob. Agents*, 2006, **27**, 120–124.
- 44 Y. Cao, H. Yin, W. Wang, P. Pei, Y. Wang, X. Wang, J. Jiang, S. Z. Luo and L. Chen, *Amino Acids*, 2020, **52**, 1–14.
- 45 T. Do, D. Devine and P. D. Marsh, *Clin. Cosmet. Investig. Dent.*, 2013, **5**, 11–19.
- 46 A. H. Nobbs and H. F. Jenkinson, *Microbes Infect.*, 2015, **17**, 484–492.
- 47 M. Haque, M. Sartelli and S. Z. Haque, *Dent. J.*, 2019, **7**, 1–19.
- 48 M. W. R. Pletz, L. McGee, O. Burkhardt, H. Lode and K. P. Klugman, *Eur. J. Clin. Microbiol. Infect. Dis.*, 2005, **24**, 58–60.
- 49 J. A. A. Hoogkamp-Korstanje and J. Roelofs-Willemse, *J. Antimicrob. Chemother.*, 2000, **45**, 31–39.
- 50 P. Suci and M. Young, *Arch. Oral Biol.*, 2011, **56**, 1055–1063.
- 51 C. D. Cruz, S. Shah and P. Tammela, *BMC Microbiol.*, 2018, **18**, 1–9.
- 52 J. Chotitumnavee, T. Parakaw, R. L. Srisatjaluk, C. Pruksaniyom, S. Pisitpipattana, C. Thanathipanont, T. Amarasingh, N. Tiankhum, N. Chimchawee and N. Ruangsawasdi, *J. Dent. Sci.*, 2019, **14**, 7–14.
- 53 B. Zhu, L. C. Macleod, T. Kitten and P. Xu, *Future Microbiol.*, 2018.
- 54 J. Kreth, J. Merritt and F. Qi, *DNA Cell Biol.*, 2009, **28**, 397–403.
- 55 A. M. Martini, B. S. Moricz, A. K. Ripperger, P. M. Tran, M. E. Sharp, A. N. Forsythe, K. Kulhankova, W. Salgado-Pabón and B. D. Jones, *Front. Microbiol.*, 2020, **11**, 1–15.

- 56 J. Van Houte, *J Dent Res*, 1994, **73**, 672–681.
- 57 M. Matsumoto-Nakano, *Jpn. Dent. Sci. Rev.*, 2018, **54**, 22–29.
- 58 J. H. Merritt, D. E. Kadouri and G. A. O'Toole, in *Current Protocols in Microbiology*, John Wiley & Sons, Inc., Hoboken, NJ, USA, 2005.
- 59 S. Banavar Ravi, S. Nirupad, P. Chippagiri and R. Pandurangappa, *Int. J. Dent.*, 2017, **2017**, 1–5.
- 60 A. R. Petosa, D. P. Jaisi, I. R. Quevedo, M. Elimelech and N. Tufenkji, *Environ. Sci. Technol.*, 2010, **44**, 6532–6549.
- 61 M. F. H. Jr, S. K. Lower, P. A. Maurice, R. L. Penn, N. Sahai, D. L. Sparks and B. S. Twining, 2008, **319**, 1631–1636.
- 62 K. Ikuma, A. W. Decho and B. L. T. Lau, *Front. Microbiol.*, 2015, **6**, 1–6.
- 63 W. H. Bowen, R. A. Burne, H. Wu and H. Koo, *Trends Microbiol.*, 2018, **26**, 229–242.
- 64 T. C. Zhang and P. L. Bishop, *Water Res.*, 1994, **28**, 2267–2277.
- 65 D. Davies, *Nat. Rev. Drug Discov.*, 2003, **2**, 114–122.
- 66 H. Devlin, D. Hiebner, C. Barros, S. Fulaz, L. Quinn, S. Vitale and E. Casey, *Colloids Surfaces B Biointerfaces*, 2020, **193**, 111123.
- 67 L. C. Powell, M. Abdulkarim, J. Stokniene, Q. E. Yang, T. R. Walsh, K. E. Hill, M. Gumbleton and D. W. Thomas, *npj Biofilms Microbiomes*, 2021, **7**, 13.
- 68 A. Abbaszadegan, Y. Ghahramani, A. Gholami, B. Hemmateenejad, S. Dorostkar, M. Nabavizadeh and H. Sharghi, *J. Nanomater.*, 2015, **2015**, 1–8.
- 69 K. Forier, K. Raemdonck, S. C. De Smedt, J. Demeester, T. Coenye and K. Braeckmans, *J. Control. Release*, 2014, **190**, 607–623.
- 70 C. H. N. Barros, S. Fulaz, S. Vitale, E. Casey and L. Quinn, *PLoS One*, 2020, **15**, 1–15.
- 71 S. Vihodceva, A. Šutka, M. Sihtmäe, M. Rosenberg, M. Otsus, I. Kurvet, K. Smits, L. Bikse, A. Kahru and K. Kasemets, *Nanomaterials*, 2021, **11**, 1–26.
- 72 E. M. Hetrick, J. H. Shin, H. S. Paul and M. H. Schoenfisch, *Biomaterials*, 2009, **30**, 2782–2789.

Chapter 6: Conclusions & Future Work

6.1. Conclusions

The main aim of this thesis was to tackle problems in dental healthcare by using nanotechnology with ultrasound. A potential promising local treatment has been developed that allows for controlled and rapid release of antibacterial agents at the site of infection. With limited drugs in the pipeline and current antimicrobial agents becoming less effective,^{1,2} this work shows potential to overcome issues of increasing drug resistance, by localised delivery and enhanced antibacterial activity.

To accelerate particle-based therapies into dental practices, a suitable drug delivery system was designed. The first chapter focused on accomplishing a one-step procedure to encapsulate cetylpyridinium chloride into silica nanoparticles. The release behaviour of **CPC@SNP** was investigated with a widely used clinical tool, an ultrasonic scaler. The key finding from these studies showed the drug release kinetics were controlled by US and was essential for fast release of CPC. It was strongly assumed the mechanism of release was due to effects of cavitation produced from the ultrasonic tip. For example, rapid bubble formation and implosion can cause high energy shockwaves, that upon collision with surfaces can lead to damage. Also, cavitation could be responsible producing hydroxy free radicals in water upon changes to the local pressure, generating high temperatures and pressure.^{3,4} A limitation of this work was the detection of cavitation bubbles and the dynamics around the ultrasonic tip. In the future this can be investigated with chemiluminescence.⁵ However, in this work the mode of release was validated by HR-TEM images, which showed physical changes

to the silica surface, a consequence of mechanical and thermal effects produced from US.

Previous works have commonly reported US-responsive SNPs as the drug carrier designed to focus on preventing uncontrolled release using surface-modifications.^{6,7} These have required complex multi-step procedures, additional characterisation and purification steps.⁸ As a result, can increase the risks of compromising the safety and toxicity of NPs for clinical translation. Furthermore, the majority of silica NP systems have been developed for the ultrasonic-triggered release of anticancer agents.⁹ In this work, a simple and reproducible synthesis of a core@shell silica NP was demonstrated with a one-pot process. This work contributes to the literature as it is the first ultrasound-responsive silica drug delivery system to release antibacterial agents.

The research has also shown to enhance the antimicrobial efficiency of CPC by being encapsulated in silica. CPC is a frequently used antimicrobial agent that is at risk of potential bacterial drug resistance.¹⁰ Due to the vast majority of *in vitro* studies conducted on planktonic bacteria, in this work mature biofilms consisting of *S. sanguinis* were used. This was a better representation to test the antibacterial activity and against a species important to oral health. Until now, ultrasonic scalers have only been used for plaque removal in the dental clinic, which is not sufficient enough. The combination of **CPC@SNP** with US was essential to achieving a potent synergistic antimicrobial effect. These findings have significant implications, as **CPC@SNP** was ineffective without US and vice-versa. Not only was US important for the release of CPC but for mechanical disruption to the biofilm. This could have been by improved dispersion of **CPC@SNP** or permeabilization to the cell membrane to increase the susceptibility to the drug loaded SNPs.^{11,12}

Finally, the last chapter builds on the work of **CPC-SNP**. This showed the drug delivery system could be adapted to incorporate antibiotics, such as CPX. The relevance of this work highlighted **CPC-SNP** could be used as a model drug delivery system to include other drugs. It could interest other researchers to conduct further studies using the synthesis methods developed in this thesis. For example, changing the sizes of **CPX-SNP**, effected the release kinetics with US and the antibacterial activity.

6.2. Clinical relevance & Future work

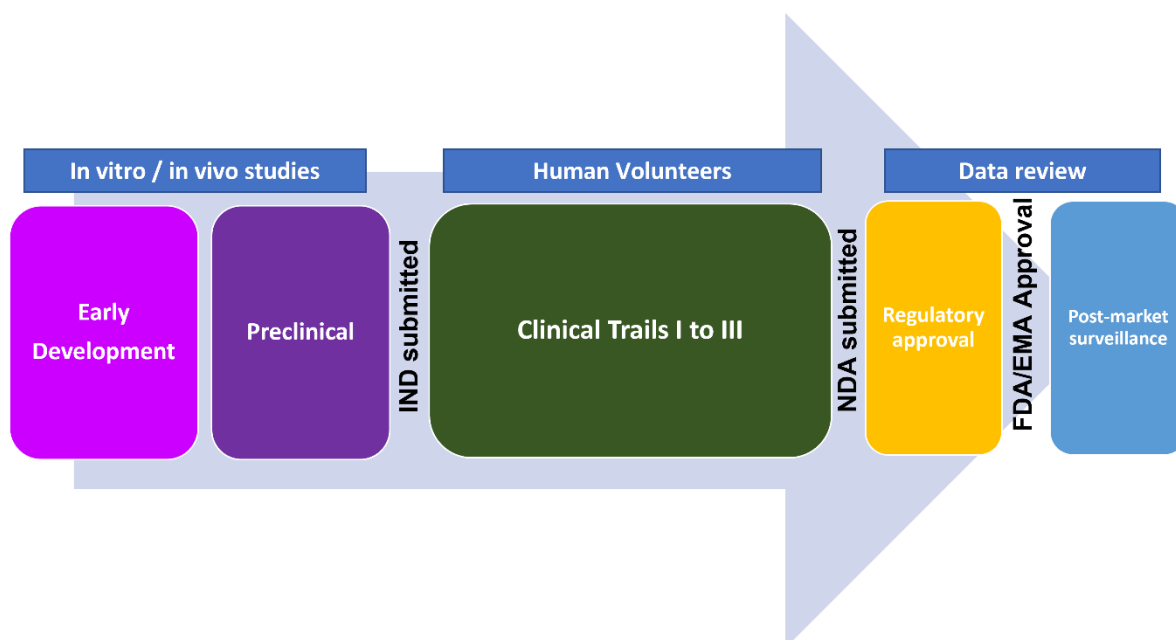


Figure 6. 1: Timeline to show the potential pathway and steps required to develop drug loaded SNPs as a treatment for dental application. IND: investigational new drug. NDA: new drug application. FDA: food and drug administration. EMA: European medicines agency.

The **CPC-SNP** have been envisioned to be formulated into a paste or a solution, so that it can be applied directly to the site of infection in the oral cavity. The administration would need a specialist, such as dental clinician or hygienist. The ultrasonic scaler tip would provide vibrations that can stimulate the active drug and

disrupt the biofilm. This would be a short as 10 seconds of US and then 30-minute wait before rinsing would be needed. However, with further studies this time could be improved. This kind of regime would ideally need a routine check-up to examine the prevention of caries, periodontal and peri-implant infections to provide a more effective treatment.

Before the end goal of a drug particle treatment used as a clinical application, there are other milestones that would need to be met, as shown in **Figure 6. 1**. The research and work in this thesis, is still at the early development stage. Synthesis routes and US release studies have been established. In the short term, screening of other antibiotics and antibacterial agents can be used in a nanoparticle system. This would build a library of drug particle therapies that could be tested for a range of oral infections and diseases, but also help the fight against the rise in antimicrobial resistance. More pre-clinical studies, both *in vitro* and *in vivo*, would be essential to understanding the mechanism of action of the SNPs on various bacterial species. Currently, reported in this work were single species biofilms, consisting of oral bacteria designed as a proof-of-concept model. Therefore, not only testing on different strains of Gram-negative and Gram-positive bacteria is needed, but also multi-species to replicate the complexity of an oral biofilm and the determine the antimicrobial efficacy. In addition, taking into account the harsh conditions of the microenvironment in the oral cavity, such as saliva, interaction with the tooth surfaces and pH.

Other short-term steps that would be necessary, would be the formulation of the drug loaded particles. Optimisation of the particle formulation will allow for ease of administration at the infected site. Like any medicine approved, the formulation is essential for scalability and especially for stability, biodegradability, and functionality in

various conditions. The dosage contained in the formulation is important as well, which links to the safety and efficacy of nanoparticle-based therapies. Many nanoparticle therapies are comprised during the clinical trials stage and are not approved by the regulatory board. One of this reason is because of their toxicity to humans and the uncertainty of the effect of small sizes. In this case, the **CPC-SNP** and **CPX-SNP** were larger than 100 nm and thought the toxicity to healthy mammalian cells would not be compromised. However, the safety profile of SNPs is vital, and assays would access the intracellular accumulation in both bacterial and mammalian cells is important. For example, imaging experiments to track the uptake into cells and flow cytometry is a technique can be used to quantify particle internalisation.

In the long-term, the drug loaded SNPs would need approval to conduct clinical trials from phases I to III. This would consist of healthy and patient volunteers where the dosage regime would be tested alongside the safety and efficacy. Finally, the SNP treatment with US to be used in the dental clinic would need overall approval from a regulatory board, such as from Food and Drug Administration or European medicine agency.

This multi-disciplinary work has initiated the potential for a new treatment using US for antibiotic delivery in dental healthcare. However, it is relevant to other areas of healthcare, where localised treatment of infection is challenging, such as prosthetics and catheters.

6.3. References

- 1 B. Aslam, W. Wang, M. I. Arshad, M. Khurshid, S. Muzammil, M. H. Rasool, M. A. Nisar, R. F. Alvi, M. A. Aslam, M. U. Qamar, M. K. F. Salamat and Z. Baloch, *Infect. Drug Resist.*, 2018, **11**, 1645–1658.
- 2 J. A. Al-Tawfiq, H. Momattin, A. Y. Al-Ali, K. Eljaaly, R. Tirupathi, M. B. Haradwala, S. Areti, S. Alhumaid, A. A. Rabaan, A. Al Mutair and P. Schlagenhauf, *Infection*, 2022, **50**, 553–564.
- 3 S. C. Lea, G. J. Price and A. D. Walmsley, *Ultrason. Sonochem.*, 2005, **12**, 233–236.
- 4 N. Vyas, E. Pecheva, H. Dehghani, R. L. Sammons, Q. X. Wang, D. M. Leppinen and A. D. Walmsley, *PLoS One*, 2016, **11**, 2–13.
- 5 G. J. Price, T. J. Tiong and D. C. King, *Ultrason. Sonochem.*, 2014, **21**, 2052–2060.
- 6 A. Sikder, A. Chaudhuri, S. Mondal and N. D. P. Singh, *ACS Appl. Bio Mater.*, 2021, **4**, 4667–4683.
- 7 C. A. Cheng, T. Deng, F. C. Lin, Y. Cai and J. I. Zink, *Theranostics*, 2019, **9**, 3341–3364.
- 8 L. Tang and J. Cheng, *Nano Today*, 2013, **8**, 290–312.
- 9 A. Rahikkala, S. A. P. Pereira, P. Figueiredo, M. L. C. Passos, A. R. T. S. Araújo, M. L. M. F. S. Saraiva and H. A. Santos, *Adv. Biosyst.*, 2018, **2**, 1–33.
- 10 P. K. Sreenivasan, V. I. Haraszthy and J. J. Zambon, *Lett. Appl. Microbiol.*, 2013, **56**, 14–20.
- 11 M. A. Oberli, C. M. Schoellhammer, R. Langer and D. Blankschtein, *Ther. Deliv.*, 2014, **5**, 843–857.
- 12 S. Gopalakrishnan, A. Gupta, J. M. V. Makabenta, J. Park, J. J. Amante, A. N. Chattopadhyay, D. Matuwana, C. J. Kearney and V. M. Rotello, *Adv. Healthc. Mater.*, 2022, **2201060**, 1–8.

List of Achievements

Publications

- Application note in collaboration with Oxford HighQ: Drug unloading measurement of APIs on a particle-by-particle basis, Controlled Release Society, B. Ash, G. Baekelandt, A. Trichet, M. Manhota and Z. Pikramenou, 2021.

Conferences presentations

- **Oral Microbiology and Immunology Conference (OMIG)**, Wales, March 2018
 - Oral presentation: M. Manhota, R. Sammons, S. Kuehne, H. Dehghani, Z. Pikramenou and A.D. Walmsley. Silica Particles as a Drug Delivery System for Antimicrobial Agents in Dental Applications
 - Award: Runner-up for best oral presentation
- **UKSB Biomaterials Conference**, Bath, June 2018
 - Oral presentation: M. Manhota, N. Vyas, S. Claire, G. Li, R. Sammons, S. Kuehne, H. Dehghani, Z. Pikramenou and A.D. Walmsley. Silica Particles as a Drug Delivery System for Antimicrobial Agents in Dental Applications.
- **European Biological Inorganic Chemistry Conference (EuroBIC)**, Birmingham, August 2018
 - Poster, 3-minute oral flash and 1 minute video presentation: M. Manhota, G. Li, R. Sammons, S. Kuehne, A. D. Walmsley and Z. Pikramenou. Mesoporous Silica Particles as a Drug Delivery System for Antimicrobial Agents in Dental Applications.

- Award: Best 1 minute video presentation
- **Research School of Chemistry Liaison Committee (RSLC)**, Birmingham, August 2019
 - M. Manhota, R. Sammons, S. Kuehne, A. D. Walmsley and Z. Pikramenou. Nanoparticles for Anti-Bacterial Delivery in Dentistry
 - Award: Best oral presentation
- **Sci-Phy Advisory board meeting**, Online, March 2021
 - M. Manhota, R. Sammons, S. Kuehne, A. D. Walmsley and Z. Pikramenou. Nanoparticles for Anti-Bacterial Delivery in Dentistry